



**Molecular Simulation Studies of Adsorption
and Separation of Gases in Nanoporous
Molecular Crystals**

Siyuan Yang

Supervisors: Dr. Lifeng Ding, Prof. Andrew I. Cooper, Dr. Ruiyao Wang

Thesis submitted in accordance with the requirements of the University of Liverpool
for the degree of Doctor of Philosophy

September 2019

Contents

Abstract.....	4
Acknowledgements.....	5
List of Abbreviations	6
List of Publications and Publish-in-Process works	10
Chapter 1 Introduction	11
1.1 Microporous Materials.....	12
1.2 Porosity	12
1.3 Porous Molecular Crystals.....	14
1.4 Porous Imine Cages	19
1.5 Carbon-Carbon Cages.....	20
1.6 Boronate Ester Bond-based Cages.....	20
1.7 Adsorption/separation with porous materials	21
1.8 Aim of the thesis	27
1.8 References.....	27
Chapter 2 Methodology.....	47
2.1 Gas Adsorption in Porous Materials	48
2.3 Geometric Characterization of Porous Crystalline Materials	49
2.3.1 Pore size measurement	49
2.3.2 Surface area	50
2.3.3 Accessible surface area and accessible volume.....	50
2.3.4 Pore size distribution	51
2.3.5 Radial distribution function.....	51
2.4 Molecular Simulation	52
2.4.1 Molecular dynamic simulation.....	52
2.4.2 Ensembles.....	52
2.4.3 Monte Carlo simulation.....	55
2.4.4 Heat of adsorption	62
2.4.5 Free energy profile	63
2.5 Interatomic Potentials	64
2.5.1 Bond stretching.....	65
2.5.2 Angle bending.....	67
2.5.3 Torsional and improper torsional terms.....	67
2.5.4 van der Waals interaction	69
2.5.5 Electrostatic interaction	71
2.5.6 Quantum sieving effect.....	72
2.6 Advanced Simulation methods	73
2.6.1 Configuration biased Monte Carlo method (CBMC).....	73
2.6.2 Continuous fractional component Monte Carlo method (CFCMC).....	75

2.6.3 Hybrid GCMC/MD simulation.....	77
2.7 Computational Software Used.....	79
2.7.1 RASPA package.....	79
2.7.2 Zeo++ package.....	79
2.7.3 Accelry Materials Studio 7.0.....	80
2.8 References.....	80
Chapter 3 Understanding the effect of host flexibility on the adsorption of CH₄, CO₂ and SF₆ in porous organic cages	87
3.1 Introduction.....	88
3.2 Methodology.....	90
3.3 Result and Discussion.....	93
3.3.1 Adsorption isotherms of CH ₄ , CO ₂ , and SF ₆ in CC3-R.....	93
3.3.2 Adsorption positions of CH ₄ , CO ₂ and SF ₆ in CC3-R.....	94
3.3.3 Structural dynamics of CC3-R loaded with CH ₄ , CO ₂ and SF ₆	96
3.5 Conclusion.....	98
3.6 References.....	99
Chapter 4 A molecular-level understanding of linear and branched alkanes adsorption and separation in porous organic cages	102
4.1 Introduction.....	103
4.2 Methodology.....	106
4.3.1 Flexibility effects on linear hydrocarbon adsorption.....	110
4.3.2 Flexibility effects on branched hydrocarbon adsorption.....	114
4.3.3 Competitive adsorption.....	126
4.4 Conclusion.....	128
4.6 References.....	129
Chapter 5 Molecular simulations on volatile nuclides and hydrogen isotope separation	133
5.1 Introduction.....	134
5.2 Computational methodology.....	135
5.3 Results and discussion.....	139
5.4 Conclusion.....	149
5.5 References.....	150
Chapter 6 Conclusion	157
Appendix	160
A.1. Porous Organic Cages in The Cooper's Group.....	161
A.2. Cage special force field for CC3-R.....	168
A.3. Cage special force field validation.....	171
A.4. Force fields validation for alkane adsorptions.....	173
A.5. PMCs molecular units Database.....	174
A.6 OPLS nonbonding parameters.....	184
A.7 Simulation inputs and computational expanse.....	198

Abstract

To date, gas adsorption simulations at a molecular level have been usually carried out using the grand canonical Monte Carlo (GCMC) method, most of which ignore the structural flexibility of the adsorbents. This thesis aims to investigate the flexibility effect on the adsorption and separation behaviours of the porous molecular crystals. Computational results showed the importance of flexibility of porous molecular crystals on these applications. Structure analysis methods were applied to understand and quantify this effect.

Molecular dynamics (MD) simulations that capture the dynamic evolution of a system require a fixed number of particles in the simulation box. We use a hybrid GCMC/MD scheme to include host flexibility in gas adsorption simulations. We study the adsorption of three gases— CH_4 , CO_2 , and SF_6 —in a porous organic cage (POC) crystal, CC3-R, whose structural flexibility is known by experiment to play an important role in the adsorption of large guest molecules. The results suggested that hybrid GCMC/MD simulations could reproduce experimental adsorption results, without modifying the generic force fields. Hybrid GCMC/MD adsorption simulations can accurately reproduce experimental adsorption isotherm of SF_6 in CC3-R. This work also provides a molecular-level understanding of the cooperative adsorption mechanism of SF_6 in the CC3-R molecular crystal.

Linear and branch alkanes adsorption and separation in CC3-R cage were simulated to investigate the flexibility effects further. The simulation results suggested that cage flexibility showed a negligible effect on the adsorption capacity of linear alkane (C4 to C8) adsorption. However, simulations showed that cage flexibility tended to adapt branched alkanes' adsorption in POC. It was concluded that cage flexibility showed significant influence on the branched alkanes adsorption. Especially for branched alkanes with long chains, such as 22-

dimethylbutane, 23-dimethylbutane, 22-dimethylpentane, 23-dimethylpentane, and 33-dimethylpentane, flexible cage showed the possibility of the uptake, which the rigid model was incapable of. In this section, the flexibility effects were further established.

Furthermore, adsorption simulations with both flexible and rigid hosts were applied to screen CH_3I and I_2 capture in porous molecular crystals at low concentrations. The rigid approach largely overestimated their capture performance, which could compromise the accuracy of the screen result. CC3R, CC3RS were POCs with the best I_2 capture material among our studied range. Furthermore, GCMC/MD simulation with host flexibility included showed that 6ET-RCC3, CC3S and the cocrystal possessed the excellent capability to separate H_2/D_2 .

Acknowledgements

I would like to express my sincere thanks to Dr. Lifeng Ding for giving me this opportunity to study as a PhD candidate within his group. He has provided me with not only academic but life guidance for the past four years. I am grateful for his constant patience and encouragement during this journey, without which none of this would be possible. Thanks to his trust and correction, which is invaluable.

Also, I would like to thank my second supervisors Prof. Andy Cooper and Dr. Ruiyao Wang. For the guidance on the paper publication and the chance to participate in the leading project. Notably, Prof. Cooper allowed me to study in his group, which largely accelerated my progress.

A special thanks to Dr. Linjiang Chen, who introduced and helped me build the flexible host adsorption simulation system, which is the core of my PhD project. It is such a pleasure to work next to him, and his talent has inspired my research journey.

Finally, I want to dedicate this thesis to my grandparents and parents, I have received

uncompromised love and trust from them, and I hope my work could make them proud. In the last line, I would like to thank Xuening Deng, who always supports me no matter what.

List of Abbreviations

2mb-C5	2-methylbutane
2mp-C6	2-methylpentane
2mh-C7	2-methylhexane
22dmb-C6	22-dimethylbutane
22dmp-C7	22-dimethylpentane
23dmb-C6	23-dimethylbutane
23dmp-C7	23-dimethylpentane
24dmp-C7	24-dimethylpentane
223tmb-C7	223-trimethylbutane
3mp-C6	3-methylpentane
3mh-C7	3-methylhexane
33dmp-C7	33-dimethylpentane
AV	alanyl-L-valine or accessible volume
ASA	accessible surface area
BET	Brunauer-Emmett-Teller
CC	Cooper's cage
COF	covalent organic framework
CSD	Cambridge Structure Database
CSP	crystal structure prediction
CHDA	R,R- or S,S-cyclohexanediamine
CB[n]	cucurbit[n]uril
CSA	Connolly surface area
CIF	crystallographic information file

CSFF	cage specific force field
CVFF	consistent valence force field
CBMC	configuration biased Monte Carlo
CFCMC	continuous fractional component Monte Carlo
D_i or LCD	largest included sphere
D_f or PLD	largest free sphere
DFT	density function theory
dmp-C5	dimethylpropane
E_{bend}	three-body bending potentials
$E_{\text{electrostatic}}$	electrostatic interaction
E_{stretch}	two-body stretching potentials
E_{torsion}	four-body torsional potentials
E_{total}	sum of total energy
E_{VDW}	Van der Waals interaction
$E_{\text{improper torsion}}$	four body improper torsional potentials
FH	Feynman-Hibbs
GC	chromatography
GCMC	grand canonical Monte Carlo
GCMC/MD	grand canonical Monte Carlo/molecular dynamic
H	enthalpy
HOMC	hybrid osmotic Monte Carlo
HOA or Q_{st}	heat of adsorption
HOD	heat of desorption
IUPAC	International Union of Pure and Applied Chemistry
IV	L-isoleucyl-L-valine
iso-C4	isobutane
K_h	Henry coefficient
LJ	Lenard-Jones

LTA	Linda type A sieve
LDAC	the largest diameter along the accessible channel
MOF	Matal-organic framework
MC	Monte Carlo
MD	molecular dynamic
NPT	isothermal-isobaric ensamble
NVT	canonical ensamble
NPH	isoenthalpic-isobaric ensamble
nC ₄	butane
nC ₅	pentane
nC ₆	hexane
nC ₇	heptane
nC ₈	octane
OPLS	optimized potential for liquid simulation
P	pressure
PAF	porous aromatic framework
PCFF	polymer consistent force field
PMC	porous molecular crystal
PLE	pore limiting envelope
POC	porous organic cage
PXRD	powder X-ray diffraction
PSD	pore size distribution
PI-GCMC	path integral grand canonical Monte Carlo
RDF	radial distribution functions
SSA	solvent surface area
TPP	tris-o-phenylenedioxycyclotriphospha-zene
TTBI	triptycenetrizbenzimidazolone
TBC4	<i>p-tert</i> -butylcalix[4]arene

TFB	1,3,5-triformylbenzene
TrapPE	transferable potential for phase equilibrium
μ	chemical potential
UFF	universal force field
UA	united atom
VA	L-valyl-L-alanine
VI	L-valyl-L-isoleucine
vdW	van der Waals
XRD	X-ray diffraction
ZIF	Zeolitic imidazolate framework

List of Publications and Publish-in-Process works

Siyuan Yang, Linjiang Chen, Daniel Holden, Ruiyao Wang, Yuanyuan Chen, Mona Wells, Andrew I. Cooper, and Lifeng Ding; “Understanding the Effect of Flexibility on the Adsorption of CH₄, CO₂ and SF₆ in Porous Organic Cages”; *Z. Kristallogr*, DOI:10.1515/zkri-2018-2150, (2019)

Siyuan Yang, Linjiang Chen, Ruiyao Wang, Andrew I. Cooper, and Lifeng Ding; “A molecular-level understanding of linear and branched Alkanes Adsorption and Separation in Porous Organic Cages.”; publish in progress.

Siyuan Yang, Linjiang Chen, Ruiyao Wang, Andrew I. Cooper, and Lifeng Ding; “A Top-down Screening Approach of Porous Molecular Crystals for the Adsorption and Separation of Volatile Radioactive Iodine and Methyl Iodide”; publish in progress.

Ming Liu, Linda Zhang, Marc A. Little, Venkat Kapil, Michele Ceriotti, Siyuan Yang, Linjiang Chen, Lifeng Ding, Daniel L. Holden¹, Rafael Balderas-Xicohténcatl, Donglin He, Rob Clowes, Samantha Y. Chong, Gisela Schütz, Michael Hirscher, Andrew I. Cooper; “Barely porous organic cages for hydrogen isotope separation”; *Science*, DOI: aax7427, (2020)

Chapter 1

Introduction

1.1 Microporous Materials

The International Union of Pure and Applied Chemistry (IUPAC) classified porous materials into several categories by their pore sizes, which includes macropores (50 - 1000 nm), mesopores (2 - 50 nm) and micropores (0.2 - 2.0 nm). For the last four years, my work has mainly focused on studying adsorption and separation applications of porous materials within the microporous region. Materials with micropores are essential in many applications, such as gas separation, gas storage, catalysis, sensor and gas storage.¹⁻⁵ With comparable pore size to guest molecules, microporous materials are possible to adsorb them at relatively low pressures.⁶ These applications are commonly found in extended network materials^{4,5,7,8}, such as zeolites, active carbon, polymers⁹, covalent organic frameworks (COFs)⁵, metal-organic frameworks (MOFs)¹⁰ and zeolitic imidazolate frameworks (ZIFs)¹¹. Strong coordinative bonds or covalent bonds are required to form these extended network materials. Computational studies have been extensively exercised to simulate gas adsorption in the extended network porous materials by treating the extended network as rigid structure.¹²⁻¹⁴ on the other hand, porous molecular crystals (PMCs) with no extended network are one intriguing type of materials, and inclining attentions have been put on the investigation of this kind, such as calix[n]arenes¹⁵, dipeptides¹⁶, cucurbit[n]urils¹⁷, and porous organic cages¹⁸⁻²². PMCs with decent permanent porosity are relatively rare. This category of crystals is neither bonded by covalent bonds nor coordination bonds, which renders them considerable local flexibility. High flexibility may lead to structural changes, which can facilitate guest molecular adsorption and diffusion.^{23,24} Hence, the porosities of PMCs are rather ambiguous to define, which are described in the next section.

1.2 Porosity

Porosity can be defined as the persistent empty pores that are interconnected with channels in a specific guest molecule. This definition is valid when the pore apertures are much wider than

the dimension of guest molecules.³ However, the aperture size of microporous materials, especially PMCs in this thesis (all or at least most with an aperture smaller than 1 nm), are quite close to or even smaller than the size of some sorbates but experimentally accessible which make the porosity is hard to define. “Pore without porosity” was termed to address this issue that the material contains permanent pore with no guest-sized channel connection.⁷ The existence of this term suggests the analysis of the static structures of microporous materials, especially PMCs, are not sufficient to describe and understand their porosities. Porosities of PMCs can be categorised as extrinsic porosity and intrinsic porosity.²⁵ Extrinsic porosity is formed by the inefficient packing of discrete PMC units, and intrinsic porosity results from the prefabricated void of the PMC units. The examples of PMCs with extrinsic porosities are presented in figure 1.1. The Dianin’s compounds (figure 1.1 up row) packs to forms the 1D channel during crystallisation allow the diffusion of guest molecules,^{26,27} as well as tris-*o*-phenylenedioxycyclotriphospha-zene (TPP), forms the extrinsic 1D channel that allows the adsorption of CH₄.^{28,29} Materials with intrinsic porosity are also quite attractive. The family of calix[n]arenes (n=4 to 9) are oligomeric macrocycles with intrinsic holes³⁰, and they were reported with decent guest molecules adsorption performance and cooperative diffusion mechanisms.^{23,30,31} Recently, a family of cage-like crystals has been synthesised by reversible bond formation reaction.³² There are several different shape persistence cage-like crystals have been synthesized. Mastalerz et al. presented several adamantoid [4+6] cage crystals.^{32,33} The heme-like coordinational nanoporous molecular crystals triptycenetrisbenzimidazolone (TTBI) synthesized by Oppel’s group, which shows a high Brunauer-Emmett-Teller (BET) surface area of 2796 m²g⁻¹.³⁴ Zhang’s group reported an organic cage crystal with excellent CO₂ selectivity over N₂ with negligible BET surface area around 10m²g⁻¹.³⁵ There are also some organic molecular crystals with covalent bond enforced porosity which have been discovered for many years, for example, cavitands³⁶, cryptophanes³⁷, carcerands³⁸. Nevertheless, these groups of molecules have not been reported with permanent micro-porosity. The next section will detailed review the progress of PMCs investigation.

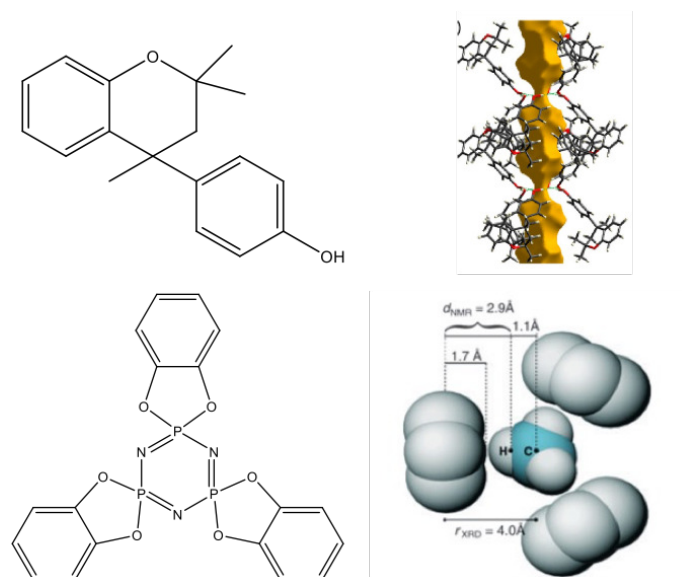


Figure 1.1. Structures of extrinsic porous materials Dianin's compound^{26,27} and its 1D extrinsic channel (up row), and TPP^{28,29} with its host-guest interaction (down row)

1.3 Porous Molecular Crystals

Unlike the porous network materials, such as MOFs or COFs, PMCs with permanent porosity are rather rare. Compared to more than 70,000 MOFs have been deposited to Cambridge Structure Database (CSD) recently³⁹, there are only 481 of PMCs were recognised.⁴⁰ PMCs are different from the porous network materials. These units tend to densely pack with each other to reach the energy preference, which hardly leads to permanent porosity. However, PMCs show several unique properties that intrigue effort of researchers, such as (1) solubility in universal organic solvent,^{41,42} (2) "mix-and-match" properties that allow the mixture of PMCs units to form mixture crystals with mixed functionality,²¹ (3) relevant higher flexibility allows researchers to investigate the dynamic porosity and cooperative porosity.⁴³ Here, I will introduce the current progress of PMCs according to figure 1.2.

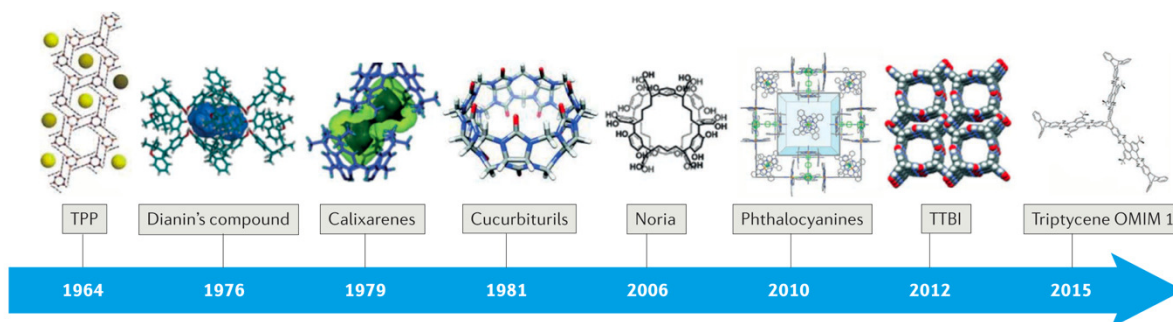


Figure 1.2. The timeline of the development of porous molecular crystals that taken from the works of Cooper et al.⁴⁴

In 1964, Allcock et al. presented the TPP (figure 1.1, down row) which a molecule with “paddle-wheel” structure.⁴⁵ As we discussed above, the molecule packed with each other to form a crystalline structure with a 1D channel (figure 1.3). Sozzani et al. presented the channel for the first time and reported the aperture of the 1D channel is 4.6 Å.⁴⁶ Various gases molecule shows the capability to diffuse in and loaded at this 1D channel including Ar, N₂, O₂, H₂, CH₄, CO₂ and even I₂.⁴⁶⁻⁴⁸

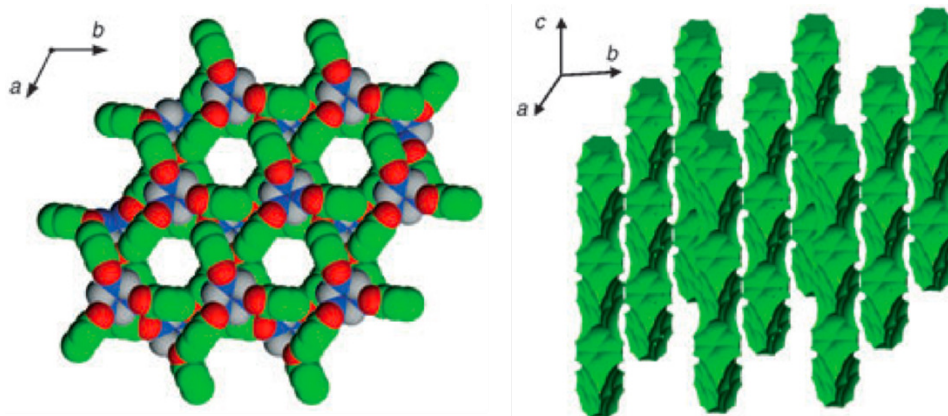


Figure 1.3. The crystal structure and its 1D channels of $3 \times 3 \times 3$ supercell TPP that taken from the work of Sozzani.⁴⁶ The double layers of molecules are presented on the left, where the channel is one the right with computed by Fourier difference maps.

As we mentioned above, Barrer et al. presented the very first PMCs Dianin's compound (figure 1.1) with the capability to adsorb several gases in its extrinsic channel in 1976.^{26,27} The Dianin's compounds can form inclusion complexes during the crystallisation from solution, or it can

capture gases in its pure solid form.²⁶ Barrer et al. suggest Dianin's compound is less rigid than zeolite, while the guest molecules can diffuse through the small aperture into the cavities.²⁶ The observation eventually led to the concept of "pore without porosity".

Later in 1984, Gutsche et al. presented calix[n]arenes that were formed with van der Waals interaction between each discrete unit.⁴⁹ Calix[n]arenes are a group of macrocycle compounds with "cup-like" intrinsic pores that allow the accommodation of several guest molecules.¹⁵ Those calix[n]arenes can be tailored by changing the number (n) of periodic units in a molecule, and the X, R₁, R₂ of each unit (figure 1.4) Barbour et al. reported the closed-packed calix[4]arene (figure 1.4, **1**) could adsorb freons and CH₄ into its interstitial pore (extrinsic pore in this thesis), and keep them even above their boiling point.⁵⁰ The disassembling of the crystal is required to release those gases. Other common calix[4]arenes were also presented in figure 1.2.

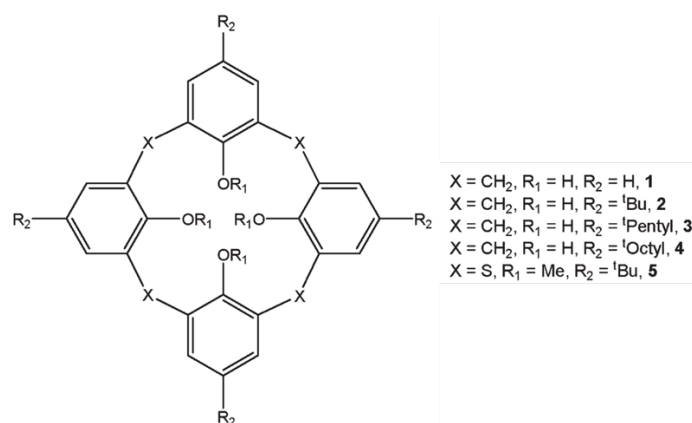


Figure 1.4. The schematic diagrams of calix[4]arenes 1-5 taken from the work of Barbour & Atwood et al. **1**, *p*-H-calix[4]arene;⁵⁰ **2**, *p*-*tert*-butylcalix[4]arene (TBC4);⁵¹⁻⁵⁵ **3**, *p*-*tert*-pentylcalix[4]arene;⁵⁵ **4**, *p*-*tert*-octylcalix[4]arene;⁵⁵ **5**, 5,11,17,23-tetra-*tert*-butyl-25,26,27,28-tetra-methoxy-2,8,14,20-tetrathiacalix[4]arene.⁵⁶

In 1981, Mock et al. named the macrocycle methylene-bridge glycoluril hexamer as "cucurbituril" due to the geometrically alike to Cucurbitaceae family.¹⁷ Figure 1.5 shows the structure of cucurbit[n]uril (CB[n], n = 5 to 8), the sizes of apertures and cavities are increase with the n. Considerable attention has been focused on this family of compounds due to their

intriguing properties, such as the strong binding towards ferrocene derivatives,^{57–59} exploring of new topologies,^{56–58} molecular machines,^{63–67} peptide recognition^{68–74} and the application in drug delivery^{75–81}. However, the adsorption and separation applications based on CB[n]s are rather rare. Seo & Kim reported CB[6] with excellent capacity towards C₂H₂ with ca. 4 mol/mol at 196 K.⁸² CB[7] tends to be amorphous in solid state due to the “odd-even” effect.⁸³ However, the CB[7] shows the distinguished CO₂ selectivity towards CH₄ and N₂.⁸⁴ The theoretical study of H₂S adsorption in CB[7] shows the great promising that up to 5 H₂S molecules can be loads in a cucurbit cavity with bonded energy of -0.1 eV, while -0.3 eV on the sidewall⁸⁵

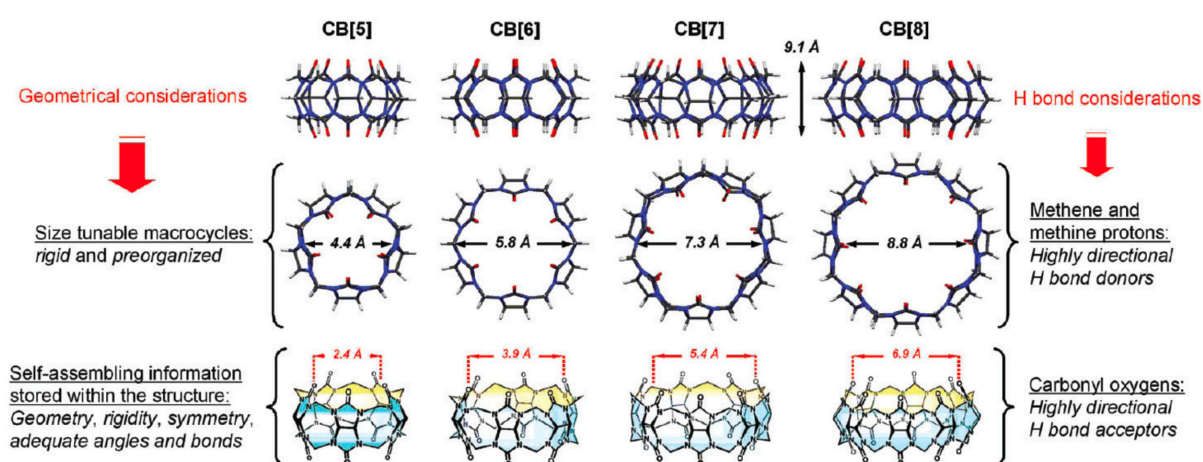


Figure 1.5. The top and side view of CB[5],⁸⁶ CB[6],⁸⁷ CB[7]⁸⁶ and CB[8]⁸⁶ that taken from the work of Bardelang & Ratcliff et al.⁸³ The depth and the smallest and widest van der Waals free diameters of these CB[n]s are presented in this diagrams.

Similarly, a paddle-wheel-shaped molecule, Noria, was synthesised and formed the porous structure in amorphous states.^{88,89} The BET surface area that was measured with N₂ is 40 m²/g. With the loading of CO₂, the BET surface area was expanded to 280 m²/g.

Dipeptides with permanent porosity are attractive due to its inherent biocompatibility.^{90,91} Sozzani et al. reported the first batch dipeptides, which include L-alanyl-L-valine (AV), L-valyl-L-alanine (VA), L-isoleucyl-L-valine (IV) and L-valyl-L-isoleucine (VI) with channels that allows the adsorption of CO₂, CH₄ and H₂.⁹² These four crystalline dipeptides contain 1D channels with the diameters of 5.0 Å, 4.7 Å, 3.9 Å and 3.7 Å respect to the sequence above.⁹²

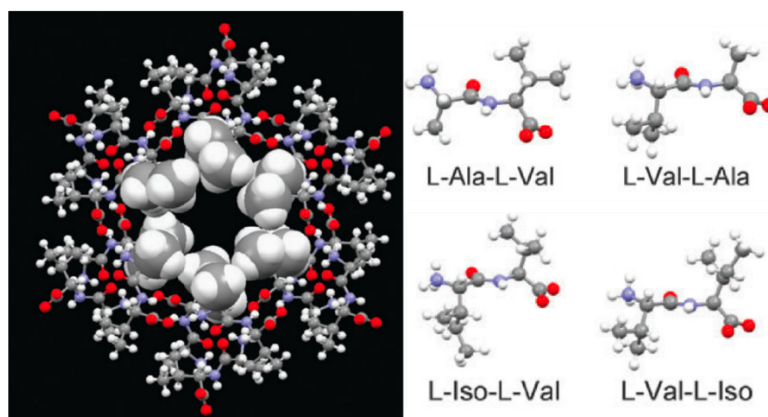


Figure 1.6. Crystal structure of AV and its 1D channel that taken from the work of Sozzani et al.⁹² (Left) The chemical structure of L-alanyl-L-valine (AV), L-valyl-L-alanine (VA), L-isoleucyl-L-valine (IV) and L-valyl-L-isoleucine (VI)

Hulliger et al. reported that the Langmuir surface area of TPP is 240 m²/g, was insufficient for the storage of gases.⁹³ Mastalerz et al. reported a rational approach to construct the TTBI with permanent porosity and high Langmuir of 3020 m²/g.³⁴ As it is shown in figure 1.7, TBBI units are assembled by hydrogen bond, and two 1D channels are labelled as pore **A** and pore **B**. The pore **A** is the 1D channel with the average diameter of 14.5 Å, and the pore **B** is slit-like. The TBBI shows the capacity of 33.7 mmol/g towards N₂ at 77 K and selectivity of CO₂ to CH₄ at 273 K is around 4.³⁴

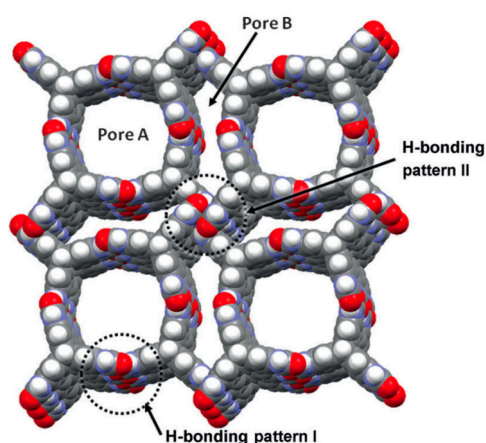


Figure 1.7. The crystal structure of 2 × 2 × 2 supercell of TTBI that taken from the work of Mastalerz et al.³⁴

1.4 Porous Imine Cages

Compare to those PMCs described above, the unique class of PMCs with shape-persistent cages attracts even more attention and develops rapidly. MacDowell reported the very first imine cages with the “one-pot” high yielding in 1988.⁹⁴ The reversible condensation reaction of amines and aldehydes to imines inspires the blooming of PMCs. Later in 2006, Warmuth et al. applied imine condensation to synthesis group of porous imine cages,⁹⁵ however, none of them was reported with a crystal structure.

In 2008, Mastalerz et al. presented a porous imine cage by the condensation of 4 components C_{3v} -symmetric triaminotriptycene and 6 components 4-*tert*-butyl salicyldialdehyde.⁹⁶ Later in 2011, They characterised this [4 + 6] imine cages and presented it with decent BET surface area 1377 m²/g and capability to adsorb several gases.³³ Subsequently, Mastalerz et al. investigated the influence of 4-position and the phenolic hydroxyl group of salicyldialdehyde on the formation of cages, and they found the phenolic hydroxyl group is significant for the formation of cages.⁹⁷⁻⁹⁹ The porous imine cages from Cooper’s group are listed in figure S1 to S10.

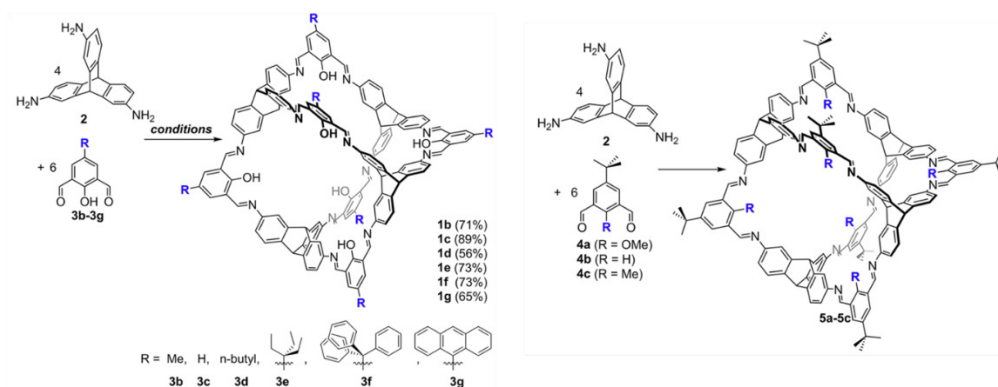


Figure 1.8. influence on the [4+6] imine cages with different substituents on 4-position (left) and hydroxyl group (right) that taken from the work of Mastalerz¹⁰⁰

Subsequently, Mastalerz et al. reported an amorphous [4 + 4] imine cage with the capability to adsorb 18.2 wt % CO₂ at ambient condition and functional selectivity of CO₂/N₂ (34).¹⁰¹ They demonstrated the [2 + 3] later in 2012,¹⁰² and the large [12 + 8] imine cage with a pore size of

2 nm and BET surface of 3758 m²/g.¹⁰³

Zhang et al. reported a [2 + 3] imine cage synthesised by imine condensation in 2010.³⁵ With low void volume, the capacity was quite low. However, the selectivity of CO₂ over N₂ is exceptionally high (73). Similar to Mastalerz, Zhang et al. subsequently reported other [2 + 3] imine cages by moderating the periphery of these cages and expand the CO₂ selectivity to 138.¹⁰⁴ However, the small internal void restricts the application of these materials.

1.5 Carbon-Carbon Cages

Other than imine condensation, Doonan et al. presented the unprecedented directly carbon-carbon bonded porous cages with 20 % of yield.¹⁰⁵ This reaction generally lead to rapid precipitation, the BET surface area can reach to 1153 m²/g.

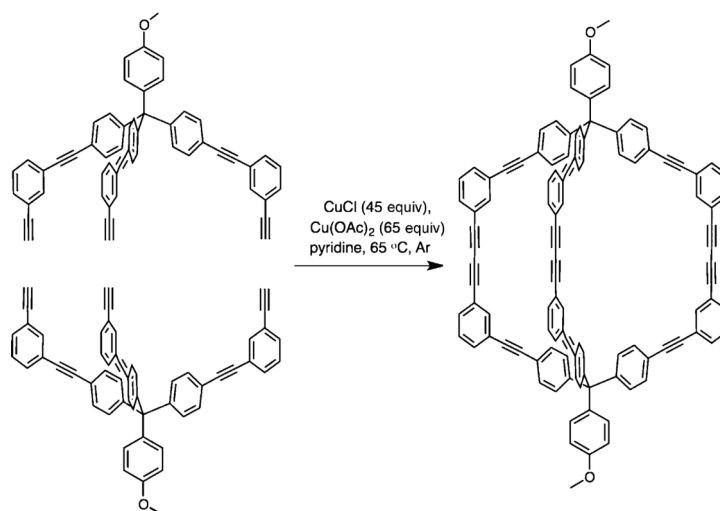


Figure 1.9. Scheme for the synthesis of carbon-carbon cage from the work of Doonan et al.¹⁰⁵

1.6 Boronate Ester Bond-based Cages

To reach to the larger cavity, Mastalerz et al. produce the [8 + 12] cage by using boronate ester chemistry.¹⁰³ This method was previously applied on the COF synthesis, the reversible nature

leads to decent crystalline materials.⁵ This Boronate ester bond-based cage shows the highest BET surface among the PMCs of far (3758 m²/g). The internal cavity is 2.3 nm, which made the cage the first mesoporous PMC.

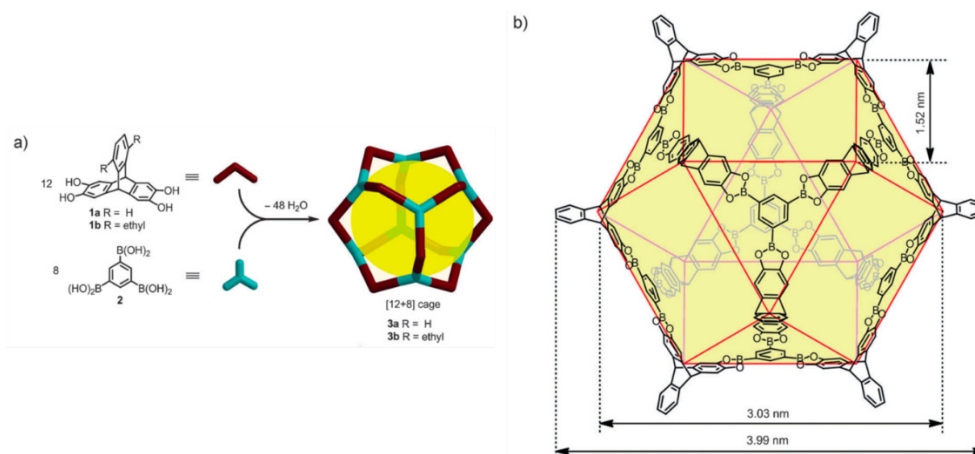


Figure 1.10. (a) The reaction scheme of this [8 + 12] boronate ester bond-based cage and (b) the scaffold of this cage. This figure is taken from the work of Mastalerz et al¹⁰³

1.7 Adsorption/separation with porous materials

Microporous materials underpin a range of industrial gas adsorption and separation processes.^{4,7,8} An accurate understanding of gas adsorption in microporous materials is, therefore, the key to the design of new materials for efficient adsorption and separation. Microporous materials such as metal-organic frameworks (MOFs)¹⁰, covalent-organic frameworks (COFs)¹⁰⁶, zeolitic imidazolate framework (ZIFs)¹⁰⁷, porous aromatic frameworks (PAFs)¹⁰⁸ and porous molecular crystals^{18,32} have emerged as new adsorbents for gas adsorption and separation performances. More recently, porous molecular solids have attracted growing interest in gas adsorption and separation applications.^{9,18,19,21} Unlike MOFs and COFs, which are extended framework structures, porous molecular solids are assembled by close packing of discrete molecular subunits, such as calixarenes and cage-like molecules.^{30,109} Molecular crystals result from the balance of many competing, weak interactions, such as van der Waals (vdW) and electrostatic interactions. The discrete molecular subunits are not connected by strong chemical bonds, which leads to distinct properties such as structural flexibility and

solution processability.^{110–112}

Molecular simulations are a powerful tool for characterising porosity in microporous materials, in principle allowing us to identify optimal structures for a target adsorption/separation application.^{113,114} Most of the existing simulations of gas adsorption in microporous materials—such as MOFs, COFs, ZIFs and PAFs,^{115–118} as well as porous molecular crystals^{119,120}—have been carried out with the GCMC method while treating the host adsorbent structures as rigid, which is referred to here as the “rigid host model”. However, adsorption-induced structural changes to the host adsorbent are commonplace in various classes of microporous materials.^{114,28,121,122} Any dynamic flexibility of the host structure cannot be accounted for by simulations based on the rigid host model, which typically uses the time- and volume-averaged crystal structure from X-ray crystallography.

1.7.1 Small gases adsorption

Molecular-level adsorption simulations for MOFs and COFs were presented with a good match to the experiments based on generic force fields.^{123–136} For example, Lee et al. reported GCMC simulations to show the excellent capability to reproduce the methane adsorption isotherms for IRMOF-1, HKUST-1 and Co-MOF-74 at 298K with both DREIDING and UFF.¹²³ Duren et al. reported results computed by GCMC simulations with an excellent match to IRMOF-1 and IRMOF-6 experiment data. Kawakami et al. tested the framework electrostatic effects on the CO₂ adsorption, which the loading of CO₂ is largely influenced.¹³⁷ Snurr et al. showed charge is a crucial factor in reproducing the experiment adsorption results for MOF-5 at several temperatures.¹³⁸ Zhong et al. shows electrostatic effect contribute 20-30% of CO₂ adsorption at low pressure in IRMOF-14, IRMOF-17 and MOF-177 at 298K.¹³⁹ Nieto-Draghi et al. show electrostatic interactions are important for the reproduction of ZIFs adsorption results, especially at low pressure.¹⁴⁰ Sunrr et al. identified the preferred adsorption site for CO₂ in MOF-5.¹⁴¹ The preference adsorption site is important for gases to capture at low pressure. Hannongbua et al. investigated the adsorption site and the binding energy of CH₄ and CO₂ in

MOF-5 and explained the stronger CO₂ adsorption.¹⁴² Zhong et al. investigated the effects of surface area, pore size and topology on the CO₂ adsorption in several MOFs, and MOFs with pore size between 1 to 2 nm are capable of reaching high uptake.¹³⁹ These effects have also been investigated by Sunrr et al. that smaller pores benefit the CO₂ adsorption at low pressure.¹⁴³ Laird et al. investigated the topology effects on the CO₂ adsorption.¹⁴⁴ The rigid host approach shows proper capability for CO₂ adsorption data reproduction of general MOFs. The MILs are a series of MOFs with “breathing” structure transformation induced by adsorption.¹⁴⁵ The structure of MIL-53(AL) can transfer from narrow pore (np) to large pore (lp). Simple GCMC simulation is not capable of the gas adsorption prediction for this type of materials. Various materials such as carbon^{146,147}, zeolites^{148–150}, MOFs^{151,152} and pillared clays¹⁵³ have been tested for the SF₆ adsorption. The simulation work on the SF₆ adsorption is scarce.

1.7.2 Alkanes and branched alkanes adsorption and separation

The adsorption and separation of linear alkanes and branched alkanes isomers is significant in the petrochemical industry. Currently, catalytic isomerisation is the conventional technique to convert linear alkane to the corresponding branched isomers.¹⁵⁴ The mixture of alkanes isomers produced by isomerisation processes usually need to be separated, and the non-isomerized linear alkanes ought to be recycled. Conventionally, the energetic expensive cryogenic distillation is applied for industrial level separation of hydrocarbons. Porous material-based adsorption separation is a cost-effective alternative approach to separate hydrocarbons. Currently, there are limited porous material species used commercially, which are only for certain types of alkane mixture separation, such as Linde type A (LTA) sieve, which shows decent separation capability of linear alkanes towards branched alkanes, the mono-branched and di-branched alkanes can be accumulated as the product in consequence. However, the di-branched alkanes are generally most desirable. Hence, a selective adsorptive separation material with suitable linear and mono-branched alkane adsorption properties is required.^{155,156}

The adsorption and separation studies of MOFs, as the next generation of nanoporous materials

to zeolites, have been studied intensively. Yaghi et al. reported the high CH₄ and H₂ storage capacities material MOF-1 and established the linkage between the petrochemical industry with MOFs.¹⁵⁷ Later on, Pan et al. exported experimentally [Cu(hfipbb)(H₂hfipbb)_{0.5}] as the first adsorbent that capable of separating butane (nC₄) from longer linear alkanes and olefins.¹⁵⁸ Bloch and coworkers characterized the MOF Fe₂(dobdc) with open metal sites that exhibited excellent separation capability of ethylene/ethane and propylene/propane mixtures at 318K.¹⁵⁹ Denayer *et al.* demonstrated the confine pores of the tetrahedral cages of the Uio-66 and its functionalized analogues, Uio-66-Me, Uio-66-NO₂ and UiO-66-Me₂ causes good adsorption and stereoselective capabilities towards linear alkanes, alkenes, and aromatic compounds.¹⁶⁰ More recently, pulse gas-chromatographic (GC) technique^{161,162} was used to study the adsorption and separation properties of Al-fumarate MOF towards a wide range of hydrocarbon guests. Successful separation of linear alkanes (nC₅ to nC₈) and the di-branched/tri-branched isomers with an adsorption enthalpy difference over 10 kJ/mol has been observed in Al-fumarate. The high adsorption enthalpy difference was responsible for the longer retaining time of linear alkane in Al-fumarate MOF, which subsequently led to a separation of linear and branched alkanes.¹⁶³ Zeolite Imidazolate frameworks (ZIFs), as a sub-family of MOFs, were also reported to have adsorption-based separation ability to alkane isomers. Such as separation applications of biobutanol,¹⁶⁴ C₂/C₃ hydrocarbons,¹⁶⁵ and high kinetic selectivity for the linear alkanes¹⁶⁶ were found in ZIF-8. The adsorption of nC₄ to nC₁₂ in silicalite was simulated by Smit and Siepmann.¹⁶⁷ The longer linear (nC₄ to nC₂₅) alkane chains have also been simulated and analysed under low coverage.¹⁶⁸ Later, Vlucht et al.¹⁶⁹ and Schenk et al.¹⁷⁰ investigated the linear alkane and its branched isomers for both adsorption and binary competitive adsorption separation capability. The “squeezing out” effect was proposed that linear alkane can easily replace its branched isomer due to the higher packing efficiency in the silicalite channels. Calero et al. investigated the entropy effects on the multi-component linear and branched alkanes mixture adsorptions.^{171,172} Snurr et al. simulated the adsorption of methane and butane, and the binary mixture in IRMOFs, and investigated the influence of linkers on the adsorption and separation applications.¹⁷³ Fox et al. explored the temperature dependence of adsorption

and selectivity capabilities of silicalite-1, AlPO₄-5, and ITQ-22 towards pure and mixed linear, branched, and cyclic alkanes.^{174,175}

1.7.3 CH₃I and I₂ capture and storage

Nuclear energy is a clean and sustainable solution for the upsurging global energy needs.¹⁷⁶ It remains a challenging task to treat the volatile radioactive gaseous waste which could potentially cause significant harm to the environment.¹⁷⁷ The off-gas produced from reprocessing the used nuclear fuel containing a large amount of harmful radioactive gaseous iodine (I₂) and methyl iodide (CH₃I).^{178,179} I¹²⁹ is a particularly long half-life (1.57×10^7 years) contaminant.¹⁷⁹ The elemental form of these radioactive iodines usually reacts with hydrocarbon to yield alkyl iodides, mostly CH₃I. The immediate capture of radioactive I₂ and CH₃I is required as they directly affect the human's metabolic system.¹⁸⁰ Deuterium (D) is the isotope of hydrogen with the natural abundance of 0.0156 %. Deuterium enrichment has good significance to nuclear fusion application. Other than that, deuterium can be applied as the neutron moderator, deuterium arc lamps, nonradioactive tracers et al.

Various methods exist for the removal of the gaseous radioactive iodine compounds. Such as wet scrubbing, dry dusting, precipitation and adsorption.¹⁷⁹ The adsorption-based method is relatively more cost-efficient and reliable than other systems. Active carbon and zeolites, as widely used adsorbents for gas separation applications,¹⁸¹ has been used exclusively for the removal of the radioactive iodine compounds leaked from nuclear plants.^{182,183,184,185} However, they are not suitable for purifying the off-gas produced from reprocessing the used nuclear fuel due to the limited capacity and the safety concerns.¹⁸⁶ Recently, experimental and computational efforts have been made to investigate iodine compounds capture performance using metal-organic frameworks (MOFs). Nenoff and co-workers reported the ZIF-8 was a MOF with suitable pore aperture size (3.4 Å), large surface area and excellent chemical and thermal stability for I₂ capture.^{107,187} More recently, Nenoff and co-workers found the Cu-BTC was capable of capturing I₂ from the stream mixture of I₂ and water vapour.¹⁸⁸ Assfour et al.

screened I₂ adsorption with 12 MOFs at ambient temperature using molecular modelling method. They found pore volume and surface area could considerably influence the storage capacity, such as NU-110 which showed the highest surface area (7400 m²/g) and reached a capacity of 13 g/g adsorption of I₂ at 1bar.¹⁸⁹ The adsorption and separation of I₂ and CH₃I in MIL-53(Al), MIL-120(Al) and HKUST-1(Cu) were investigated by Yoon et al. using density functional theory (DFT) calculations and molecular dynamic (MD) simulations. They found the interaction energy between these iodine species and MOFs is significant for promoting the adsorption of I₂ and CH₃I.¹⁹⁰ More recently, Zhang and co-worker screened 21 ZIFs to investigate the iodine uptake in the water-containing system. They found that topology types that led to large pore and high surface area caused high loading capacity.¹⁹¹ Yang and co-workers screened I₂ and CH₃I adsorption capability of 187 COFs at 423 K and suggested that 3D-COFs performed better than 2D-COFs. 3D-Py-COF was identified to have the highest I₂ adsorption capability (16.7 g/g), and COF-103 showed the highest CH₃I uptake (2.8 g/g).¹⁹²

1.7.4 H₂/D₂ separation

Deuterium (D) is a heavy isotope of hydrogen with a low natural population (0.0156 %). Industrially D₂ is produced by electrolysis of heavy water and then extracted with Girdler-sulfide process or cryogenic distillation at 24 K.¹⁹³ Both techniques are energetically expensive and require multiple enrichment steps.¹⁹⁴ Beenarkker et al. proposed an attractive method based on kinetic quantum effect (KQS) that quantum effect matters as the size difference between pore and hydrogen molecule is close to de Broglie wavelength.¹⁹⁵ Quantum sieving (QS) effect has been tested for the D₂ separation from H₂/D₂ mixture and confined ultrafine apertures (3 Å) are required,¹⁹⁶ which typically leads to small pores volume and limited capacities.

D₂ is produced by energetic expensive cryogenic distillation at 24K.¹⁹⁷ The porous materials separation methods are intriguing for D₂ capture application, which is also called as quantum sieving. This method was first proposed by Beenakker, which adsorption of hard spheres that higher zero-point energy of lighter molecule cause the reduction of uptakes, and enrich the

heavier molecule.¹⁹⁸ Later, Wang et al.¹⁹⁹ and Challa et al.²⁰⁰ conducted grand canonical Monte Carlo (GCMC) simulation with Feynman's path-integral (PI) algorithm of hydrogen isotopes in single-walled carbon nanotubes (SWNT) at 20 K. Feynman-Hibbs (FH) effective potential approximation is a method to address the quantum effect.²⁰¹ Subsequently, theoretical and experimental investigations were performed on several porous materials.^{202–214}

1.8 Aim of the thesis

This thesis aims to investigate the flexibility effect on the adsorption and separation performance of PMCs. We start with small gases adsorption in CC3R, and then linear and branched alkanes adsorptions. We found that the flexibility of PMCs plays a vital role in the adsorption of gases with similar dimension to the sizes of pores. GCMC/MD simulation (flexible host approach) can excellently reproduce the experimental adsorption isotherm (SF₆). However, flexible host approach is computationally expensive. A top-down strategy has been proposed to find PMCs with proper CH₃I/I₂ capture capability.

1.9 References

1. Cheetham, A. K., Férey, G. & Loiseau, T. Anorganische Materialien mit offenen Gerüsten. *Angew. Chemie* **111**, 3466–3492 (2002).
2. Price, S. L. *et al.* Modelling organic crystal structures using distributed multipole and polarizability-based model intermolecular potentials. *Phys. Chem. Chem. Phys.* **12**, 8478–8490 (2010).
3. Lloyd, G. O. Crystal Engineering of Porosity. (2006).
4. Kitagawa, S., Kitaura, R. & Noro, S. Functional porous coordination polymers. *Angew. Chemie - Int. Ed.* **43**, 2334–2375 (2004).
5. Cote, A. P. Porous, Crystalline, Covalent Organic Frameworks. *Science (80-.)*. **310**,

- 1166–1170 (2005).
6. Hernández, M. A., Rojas, F. & Lara, V. H. Nitrogen-sorption characterization of the microporous structure of clinoptilolite-type zeolites. *J. Porous Mater.* **7**, 443–454 (2000).
 7. Barbour, L. J. Crystal porosity and the burden of proof. *Chem. Commun.* 1163 (2006). doi:10.1039/b515612m
 8. Cheetham, A. K., Férey, G. & Loiseau, T. Open-Framework Inorganic Materials. *Angew. Chemie Int. Ed.* **38**, 3268–3292 (1999).
 9. McKeown, N. B. Nanoporous molecular crystals. *J. Mater. Chem.* **20**, 10588 (2010).
 10. Yaghi, O. M. *et al.* Reticular synthesis and the design of new materials. *Nature* **423**, 705–714 (2003).
 11. Cundy, C. S. & Cox, P. A. The hydrothermal synthesis of zeolites: Precursors, intermediates and reaction mechanism. *Microporous Mesoporous Mater.* **82**, 1–78 (2005).
 12. Getman, R. B., Bae, Y.-S., Wilmer, C. E. & Snurr, R. Q. Review and Analysis of Molecular Simulations of Methane, Hydrogen, and Acetylene Storage in Metal–Organic Frameworks. *Chem. Rev.* **112**, 703–723 (2011).
 13. Han, S. S., Mendoza-Cortés, J. L. & Goddard, W. a. Recent advances on simulation and theory of hydrogen storage in metal-organic frameworks and covalent organic frameworks. *Chem. Soc. Rev.* **38**, 1460–1476 (2009).
 14. Garberoglio, G., Uni, V., V, V. S. & Tn, P. V. Computer Simulation of the Adsorption of Light Gases in Covalent Organic Frameworks Computer Simulation of the Adsorption of Light Gases in Covalent Organic Frameworks. 12154–12158 (2007). doi:10.1021/la701736m
 15. Gutsche, C. D. the Calixarenes. *Top. Curr. Chem.* **123**, 1–47 (1984).
 16. McKeown, N. B. Nanoporous molecular crystals. *J. Mater. Chem.* **20**, 10588 (2010).
 17. Lagona, J., Mukhopadhyay, P., Chakrabarti, S. & Isaacs, L. The cucurbit[n]uril family. *Angew. Chemie - Int. Ed.* **44**, 4844–4870 (2005).
 18. Holst, J. R., Trewin, A. & Cooper, A. I. Porous organic molecules. *Nat. Chem.* **2**, 915–

- 920 (2010).
19. Tian, J., Thallapally, P. K. & McGrail, B. P. Porous organic molecular materials. *CrystEngComm* **14**, 1909 (2012).
 20. Mastalerz, M. Permanent porous materials from discrete organic molecules-towards ultra-high surface areas. *Chem. - A Eur. J.* **18**, 10082–10091 (2012).
 21. Hasell, T., Chong, S. Y., Schmidtman, M., Adams, D. J. & Cooper, A. I. Porous organic alloys. *Angew. Chemie - Int. Ed.* **51**, 7154–7157 (2012).
 22. Cooper, A. I. Molecular organic crystals: From barely porous to really porous. *Angew. Chemie - Int. Ed.* **51**, 7892–7894 (2012).
 23. Atwood, J. L., Barbour, L. J., Jerga, A. & Schottel, B. L. Guest transport in a nonporous organic solid via dynamic van der Waals cooperativity. *Science (80-.)*. **298**, 1000–1002 (2002).
 24. Atwood, J. L., Barbour, L. J. & Jerga, A. Storage of methane and freon by interstitial van der Waals confinement. *Science (80-.)*. **296**, 2367–2369 (2002).
 25. Jelfs, K. E. & Cooper, A. I. Molecular simulations to understand and to design porous organic molecules. *Curr. Opin. Solid State Mater. Sci.* **17**, 19–30 (2013).
 26. Barrer, R. M. & Shanson, V. H. Dianin's compound as a zeolitic sorbent. *J. Chem. Soc. Chem. Commun.* 333 (1976). doi:10.1039/c39760000333
 27. Imashiro, F., Yoshimura, M. & Fujiwara, T. 'Guest-free' dianin's compound. *Acta Crystallogr. Sect. C Cryst. Struct. Commun.* **54**, 1357–1360 (1998).
 28. Andreetti, G. D., Ungaro, R. & Pochini, A. Crystal and Molecular Structure of Cyclo{quater[(5-t-butyl-2-hydroxy-1,3- phenylene)methylenel) Toluene (1 : 1) Clathrate. *J. Chem. Soc. Chem. Commun.* 1005–1007 (1979).
 29. Sozzani, P., Bracco, S., Comotti, A., Ferretti, L. & Simonutti, R. Methane and carbon dioxide storage in a porous van der Waals crystal. *Angew. Chemie - Int. Ed.* **44**, 1816–1820 (2005).
 30. Dalgarno, S. J., Thallapally, P. K., Barbour, L. J. & Atwood, J. L. Engineering void space in organic van der Waals crystals: calixarenes lead the way. *Chem. Soc. Rev.* **36**, 236–

- 245 (2007).
31. Atwood, J. L., Barbour, L. J. & Jerga, A. Storage of Methane and Freon by Interstitial van der Waals Confinement. *Science (80-.)*. **296**, 2367–2369 (2002).
 32. Mastalerz, M. Shape-persistent organic cage compounds by dynamic covalent bond formation. *Angew. Chemie - Int. Ed.* **49**, 5042–5053 (2010).
 33. Mastalerz, M., Schneider, M. W., Oppel, I. M. & Presly, O. A salicylbisimine cage compound with high surface area and selective CO₂/CH₄ adsorption. *Angew. Chemie - Int. Ed.* **50**, 1046–1051 (2011).
 34. Mastalerz, M. & Oppel, I. M. Rational construction of an extrinsic porous molecular crystal with an extraordinary high specific surface area. *Angew. Chemie - Int. Ed.* **51**, 5252–5255 (2012).
 35. Jin, Y., Voss, B. A., Noble, R. D. & Zhang, W. A shape-persistent organic molecular cage with high selectivity for the adsorption of CO₂ over N₂. *Angew. Chemie - Int. Ed.* **49**, 6348–6351 (2010).
 36. Cram, D. J. Cavitands: Organic Hosts with Enforced Cavities. *Science (80-.)*. **219**, 1177–1183 (1983).
 37. Collet, A. Cyclotrimeratrylenes and cryptophanes. *Tetrahedron* **43**, 5725–5759 (1987).
 38. Leontiev, A. V. & Rudkevich, D. M. Encapsulation of gases in the solid state. *Chem. Commun.* **4**, 1468–1469 (2004).
 39. Moghadam, P. Z. *et al.* Development of a Cambridge Structural Database Subset: A Collection of Metal-Organic Frameworks for Past, Present, and Future. *Chem. Mater.* **29**, 2618–2625 (2017).
 40. Evans, J. D. *et al.* Computational identification of organic porous molecular crystals. *CrystEngComm* **18**, 4133–4141 (2016).
 41. Hasell, T., Chong, S. Y., Jelfs, K. E., Adams, D. J. & Cooper, A. I. Porous organic cage nanocrystals by solution mixing. *J. Am. Chem. Soc.* **134**, 588–598 (2012).
 42. Makhseed, S. *et al.* Polymers of intrinsic microporosity (PIMs): robust, solution-processable, organic nanoporous materials. *Chem. Commun.* 230 (2004).

- doi:10.1039/b311764b
43. Yang, S. *et al.* Understanding the effect of host flexibility on the adsorption of CH₄, CO₂ and SF₆ in porous organic cages. (2019).
 44. Hasell, T. & Cooper, A. I. Porous organic cages: Soluble, modular and molecular pores. *Nat. Rev. Mater.* **1**, (2016).
 45. Allcock, H. R. & Siegel, L. A. Phosphonitrilic Compounds . 111 Molecular Inclusion Compounds of Tris (o-phenylenedioxy) phosphonitrile Trimer. *J. Am. Chem. Soc.* **80**, 5140–5144 (1964).
 46. Sozzani, P., Bracco, S., Comotti, A., Ferretti, L. & Simonutti, R. Methane and carbon dioxide storage in a porous van der Waals crystal. *Angew. Chemie - Int. Ed.* **44**, 1816–1820 (2005).
 47. Hertzsch, T., Budde, F., Weber, E. & Hulliger, J. Supramolecular-wire confinement of I₂ molecules in channels of the organic zeolite tris(o-phenylenedioxy)cyclotriphosphazene. *Angew. Chemie - Int. Ed.* **41**, 2281–2284 (2002).
 48. Sozzani, P., Comotti, A., Bracco, S. & Simonutti, R. A family of supramolecular frameworks of polyconjugated molecules hosted in aromatic nanochannels. *Angew. Chemie - Int. Ed.* **43**, 2792–2797 (2004).
 49. Jorgensen, W. L., Madura, J. D. & Swenson, C. J. Optimized Intermolecular Potential Functions for Liquid Hydrocarbons. *J. Am. Chem. Soc.* **106**, 6638–6646 (1984).
 50. Atwood, J. L. Storage of Methane and Freon by Interstitial van der Waals Confinement. *Science (80-)*. **296**, 2367–2369 (2002).
 51. Atwood, J. L., Barbour, L. J., Jerga, A. & Schottel, B. L. Guest transport in a nonporous organic solid via dynamic van der Waals cooperativity. *Science (80-)*. **298**, 1000–1002 (2002).
 52. J.L., A., L.J., B. & A., J. Polymorphism of pure p-tert-butylcalix[4]arene: Conclusive identification of the phase obtained by desolvation. *Chem. Commun.* 2952–2953 (2002).
 53. Atwood, J. L., Barbour, L. J. & Jerga, A. A new type of material for the recovery of hydrogen from gas mixtures. *Angew. Chemie - Int. Ed.* **43**, 2948–2950 (2004).

54. Atwood, J. L., Barbour, L. J., Thallapally, P. K. & Wirsig, T. B. A crystalline organic substrate absorbs methane under STP conditions. *Chem. Commun.* 51–53 (2005). doi:10.1039/b416752j
55. Thallapally, P. K. *et al.* Organic crystals absorb hydrogen gas under mild conditions. *Chem. Commun.* 5272–5274 (2005). doi:10.1039/b511341e
56. Thallapally, P. K., Lloyd, G. O., Atwood, J. L. & Barbour, L. J. Diffusion of water in a nonporous hydrophobic crystal. *Angew. Chemie - Int. Ed.* **44**, 3848–3851 (2005).
57. Kim, D. *et al.* Direct synthesis of polymer nanocapsules with a noncovalently tailorable surface. *Angew. Chemie - Int. Ed.* **46**, 3471–3474 (2007).
58. Moghaddam, S., Inoue, Y. & Gilson, M. K. Host-Guest Complexes with Protein-Ligand-Like Affinities: Computational Analysis and Design. **5**, 379–390 (2010).
59. Rekharsky, M. V *et al.* A synthetic host-guest system achieves avidin-biotin affinity by overcoming enthalpy–entropy compensation. **104**, 20737–20742 (2007).
60. Ko, Y. H. *et al.* Designed Self-Assembly of Molecular Necklaces Using Host-Stabilized Charge-Transfer Interactions. *J. Am. Chem. Soc.* **126**, 1932–1933 (2004).
61. Park, K. M. *et al.* Construction of a square-wave-shaped one-dimensional polyrotaxane using a preorganized l-shaped pseudorotaxane. *Supramol. Chem.* **14**, 153–158 (2002).
62. Park, K. M. *et al.* Designed self-assembly of molecular necklaces. *J. Am. Chem. Soc.* **124**, 2140–2147 (2002).
63. Woo, S. J. *et al.* Molecular loop lock: A redox-driven molecular machine based on a host-stabilized charge-transfer complex. *Angew. Chemie - Int. Ed.* **44**, 87–91 (2004).
64. Jeon, W. S. *et al.* A [2]pseudorotaxane-based molecular machine: Reversible formation of a molecular loop driven by electrochemical and photochemical stimuli. *Angew. Chemie - Int. Ed.* **42**, 4097–4100 (2003).
65. Letters, N. Cucurbit[7]uril and o-Carborane Self-Assemble to Form a Molecular Ball Bearing. *Nano Lett.* 6–8 (2002).
66. Day, A. I. *et al.* A Cucurbituril-Based Gyroscane: A New Supramolecular Form. *Angew. Chemie* **114**, 285–287 (2002).

67. Wook Lee, J., Kim, K. & Kim, K. A kinetically controlled molecular switch based on bistable [2]rotaxane. *Chem. Commun.* 1042–1043 (2002). doi:10.1039/b103380h
68. Reczek, J. J., Kennedy, A. A., Halbert, B. T. & Urbach, A. R. Multivalent recognition of peptides by modular self-assembled receptors. *J. Am. Chem. Soc.* **131**, 2408–2415 (2009).
69. Zhang, H., Grabenauer, M., Bowers, M. T. & Dearden, D. V. Supramolecular modification of ion chemistry: Modulation of peptide charge state and dissociation behavior through complexation with cucurbit[n]uril (n = 5, 6) or α -cyclodextrin. *J. Phys. Chem. A* **113**, 1508–1517 (2009).
70. Bailey, D. M., Hennig, A., Uzunova, V. D. & Nau, W. M. Supramolecular tandem enzyme assays for multiparameter sensor arrays and enantiomeric excess determination of amino acids. *Chem. - A Eur. J.* **14**, 6069–6077 (2008).
71. Rekharsky, M. V. *et al.* Chiral recognition in cucurbituril cavities. *J. Am. Chem. Soc.* **128**, 14871–14880 (2006).
72. Heitmann, L. M., Taylor, A. B., Hart, P. J. & Urbach, A. R. Sequence-specific recognition and cooperative dimerization of N-terminal aromatic peptides in aqueous solution by a synthetic host. *J. Am. Chem. Soc.* **128**, 12574–12581 (2006).
73. Bush, M. E., Bouley, N. D. & Urbach, A. R. Charge-mediated recognition of N-terminal tryptophan in aqueous solution by a synthetic host. *J. Am. Chem. Soc.* **127**, 14511–14517 (2005).
74. Buschmann, H. J., Schollmeyer, E. & Mutihac, L. The formation of amino acid and dipeptide complexes with α -cyclodextrin and cucurbit[6]uril in aqueous solutions studied by titration calorimetry. *Thermochim. Acta* **399**, 203–208 (2003).
75. Uzunova, V. D., Cullinane, C., Brix, K., Nau, W. M. & Day, A. I. Toxicity of cucurbit[7]uril and cucurbit[8]uril: An exploratory in vitro and in vivo study. *Org. Biomol. Chem.* **8**, 2037–2042 (2010).
76. Wheate, N. J. *et al.* Novel platinum(II)-based anticancer complexes and molecular hosts as their drug delivery vehicles. *Dalt. Trans.* 5055–5064 (2007). doi:10.1039/b704973k

77. Kemp, S. *et al.* Encapsulation of platinum(II)-based DNA intercalators within cucurbit[6,7,8]urils. *J. Biol. Inorg. Chem.* **12**, 969–979 (2007).
78. Bali, M. S., Buck, D. P., Coe, A. J., Day, A. I. & Collins, J. G. Cucurbituril binding of trans- $[\text{PtCl}(\text{NH}_3)_2]_2(\mu\text{-NH}_2(\text{CH}_2)_8\text{NH}_2)]^{2+}$ and the effect on the reaction with cysteine. *Dalt. Trans.* **2**, 5337–5344 (2006).
79. Wheate, N. J., Buck, D. P., Day, A. I. & Collins, J. G. Cucurbit[n]uril binding of platinum anticancer complexes. *Dalt. Trans.* 451–458 (2006). doi:10.1039/b513197a
80. Jeon, Y. J., Kim, S., Ko, H. & Sakamoto, S. Electronic Supplementary Information Novel Molecular Drug Carrier : Encapsulation of Oxaliplatin in Cucurbit [7] uril and Its Effects on Stability and Reactivity of the Drug. *Sci. Technol.* 7–9 (2005).
81. Wheate, N. J. *et al.* Multi-nuclear platinum complexes encapsulated in cucurbit[n]uril as an approach to reduce toxicity in cancer treatment. *Chem. Commun.* **4**, 1424–1425 (2004).
82. Lim, S. *et al.* Cucurbit [6] uril : Organic Molecular Porous Material with Permanent Porosity , Exceptional Stability , and Acetylene Sorption Properties. *Zuschriften* 3400–3403 (2008). doi:10.1002/ange.200800772
83. Bardelang, D. *et al.* Cucurbit[n]urils (n = 5-8): A comprehensive solid state study. *Cryst. Growth Des.* **11**, 5598–5614 (2011).
84. Tian, J. *et al.* Cucurbit[7]uril: An amorphous molecular material for highly selective carbon dioxide uptake. *Chem. Commun.* **47**, 7626–7628 (2011).
85. Ganji, M. D. & Danesh, N. Adsorption of H₂S molecules by cucurbit[7]uril: An ab initio vdW-DF study. *RSC Adv.* **3**, 22031–22038 (2013).
86. Kim, J. *et al.* New cucurbituril homologues: Syntheses, isolation, characterization, and X-ray crystal structures of cucurbit[n]uril (n = 5, 7, and 8). *J. Am. Chem. Soc.* **122**, 540–541 (2000).
87. Freeman, W. A., Mock, W. L. & Shih, N. Y. Cucurbituril. *J. Am. Chem. Soc.* **103**, 7367–7368 (1981).
88. Tian, J., Thallapally, P. K., Dalgarno, S. J., McGrail, P. B. & Atwood, J. L. Amorphous

- molecular organic solids for gas adsorption. *Angew. Chemie - Int. Ed.* **48**, 5492–5495 (2009).
89. Kudo, H. *et al.* Molecular waterwheel (noria) from a simple condensation of resorcinol and an alkanedial. *Angew. Chemie - Int. Ed.* **45**, 7948–7952 (2006).
90. Rajangam, K. *et al.* Heparin Binding Nanostructures to Promote Growth of Blood Vessels. (2006).
91. Ulijn, R. V & Smith, A. M. Designing peptide based nanomaterials. *Chem. Soc. Rev.* **37**, 664–675 (2008).
92. Comotti, A., Bracco, S., Distefano, G. & Sozzani, P. Methane, carbon dioxide and hydrogen storage in nanoporous dipeptide-based materials. *Chem. Commun.* 284–286 (2009). doi:10.1039/b820200a
93. Couderc, G., Hertzsch, T., Behrnd, N., Kra, K. & Hulliger, J. Reversible sorption of nitrogen and xenon gas by the guest-free zeolite tris (o -phenylenedioxy) cyclotriphosphazene (TPP). *Microporous Mesoporous Mater.* **88**, 170–175 (2006).
94. MacDowell, D. & Nelson, J. Facile synthesis of a new family of cage molecules. *Tetrahedron Lett.* **29**, 385–386 (1988).
95. Liu, X., Liu, Y., Li, G. & Warmuth, R. One-pot, 18-component synthesis of an octahedral nanocontainer molecule. *Angew. Chemie - Int. Ed.* **45**, 901–904 (2006).
96. Mastalerz, M. One-pot synthesis of a shape-persistent endo-functionalised nano-sized adamantoid compound. *Chem. Commun.* 4756–4758 (2008). doi:10.1039/b808990f
97. Reinhard, D., Schöttner, L., Brosius, V., Rominger, F. & Mastalerz, M. Synthesis of para-aryl-substituted salicyldialdehydes. *European J. Org. Chem.* **2015**, 3274–3285 (2015).
98. Schneider, M. W. *et al.* Periphery-substituted [4+6] salicylbisimine cage compounds with exceptionally high surface areas: Influence of the molecular structure on nitrogen sorption properties. *Chem. - A Eur. J.* **18**, 836–847 (2012).
99. Schneider, M. W., Lechner, L. G. & Mastalerz, M. Uniform porous nanospheres of discrete shape-persistent organic cage compounds. *J. Mater. Chem.* **22**, 7113–7116

- (2012).
100. Mastalerz, M. Porous Shape-Persistent Organic Cage Compounds of Different Size, Geometry, and Function. *Acc. Chem. Res.* **51**, 2411–2422 (2018).
 101. Elbert, S. M., Rominger, F. & Mastalerz, M. Synthesis of a Rigid C_{3v}-Symmetric Tris-salicylaldehyde as a Precursor for a Highly Porous Molecular Cube. *Chem. - A Eur. J.* **20**, 16707–16720 (2014).
 102. Schneider, M. W., Oppel, I. M. & Mastalerz, M. Exo-functionalized shape-persistent [2+3] cage compounds: Influence of molecular rigidity on formation and permanent porosity. *Chem. - A Eur. J.* **18**, 4156–4160 (2012).
 103. Zhang, G., Presly, O., White, F., Oppel, I. M. & Mastalerz, M. A permanent mesoporous organic cage with an exceptionally high surface area. *Angew. Chemie - Int. Ed.* **53**, 1516–1520 (2014).
 104. Jin, Y. *et al.* Highly CO₂-Selective Organic Molecular Cages: What Determines the CO₂ Selectivity. *J. Am. Chem. Soc.* **133**, 6650–6658 (2011).
 105. Avellaneda, A. *et al.* Kinetically controlled porosity in a robust organic cage material. *Angew. Chemie - Int. Ed.* **52**, 3746–3749 (2013).
 106. Cote, A. P. Benin, A. I. Ockwig, N. W. O’Keeffe, M. Matzger, A. J. Yaghi, O. M. Porous, Crystalline, Covalent Organic Frameworks. *Science (80-.)*. **310**, 1166–1170 (2005).
 107. Park, K. S. *et al.* Exceptional chemical and thermal stability of zeolitic imidazolate frameworks. *Proc. Natl. Acad. Sci. U. S. A.* **103**, 10186–10191 (2006).
 108. Ben, T. *et al.* Targeted Synthesis of a Porous Aromatic Framework with High Stability and Exceptionally High Surface Area. *Angew. Chemie* **121**, 9621–9624 (2009).
 109. Tozawa, T. *et al.* Porous organic cages. *Nat. Mater.* **8**, 973–978 (2009).
 110. Jones, J. T. a. *et al.* On-Off Porosity Switching in a Molecular Organic Solid. *Angew. Chemie Int. Ed.* **50**, 749–753 (2011).
 111. Kewley, A. *et al.* Porous Organic Cages for Gas Chromatography Separations. *Chem. Mater.* **27**, 3207–3210 (2015).
 112. Mitra, T. *et al.* A soft porous organic cage crystal with complex gas sorption behavior.

- Chem. - A Eur. J.* **17**, 10235–10240 (2011).
113. Krishna, R. & van Baten, J. M. In silico screening of metal-organic frameworks in separation applications. *Phys. Chem. Chem. Phys.* **13**, 10593–10616 (2011).
114. Holden, D. *et al.* Gas Diffusion in a Porous Organic Cage: Analysis of Dynamic Pore Connectivity Using Molecular Dynamics Simulations. *J. Phys. Chem. C* **118**, 12734–12743 (2014).
115. Babarao, R., Dai, S. & Jiang, D. E. Functionalizing porous aromatic frameworks with polar organic groups for high-capacity and selective CO₂ separation: A molecular simulation study. *Langmuir* **27**, 3451–3460 (2011).
116. Smit, B. & Krishna, R. Monte Carlo simulations in zeolites. *Curr. Opin. Solid State Mater. Sci.* **5**, 455–461 (2001).
117. Düren, T., Bae, Y.-S. & Snurr, R. Q. Using molecular simulation to characterise metal-organic frameworks for adsorption applications. *Chem. Soc. Rev.* **38**, 1237 (2009).
118. Krishna, R. Diffusion in porous crystalline materials. *Chem. Soc. Rev.* **41**, 3099 (2012).
119. Chen, L. *et al.* Separation of rare gases and chiral molecules by selective binding in porous organic cages. *Nat. Mater.* **13**, 954–60 (2014).
120. Pulido, A. *et al.* Functional materials discovery using energy-structure-function maps. *Nature* **543**, 657–664 (2017).
121. Liu, Y. *et al.* Reversible structural transition in MIL-53 with large temperature hysteresis. *J. Am. Chem. Soc.* **130**, 11813–11818 (2008).
122. Jones, J. T. A. *et al.* On-off porosity switching in a molecular organic solid. *Angew. Chemie - Int. Ed.* **50**, 749–753 (2011).
123. Lee, S.-J. & Bae, Y.-S. Can metal-organic frameworks attain new DOE targets for on-board methane storage by increasing methane heat of adsorption? *J. Phys. Chem. C* **118**, 19833–19841 (2014).
124. Düren, T., Sarkisov, L., Yaghi, O. M. & Snurr, R. Q. Design of new materials for methane storage. *Langmuir* **20**, 2683–2689 (2004).
125. Kondo, M. *et al.* Rational synthesis of stable channel-like cavities with methane gas

- adsorption properties: [Cu₂(pzdc)₂(L)_n] (pzdc = pyrazine-2, 3-dicarboxylate; L = a pillar ligand). *Angew. Chemie Int. Ed.* **38**, 140–143 (1999).
126. Noro, S., Kitagawa, S., Kondo, M. & Seki, K. A new, methane adsorbent, porous coordination polymer [CuSiF₆(4, 4'-bipyridine)₂]_n. *Angew. Chemie Int. Ed.* **39**, 2081–2084 (2000).
127. Noro, S. *et al.* Framework engineering by anions and porous functionalities of Cu(II)/4, 4'-bpy coordination polymers. *J. Am. Chem. Soc.* **124**, 2568–2583 (2002).
128. Furukawa, H. & Yaghi, O. M. Storage of hydrogen, methane, and carbon dioxide in highly porous covalent organic frameworks for clean energy applications. *J. Am. Chem. Soc.* **131**, 8875–8883 (2009).
129. Gallo, M. & Glossman-Mitnik, D. Fuel gas storage and separations by metal-organic frameworks: Simulated adsorption isotherms for H₂ and CH₄ and their equimolar mixture. *J. Phys. Chem. C* **113**, 6634–6642 (2009).
130. Garberoglio, G., Skoulidas, A. I. & Johnson, J. K. Adsorption of gases in metal organic materials: comparison of simulations and experiments. *J. Phys. Chem. B* **109**, 13094–13103 (2005).
131. Yang, Q. & Zhong, C. Molecular simulation of carbon dioxide/methane/hydrogen mixture adsorption in metal-organic frameworks. *J. Phys. Chem. B* **110**, 17776–17783 (2006).
132. Yang, Q. & Zhong, C. Electrostatic-field-induced enhancement of gas mixture separation in metal-organic frameworks: a computational study. *Chemphyschem a Eur. J. Chem. Phys. Phys. Chem.* **7**, 1417–1421 (2006).
133. Wang, S. Comparative molecular simulation study of methane adsorption in metal-organic frameworks. *Energy & fuels* **21**, 953–956 (2007).
134. Lan, J., Cao, D. & Wang, W. High uptakes of methane in Li-doped 3D covalent organic frameworks. *Langmuir* **26**, 220–226 (2010).
135. Mendoza-Cortés, J. L., Han, S. S., Furukawa, H., Yaghi, O. M. & Goddard III, W. A. Adsorption mechanism and uptake of methane in covalent organic frameworks: theory

- and experiment. *J. Phys. Chem. A* **114**, 10824–10833 (2010).
136. Eddaoudi, M. *et al.* Systematic Design of Pore Size and Functionality in Isoreticular MOFs and Their Application in Methane Storage. **295**, 32–34 (2002).
137. Kawakami, T. *et al.* Theoretical studies of spin arrangement of adsorbed organic radicals in metal-organic nanoporous cavity. *Polyhedron* **20**, 1197–1206 (2001).
138. Walton, K. S. *et al.* Understanding inflections and steps in carbon dioxide adsorption isotherms in metal-organic frameworks. *J. Am. Chem. Soc.* **130**, 406–407 (2008).
139. Yang, Q., Zhong, C. & Chen, J.-F. Computational study of CO₂ storage in metal-organic frameworks. *J. Phys. Chem. C* **112**, 1562–1569 (2008).
140. Pérez-Pellitero, J. *et al.* Adsorption of CO₂, CH₄, and N₂ on zeolitic imidazolate frameworks: experiments and simulations. *Chem. Eur. J.* **16**, 1560–1571 (2010).
141. Dubbeldam, D., Frost, H., Walton, K. S. & Snurr, R. Q. Molecular simulation of adsorption sites of light gases in the metal-organic framework IRMOF-1. *Fluid Phase Equilib.* **261**, 152–161 (2007).
142. Pianwanit, A. *et al.* The optimal binding sites of CH₄ and CO₂ molecules on the metal-organic framework MOF-5: ONIOM calculations. *Chem. Phys.* **349**, 77–82 (2008).
143. Bae, Y.-S. *et al.* Strategies for characterization of large-pore metal-organic frameworks by combined experimental and computational methods. *Chem. Mater.* **21**, 4768–4777 (2009).
144. Morris, W. *et al.* A combined experimental-computational study on the effect of topology on carbon dioxide adsorption in zeolitic imidazolate frameworks. *J. Phys. Chem. C* **116**, 24084–24090 (2012).
145. Ramsahye, N. A. *et al.* Charge distribution in metal organic framework materials: transferability to a preliminary molecular simulation study of the CO₂ adsorption in the MIL-53 (Al) system. *Phys. Chem. Chem. Phys.* **9**, 1059–1063 (2007).
146. Cho, W.-S., Lee, K.-H., Chang, H.-J., Huh, W. & Kwon, H.-H. Evaluation of pressure-temperature swing adsorption for sulfur hexafluoride (SF₆) recovery from SF₆ and N₂ gas mixture. *Korean J. Chem. Eng.* **28**, 2196–2201 (2011).

147. Chiang, Y.-C. & Wu, P.-Y. Adsorption equilibrium of sulfur hexafluoride on multi-walled carbon nanotubes. *J. Hazard. Mater.* **178**, 729–738 (2010).
148. Cao, D. V & Sircar, S. Heats of adsorption of pure SF₆ and CO₂ on silicalite pellets with alumina binder. *Ind. Eng. Chem. Res.* **40**, 156–162 (2001).
149. Murase, H., Imai, T., Inohara, T. & Toyoda, M. Use of zeolite filter in portable equipment for recovering SF₆ in SF₆/N₂ mixtures. *IEEE Trans. Dielectr. Electr. Insul.* **11**, 166–173 (2004).
150. Toyoda, M. *et al.* SF₆ reclaiming from SF₆/N₂ mixtures by gas separation with molecular sieving effect. *IEEE Trans. Power Deliv.* **18**, 442–448 (2003).
151. Kim, M.-B., Lee, S.-J., Lee, C. Y. & Bae, Y.-S. High SF₆ selectivities and capacities in isostructural metal-organic frameworks with proper pore sizes and highly dense unsaturated metal sites. *Microporous mesoporous Mater.* **190**, 356–361 (2014).
152. Senkowska, I., Barea, E., Navarro, J. A. R. & Kaskel, S. Adsorptive capturing and storing greenhouse gases such as sulfur hexafluoride and carbon tetrafluoride using metal-organic frameworks. *Microporous mesoporous Mater.* **156**, 115–120 (2012).
153. Bandoz, T. J., Jagiełło, J. & Schwarz, J. A. Adsorption of sulfur hexafluoride and propane at temperatures near ambient on pillared clays. *J. Chem. Eng. Data* **41**, 880–884 (1996).
154. Vermeiren, W. & Gilson, J. P. Impact of zeolites on the petroleum and petrochemical industry. *Top. Catal.* **52**, 1131–1161 (2009).
155. Wayne, E. E. & Stephen, S. C. United States Patent. (1989).
156. Stephen, S. C. & Wayne, E. E. United States Patent. (1991).
157. Li, H., Eddaoudi, M., O’Keeffe, M. & Yaghi, O. M. Design and synthesis of an exceptionally stable and highly porous metal-organic framework. *Nature* **402**, 276–279 (1999).
158. Pan, L., Olson, D. H., Ciemolowski, L. R., Heady, R. & Li, J. Separation of hydrocarbons with a microporous metal-organic framework. *Angew. Chemie - Int. Ed.* **45**, 616–619 (2006).

159. Bloch, E. D. *et al.* Hydrocarbon Separations in a Metal-Organic Framework with Open Iron(II) Coordination Sites. *Science (80-.)*. **335**, 1606–1610 (2012).
160. Duerinck, T. *et al.* Understanding hydrocarbon adsorption in the uio-66 metal-organic framework: Separation of (un)saturated linear, branched, cyclic adsorbates, including stereoisomers. *J. Phys. Chem. C* **117**, 12567–12578 (2013).
161. Denayer, J. F. *et al.* Pore mouth versus intracrystalline adsorption of isoalkanes on ZSM-22 and ZSM-23 zeolites under vapour and liquid phase conditions. *Chem. Commun. (Camb)*. 1880–1881 (2003). doi:10.1039/b304320g
162. Tielens, F. *et al.* Adsorption of the Butene Isomers in Faujasite: A Combined ab-Initio Theoretical and Experimental Study. *J. Phys. Chem. B* **107**, 11065–11071 (2003).
163. Bozbiyik, B., Lannoeye, J., De Vos, D. E., Baron, G. V. & Denayer, J. F. M. Shape selective properties of the Al-fumarate metal–organic framework in the adsorption and separation of n-alkanes, iso-alkanes, cyclo-alkanes and aromatic hydrocarbons. *Phys. Chem. Chem. Phys.* **18**, 3294–3301 (2016).
164. Cousinsaintremi, J. *et al.* Biobutanol separation with the metal-organic framework ZIF-8. *ChemSusChem* **4**, 1074–1077 (2011).
165. Pan, Y. & Lai, Z. Sharp separation of C2/C3 hydrocarbon mixtures by zeolitic imidazolate framework-8 (ZIF-8) membranes synthesized in aqueous solutions. *Chem. Commun.* **47**, 10275 (2011).
166. Peralta, D., Chaplais, G., Simon-Masseron, A., Barthelet, K. & Pirngruber, G. D. Separation of C 6 paraffins using zeolitic imidazolate frameworks: Comparison with zeolite 5A. *Ind. Eng. Chem. Res.* **51**, 4692–4702 (2012).
167. Adhangale, P. & Keffer, D. A Grand Canonical Monte Carlo Study of the Adsorption of Methane , Ethane , and Their Mixtures in One-Dimensional Nanoporous Materials. *Simulation* 10455–10461 (2002). doi:10.1021/la020228v
168. Smit, B. & Siepmann, J. I. Simulating the adsorption of alkanes in zeolites. *Science (80-.)*. **264**, 1118–1120 (1994).
169. Vlught, T. J. H., Krishna, R. & Smit, B. Molecular Simulations of Adsorption Isotherms

- for Linear and Branched Alkanes and Their Mixtures in Silicalite. *J. Phys. Chem. B* **103**, 1102–1118 (1999).
170. Schenk, M., Vidal, S. L., Vlugt, T. J. H., Smit, B. & Krishna, R. Separation of Alkane Isomers by Exploiting Entropy Effects during Adsorption on Silicalite-1: A Configurational-Bias Monte Carlo Simulation Study. 1558–1570 (2001).
171. Calero, S., Smit, B. & Krishna, R. Separation of linear, mono-methyl and di-methyl alkanes in the 5-7 carbon atom range by exploiting configurational entropy effects during sorption on silicalite-1. *Phys. Chem. Chem. Phys.* **3**, 4390–4398 (2001).
172. Calero, S., Smit, B. & Krishna, R. Configurational entropy effects during sorption of hexane isomers in silicalite. *J. Catal.* **202**, 395–401 (2001).
173. Duren, T. & Snurr, R. Q. Assessment of Isoreticular Metal - Organic Frameworks for Adsorption Separations: A Molecular Simulation Study of Methane / n -Butane Mixtures. *J. Phys. Chem. B.* **108**, 15703–15708 (2004).
174. Fox, J. P., Rooy, V. & Bates, S. P. Simulating the adsorption of linear, branched and cyclic alkanes in silicalite-1 and AlPO4-5. *Microporous Mesoporous Mater.* **69**, 9–18 (2004).
175. Fox, J. P. & Bates, S. P. Simulating the adsorption of binary and ternary mixtures of linear, branched, and cyclic alkanes in zeolites. *J. Phys. Chem. B* **108**, 17136–17142 (2004).
176. Chu, S. & Majumdar, A. Opportunities and challenges for a sustainable energy future. *Nature* **488**, 294–303 (2012).
177. Ewing, R. C. & von Hippel, F. N. Nuclear Waste Management in the United States — Starting Over. *Science (80-.)*. (2008).
178. Committee, N. E. A. & Installations, N. NEA / CSNI / R (2007) 1 Unclassified. 1–60 (2007).
179. Haefner, D. & Tranter, T. Methods of gas phase capture of iodine from fuel reprocessing off-gas: A literature survey. (2007). doi:10.2172/911962
180. Lee, W. E., Ojovan, M. I., Stennett, M. C. & Hyatt, N. C. Immobilisation of radioactive

- waste in glasses, glass composite materials and ceramics. *Adv. Appl. Ceram.* **105**, 3–12 (2006).
181. Angin, D., Köse, T. E. & Selengil, U. Production and characterization of activated carbon prepared from safflower seed cake biochar and its ability to absorb reactive dyestuff. *Appl. Surf. Sci.* **280**, 705–710 (2013).
182. Jubin, R. T. *Airborn Waste Management Technology Applicable for Use in Reprocessing Plants for Control of Iodine and Other Off-Gas Constituents.* (1988).
183. Zhou, J., Hao, S., Gao, L. & Zhang, Y. Study on adsorption performance of coal based activated carbon to radioactive iodine and stable iodine. *Ann. Nucl. Energy* **72**, 237–241 (2014).
184. Chapman, K. W., Chupas, P. J. & Nenoff, T. M. Radioactive iodine capture in silver-containing mordenites through nanoscale silver iodide formation. *J. Am. Chem. Soc.* **132**, 8897–8899 (2010).
185. Fang, C. *et al.* Adsorption of gaseous radioactive iodine by Ag/13X zeolite at high temperatures. *J. Radioanal. Nucl. Chem.* 1883–1889 (2014). doi:10.1007/s10967-014-3736-3
186. Chibani, S., Chiter, F., Cantrel, L. & Paul, J. F. Capture of Iodine Species in MIL-53(Al), MIL-120(Al), and HKUST-1(Cu) Periodic DFT and Ab-Initio Molecular Dynamics Studies. *J. Phys. Chem. C* **121**, 25283–25291 (2017).
187. Sava, D. F. *et al.* Capture of volatile iodine, a gaseous fission product, by zeolitic imidazolate framework-8. *J. Am. Chem. Soc.* **133**, 12398–12401 (2011).
188. Sava, D. F. *et al.* Competitive I₂ Sorption by Cu-BTC from Humid Gas Streams. *Chem. Mater.* **25**, 2591–2596 (2013).
189. Assfour, B., Assaad, T. & Odeh, A. In silico screening of metal organic framework for iodine capture and storage. *Chem. Phys. Lett.* **610–611**, 45–49 (2014).
190. Pham, T. C. T. *et al.* Capture of iodine and organic iodides using silica zeolites and the semiconductor behaviour of iodine in a silica zeolite. *Energy Environ. Sci.* (2016). doi:10.1039/C5EE02843D

191. Yuan, Y., Dong, X., Chen, Y. & Zhang, M. Computational screening of iodine uptake in zeolitic imidazolate frameworks in a water-containing system. *Phys. Chem. Chem. Phys.* **18**, 23246–23256 (2016).
192. Lan, Y., Tong, M., Yang, Q. & Zhong, C. Computational screening of covalent organic frameworks for the capture of radioactive iodine and methyl iodide. *CrystEngComm* **19**, 4920–4926 (2017).
193. Rae, H. K. *Separation of hydrogen isotopes*. (1978).
194. Tanaka, H. *et al.* Quantum effects on hydrogen isotopes adsorption in nanopores. *J. Low Temp. Phys.* **157**, 352–373 (2009).
195. Beenakker, J. J. M., Borman, V. D. & Krylov, S. Y. Molecular transport in subnanometer pores: zero-point energy, reduced dimensionality and quantum sieving. *Chem. Phys. Lett.* **232**, 379–382 (1995).
196. Adil, K. *et al.* Gas/vapour separation using ultra-microporous metal–organic frameworks: insights into the structure/separation relationship. *Chem. Soc. Rev.* **46**, 3402–3430 (2017).
197. Keyser, G. M., McConnell, D. B., Anyas-Wiess, N. & Korkby, P. Heavy Water Distillation In Separation of Hydrogen Isotopes. *Am. Chem. Soc. Washington, DC* **68**, 126–133 (1978).
198. Beenakker, J. J. M., Borman, V. D. & Krylov, S. Y. Molecular transport in subnanometer pores: zero-point energy, reduced dimensionality and quantum sieving. *Chem. Phys. Lett.* **232**, 379–382 (1995).
199. Wang, Q., Challa, S. R., Sholl, D. S. & Johnson, J. K. Quantum sieving in carbon nanotubes and zeolites. *Phys. Rev. Lett.* **82**, 956–959 (1999).
200. Johnson, J. K., Challa, S. R. & Sholl, D. S. Light isotope separation in carbon nanotubes through quantum molecular sieving. *Phys. Rev. B - Condens. Matter Mater. Phys.* **63**, 1–9 (2001).
201. Sesé, L. M. Feynman-Hibbs potentials and path integrals for quantum Lennard-Jones systems: Theory and Monte Carlo simulations. *Mol. Phys.* **85**, 931–947 (1995).

202. Kumar, A. V. A. & Bhatia, S. K. Is kinetic molecular sieving of hydrogen isotopes feasible? *J. Phys. Chem. C* **112**, 11421–11426 (2008).
203. Kumar, A. V. A., Jobic, H. & Bhatia, S. K. Quantum effects on adsorption and diffusion of hydrogen and deuterium in microporous materials. *J. Phys. Chem. B* **110**, 16666–16671 (2006).
204. Kowalczyk, P., Gauden, P. A. & Terzyk, A. P. Cryogenic separation of hydrogen isotopes in single-walled carbon and boron-nitride nanotubes: Insight into the mechanism of equilibrium quantum sieving in quasi-one-dimensional pores. *J. Phys. Chem. B* **112**, 8275–8284 (2008).
205. Noguchi, D. *et al.* Quantum sieving effect of three-dimensional Cu-based organic framework for H₂ and D₂. *J. Am. Chem. Soc.* **130**, 6367–6372 (2008).
206. Nguyen, T. X., Jobic, H. & Bhatia, S. K. Microscopic observation of kinetic molecular sieving of hydrogen isotopes in a nanoporous material. *Phys. Rev. Lett.* **105**, 1–4 (2010).
207. Kumar, A. V. A., Jobic, H. & Bhatia, S. K. Quantum effect induced kinetic molecular sieving of hydrogen and deuterium in microporous materials. *Adsorption* **13**, 501–508 (2007).
208. Garberoglio, G. & Johnson, J. K. Hydrogen isotope separation in carbon nanotubes: Calculation of coupled rotational and translational states at high densities. *ACS Nano* **4**, 1703–1715 (2010).
209. Garberoglio, G. Quantum sieving in organic frameworks. *Chem. Phys. Lett.* **467**, 270–275 (2009).
210. Garberoglio, G. Quantum states of rigid linear rotors confined in a slit pore: Quantum sieving of hydrogen isotopes and extreme one dimensional confinement. *Eur. Phys. J. D* **51**, 185–191 (2009).
211. Hattori, Y. *et al.* Quantum sieving effect of modified activated carbon fibers on H₂ and D₂ adsorption at 20 K. *J. Phys. Chem. B* **110**, 9764–9767 (2006).
212. Zhao, X., Villar-Rodil, S., Fletcher, A. J. & Thomas, K. M. Kinetic isotope effect for H₂ and D₂ quantum molecular sieving in adsorption/desorption on porous carbon materials.

- J. Phys. Chem. B* **110**, 9947–9955 (2006).
213. Chen, B. *et al.* Surface interactions and quantum kinetic molecular sieving for H₂ and D₂ adsorption on a mixed metal-organic framework material. *J. Am. Chem. Soc.* **130**, 6411–6423 (2008).
214. Kowalczyk, P., Gauden, P. A., Terzyk, A. P. & Furmaniak, S. Impact of the carbon pore size and topology on the equilibrium quantum sieving of hydrogen isotopes at zero coverage and finite pressures. *J. Phys. Condens. Matter* **21**, (2009).

Chapter 2

Methodology

2.1 Gas Adsorption in Porous Materials

Adsorption is a process that adsorbates bond on the surface of an adsorbent. Adsorption can happen either chemically (chemisorption) or physically (physisorption). Chemisorption is adsorption involves the formation of chemical bonds between adsorbates and the surface of the adsorbent, where the bonding energy is generally intense (over 100 kJ/mol). Physisorption is an adsorption process based on the Van der Waals (vdW) interaction. Compare with chemisorption, the bonding energy of physisorption is weaker (less than 30 kJ/mol).¹ Gas adsorption in porous materials is usually quantified through adsorption isotherms which are the amount of gas adsorbed at a constant temperature as a function of pressure. The adsorption isotherms can be divided into six different classifications. The type I isotherms are the most common isotherms that happen in the microporous materials with relatively small external surfaces, where the most adsorption occurred at the low-temperature range; Type II isotherms is a monolayer-multilayer adsorption process that generally found in non-porous and macroporous materials, with the coverage of monolayer at the “B” point, the multilayer adsorption happens subsequently; Type III isotherms is convex x-axis which is similar to the type II isotherm, without the stepwise adsorption process, the unrestricted multilayer adsorption is processed with the strong guest-guest interactions; Type IV isotherms is a stepwise adsorption process include multilayer adsorption followed by capillary condensation in mesoporous materials, and the narrow capillary leads to the hysteresis loop. The initial part of type IV isotherms corresponds to the monolayer-multilayer type II isotherm; The difference between type V with type IV isotherms is similar to the type III to type II, where the multilayer adsorption occurred directly; Type VI isotherms show the stepwise multilayer adsorption process. Each step-height represents the adsorption capacity of each monolayer. (figure 2.1)²

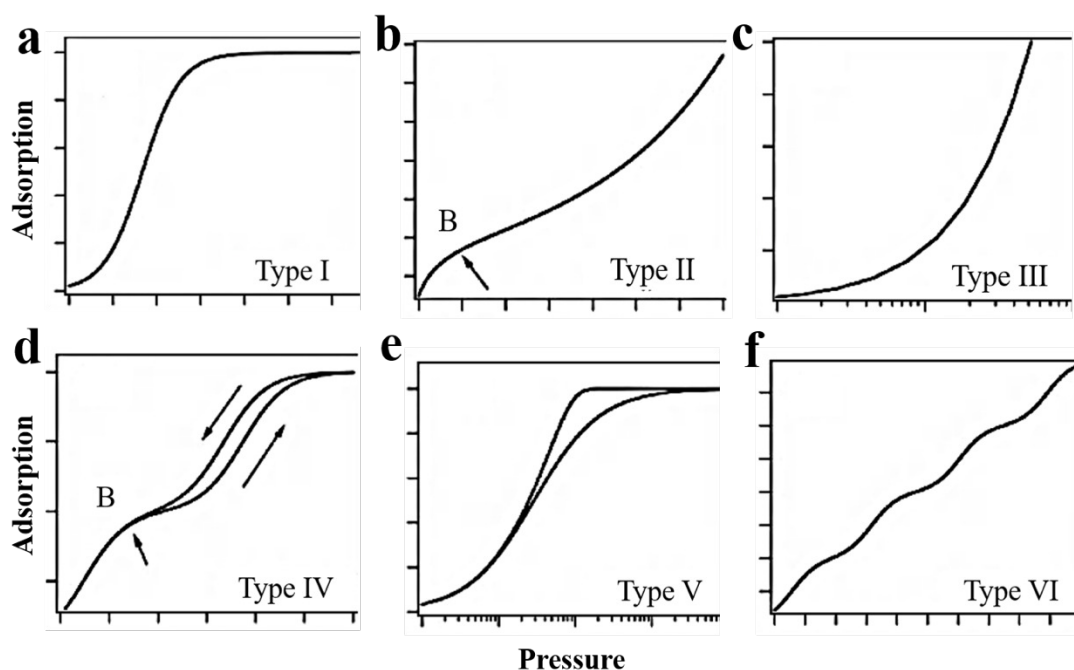


Figure 2.1. The six types of adsorption isotherms that classified by IUPAC.²

2.3 Geometric Characterization of Porous Crystalline

Materials

2.3.1 Pore size measurement

Automated computational characterisation of porous materials could be an arduous task. Foster et al. proposed an approach based on Delaunay decomposition to find the largest included (D_i) and largest free (D_f) spheres.³ The D_i represents the largest sphere refer the largest cavity of a porous material, and D_f is the sphere that capable of moving freely over the channel of a porous material, which also associates with the aperture of the channel. The empty Delaunay sphere frequently superimposes to form the channel and define the D_i and D_f .³ The pore size measurements are conducted with Zeo++ in this thesis.⁴

2.3.2 Surface area

Surface area is an important factor to characterise porous materials. The structure of periodical crystalline porous materials is generally determined by single-crystal X-ray diffraction (XRD) or powder X-ray diffraction (PXRD). Surface area can be defined into several conceptions for different aspects, Connolly surface area (CSA)⁵ and solvent surface area (SSA). (figure 2.2) The difference between CSA and SSA is the area that draws the surface, CSA is taken from the interface between probe and materials, while SSA is taken from the centre of the probe. Surface areas in this thesis are measured by Zeo++.⁴

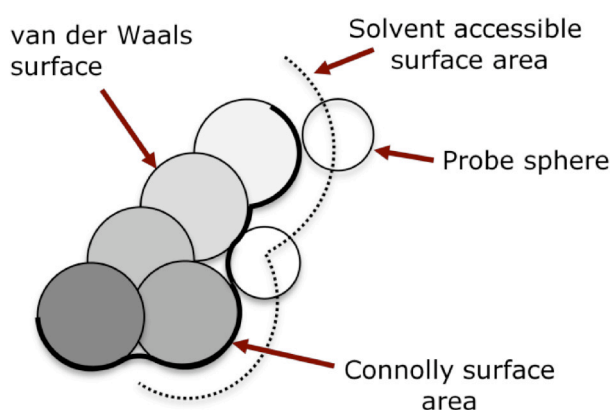


Figure 2.2. the definition of van der Waals surface, CSA and SSA from the work of Holden et al.⁶

The grid method is a way to measure the surface areas of porous materials. Just like its name, a porous material is split into a 3D grid by a specific interval, and a probe is inserted on each point of this grid. If this probe is not superimposed with any atoms of these materials, the insertion is accepted, and this position will be reported and added to the overall surface area, or this position will be rejected. The quality of this method significantly depends on the value of interval, the smaller the value is, the better the quality of the result.

2.3.3 Accessible surface area and accessible volume

ASA and AV are the critical geometric parameters for the characterisation of porous materials. Lee and Richards proposed these two parameters.⁷ Frost et al. reported the amounts of

adsorbates are strongly correlate with accessible surface area (ASA) at intermediate pressures, while the quantities of adsorbates are strongly correlating with accessible volume (AV) at high pressures.⁸ Currently, most algorithms compute ASA by Monte Carlo integration based on the work of Shrake and Rupley.⁹ However, the Monte Carlo method may overestimate ASA and AV as inaccessible pockets may be accounted. These pockets need to be excluded. Haranczyk et al. proposed a method to address inaccessible pockets by a grid-based front propagation to define channels and eliminate inaccessible pocket.⁴ Accessible surface areas and accessible volumes in this thesis are measured by Zeo++.⁴

2.3.4 Pore size distribution

Pore size distribution (PSD) histograms represent the fraction of void space volume at a range of pore size. The computational approaches were proposed by Do et al.¹⁰ and Sarkisov et al.¹¹ based on the idea of Gelb and Gubbins¹². Similar to the AV calculation, the Monte Carlo approach also used for the PSD calculation by the high-throughput software Zeo++.¹³

2.3.5 Radial distribution function

Radial distribution function (RDF) is a useful method to investigate the insight view of adsorption size. The RDF $g(r)$ is written as:

$$g_{ij}(r) = \frac{\Delta N_{ij}V}{4\pi r^2 \Delta r N_i N_j} \quad (2.1)$$

The r is the distance between species i and j , ΔN_{ij} is the number of j around i between the space from r to $r + \Delta r$, the volume and number of particles are denoted by V and N . RDF histograms in this thesis are computed with the RASPA implemented RDF computation module.¹⁴

2.4 Molecular Simulation

2.4.1 Molecular dynamic simulation

Molecular dynamic (MD) simulation is a technique to solve the position and velocity of a particle by Newton's equation of motion, and the computed position and velocity will be calculated based on the inter- and intramolecular interactions at the following step. The initial velocity of a particle is assigned randomly based on the Maxwell-Boltzmann distribution. The thermodynamic and diffusive properties can be computed with sufficient cycles of MD simulation.¹⁵ MD simulation mimics the natural procedure of particles transport and provides the trajectory for visualisation, which is unrealistic to obtain in the experiment and shows chaotic behaviour after around 50 ps.

The length of a time step is strictly relating to the speed of an MD simulation. After all, computational and time cost is the major limitation to the simulation, or most of the simulation technique will obsolete. Limited distance will move if we set the time step too small and leads to the unbearable computational resource waste. The giant time step may at least report an untrustworthy result or even instability of the integration algorithm then the simulation crash. MD simulations are conducted with RSAPA implemented module.¹⁴

2.4.2 Ensembles

In principle, For N atoms system, $6N$ variables ($3N$ positions and $3N$ velocities) are required for the description of the microscopic state of a system. This $6N$ space called phase space, and it evolves according to the laws of mechanics. For the macroscopic system, the variables such as temperature T , volume V and pressure p are the time average of the microscopic phase space. Gibbs replaced the time averaging to averaging over a group of microstates under the same macroscopic state and presented the idea of ensembles. According to the ergodic principle, ensemble averaging are identical to time averaging (infinitely long simulation). The phase-

space is noted as Γ , and the distribution relates to a probability density $p(\Gamma)$. The function form depends on the chosen ensemble.

For a single component :

$$dU(V, S, n) = -pdV + TdS + \mu dn \quad (2.2)$$

Which can be derived to:

$$dH(p, S, n) = Vdp + TdS + \mu dn \quad (2.3)$$

$$dA(V, T, n) = -pdV - SdT + \mu dn \quad (2.4)$$

$$dG(p, T, n) = Vdp - SdT + \mu dn \quad (2.5)$$

by a Legendre transformation, in which S is entropy, μ is chemical potential, n is the number of moles. The thermodynamic properties are denoted by U (internal energy), H (enthalpy), A (Helmholtz function) and G (Gibbs function). For an open system, the number of moles n can vary. Those thermodynamic properties can be transformed into new ensembles:

The *Hill energy* $L(V, S, \mu)$:

$$L = U - \mu n \quad (2.6)$$

$$dL(V, S, n) = -pdV + TdS - \mu dn \quad (2.7)$$

The *Ray energy* $R(p, S, \mu)$:

$$R = H - \mu n \quad (2.8)$$

$$dR(p, S, n) = Vdp + TdS - \mu dn \quad (2.9)$$

The *grand function* $J(T, V, \mu)$:

$$J = A - \mu n \quad (2.10)$$

$$dJ(V, T, n) = -pdV - SdT - \mu dn \quad (2.11)$$

The *Guggenheim function* $Z(p, T, \mu)$

$$Z = G - \mu n \quad (2.12)$$

$$dZ(p, T, n) = Vdp - SdT - \mu dn = 0 \quad (2.13)$$

All those functions are derived from a Legendre transformation of the internal energy $dU(V, S, n)$.

Figure 2.3 express those ensembles and their connection to the reservoirs.¹⁶ This reservoir imposes constant temperature T , pressure p and chemical potential μ . Ensembles on the left column are constant energy ensembles, and the constant temperature ensembles are on the right.

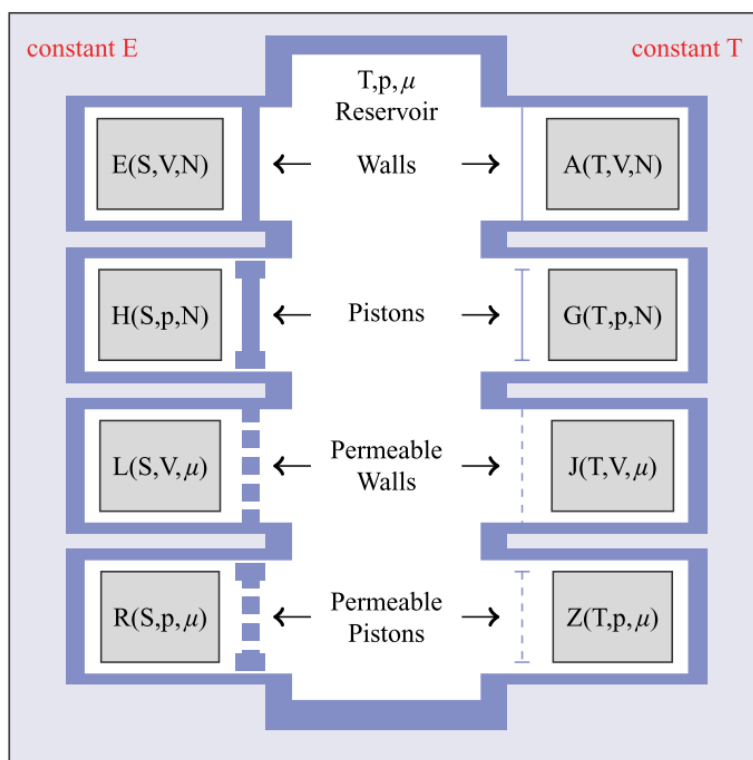


Figure 2.3. Ensembles for a single component system. The system contact with a constant temperature T , pressure p and chemical potential μ reservoir. The ensembles on the left is adiabatically isolated from the reservoir, and ensembles on the left are in thermal contact with the reservoir. The walls that not docked are allowed to move, and porous walls allow the particle change. The figure is taken from Ref. ¹⁶

MD and MC simulation conventionally samples the microcanonical ensemble by default as the total energy E , the number of particles N and volume V are kept constant. However, experiments more likely conducted under constant temperature T , the number of particles N and volume V (NVT or canonical ensemble). Hence, it is crucial to make the simulations

comparable to experiments. There are many ensembles for both MD and MC simulations. *NVE* ensemble is used for an isolated system, and the equilibrium can be achieved by altering temperature and pressure. *NVT* ensemble kept the number, volume and temperature; the systems can be equilibrated by changing the pressure and total energy. *NpT* ensemble is similar to the *NVT* ensemble, and the pressure is kept, where the total energy can be altered. For both *NVT* and *NpT* ensembles, the pressure is kept at constant by putting the system in a heat bath, and it is achieved by the thermostat in simulations, where the pressure can be controlled by barostat.¹⁷ *NpH* ensemble is quite similar to *NpT*, where the enthalpy *H* is constant, the value of instantaneous pressure and temperature is allowed to be fluctuating. In this thesis, both MD and MC simulation are used the Nose-Hoover thermostat and barostat¹⁷ that built-in RASPA software package.¹⁴

2.4.3 Monte Carlo simulation

Compare to MD, Monte Carlo (MC) is conceptually hard to understand. MC is a method to generate and measure probability distribution. There is no such ‘trajectory’ of the system is formed by MC generates snapshots. Target properties are outputted from the averages over all the computed states.¹⁸ To improve efficiency, Most MC algorithms modify the initial snapshot (so call “moves”) to form a new snapshot other than creating from scratch. This modification is called by ‘move’ and a ‘move’ can be either ‘accepted’ or ‘rejected’ by an ‘acceptance rule’. Those snapshots compose a chain called Markov chain. The time factor is not involved in this Markov chain, so only static properties can be computed by MC. MC simulation is computed by RASPA in this thesis.¹⁴

In General, MC statistical mechanics based on following assumptions:¹⁹

- (1) Ensemble averaging assumption.

The macroscopic behaviour of a system is determined by an average of an ensemble over an infinite number of random trials. This method of calculation reveals the statistical nature.

(2) Priori probabilities equal assumption.

For an macroscopic equilibrium system, energy states with the same energy have equal prior probability. This assumption is true on average rather than any individual system.

(3) Equilibrium state assumption.

The equilibrium state is the one with the maximum volume occupancy in phase space, which relates to the chance to find a certain state in a system.

As it was described above, MC is a computational method to explore probability or expectation, and the Markov Chain Monte Carlo (MCMC) method is one of the important tools.¹⁹ Infinite long MCMC gives an exact expression. However, it is unrealistic. Practically, MCMC can suggest the relative probability of each configuration. To detect those configurations with correct frequency, MCMC algorithm performs random trials on a current state, denoted as a state (o), to the new state (n), and eventually reach to the condition of detailed balance which originally used in Metropolis scheme²⁰. Those trials involve translation, rotation, insertion or deletion. While it will be accepted or rejected by the acceptance rule based on the condition of detailed balance. The probabilities of finding old state and new state are denoted as $P_{eq(o)}$ and $P_{eq(n)}$, and the conditional probability of performing trial move $o \rightarrow n$ and $n \rightarrow o$ are denoted as $\alpha(o \rightarrow n)$ and $\alpha(n \rightarrow o)$. The detail balance is defined as:

$$P_{eq(o)}\alpha(o \rightarrow n)P_{acc}(o \rightarrow n) = P_{eq(n)}\alpha(n \rightarrow o)P_{acc}(n \rightarrow o) \quad (2.14)$$

For the equilibrium in the metropolis algorithm:

$$\alpha(o \rightarrow n) = \alpha(n \rightarrow o) \quad (2.15)$$

Then:

$$P_{eq(o)}P_{acc}(o \rightarrow n) = P_{eq(n)}P_{acc}(n \rightarrow o) \quad (2.16)$$

And lead to:

$$\frac{P_{acc}(o \rightarrow n)}{P_{acc}(n \rightarrow o)} = \frac{P_{eq}(n)}{P_{eq}(o)} \quad (2.17)$$

So the Metropolis acceptance rule is written as:²⁰

$$P_{acc}(o \rightarrow n) = \min\left(1, \frac{P_{eq}(n)}{P_{eq}(o)}\right) \quad (2.18)$$

For the canonical partition function:

$$Q(N, V, T) = \frac{1}{h^3 N!} \iint e^{-\beta H(p^N, r^N)} d^N p d^N r \quad (2.19)$$

$$H = \sum_i \left(\frac{1}{2} \right) \left(\frac{p_i^2}{m_i} \right) + U(r^N) \quad (2.20)$$

Where the H is Hamiltonian, p is the linear momentum, m is the mass of particle and h^3 is the phase-space volume, $1/N!$ performs on the partition function due to classically particles in single species are indistinguishable. To further simplify this function:

$$\int e^{-\beta \left(\sum_i \left(\frac{p_i^2}{2m_i} \right) \right)} dp = \left(\int e^{-\beta \left(\frac{p^2}{2m} \right)} dp \right)^{3N} = \left(\frac{2\pi m}{\beta} \right)^{\left(\frac{3}{2} \right) N} \quad (2.21)$$

As de Broglie relation defined:

$$p_x = \frac{h}{\Lambda} \quad (2.22)$$

Where the h is the Plank constant and Λ is the de Broglie wavelength, then:

$$\frac{\left(\frac{1}{2} \right) p_x^2}{m} = \left(\frac{1}{2} \right) k_B T \quad (2.23)$$

So the de Broglie wavelength can be defined as:

$$\Lambda \equiv \left(\frac{h^2 \beta}{2\pi m} \right)^{\frac{1}{2}} \quad (2.24)$$

Hence, with the momentum integration:

$$\frac{1}{h^3 N!} \iint e^{-\beta H(p^N, r^N)} d^N p d^N r = \frac{1}{\Lambda^3 N!} \int e^{-\beta U(r^N)} d^N r \quad (2.25)$$

2.4.3.1 Canonical MC

The canonical ensemble impose the number of particle N , temperature T and volume V , and the partition function Q is written as ^{21,22}

$$Q(N, V, T) = \frac{1}{\Lambda^3 N!} \int e^{-\beta U(r^N)} d^N r \quad (2.26)$$

The $U(r^N)$ is the total energy of the system with particles at positions r^N , and the probability of these positions is proportional to $e^{-\beta U(r^N)}$. As described before, MC is conducted to get the average properties. For the NVT ensemble, the ordinary equation is written as:

$$\langle A(r^N) \rangle = \frac{\int A(r^N) e^{-\beta U(r^N)} d^N r}{\int e^{-\beta U(r^N)} d^N r} \quad (2.27)$$

And the acceptance rule of particle moves involve translation and rotation is:

$$acc(o \rightarrow n) = \min\left(1, e^{-\beta[U_n(r^N) - U_o(r^N)]}\right) \quad (2.28)$$

2.4.3.2 NpT ensemble

The NpT ensemble samples the phase space with constant N , p and T .^{23,24} Compare to the canonical ensemble, NpT ensemble allows the volume change attempt. The volume change from V to V' by ΔV that taken from a random number from a defined range $[-\Delta V_{min}, \Delta V_{max}]$,

The partition function was proposed by Guggenheimer:²⁵

$$\Delta(N, p, T) = \frac{C}{\Lambda^3 N!} \int V^N e^{-\beta p V} \left(\int e^{-\beta U(s^N; h)} d^N s \right) dV \quad (2.29)$$

The factor C is introduced to make the partition function dimensionless.²⁶⁻²⁸ It is volume scale factor but cannot be defined in general.²⁹ The general choice include $C = \beta p$ and $C = N/V$, However, the difference is not important in simulation due to the cancellation of the prefactors, and the average is defined as:

$$\langle A \rangle_{NpT} = \frac{1}{\Delta(N, p, T)} \int e^{-\beta p V} V^N \int A(s^N) e^{-\beta U(s^N; h)} d^N s dV \quad (2.30)$$

With the change of volume, the enthalpy changes with it:

$$\Delta H = \Delta U + p \Delta V - \frac{N}{\beta} \ln \left(\frac{V^n}{V^o} \right) \quad (2.31)$$

So the acceptance rule can be written as:

$$\frac{acc(o \rightarrow n)}{acc(n \rightarrow o)} = \frac{V_n^N e^{-\beta p V_n} e^{-\beta U_n(s^N; h)}}{V_o^N e^{-\beta p V_o} e^{-\beta U_o(s^N; h)}} = \left(\frac{V_n}{V_o} \right)^N e^{-\beta p (V_n - V_o)} e^{-\beta (U_n(s^N; h) - U_o(s^N; h))} \quad (2.32)$$

$$acc(V_o \rightarrow V_n) = \min(1, e^{-\beta \Delta H}) \quad (2.33)$$

However, the volume may also change in $\ln(V)$, and the partition function change to:

$$\Delta(N, p, T) = \frac{\beta p}{\Lambda^{3N} N!} \int V^{N+1} e^{-\beta p V} \left(\int e^{-\beta U(s^N; h)} d^N s \right) dV \quad (2.34)$$

The probability of finding such a volume is:

$$P(s^N, V) \propto V^{N+1} e^{-\beta p V} e^{-\beta U(s^N; h)} \quad (2.35)$$

The enthalpy change with the volume is:

$$\Delta H = \Delta U + p \Delta V - \frac{N+1}{\beta} \ln \left(\frac{V^n}{V^o} \right) \quad (2.36)$$

The acceptance rule for the particle is identical with the NVT ensemble:

$$\frac{acc(o \rightarrow n)}{acc(n \rightarrow o)} = \frac{V_n^N e^{-\beta p V_n} e^{-\beta U_n(s^N; h)}}{V_o^N e^{-\beta p V_o} e^{-\beta U_o(s^N; h)}} = \frac{e^{-\beta U_n(s^N; h)}}{e^{-\beta U_o(s^N; h)}} = e^{-\beta [U_n(s^N; h) - U_o(s^N; h)]} \quad (2.37)$$

2.4.3.3 Gibbs ensemble

The Vapour-Liquid Equilibrium (VLE) curves can be directly computed by the Gibbs ensemble.^{30,31} Gibbs ensemble combines NVT , μVT and NpT ensembles with two separate microscopic regions. For a divided NVT ensemble system, $V_I + V_{II} = V$ and $N_I + N_{II} = N$, where the I and II denotes the two divided systems. The partition function is defined as:

$$Q_{NVT}^{Gibbs} \equiv \frac{1}{\Lambda^{3N} N!} \sum_{N_I=0}^N \binom{N}{N_I} \int_0^V (V_I)^{N_I} (V_{II})^{N_{II}} \left(\int e^{-\beta U(s_{II}^{N_{II}}; h)} d^{N_{II}} s_{II} \int e^{-\beta U(s_I^{N_I}; h)} d^{N_I} s_I \right) dV_I \quad (2.38)$$

the probability of finding N_I particles in a certain form is written as:

$$P(N_I, V_I, s_I^{N_I}, s_{II}^{N_{II}}) \propto \frac{(V_I)^{N_I} (V_{II})^{N_{II}}}{N_I! N_{II}!} e^{-\beta (U(s_I^{N_I}; h) + U(s_{II}^{N_{II}}; h))} \quad (2.39)$$

The Gibbs ensemble conduct simulation in the following steps:

- (1) Translation, rotation of particles. This step is following the NVT ensemble.
- (2) Box volumes change (keep total system volume, $V = V_1 + V_2$), and the acceptance rule is:

$$acc(o \rightarrow n) = \min \left(1, \left(\frac{V_I(n)}{V_I(o)} \right)^{N_I+1} \left(\frac{V_{II}(n)}{V_{II}(o)} \right)^{N_{II}+1} e^{-\beta \Delta(u s^N)} \right) \quad (2.40)$$

(3) Exchange of particles between two boxes. For a component j exchange to another system, the acceptance rule is:

$$acc(o \rightarrow n) = \min \left(1, \frac{N_{I,j} V_{II}}{(N_{II,j} + 1) V_I} e^{-\beta (u(s_n^N) - u(s_o^N))} \right) \quad (2.41)$$

(4) NpT ensemble that allows the VI and VII changed independently, and the acceptance rule for the changing of VI, while the VII keep unchanged, is:

$$acc(o \rightarrow n) = \min \left(1, e^{-\beta \Delta U_I - \beta p (V_I(n) - V_I(o)) + (N_I+1) \ln \left(\frac{V_I(n)}{V_I(o)} \right)} \right) \quad (2.42)$$

2.4.3.4 Grand canonical ensemble

Grand canonical (μVT) ensemble is the most commonly used ensemble for adsorption simulation.³² This ensemble imposes the chemical potential μ , volume V and temperature T , and the partition function is:

$$Q(\mu, V, T) = \sum_{N=0}^{\infty} \frac{V^N e^{\beta \mu N}}{\Lambda^{3N} N!} \int e^{-\beta U(s^N; h)} d^N s \quad (2.43)$$

and the probability of a configuration is:

$$P(s^N, V) \propto \frac{V^N e^{\beta \mu N}}{\Lambda^{3N} N!} e^{-\beta U(s^N; h)} \quad (2.44)$$

The acceptance rule for several trials are list below:

(1) Particle move

$$\frac{acc(o \rightarrow n)}{acc(n \rightarrow o)} = \frac{\frac{V^N e^{\beta \mu N}}{\Lambda^{3N} N!} e^{-\beta U_n(s^N; h)}}{\frac{V^N e^{\beta \mu N}}{\Lambda^{3N} N!} e^{-\beta U_o(s^N; h)}} = e^{-\beta [U_n(s^N; h) - U_o(s^N; h)]} \quad (2.45)$$

(2) Insertion

$$\frac{acc(o \rightarrow n)}{acc(n \rightarrow o)} = \frac{\frac{V^{N+1} e^{\beta \mu (N+1)}}{\Lambda^{3(N+1)} (N+1)!} e^{-\beta U_n(s^{N+1}; h)}}{\frac{V^N e^{\beta \mu N}}{\Lambda^{3N} N!} e^{-\beta U_o(s^N; h)}} = \frac{V e^{\beta \mu}}{\Lambda^3 (N+1)} e^{-\beta [U_n(s^{N+1}; h) - U_o(s^N; h)]} \quad (2.46)$$

(3) Deletion

$$\frac{acc(o \rightarrow n)}{acc(n \rightarrow o)} = \frac{\frac{V^{N-1} e^{\beta\mu(N-1)}}{\Lambda^{3(N-1)} (N-1)! e^{-\beta U_n(s^{N-1}; h)}}}{\frac{V^N e^{\beta\mu N}}{\Lambda^{3N} N! e^{-\beta U_o(s^N; h)}}} = \frac{\Lambda^3 N}{V e^{\beta\mu}} e^{-\beta[U_n(s^{N-1}; h) - U_o(s^N; h)]} \quad (2.47)$$

The pressure p is related to the chemical potential μ and fugacity f , which written as:

$$\beta\mu = \beta\mu_{IG}^0 + \ln(\beta f) \quad (2.48)$$

The chemical potential μ is defined as:

$$\mu_{IG}^0 \equiv \frac{\ln(\Lambda^3)}{\beta} \quad (2.49)$$

Fugacity is a close term to the pressure that describe the activity of gas. The fugacity coefficient ϕ is written as:

$$\phi = \frac{f}{p} = \exp\left[\frac{g(T, p) - g^{IG}(T, p)}{RT}\right] = \exp\left[\frac{\int_0^p \left(\frac{z-1}{p}\right)_T dp}{RT}\right] \quad (2.50)$$

The $g(T, p)$ is Gibbs free energy and IG indicates the idea gas, z is the compressibility. For ideal gas, $f = p$ (p close to 0) and the fugacity and pressure can be converted. For components in mixtures, the fugacity of certain gas can take from the fugacity of its pure gas by the Lewis-Randall rule,³³ or compute by the certain equation of state with appropriate mixing rules.³⁴ The acceptance rules for insertion and deletion are listed below:

(1) Insertion

$$acc(N \rightarrow N + 1) = \min\left(1, \frac{\beta V \phi p}{N + 1} e^{-\beta[U_n(s^{N+1}; h) - U_o(s^N; h)]}\right) \quad (2.51)$$

(2) Deletion

$$acc(N \rightarrow N - 1) = \min\left(1, \frac{N}{\beta V \phi p} e^{-\beta[U_n(s^{N-1}; h) - U_o(s^N; h)]}\right) \quad (2.52)$$

2.4.4 Heat of adsorption

The heat of adsorption q or adsorption enthalpy $-\Delta H$ is a vital thermodynamic property to understand the adsorption and capture capability a material. For a host (h) system with guest (g) loading of θ , the heat of adsorption is defined by Clausius-Clapeyron equation:³⁵

$$-q = \Delta H = k_B \left(\frac{\partial \ln \left[\frac{P}{P_0} \right]}{\partial T^{-1}} \right)_{\theta} = \left(\frac{\partial \ln \left[\frac{P}{P_0} \right]}{\partial \beta} \right)_{\theta} \quad (2.53)$$

$$\beta = \frac{1}{k_B T} \quad (2.54)$$

The p is the pressure and denoted with 0 refer to the reference pressure, T is the temperature. For a certain temperature, the adsorption quantity θ can be defined as a function of P :

$$\theta = K_H V P \quad (2.55)$$

This linear function is sufficient when the $P \rightarrow 0$, and K_H is know as Henry coefficient, and V is the volume of a host. Then the heat of adsorption function can be written as:

$$-q = \Delta H = - \frac{\partial \ln \left[\frac{K_H}{K_{H0}} \right]}{\partial \beta} \quad (2.56)$$

Similar to P_0 , K_{H0} is the Henry coefficient at reference state. The Henry coefficient can be computed by Widom's test particle method.³⁶⁻³⁸

$$K_H = \beta e^{-\beta \mu_{ex}} = \beta \times \frac{\langle e^{-\beta \mu^+} \rangle_H}{\langle e^{-\beta \mu_{IG}^+} \rangle_{EB}} \quad (2.57)$$

The μ is the chemical potential of guest molecules, and ex stands for the excess, and μ^+ is the energy of a test molecule. The $\langle \dots \rangle$ stand for the average, and $\langle \dots \rangle_H$ and $\langle \dots \rangle_{EB}$ are the average over the host-guest configurations and test in an empty box (ideal gas).

For canonical ensemble (NVT), the heat of adsorption is:^{35,39}

$$-q = \Delta H = \langle U_1 \rangle_1 - \langle U_0 \rangle_0 - \langle U_g \rangle - \frac{1}{\beta} \quad (2.58)$$

The U is the energy and the denoted number 1 and 2 refer to the number of guest molecule, while the $\langle \dots \rangle_N$ stands for the ensemble average (NVT).

For grand canonical (μVT) ensemble, the number of guests is changed with the process of simulation. For the single guest molecule change, the potential energy difference is:

$$\langle U_{N+1} \rangle_{N+1} - \langle U_N \rangle_N \approx \left(\frac{\partial \langle U \rangle_\mu}{\partial \langle N \rangle_\mu} \right)_\beta = \frac{\langle U \times N \rangle_\mu - \langle U \rangle_\mu \langle N \rangle_\mu}{\langle N^2 \rangle_\mu - \langle N \rangle_\mu \langle N \rangle_\mu} \quad (2.59)$$

The $\langle \dots \rangle_\mu$ is the grand canonical ensemble average, and the heat of adsorption is written as:

$$-q = \Delta H = \frac{\langle U \times N \rangle_\mu - \langle U \rangle_\mu \langle N \rangle_\mu}{\langle N^2 \rangle_\mu - \langle N \rangle_\mu \langle N \rangle_\mu} - \langle N_g \rangle - \frac{1}{\beta} \quad (2.60)$$

This function gives the heat of adsorption at zero loading, which also defined as the isosteric heat of adsorption. The heat of adsorption is computed by RASPA software package in this thesis.¹⁴

2.4.5 Free energy profile

Molecular diffusion in nanometer confinements, such as those present in the crystal structures simulated here, can be so slow that the timescale for a particle to hop from one free-energy minimum to the next becomes too large to be reached by routine application of molecular

dynamics simulations. For example, a guest molecule may be trapped inside a cage molecule, and the actual time needed for it to escape through a cage window is negligible compared to the time it spends inside the cage. Such a process can be considered an activated process, which may be alternatively probed by rare-event simulation methods such as transition state theory (TST). A comprehensive demonstration of the method in studying the transport of adsorbates in nanoporous adsorbents was given by Dubbeldam et al.⁴⁰

Free energy profiles were calculated using Monte Carlo simulations in the canonical (NVT) ensemble, together with the Widom particle insertion method. During the simulation, a probe molecule (i.e., H_2 or D_2) was inserted at many random positions in the cage crystal structure to measure the energy required for or obtained by each of the insertions of the molecule into the system. This energy is mapped onto the reaction coordinate q to produce a free energy profile by:

$$\beta F(q) = -\ln\langle e^{-\beta\Delta U}\rangle_N \quad (2.61)$$

here $\beta = 1/(k_B T)$ with k_B being the Boltzmann constant and T is the temperature, and $\langle e^{-\beta\Delta U}\rangle_N$ is the average Boltzmann factor of all N sampled positions in the plane perpendicular to the reaction coordinate q . Free energy profile is computed by RASPA software package in this thesis.¹⁴

2.5 Interatomic Potentials

Classical molecular simulation approaches describe the energy of a host and guest system through the sum of inter- and intra-molecular interactions which are described by force fields. Such classical approaches do not consider the degree of freedom of electrons, which saves the computational effort to address electrons interactions by using Born-Oppenheimer

approximation.⁴¹ By removing the complicity of electron motions, we can simulate systems with a large number of atoms (up to thousands) in affordable time length. The interatomic potential can be divided and calculate separately. The expression for the sum of total energy is:

$$E_{\text{Total}} = E_{\text{stretch}} + E_{\text{bend}} + E_{\text{torsion}} + E_{\text{improper torsion}} + E_{\text{electrostatic}} + E_{\text{VDW}} \quad (2.62)$$

The E_{stretch} stands for the two-body stretching potential, E_{bend} is the three-body bending potential, and E_{torsion} , $E_{\text{improper torsion}}$ are four-body torsional potential. The summation of these four potentials is bonded potential. The non-bonding interaction is the summation of the electrostatic potential ($E_{\text{electrostatic}}$) and van der Waals potential (E_{VDW}).

Force fields were designed to reproduce the structure properties, adsorption, diffusion of materials. An important feature of a force field is their transferability, as a special force field parametrisation for each material may significantly compromise most of the method introduced in this section. However, transferability compromises accuracy. Practitioners should find a balance between them.

2.5.1 Bond stretching

As mentioned above, bonded terms can be briefly described as the summation of bond stretch, angle bending, dihedral and improper torsion terms. Bond stretch potential terms are usually described through the Hook's law:

$$E_{\text{stretch}} = k_b(r - b_0)^2 \quad (2.63)$$

Hooke's law is a relatively simple expression, and CHARMM used the equation,^{42,43} AMBER,^{44,45} DREIDING⁴⁶ and OPLS⁴⁷⁻⁵⁰ force field as the default setting. This equation shows the energy E_{stretch} changes with the distance r to the force field defined reference b_0 .

An alternative expression addressing the bond stretch is Morse function⁵¹,

$$E_{stretch} = D_e \{1 - \exp(-a(r - b_0))\}^2 \quad (2.64)$$

$$a = w \sqrt{\frac{\mu}{2D_e}}, \quad w = \sqrt{\frac{k}{\mu}} \quad (2.65)$$

Where D_e is the energy depth of the potential, μ is the reduced mass of two atoms, w is the angular frequency of the bond and b_0 is the bond length.

The scheme for both Morse potential and harmonic potential shown in figure 2.4. Morse potential is generally more complex than Hooke's law. It specifically describes the vibration near the equilibrium point and dissociation of a bond. However, the major drawback of this function is computationally expensive, and three parameters need to predefine. The harmonic potential is relatively computational and straightforward affordable. It describes the bond vibration well around the equilibrium point, and energy increasing dramatically with the length difference to the reference bond length. Usually, the harmonic potential is sufficient for the bond energy description of physisorption and diffusion of particles, as no bonds breaking is involved.

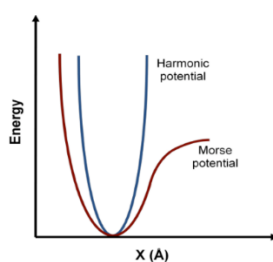


Figure 2.4. The curves for the harmonic potential (Hook's law, blue) and the Morse potential (red) that from the work of Daniel Holden.⁶

2.5.2 Angle bending

Several expressions can describe angle bending potentials. For CHARMM,^{42,43} AMBER,^{44,45} and OPLS⁴⁷⁻⁵⁰, they are parameterised by the harmonic potential:

$$E_{bending} = \frac{k}{2}(\theta - \theta_0)^2 \quad (2.66)$$

The k stands for the bending energy constant and the θ and θ_0 are the bond angle and reference bond angle defined in the force field respectively. DREIDING⁴⁶ uses the harmonic cosine function:

$$E_{bending} = k[\cos(\theta) - \cos(\theta_0)] \quad (2.67)$$

Similar to the harmonic potential, k is the bending energy constant and θ and θ_0 are the bond angle and reference bond angle defined in the force field.

2.5.3 Torsional and improper torsional terms

The magnitudes of both bond stretching and angle bending are quite large, and substantial energy is needed to provide deformation from their reference values. Hence, torsional terms show more capability to vary the structure. Similar to the bonding stretching and angle bending terms, torsional and improper torsion terms, the four-body dihedral motion is based on the understanding of the energy barriers of bond rotation. Quantum mechanical calculation suggests that the rotational barriers are caused by the antibonding interaction of two opposite atoms of a four-body system. The staggered conformation leads to the minimum antibonding interaction, and the eclipsed conformation causes the maximum. Hence, many force fields have tried to model such changes:

$$E_{torsion} = \sum_{n=0}^N \frac{V_n}{2} [1 + \cos(nw - \gamma)] \quad (2.68)$$

$$E_{torsion} = \sum_{n=0}^N C_n \cos(w)^n \quad (2.69)$$

The w is the angle of the torsion, and V_n stands for the barrier's height, n is the multiplicity that defines the number of minimal points, and γ defines the where the minimum points should locate.

For an atom vibrate in-and-out a plane defined by three atoms, it is necessary to define an energy term that maintains this four-body system in the favourable energy state. For example, cyclobutanone, which structure is experimental confirmed that the oxygen atom is in the same planar of the three adjacent carbon atoms.⁴¹ Without consideration of the improper dihedral term, the C-C=O angle is most likely vibrating close to its reference angle 120° and locate out of planar (figure 2.5).



Figure 2.5. The predicted conformation of cyclobutane with (left) or without (right).

There are several approaches to describe this out-of-plane term that maintain the reference improper torsion angle, for example:

$$E_{improper\ torsion} = k(1 - \cos(2w)) \quad (2.70)$$

The definition is similar to the equation discussed above.

2.5.4 van der Waals interaction

The van der Waals interaction is the combination of long-range dispersive interaction and short-range repulsive interaction. The long-range dispersive interaction is the response for the attractive force between atoms. London applied quantum mechanics to describe this dispersive interaction, so this interaction is also referred to as the London dispersion force.⁵² This dispersive interaction is caused by the instantaneous fluctuations of electron clouds of an atom, while the electron clouds fluctuation of the adjacent atoms is induced by this fluctuation then cause the attractive interaction. The Pauli principle can understand the repulsive interaction that two electrons with the same spin are prohibited, the repulsive force forbids them to exist in the same region of space. The repulsive force increases dramatically with the decreasing of atoms distance, the pressing cause electron density shift that causes the repulsion between nuclei.

To model attractive and repulsive interaction, a force field should accurately reproduce the potential curve. The 12-6 Lennard-Jones (LJ) interaction is the most commonly used expression:

$$E_{VDW} = 4\varepsilon \left[\left(\frac{\sigma}{r} \right)^{12} - \left(\frac{\sigma}{r} \right)^6 \right] \quad (2.71)$$

The ε is potential well and σ is the collision diameter where the separation energy is zero, this expression is rather computational cheap, as the known of $\left(\frac{\sigma}{r} \right)^6$, $\left(\frac{\sigma}{r} \right)^{12}$ is easy to compute. The other expression is known as 9-6 LJ potential:

$$E_{VDW} = \varepsilon \left[2 \left(\frac{\sigma}{r} \right)^9 - 3 \left(\frac{\sigma}{r} \right)^6 \right] \quad (2.72)$$

Another function form is the Hill or Buckingham potential function:

$$E_{VDW} = a \exp(-br) - \left(\frac{c}{r} \right)^6 \quad (2.73)$$

There are three redefinable parameters rather than two parameters in LJ potential function (ϵ and σ). However, LJ potential is commonly used for practitioners. Generic force fields are generally parameterize based on atoms. In order to combine two defined parameters of different type of atoms, there are three common mixing rules:

(1) Lorentz-Berthelot

$$\epsilon_{ij} = \sqrt{\epsilon_i \epsilon_j} \quad \sigma_{ij} = \frac{\sigma_i + \sigma_j}{2} \quad (2.74)$$

(2) Jorgensen

$$\epsilon_{ij} = \sqrt{\epsilon_i \epsilon_j} \quad \sigma_{ij} = \sqrt{\sigma_i \sigma_j} \quad (2.75)$$

(3) Waldman-Hagler

$$\epsilon_{ij} = \frac{2\sigma_i^3 \sigma_j^3}{\sigma_i^6 + \sigma_j^6} \sqrt{\epsilon_i \epsilon_j} \quad \sigma_{ij} = \left(\frac{\sigma_i^6 + \sigma_j^6}{2} \right)^{\frac{1}{6}} \quad (2.76)$$

Table 2.1 listed several van der Waals expressions and mixing rules for some generic force fields. Other than the zero-energy distance σ , the equilibrium distance R was also implemented in some force fields. Where the $R = 2^{\frac{1}{6}}\sigma$

Table 2.1. The van der Waals potentials expressions for several generic force fields.

<i>Force Fields</i>	<i>Potential Energy expressions</i>	<i>Mixing Rules</i>
CHARMM ^{42,43}	$E_{VDW} = \varepsilon \left[\left(\frac{R}{r_{ij}} \right)^{12} - 2 \left(\frac{R}{r_{ij}} \right)^6 \right]$	Lorentz-Berthelot
AMBER ^{44,45}	$E_{VDW} = \varepsilon \left[\left(\frac{R}{r_{ij}} \right)^{12} - 2 \left(\frac{R}{r_{ij}} \right)^6 \right]$	Lorentz-Berthelot
OPLS ⁴⁷⁻⁵⁰	$E_{VDW} = 4\varepsilon \left[\left(\frac{\sigma}{r} \right)^{12} - \left(\frac{\sigma}{r} \right)^6 \right]$	Jorgensen
DREIDING ⁴⁶	$E_{VDW} = \varepsilon \left[\left(\frac{R}{r_{ij}} \right)^{12} - 2 \left(\frac{R}{r_{ij}} \right)^6 \right]$	Lorentz-Berthelot
UFF ⁵³	$E_{VDW} = \varepsilon \left[\left(\frac{R}{r_{ij}} \right)^{12} - 2 \left(\frac{R}{r_{ij}} \right)^6 \right]$	Lorentz-Berthelot
TraPPE ⁵⁴	$E_{VDW} = 4\varepsilon \left[\left(\frac{\sigma}{r} \right)^{12} - \left(\frac{\sigma}{r} \right)^6 \right]$	Lorentz-Berthelot
CSFF ⁵⁵	$E_{ij} = \varepsilon_{ij} \left[2 \left(\frac{\sigma_{ij}}{r} \right)^9 - 3.6 \left(\frac{\sigma_{ij}}{r} \right)^6 \right]$	Waldman-Hagler

The van der Waals potential need to be cut at certain distant, which so called “cut-off” distance. For MC simulation, the cut-off distance can be applied due to the van der Waals potentials are negligible at that distance. However, simply cut of the energy may lead to force divergence. In general, the van der Waals potential can be switched to a smooth function.⁵⁶⁻⁵⁸

$$E_{VDW} = \begin{cases} E_{VDW} & r_{ij} < r_{on} \\ E_{VDW} \times \frac{(r_{off}^2 - r^2)(r_{off}^2 + 2r^2 - 3r_{on})}{(r_{on}^2 - r_{off}^2)^3} & r_{on} \leq r_{ij} \leq r_{off} \\ 0 & r_{ij} > r_{off} \end{cases} \quad (2.77)$$

2.5.5 Electrostatic interaction

Charge distribution of a molecule rarely equal due to the electronegativity of elements are different, atoms with stronger electronegativity attract electrons more than the less electronegative atoms. The typical approach to describe electrostatic interaction is defined as partial charge at each atom centre, then interacted by Coulomb’s law. The partial charge

generally uses fractional electron which either positive or negative. The way to calculate partial charges is the quantum level calculation. Such as ChelpG⁵⁹, a method to fit electron potential and obtain partial charge. Coulomb's law is commonly used to calculate electrostatic interaction:

$$E_{electrostatic} = \frac{1}{4\pi\epsilon_0} \sum_{i<j} \frac{q_i q_j}{|r_i - r_j|} = \frac{1}{8\pi\epsilon_0} \sum_{i \neq j} \frac{q_i q_j}{|r_i - r_j|} \quad (2.78)$$

The q_i and q_j are the partial charges of atoms "i" and "j" while the $|r_i - r_j|$ is the distance between atom "i" and "j". The ϵ_0 is the electric permittivity of free space ($8.8541878176 \times 10^{-12} F/m$). The two expressions are rather similar, the first expression explicitly computes all pairs, and the second expression simply divided by 2 to compensate the double counting. One method to simplify this calculation uses the Ewald transformation method.⁶⁰⁻⁶²

2.5.6 Quantum sieving effect

Beenakker et al. introduced the isotope separation principle in 1995 that isotope separation becomes possible as the size difference between pore and aimed particle is near the particle's de Broglie wavelength.⁶³ FH tail potential⁶⁴ modification is used in this section to address the quantum effects in molecular-level simulations. The potentials can be listed below:

$$U_{FH}(r_{ij}) = U_C(r_{ij}) + \frac{\hbar^2}{24\mu_{ij}k_B T} \left[U_C''(r_{ij}) + 2 \frac{U_C'(r_{ij})}{r_{ij}} \right] \quad (2.79)$$

Where the r_{ij} is the distance between particles i and j , \hbar is the reduced Planck constant, k_B is the Boltzmann constant, and μ_{ij} is the reduced mass of particles i and j , which is calculated by the equation $m_i m_j / (m_i + m_j)$. $U_C(r_{ij})$ is the Lenard-Jones (LJ) potential. With the combination of Coulomb potential, the detail nonbonding interaction is presented below:

$$U^{tot}(r_{ij}) = 4\epsilon_{ij} \left[\left(\frac{\sigma_{ij}}{r_{ij}} \right)^{12} - \left(\frac{\sigma_{ij}}{r_{ij}} \right)^6 \right] + \frac{4\epsilon_{ij}}{r_{ij}^2} \frac{\hbar^2}{24\mu_{ij}k_B T} \left[132 \left(\frac{\sigma_{ij}}{r_{ij}} \right)^{12} - 30 \left(\frac{\sigma_{ij}}{r_{ij}} \right)^6 \right] + \frac{q_i q_j}{4\pi\epsilon_0 r_{ij}} \quad (2.80)$$

2.6 Advanced Simulation methods

2.6.1 Configuration biased Monte Carlo method (CBMC)

Many techniques have been developed to improve the converge of conventional Widom method.⁶⁵ It is time-consuming for long-chain molecule successful insertion from the gas phase. This method primarily reduce the rejection rate that caused by high energy overlaps. The principle of CBMC method is growing the molecule to an acceptable configuration that based on the work of Rosenbluth and Rosenbluth.⁶⁶ Vlogt et al. proposed a procedure for CBMC simulation:⁶⁷ CBMC simulation is conducted by RASPA software package.¹⁴

(1) Bond length modification

A branch atom (b) is chosen randomly, and the bond length (l) change probability is written as:

$$P(l)dl = e^{-\beta\mu^{bond(l)}} db \quad (2.81)$$

$$P(l)dl = l^2 e^{-\beta\mu^{bond(l)}} dl \quad (2.82)$$

The acceptance rule is given by:

$$acc(o \rightarrow n) = \min\left(1, \frac{l(n)}{l(o)} e^{-\beta(\mu^{bond(l(n))} - \mu^{bond(l(o))})}\right) \quad (2.83)$$

(2) Bond angle modification

Similar to the bond length change, at an atom position b , probability of angle (θ) is written as:

$$P(\theta)d\theta = e^{-\beta\mu^{bend(\theta)}} db \quad (2.84)$$

$$P(\theta)d\theta = \sin(\theta) e^{-\beta\mu^{bend}(\theta)} \quad (2.85)$$

The acceptance is:

$$acc(o \rightarrow n) = \min\left(1, \frac{\sin(\theta(n))}{\sin(\theta(o))} e^{-\beta(\mu^{bend}(\theta(n)) - \mu^{bend}(\theta(o)))}\right) \quad (2.86)$$

(3) Rotation

The rotation is similar to the bond bending, and this move changes the bend angle, so the acceptance rule is:

$$acc(o \rightarrow n) = \min\left(1, e^{-\beta(\mu^{bend}(\theta(n)) - \mu^{bend}(\theta(o)))}\right) \quad (2.87)$$

Unfortunately, this method failed on the torsional angles distribution generation

Siepmann et al. introduced the CBMC method that allows the assembly of the molecule along the process of MC.⁶⁸⁻⁷⁰ The potential energy of a molecule is decomposed into two parts:

$$E = E_{int} + E_{ext} \quad (2.88)$$

The E_{int} part represents the potential energy of an internally bonded molecule, which is used to generate the trial positions and orientation. For an existing segment, a set of k trial positions are generated respect to the internal potential E_{int} change from segment to segment connects with a segment at the trial position. The external energy E_{ext} of each trial position will be calculated. For a trial position j on segment i , the acceptance rate is:

$$P_i(j) = \frac{\exp[-\beta E_i^{ext}(j)]}{\sum_{i=1}^k \exp[-\beta E_i^{ext}(i)]} = \frac{\exp[-\beta E_i^{ext}(j)]}{W(i)} \quad (2.89)$$

The selected trial orientation will be added to the previous segment and the procedure mentioned above will repeat until the entire molecule has been grown. For this molecule, the Rosenbluth factor W^{new} is given by

$$W^{\text{new}} = \prod_i w(i) \quad (2.90)$$

2.6.2 Continuous fractional component Monte Carlo method (CFCMC)

Shi and Maginn developed this method based on conventional Monte Carlo methods.⁷¹ Partial insertions and deletions of guest particles method are implemented by a continuous coupling parameter and adaptive bias potential. A guest molecule is inserted into an open system while a parameter λ scales the interaction with the surrounding host atoms and guest atoms. Note that only the intermolecular interaction will be considered during insertion and deletion for CFCMC technique. In the original work of Shi and Maginn, this utility was achieved by the modification of Lennard-Jones function and Coulomb's law:

$$U_{\text{non-bonding}}(r) = \left\{ \frac{1}{\left[\frac{1}{2}(1-\lambda)^2 + \left(\frac{r}{\sigma}\right)^6 \right]^2} - \frac{1}{\left[\frac{1}{2}(1-\lambda)^2 + \left(\frac{r}{\sigma}\right)^6 \right]} \right\} + \lambda^5 \frac{q_i q_j}{4\pi\epsilon_0 r_{ij}} \quad (2.91)$$

For the scaling factor λ , it will be kept in-between $\lambda = 0$ and $\lambda = 1$. There is no intermolecular interaction when $\lambda = 0$ and the function expression is the same as the classical Lennard-Jones function and Coulomb's law when $\lambda = 1$. For CFCMC method, every atom of the guest molecule can be treated individually with its scale factor λ . The fluctuation of the scaling factor treats each atom as a balloon. CFCMC uses similar moves, such as translation, rotations. However, for the unique parameter λ , the additional algorithm needs to be implemented to achieve the change of λ by using $\lambda(n) = \lambda(o) + \Delta\lambda$. The magnitude of $\Delta\lambda$ is chosen and adjusted

to ensure a nearly 50% acceptance. Another factor η is used on λ to avoid λ stuck in a certain range, There are three possibilities after the change of λ :

(1) $\lambda(n)$ is in the range of 0 to 1:

Only the scaling factor λ and intermolecular potential are changed, and the number of atoms in the system and their positions is kept unchanged, while this acceptance probability is given by

$$P_{acc} = \min\left(1, e^{-\beta[U(n)-U(o)]+\eta(\lambda(n))-\eta(\lambda(o))}\right) \quad (2.92)$$

(2) $\lambda(n)$ exceeds 1:

When the scaling factor surpasses 1, for example, when the $\lambda(n) = 1 + a$, which means this particular atom is fully present with $\lambda = 1$ and another particle with $\lambda = a$ will be inserted into the system. In the original work of Shi and Maginn, virtual particles will be taken out and store in computer memory.

(3) smaller than 0:

When $\lambda(n)$ is less than 0, for example, $\lambda(n) = -a$, this particular fractional atom will be erased and replaced with a fractional atom which $\lambda(n) = 1 - a$.

The acceptance rules for insertion and deletion with μ VT ensemble are:

$$P_{acc}(N \rightarrow N + 1) = \min\left(1, \frac{f\beta V}{N + 1} e^{\eta(\lambda(n))-\eta(\lambda(o))} e^{-\beta[U(n)-U(o)]}\right) \quad (2.93)$$

$$P_{acc}(N \rightarrow N - 1) = \min\left(1, \frac{N}{f\beta V} e^{\eta(\lambda(n))-\eta(\lambda(o))} e^{-\beta[U(n)-U(o)]}\right) \quad (2.94)$$

Both CBMC and CFCMC are designed to overcome the low acceptance ratio problem of insertion and deletion of big guest molecules or highly dense guest molecules in an adsorbent system. CFCMC simulation is conducted by RASPA software package in this thesis.¹⁴

2.6.3 Hybrid GCMC/MD simulation

Traditionally, GCMC simulation is the most efficient technique to predict adsorption isotherms that the number of adsorbates is allowed to fluctuate to achieve an equilibrium under the defined chemical potential (μ) and temperature (T). However, this technique can not directly predict the adsorption isotherm of a flexible porous material, a reparameterization is required. However, reparameterize a force field for each flexible system is at least inefficient, more importantly, the flexibility effects of adsorbent on the adsorption property are neglected. A simulation is an efficient tool that allows us directly observe the microscopic world, and it is such a shame if we did not further explore the dance between hosts and guests. MD simulation generally allows the vibrations of a host molecule, but the number of a guest molecule is kept constant among the computation.

Hybrid osmotic Monte Carlo (HOMC) simulation is one of the methods that combine both GCMC and MD algorithm.⁷² The osmotic thermodynamic ensemble is appropriate to describe the flexibility of an adsorption system ($N_{\text{host}}\mu_{\text{ads}}\sigma T$),⁷³ the host atom number (N_{host}), adsorbate chemical potential (μ_{ads}), is kept consistent, stress (σ , at an isotropic system, it is simply the pressure P) and temperature (T) is kept constant, while the simulation volume and number of molecules are changed to equilibrium. This is a hybrid statistic ensemble that combines NpT and μ VT ensembles, and the probability is written as:

$$P(s, V, N_{\text{ads}}) \propto \frac{V^N e^{\beta\mu_{\text{ads}}N_{\text{ads}}}}{\Lambda_{\text{host}}^{3N_{\text{host}}} N_{\text{host}}! \Lambda_{\text{ads}}^{3N_{\text{ads}}} N_{\text{ads}}!} e^{-\beta(U(s;h)+pV)} \quad (2.95)$$

$$\Lambda_{host} = \frac{h}{\sqrt{2\pi m_{host} k_B T}}, \quad \Lambda_{ads} = \frac{h}{\sqrt{2\pi m_{ads} k_B T}} \quad (2.96)$$

There are four types of moves:

(1) Particle move

$$\frac{acc(o \rightarrow n)}{acc(n \rightarrow o)} = \frac{\left(\frac{1}{\Lambda_{host}^{3N_{host}} N_{host}!}\right) \left(\frac{V^N e^{\beta \mu_{ads} N_{ads}}}{\Lambda_{ads}^{3N_{ads}} N_{ads}!}\right) e^{-\beta(U_n(r)+pV)}}{\left(\frac{1}{\Lambda_{host}^{3N_{host}} N_{host}!}\right) \left(\frac{V^N e^{\beta \mu_{ads} N_{ads}}}{\Lambda_{ads}^{3N_{ads}} N_{ads}!}\right) e^{-\beta(U_o(r)+pV)}} = e^{-\beta[U_n(s^N;h)-U_o(s^N;h)]} \quad (2.97)$$

(2) Insertion

$$\begin{aligned} \frac{acc(o \rightarrow n)}{acc(n \rightarrow o)} &= \frac{\left(\frac{1}{\Lambda_{host}^{3N_{host}} N_{host}!}\right) \left(\frac{V^{N+1} e^{\beta \mu_{ads} (N_{ads}+1)}}{\Lambda_{ads}^{3(N_{ads}+1)} (N_{ads}+1)!}\right) e^{-\beta(U_n(s^{N+1};h)+pV)}}{\left(\frac{1}{\Lambda_{host}^{3N_{host}} N_{host}!}\right) \left(\frac{V^N e^{\beta \mu_{ads} N_{ads}}}{\Lambda_{ads}^{3N_{ads}} N_{ads}!}\right) e^{-\beta(U_o(s^N;h)+pV)}} \\ &= \frac{V e^{\beta \mu_{ads}}}{\Lambda_{ads}^3 (N_{ads}+1)} e^{-\beta[U_n(s^N;h)-U_o(s^N;h)]} \end{aligned} \quad (2.98)$$

(3) Deletion

$$\begin{aligned} \frac{acc(o \rightarrow n)}{acc(n \rightarrow o)} &= \frac{\left(\frac{1}{\Lambda_{host}^{3N_{host}} N_{host}!}\right) \left(\frac{V^{N-1} e^{\beta \mu_{ads} (N_{ads}-1)}}{\Lambda_{ads}^{3(N_{ads}-1)} (N_{ads}-1)!}\right) e^{-\beta(U_n(s^{N-1};h)+pV)}}{\left(\frac{1}{\Lambda_{host}^{3N_{host}} N_{host}!}\right) \left(\frac{V^N e^{\beta \mu_{ads} N_{ads}}}{\Lambda_{ads}^{3N_{ads}} N_{ads}!}\right) e^{-\beta(U_o(s^N;h)+pV)}} \\ &= \frac{\Lambda_{ads}^3 N_{ads}}{V e^{\beta \mu_{ads}}} e^{-\beta[U_n(s^{N-1};h)-U_o(s^N;h)]} \end{aligned} \quad (2.99)$$

(4) Volume change

$$\begin{aligned} \frac{acc(o \rightarrow n)}{acc(n \rightarrow o)} &= \frac{\left(\frac{1}{\Lambda_{host}^{3N_{host}} N_{host}!}\right) \left(\frac{V_n^N e^{\beta \mu_{ads} N_{ads}}}{\Lambda_{ads}^{3N_{ads}} N_{ads}!}\right) e^{-\beta(U_n(s^N;h)+pV_n)}}{\left(\frac{1}{\Lambda_{host}^{3N_{host}} N_{host}!}\right) \left(\frac{V_o^N e^{\beta \mu_{ads} N_{ads}}}{\Lambda_{ads}^{3N_{ads}} N_{ads}!}\right) e^{-\beta(U_o(s^N;h)+pV_o)}} \\ &= \left(\frac{V_n}{V_o}\right)^N e^{-\beta p(V_n-V_o)} e^{-\beta[U_n(s^N;h)-U_o(s^N;h)]} \end{aligned} \quad (2.100)$$

In this thesis, I applied the hybrid GCMC/MD simulation to explore the flexibility effect on adsorbents. The isoenthalpic-isobaric (NPH) ensemble is used for the MD simulation part. The number of adsorbates (N), pressure (P) and enthalpy (H) are kept consistent, and the volume and instantaneous values of temperature are allowing to variate, where the cell size changes isotropically. This ensemble allows the host to vibrate and adjust itself to adapt the loading of guest molecules. The resulted configuration then whether be accepted or rejected according to the metropolis rule of acception.²⁰ Hybrid GCMC/MD simulation is conducted by RASPA software package.¹⁴

2.7 Computational Software Used

2.7.1 RASPA package

All the adsorption and diffusion of simulations in both flexible and rigid nanoporous materials were computed by RASPA code.¹⁴ This RASPA code was developed by David Dubbeldam with the collaboration among Northwestern University (USA), the University of Amsterdam (the Netherlands), University Pablo de Olavide (Spain) and University of Delft (the Netherlands). The task-farm approach allows the simulations run in batches with the variation of temperature, pressure, etc. This approach simulates each point of an isotherm independently that compensate for the time expense of the flexible host simulation. Thermodynamic properties and structure flexibility were also extracted from the RASPA simulation results in this thesis.

2.7.2 Zeo++ package

Zeo++ is a software package for the geometric characterization for porous molecular crystals based on Voronoi decomposition.⁴ This software package were used for the pore system

analysis, including D_i , D_f , PSD, surface area and volume, location and size of inaccessible pocket *etc.*

2.7.3 Accelry Materials Studio 7.0

The visualisation of crystal structures and adsorption snapshots were conducted in Materials Studio. The Forcite and Discover models were used for the minimization of structures.⁷⁴

2.8 References

1. KURT W. KOLASINSKI. *Surface Science: Foundations of Catalysis and Nanoscience*. WILEY 2008, (2008).
2. McCusker, L. B., Liebau, F. & Engelhardt, G. Nomenclature of structural and compositional characteristics of ordered microporous and mesoporous materials with inorganic hosts. *Pure Appl. Chem.* **73**, 381–394 (2001).
3. Li, H., Laine, A. & Keeffe, M. O. Supertetrahedral Sulfide Crystals with Giant Cavities and Channels. *Science (80-)*. **283**, 1997–1999 (1999).
4. Willems, T. F., Rycroft, C. H., Kazi, M., Meza, J. C. & Haranczyk, M. Algorithms and tools for high-throughput geometry-based analysis of crystalline porous materials. *Microporous Mesoporous Mater.* **149**, 134–141 (2012).
5. Fick, A. v. On I, iquid Diffusion. *London, Edinburgh, Dublin Philos. J.* **xciv**, 59 (1855).
6. Holden, D. Understanding the Diffusion of Small Gases in Porous Organic Cages using Molecular Dynamics. (2013).
7. Lee, B. & Richards, F. M. The Interpretation of Protein Structures : Estimation of Static Accessibility. *J.Mol.Biol* **26**, 379–400 (1970).
8. Frost, H., Düren, T. & Snurr, R. Q. Effects of surface area, free volume, and heat of

- adsorption on hydrogen uptake in metal-organic frameworks. *J. Phys. Chem. B* **110**, 9565–9570 (2006).
9. Shrake, A. & Rupley, J. A. Environment and exposure to solvent of protein atoms. Lysozyme and insulin. *J. Mol. Biol.* **79**, 361–371 (1973).
 10. Do, D. D., Herrera, L. F. & Do, H. D. Journal of Colloid and Interface Science A new method to determine pore size and its volume distribution of porous solids having known atomistic configuration. *J. Colloid Interface Sci.* **328**, 110–119 (2008).
 11. Taylor, P., Sarkisov, L., Harrison, A., Sarkisov, L. & Harrison, A. Computational structure characterisation tools in application to ordered and disordered porous materials materials. *Mol. Simul.* 37–41 (2011). doi:10.1080/08927022.2011.592832
 12. Gelb, L. D. & Gubbins, K. E. Pore Size Distributions in Porous Glasses: A Computer Simulation Study. *Langmuir* **15**, 305–308 (1999).
 13. Pinheiro, M. *et al.* Characterization and comparison of pore landscapes in crystalline porous materials. *J. Mol. Graph. Model.* **44**, 208–219 (2013).
 14. Dubbeldam, D., Calero, S., Ellis, D. E. & Snurr, R. Q. RASPA: molecular simulation software for adsorption and diffusion in flexible nanoporous materials. *Mol. Simul.* **7022**, 1–21 (2015).
 15. Smit, B. & Maesen, T. L. M. Molecular Simulations of Zeolites: Adsorption, Diffusion, and Shape Selectivity. *Chem. Rev.* **108**, 4125–4184 (2008).
 16. Zemansky MW & Dittman RH. *Heat and Thermodynamics*. (McGraw-Hill, 1997).
 17. Melchionna, S., Ciccotti, G. & Lee, B. Hoover NPT dynamics for systems varying in shape and size. *Mol. Phys.* **78**, 533–544 (1993).
 18. Theodorou, D. N. Progress and outlook in Monte Carlo simulations. *Ind. Eng. Chem. Res.* **49**, 3047–3058 (2010).
 19. Tuckerman, M. E. *Statistical Mechanics : Theory And Molecular Simulation*. (Oxford University Press, 2010).
 20. Metropolis, N., Rosenbluth, A. W., Rosenbluth, M. N., Teller, A. H. & Teller, E. Equation of state calculations by fast computing machines. *J. Chem. Phys.* **21**, 1087–

- 1092 (1953).
21. Hill TR. *An introduction to statistical thermodynamics*. (Dover Publications, 1968).
 22. Fowler RH. *Statistical mechanics. The theory of the properties of matter in equilibrium*. (Cambridge: University Press, 1936).
 23. Wood WW. Monte Carlo calculations for hard disks in the isothermal-isobaric ensemble. *J Chem Phys* **48**, 415–434 (1968).
 24. WW, W. NpT ensemble Monte Carlo calculations for the hard disk fluid. *J Chem Phys* **52**, 729–741 (1970).
 25. Guggenheim EA. Grand partition functions and so-called ‘thermodynamic probability’. *J Chem Phys* **7**, 103–107 (1939).
 26. Attard P. On the density of volume states in the isobaric ensemble. *J Chem Phys* **103**, 9884–9885 (1995).
 27. Koper GJM. Length scale for the constant pressure ensemble: application to small systems and relation to Einstein fluctuation theory. *J Phys Chem* **100**, 422–432 (1996).
 28. Corti DS. Soto-Campus G. Deriving the isothermal-isobaric ensemble: the requirement of a ‘shell’ molecule and applicability to small systems. *J Chem Phys* **108**, 7959–7966 (1998).
 29. Han K-K. On the isothermal-isobaric ensemble partition function. *J Chem Phys* **115**, 7793–7794 (2001).
 30. Panagiotopoulos AZ, Quirke N, Stapelton NM & Tildesley DJ. Phase-equilibria by simulation in the Gibbs ensemble-alternative derivation, generalization and application to the mixture and membrane equilibria. *Mol Phys* **63**, 527–545 (1988).
 31. Panagiotopoulos AZ. Direct determination of the phase coexistence properties of fluids by Monte Carlo simulation in a new ensemble. *Mol Phys* **61**, 813–826 (1987).
 32. Nicholson D & Parsonage NG. *Computer simulation and the statistical mechanics of adsorption*. (Academic Press, 1988).
 33. Smith JM, Van Ness HC & Abbott MM. *Introduction to chemical engineering thermodynamics*. (Mcgraw-Hill, 2005).

34. Voros NG & Tassios DP. Vapour-liquid equilibria in nonpolar/ weakly polar systems with different types of mixing rules. *Fluid Phase Equilib.* **91**, 1–29 (1993).
35. Woods, G. B., Panagiotopoulos, A. Z. & Rowlinson, J. S. Adsorption of fluids in model zeolite cavities. *Mol. Phys.* **63**, 49–63 (1988).
36. Vlugt, T. J. H. Efficiency of parallel CBMC simulations. *Mol. Simul.* **23**, 63–78 (1999).
37. Allen, M. P. & Tildesley, D. J. *Computer Simulation of Liquids*. (Clarendon Press, 1987).
38. Widom, B. Some topics in the theory of fluids. *J. Chem. Phys.* **39**, 2808–2812 (1963).
39. Smit, B. & Siepmann, J. I. Computer simulations of the energetics and siting of n-alkanes in zeolites. *J. Phys. Chem.* **98**, 8442–8452 (1994).
40. Dubbeldam, D., Beerdsen, E., Calero, S. & Smit, B. Dynamically corrected transition state theory calculations of self-diffusion in anisotropic nanoporous materials. *J. Phys. Chem. B* **110**, 3164–3172 (2006).
41. Leach, A. R. *Molecular Modelling Principle and Application*. (2001).
42. Venable, K. J. *et al.* Update of the CHARMM all-atom additive force field for lipids: Validation on Six lipid types. *J. Phys. Chem. B* **114**, 7830–7843 (2010).
43. VANOMMESLAEGHE, K. *et al.* CHARMM General Force Field: A Force Field for Drug-Like Drug-Like Molecules Compatible with the CHARMM All-Atom Additive Biological Force Fields. *Wiley InterSci.* **31**, 671–690 (2009).
44. Wang, J., Wolf, R. M., Caldwell, J. W., Kollman, P. A. & Case, D. A. Development and Testing of a General Amber Force Field. **56531**, (2004).
45. Pérez, A. *et al.* Refinement of the AMBER force field for nucleic acids: Improving the description of α/γ conformers. *Biophys. J.* **92**, 3817–3829 (2007).
46. Mayo, S. L., Olafson, B. D., Iii, W. a G., Eb, E. & El, E. a E. T. DREIDING: A Generic Force Field for Molecular Simulations. *J. Phys. Chem.* **101**, 8897–8909 (1990).
47. Pranata, J., Wierschke, S. G. & Jorgensen, W. L. OPLS Potential Functions for Nucleotide Bases. Relative Association Constants of Hydrogen-Bonded Base Pairs in Chloroform. *J. Am. Chem. Soc.* **113**, 2810–2819 (1991).
48. Damm, W., Frontera, A., Tirado-Rives, J. & Jorgensen, W. L. OPLS all-atom force field

- for carbohydrates. *J. Comput. Chem.* **18**, 1955–1970 (1997).
49. WL, J., DS, M. & J, T. Development and Testing of the Opls All-Atom Force-Field on Conformational Energetics and Properties of Organic Liquids. *J. Am. Chem. Soc.* **118**, 11225–11236 (1996).
 50. Jorgensen, W. L. & Tirado-Rives, J. The OPLS [optimized potentials for liquid simulations] potential functions for proteins, energy minimizations for crystals of cyclic peptides and crambin. *J. Am. Chem. Soc.* **110**, 1657–1666 (1988).
 51. Morse Philip M. Diatomic molecules according to the wave mechanics. II. vibrational levels. *Phys. Rev.* **34**, 57–64 (1929).
 52. London, F. Zur Theorie und Systematik der Molekularkräfte. *Zeitschrift für Phys.* **63**, 245–279 (1930).
 53. Rappé, A. K., Casewit, C. J., Colwell, K. S., Goddard, W. A. & Skiff, W. M. UFF, a Full Periodic Table Force Field for Molecular Mechanics and Molecular Dynamics Simulations. *J. Am. Chem. Soc.* **114**, 10024–10035 (1992).
 54. Martin, M. G. & Siepmann, J. I. Transferable Potentials for Phase Equilibria. 1. United-Atom Description of n -Alkanes. *J. Phys. Chem. B* **102**, 2569–2577 (1998).
 55. Holden, D., Jelfs, K. E., Cooper, A. I., Trewin, A. & Willock, D. J. Bespoke force field for simulating the molecular dynamics of porous organic cages. *J. Phys. Chem. C* **116**, 16639–16651 (2012).
 56. Taylor, P., Adams, D. J., Adams, E. M. & Hills, G. J. Molecular Physics: An International Journal at the Interface Between Chemistry and Physics The computer simulation of polar liquids. 37–41 (2006).
 57. Andrea, T. A. *et al.* The role of long ranged forces in determining the structure and properties of liquid water @ fa @ f) The role of long ranged forces in determining the structure and properties of liquid water 8). **4576**, (1983).
 58. Steinbach, P. J. & Brooks, B. R. New Spherical-Cutoff Methods for Long-Range Forces in Macromolecular Simulation. **15**, 667–683 (1994).
 59. Breneman, C. M. & Wiberg, K. B. Determining Atom-Centered Monopoles from

- Molecular Electrostatic Potentials . The Need for High Sampling Density in Formamide Conformational Analysis. *J. Comput. Chem.* **11**, 361–373 (1990).
60. Ewald, P. P. Die Berechnung optischer und elektrostatischer Gitterpotentiale. *Ann. Phys.* **369**, 253–287 (1921).
61. de Leeuw, S. W., Perram, J. W. & Smith, E. R. Simulation of electrostatic systems in periodic boundary conditions. I. Lattice sums and dielectric constants. *Proc. R. Soc. London. A. Math. Phys. Sci.* **373**, 27–56 (1980).
62. Adams, D. J. On the use of the Ewald summation in computer simulation. *J. Chem. Phys.* **78**, 2585–2590 (1983).
63. Beenakker, J. J. M., Borman, V. D. & Krylov, S. Y. Molecular transport in subnanometer pores: zero-point energy, reduced dimensionality and quantum sieving. *Chem. Phys. Lett.* **232**, 379–382 (1995).
64. Feynman, R. P., Hibbs, A. R. & Styer, D. F. *Quantum mechanics and path integrals*. (Courier Corporation, 2010).
65. Widom, B. Some Topics in the Theory of Fluids. *J. Chem. Phys.* **39**, 2808–2812 (2005).
66. Rosenbluth, M. N. & Rosenbluth, A. W. Monte carlo calculation of the average extension of molecular chains. *J. Chem. Phys.* **23**, 356–359 (1955).
67. Vlugt, T. J. H., Krishna, R. & Smit, B. Molecular simulations of adsorption isotherms for linear and branched alkanes and their mixtures in silicalite. *J. Phys. Chem. B* **103**, 1102–1118 (1999).
68. Siepmann, J. I., Karaborni, S. & Smit, B. Simulating the critical behaviour of complex fluids. *Nature* **365**, 330–332 (1993).
69. Siepmann, J. A method for the direct calculation of chemical potentials for dense chain systems. *Mol. Phys.* **70**, 1145–1158 (1990).
70. Frenkel, D. & Siepmann, J. I. Conflgurational bias Monte Carlo: a new sampling scheme for flexible chains. *Mol. Phys.* **75**, 59–70 (1992).
71. W, S. & EJ, M. Continuous Fractional Component Monte Carlo: An Adaptive Biasing Method for Open System Atomistic Simulations. 1451–63 (2015).

72. Faller, R. & De Pablo, J. J. Constant pressure hybrid molecular dynamics-Monte Carlo simulations. *J. Chem. Phys.* **116**, 55–59 (2002).
73. Coudert, F. X., Jeffroy, M., Fuchs, A. H., Boutin, A. & Mellot-Draznieks, C. Thermodynamics of guest-induced structural transitions in hybrid organic-inorganic frameworks. *J. Am. Chem. Soc.* **130**, 14294–14302 (2008).
74. Accelry. Materials Studio 7.0. (2013).

Chapter 3

**Understanding the effect of host flexibility on
the adsorption of CH₄, CO₂ and SF₆ in porous
organic cages**

3.1 Introduction

Porosity in molecular crystals that are built from porous organic cage (POC) molecules is a function of both the stability of the molecular shape and the stability of the crystal packing. Also, the extent of interconnected porosity between intrinsic pores (inside cage molecules) and extrinsic pores (in-between cage molecules) can be affected by the structural flexibility of the molecular crystal. For example, local, transient molecular flexibility might allow diffusion guest molecules that are seemingly too large into the intrinsic cage cavity¹, while large rearrangements of the cage molecules in the solid-state can give rise to “on/off” porosity switching behaviour.² The effects of such structural flexibility in porous molecular crystals can profoundly affect practical adsorption properties, but they are still a challenge to probe and understand, both experimentally and computationally. Also, this lack of understanding thwarts the ‘intuitive’ structure-function relationships: for example, a cage that is designed to size-exclude a particular molecule in separation may nonetheless adsorb that molecule due to structural flexibility.

Porous organic cage crystals have been the subject of several previous studies on the adsorption behaviour of flexible hosts. Chen et al. showed that the dynamic window apertures of a POC molecule, CC3, allowed the diffusion of gases that would otherwise be too large to pass through the static, single-crystal structure of CC3.³ In a follow-up, computational study, it was demonstrated that the molecular flexibility of CC3 was the key to transient pore-channel formation, which would go on to influence the diffusion of gas molecules.⁴ Holden et al. further showed that taking into account the host flexibility was essential to correctly (albeit qualitatively) explain the porosity of another POC molecule.⁵ All those studies employed a combination of GCMC simulations, using a rigid host, for adsorption predictions and molecular dynamics (MD) simulations to investigate the effects of the host flexibility on the diffusion of guest molecules at pre-defined loadings. This is also common practice when studying adsorption properties of flexible framework-type materials computationally.^{6,7} By contrast,

adsorption simulations with a flexible host structure (termed as “flexible host model”, hereafter) are rare in the literature. Thijs et al. included the flexibility of the zeolite silicalite in GCMC simulations by allowing the host atoms to have translational Monte Carlo moves, thus directly investigating the influence of the framework flexibility on the adsorption of hydrocarbons.⁸ Sholl et al. developed an alternative strategy to account for the flexibility of a MOF in adsorption predictions by running standard GCMC simulations on a series of static snapshots taken from MD simulations of the MOF performed separately.⁹

In this work, we use a hybrid GCMC/MD scheme, which allows for direct sampling of host motions in adsorption simulations, to study the gas adsorption of CH₄, CO₂ and SF₆ in a porous organic cage crystal, CC3-R.¹⁰ The CC3-R cage molecule has an internal void of 80 Å³, which is accessed through the four triangular windows that arrange in a tetrahedral way around the cage centre.⁴ In the solid-state, CC3-R cages pack window-to-window, resulting in a 3-D interconnected diamondoid pore structure that runs through the centre of each cage. CC3-R crystals are simple to desolvation, giving rise to high levels of permanent microporosity with apparent Brunauer–Emmett–Teller (BET) surface areas of up to 800 m²g⁻¹, depending on the level of crystallinity.¹¹ Highly crystalline CC3-R has been shown to adsorb a variety of gases of different size and geometry, including hydrogen, nitrogen, methane, carbon dioxide, xenon, krypton and, most recently, sulfur hexafluoride.^{11–14} All previous adsorption simulations on CC3-R adopted the standard GCMC method in conjunction with the rigid host model. This treatment has been shown to require fine-tuning of the host-guest interactions to reproduce the experimental adsorption isotherms.¹³ Here, we combine the hybrid GCMC/MD scheme with some most widely used generic force fields to describe the host-guest interactions, thereby simulating the adsorption of CH₄, CO₂ and SF₆ in the fully flexible CC3-R. We show that experimental adsorption results can be reproduced correctly without altering the original force field parameters.

3.2 Methodology

The molecular simulation software for adsorption and diffusion in flexible nanoporous materials, RASPA 2.0,¹⁵ was used throughout this study. All hybrid GCMC/MD simulations included a hybrid MC/MD move, in which an MD path was computed in the isoenthalpic–isobaric (NPH) ensemble with the generated configuration accepted or rejected as per the MC sampling rule.¹⁶ Other trial MC moves included insertion, deletion, translation, rotation and reinsertion; these moves were randomly attempted with equal probabilities. All of the GCMC/MD and GCMC simulations involved an 800,000-cycle equilibration period followed by a 200,000-cycle production run; one cycle consisted of n MC moves, with n being equal to the number of adsorbate molecules (or 20, whichever is greater).

An accurate force field for the host structure is essential to account for the host flexibility correctly in GCMC/MD simulations. Recently, Holden et al. developed a bespoke force field, or the cage specific force field (CSFF), for a series of POC molecules including CC3-R.⁵ CSFF is based on the widely used polymer consistent force field (PCFF) with parameters relevant to the cage molecules fine-tuned using density functional theory calculations. CSFF was adopted to describe the flexibility of CC3 in our simulations, where quartic potentials described all bonds and angles with trigonometric potentials used for all torsions (tables S1-S3), and the denotes of atoms are shown in figure S11.

We note that we turned on the 1–4 intramolecular non-bonded interactions (CSFF) within the CC3-R molecule, which was found to be important in improving the structural stability of the cage molecule and that of the crystal packing upon loading of guest molecules. In our simulations, interatomic Lennard–Jones (LJ) interactions were dealt with differently for host–host, host–guest and guest–guest pairs. Equation 3.1 was used to calculate the LJ interactions between CC3 atoms, both intramolecular and intermolecular ones, as defined by the CSFF force field, in conjunction with the corresponding mixing rules for unlike atom pairs given by

Equation 3.2. For host-guest and guest-guest atom pairs, the LJ interactions were calculated using Equation 3.3, with the Lorentz-Berthelot mixing rules, *i.e.*, $\sigma_{ij} = 0.5(\sigma_i + \sigma_j)$, $\epsilon_{ij} = (\epsilon_i \epsilon_j)^{0.5}$.

$$E_{ij} = \epsilon_{ij} \left[2 \left(\frac{\sigma_{ij}}{r} \right)^9 - 3.6 \left(\frac{\sigma_{ij}}{r} \right)^6 \right] \quad (3.1)$$

$$\sigma_{ij} = \left[\frac{\sigma_i^6 + \sigma_j^6}{2} \right]^{1/6}, \quad \epsilon_{ij} = \frac{2\sqrt{\epsilon_i \epsilon_j} \sigma_i^3 \sigma_j^3}{\sigma_i^6 \sigma_j^6} \quad (3.2)$$

$$E_{ij} = 4\epsilon_{ij} \left[\left(\frac{\sigma_{ij}}{r} \right)^{12} - \left(\frac{\sigma_{ij}}{r} \right)^6 \right] \quad (3.3)$$

Where E_{ij} is the LJ potential between atoms i and j , separated by a distance r ; σ_{ij} is the position at which the potential is zero; ϵ_{ij} is the depth of the potential energy well. All LJ interactions were truncated beyond 12 Å. Three generic force fields—namely, DREIDING,¹⁷ OPLS,¹⁸ and UFF¹⁹—were used to assign LJ parameters to the host CC3 atoms when determining the intermolecular host-guest interactions with CH₄, CO₂ and SF₆. Electrostatic interactions were handled by the Ewald summation method with the relative precision set to 10⁻⁶. Point charges of the atoms of CC3-R were taken directly from CSFF. All non-bonded potential parameters as in table S4.

The LJ parameters of CH₄ and CO₂ were taken directly from the Transferable Potential for Phase Equilibria (TraPPE) force field.²⁰ The CH₄ molecule was treated as a united atom with the LJ parameters $\epsilon = 148$ K, $\sigma = 3.73$ Å. The CO₂ molecule was modelled as a rigid, linear three-site molecule with atomic partial charges placed on each atom (O_CO₂: -0.35 e, C_CO₂: 0.7 e); its LJ parameters were assigned as $\epsilon = 79$ K, $\sigma = 3.05$ Å for O_CO₂, and $\epsilon = 27$ K, $\sigma = 2.80$ Å for C_CO₂. The SF₆ molecule was modelled atomistically and as rigid, with the LJ parameters $\epsilon = 163.89$ K, $\sigma = 3.246$ Å for S, and $\epsilon = 27.24$ K, $\sigma = 2.954$ Å for F, taken from the 7-site model by J. Samios et al.²¹

All simulation boxes contained one unit-cell of CC3-R with periodic boundary conditions exerted in three dimensions. Using CSFF, we first optimized the (empty) CC3-R crystal structure by Baker optimization²² that implemented in RASPA 2.0¹⁵, starting with the experimentally reported, desolvated structure.¹⁰ The final CSFF-optimized CC3-R crystal structure had a cubic cell with the cell length of 24.759 Å that in excellent agreement with the experimental cell length of 24.8 Å compared to other generic force fields (OPLS²³⁻²⁵, PCFF²⁶, UFF¹⁹, DREIDING¹⁷) optimized structures, So does CC1 structure optimization (table S5). Superimposing the optimized cage molecule on top of the experimental one revealed a similarity greater than 98%, with the average root-mean-square deviation of atomic positions being 0.2 Å (table S6). We further calculated the pore size distribution (PSD) of the optimized CC3-R crystal structure, using the method from Gelb and Gubbins²⁷ as implemented in RASPA¹⁵. As shown in figure 3.1, there are two dominant pore sizes centred around 3.42 Å and 4.56 Å, which correspond to the window cavity between two neighbouring cage molecules (marked 1 in figure 3.1) and the cage cavity (marked 2 in figure 3.1), respectively. These two key pore diameters of the CSFF-optimized CC3-R are in good agreement with the values reported previously.¹³ Hence, the CSFF implemented here was able to accurately model the molecular structure of CC3-R and its crystalline packing. The CSFF-optimized CC3-R crystal structure was used in all GCMC simulations (with the rigid host model) and as the starting host configuration in all GCMC/MD simulations.

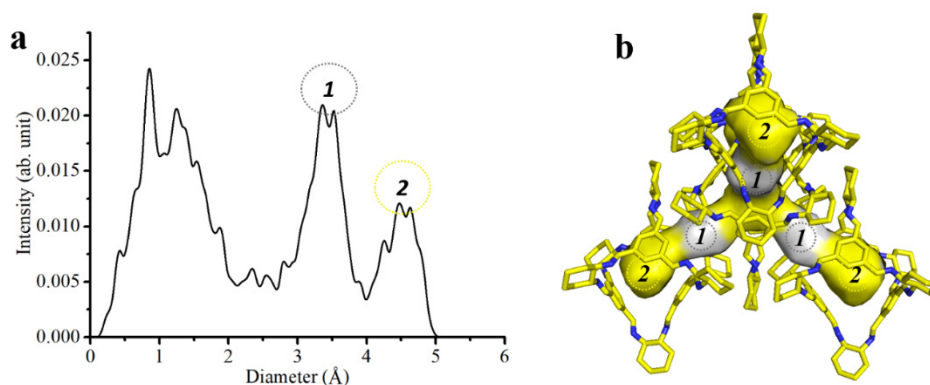


Figure 3.1. Pore size distribution (a) and the 3-D pore structure (b) of the CSFF-optimised crystal structure of CC3-R. The interstitial cavity between two adjacent cage windows is marked **1** and the cage cavity is marked **2**.

3.3 Result and Discussion

3.3.1 Adsorption isotherms of CH₄, CO₂, and SF₆ in CC3-R

Adsorption of CH₄, CO₂ and SF₆ in CC3-R was simulated with both the flexible and rigid host models to probe the effects of the CC3-R flexibility on its adsorption behaviours. Figure 3.2 summarises all simulated adsorption isotherms, which are compared with their experimental counterparts.^{10,12} For CH₄ adsorption (figure 3.2a), DREIDING based simulations performed very well in reproducing the experimental isotherm, in terms of both the adsorption amounts and the shape of the isotherm, while the use of OPLS or UFF led to considerable overestimations. Interestingly, CH₄ isotherms predicted taking into account the flexibility of CC3-R do not differ significantly from those using a rigid host, which is the case for all three generic force fields tested. Similarly, Garcia-Sanchez et al. reported that the host flexibility had little influence on the CH₄ adsorption in LTA zeolites.²⁸ By contrast, CO₂ adsorption (figure 3.2b) is sensitive to the treatment of CC3-R flexibility: the inclusion of host dynamics markedly enhances the uptake of CO₂, starting even from very low gas pressures, independent of the force-field choice for the host-guest interactions. For SF₆ (figure 3.2c), the largest molecule amongst the three gases, it becomes essential to allow the host structure to fluctuate to accommodate the amounts of adsorbates measured experimentally, even for pressures as low as 0.038 bar. Clearly, the rigid CC3-R crystal structure has less than half of the pore space accessible to SF₆ in the flexible or experimental structure. It was also shown previously that the diffusion of SF₆ through CC3-R was facilitated by the dynamic nature of the cage structure.¹² Overall, the hybrid GCMC/MD simulations, using DREIDING based host-guest interactions, were able to reproduce the experimental adsorption isotherms for all the three gases. By contrast, all the other combinations between rigid-/flexible-host and DREIDING/OPLS/UFF were prone to overestimating the uptakes of the smaller CH₄ and CO₂ and severely underestimating those of the large SF₆.

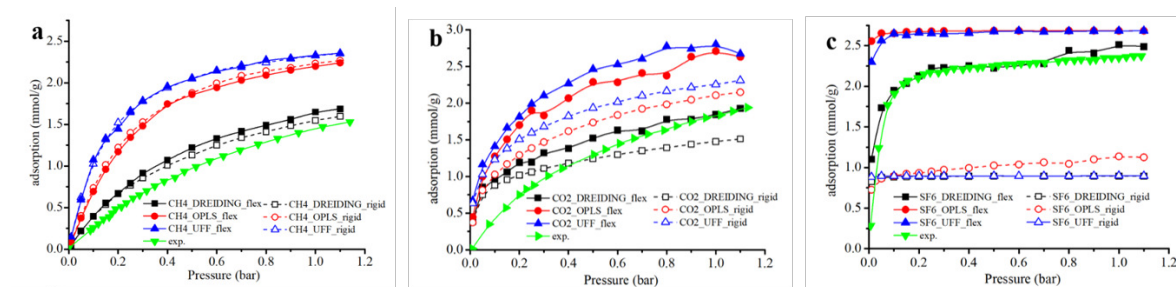


Figure 3.2. Predicted and experimental adsorption isotherms of CH₄ at 275 K (a), CO₂ at 289 K (b) and SF₆ at 273K(c) in CC3-R. The different host-guest force fields are colour-coded: black (squares), DREIDING; red (circles), OPLS; and blue (up-pointing triangles), UFF. Results based on the rigid host model and the flexible host model are indicated by unfilled symbols and filled symbols, respectively. Experimental results are shown as green, down-pointing triangles.

3.3.2 Adsorption positions of CH₄, CO₂ and SF₆ in CC3-R

To elucidate the effects of the structural flexibility of CC3-R on its adsorption of the different gases, we next focused on DREIDING based simulations with the rigid or flexible host model. Figure 3.3 shows an overly of simulation snapshots of CH₄, CO₂ and SF₆ molecules adsorbed in CC3-R at 1 bar. Simulations based on either the rigid or the flexible host model yielded similar adsorption locations of CH₄ and CO₂ in CC3-R. Both the interstitial cavities and the cage cavities (cavities *1* and *2* in figure 3.1) are accessible to CH₄ and CO₂ molecules. The linear CO₂ molecules can additionally be adsorbed at the cage windows, which are too small for the spherical CH₄ molecules. Figure 3.3a – 3.3d also shows that the flexible CC3-R allows more CH₄ and CO₂ molecules to be accommodated in the pore structure, especially in the interstitial cavities and around the cage windows; both sites are the more confined spaces than the cage cavities in the rigid CC3-R. The influence of host flexibility becomes even more pronounced for SF₆ adsorption (figure 3.3e, 3.3f). The interstitial cavities in the rigid CC3-R crystal structure are entirely inaccessible to SF₆, though each cage cavity can adsorb one SF₆ molecule. By contrast, motions of the host atoms free up pore space for SF₆ adsorption in both the interstitial and the cage cavities. This explains the huge differences in the simulated SF₆

uptakes between the rigid and flexible host models shown in figure 3.3c. In passing, we note that the SF₆ molecule located inside a rigid cage cavity is highly confined, whereas it can adopt more orientations when the cage is flexible.

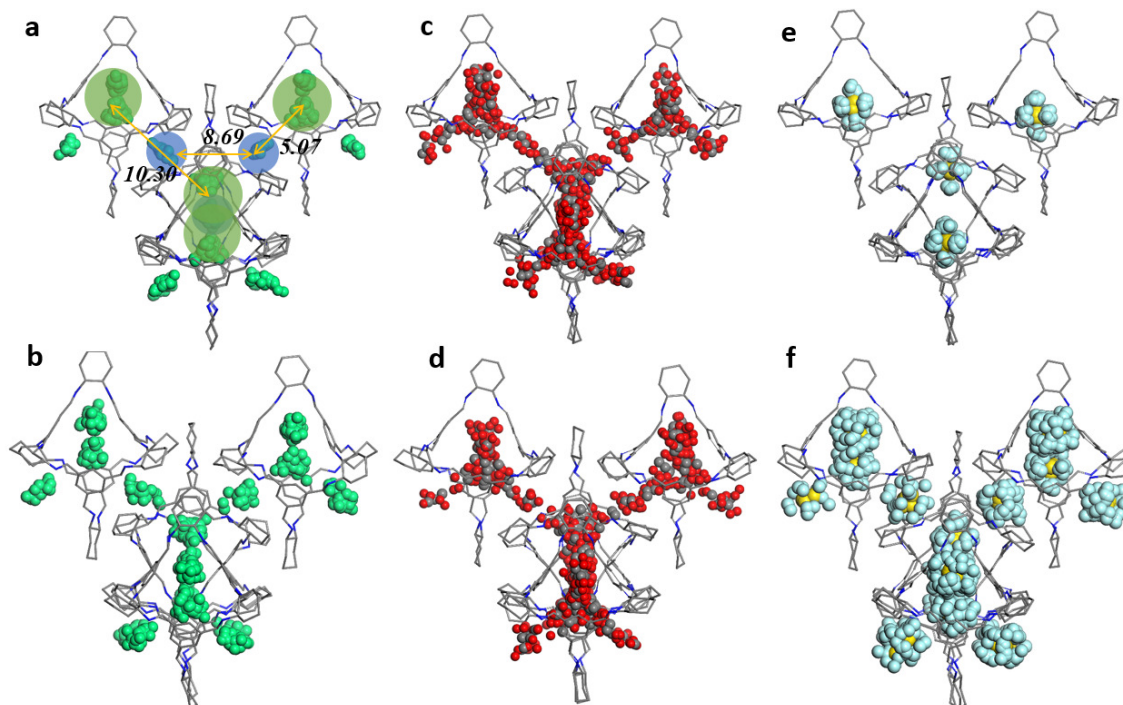


Figure 3.3. Overlay of thirty snapshots from the adsorption simulations of CH₄ (a, b; 275 K), CO₂ (c, d; 289 K), and SF₆ (e, f; 273 K) in CC3-R at 1 bar, based on the rigid host model (top) or the flexible host model (bottom): green, the united-atom representation of CH₄; grey and red, carbon and oxygen of CO₂, respectively; yellow and cyan, sulphur and fluorine of SF₆, respectively; hydrogen atoms of CC3-R are omitted for clarity, while carbon and nitrogen atoms are shown in grey and blue, respectively. The cage (green circles) and interstitial (blue circles) cavities are shown in (a); the centre-to-centre distances of cage–cage (*i.e.*, between two neighbouring cage cavities), cage–interstitial, and interstitial–interstitial cavities are 10.30, 5.07 Å, and 8.69 Å, respectively.

Radial distribution functions (RDFs) were used to characterise time-resolved conformational changes of each adsorbate molecule concerning other adsorbate molecules (figure 3.4). For CH₄ adsorption, the rigid host model and the flexible host model yielded the same characteristic CH₄–CH₄ distances, 5.18 Å and 8.87 Å (black curves in figure 3.4), measured by the two

distinct peaks of the RDFs for the pair. These distances correlate with the characteristic distance (5.07 Å) between the centres of a cage cavity and one of its adjacent interstitial cavities and with that (8.69 Å) between the centres of two neighbouring interstitial cavities (see figure 3.3a). In comparison, the SF₆–SF₆ RDFs show an additional peak at 11.00 or 11.20 Å, with the flexible or rigid host model, respectively. This corresponds to the characteristic distance (10.30 Å) between the centres of two neighbouring cage cavities. The narrower, sharper peaks in the SF₆–SF₆ RDF (flexible host), compared to those of the CH₄–CH₄ counterpart, indicate that the SF₆ molecules are more confined to the specific adsorption sites than the smaller CH₄ molecules. Again, not surprisingly, the SF₆–SF₆ RDF of the rigid host model only shows characteristic distances for SF₆ adsorbed inside different cage cavities, corroborating the simulation snapshots shown in figure 3.3e. The CO₂–CO₂ RDFs show a different picture: the adsorbed CO₂ molecules pack densely in CC3-R, with their close proximity indicated by a single, distinct RDF peak at 4.08 Å.

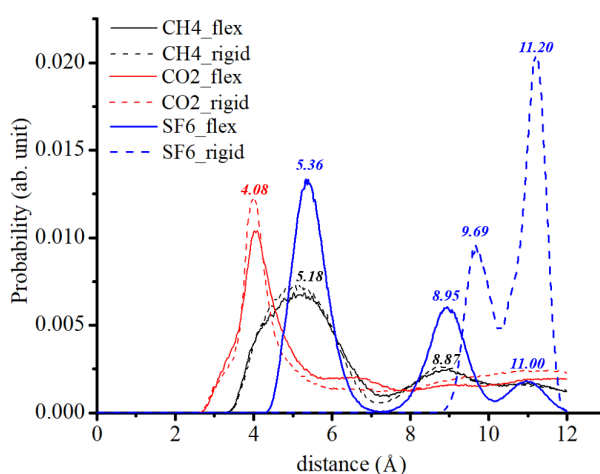


Figure 3.4. Radial distribution functions computed for CH₄–CH₄ (black; 275 K), CO₂–CO₂ (red; 289 K), and SF₆–SF₆ (blue; 273 K) during the adsorption simulations with the flexible host model (solid curves) or the rigid host model (dashed curves), all at 1 bar.

3.3.3 Structural dynamics of CC3-R loaded with CH₄, CO₂ and SF₆

We monitored pore-size changes in the flexible CC3-R loaded with CH₄, CO₂ or SF₆ at 1 bar and at the same temperatures explored above. For each system, we calculated PSD for thirty

snapshots taken from the production run of the hybrid GCMC/MD simulation, after deleting all the guest molecules in the structure. For comparison, we performed MD simulations for the empty CC3-R crystal structure at the respective temperatures and calculated PSD histograms in the same way as for the guest-loaded systems. Figure 3.5 shows overlays of such snapshots for the three gases, together with the PSD of the static crystal structure of CC3-R. The adsorption of CH₄ did not result in marked changes in the sizes of the interstitial or cage cavities (figure 3.5b). Similarly, the CO₂ adsorption did not change the crystal structure of CC3-R drastically, but still the pore-size increases in both types of cavities were noticeable (figure 3.5c). The broader, flatter PSD profiles of CO₂-loaded CC3-R indicate that the CC3-R structure was expanded more uniformly by taking up CO₂ than CH₄. More significantly, the largest guest molecule amongst the three, SF₆, expanded the host structure considerably, with the interstitial and cage cavities enlarged by approx. 0.73 Å and 0.67 Å, respectively. The fact that pore sizes in CC3-R vary depending on the adsorbate's identity suggests a cooperative adsorption mechanism in action: the host flexibility is required to facilitate guest adsorption, which in turn influences the host structure and its dynamics. The phenomenon of cooperativity is very challenging to explore by experiment, so here simulations may offer a unique insight.

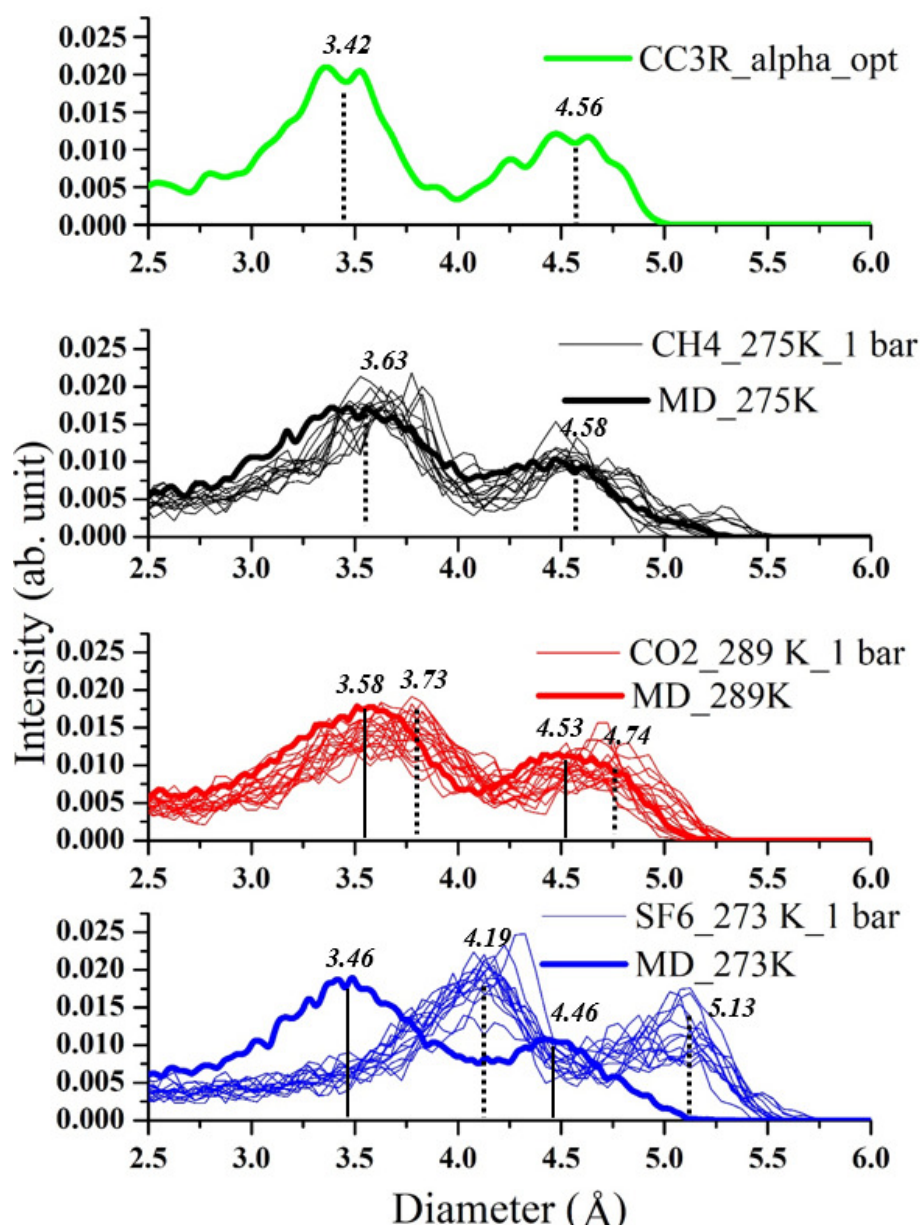


Figure 3.5. Pore size distribution (PSD) of the CSFF-optimized, static CC3-R with zero loading (a) and overlay of PSDs of thirty snapshots taken from the hybrid GCMC/MD simulations of CC3-R loaded CH₄ (b; 275 K), CO₂ (c; 289 K), or SF₆ (d; 273 K), and blank host MD simulations all at 1 bar.

3.5 Conclusion

This study shows that the structural flexibility of the porous molecular crystal CC3-R must be taken into account to adequately describe the adsorption of SF₆ and, by analogy, other large

guest molecules. On the other hand, the adsorption of small gases, such as CH₄ and CO₂, can be predicted reasonably well with the rigid host structure, requiring significantly less computational effort. More generally, we demonstrate that hybrid GCMC/MD simulations are a powerful approach for directly probing gas adsorption in flexible hosts, thus allowing for improved understanding of dynamic and cooperative adsorption events.

3.6 References

1. Holden, D. *et al.* Understanding Static, Dynamic and Cooperative Porosity in Molecular Materials. *Chem. Sci.* **00**, 1–5 (2016).
2. Jones, J. T. a. *et al.* On-Off Porosity Switching in a Molecular Organic Solid. *Angew. Chemie Int. Ed.* **50**, 749–753 (2011).
3. Chen, L. *et al.* Separation of rare gases and chiral molecules by selective binding in porous organic cages. *Nat Mater* **13**, 954–960 (2014).
4. Holden, D. *et al.* Gas Diffusion in a Porous Organic Cage: Analysis of Dynamic Pore Connectivity Using Molecular Dynamics Simulations. *J. Phys. Chem. C* **118**, 12734–12743 (2014).
5. Holden, D., Jelfs, K. E., Cooper, A. I., Trewin, A. & Willock, D. J. Bespoke force field for simulating the molecular dynamics of porous organic cages. *J. Phys. Chem. C* **116**, 16639–16651 (2012).
6. Salles, F. *et al.* Molecular insight into the adsorption and diffusion of water in the versatile hydrophilic/hydrophobic flexible MIL-53(Cr) MOF. *J. Phys. Chem. C* **115**, 10764–10776 (2011).
7. Chokbunpiam, T. *et al.* The importance of lattice flexibility for the migration of ethane in ZIF-8: Molecular dynamics simulations. *Microporous Mesoporous Mater.* **174**, 126–134 (2013).
8. Vlucht, T. J. H. Influence of Framework Flexibility on the Adsorption Properties of Hydrocarbons in the Zeolite Silicalite. 12757–12763 (2002).

9. Gee, J. A. & Sholl, D. S. Effect of Framework Flexibility on C8 Aromatic Adsorption at High Loadings in Metal-Organic Frameworks. *J. Phys. Chem. C* **120**, 370–376 (2016).
10. Tozawa, T. *et al.* Porous organic cages. *Nat. Mater.* **8**, 973–978 (2009).
11. Hasell, T., Chong, S. Y., Jelfs, K. E., Adams, D. J. & Cooper, A. I. Porous organic cage nanocrystals by solution mixing. *J. Am. Chem. Soc.* **134**, 588–598 (2012).
12. Hasell, T. *et al.* Porous organic cages for sulfur hexafluoride separation. *J. Am. Chem. Soc.* (2016). doi:10.1021/jacs.5b11797
13. Chen, L. *et al.* Separation of rare gases and chiral molecules by selective binding in porous organic cages. *Nat. Mater.* **13**, 954–60 (2014).
14. Mitra, T. *et al.* A soft porous organic cage crystal with complex gas sorption behavior. *Chem. - A Eur. J.* **17**, 10235–10240 (2011).
15. Dubbeldam, D., Calero, S., Ellis, D. E. & Snurr, R. Q. RASPA: molecular simulation software for adsorption and diffusion in flexible nanoporous materials. *Mol. Simul.* **7022**, 1–21 (2015).
16. Gilks, W. R., Best, N. G. & Tan, K. K. C. Adaptive Rejection Metropolis Sampling within Gibbs Sampling. *Appl. Stat.* **44**, 455 (1995).
17. Mayo, S. L., Olafson, B. D., Iii, W. a G., Eb, E. & El, E. a E. T. DREIDING: A Generic Force Field for Molecular Simulations. *J. Phys. Chem.* **101**, 8897–8909 (1990).
18. Jorgensen, W. L. *et al.* Development and Testing of the OLPS All-Atom Force Field on Conformational Energetics and Properties of Organic Liquids. *J. Am. Chem. Soc.* **118**, 11225–11236 (1996).
19. Rappé, A. K., Casewit, C. J., Colwell, K. S., Goddard, W. A. & Skiff, W. M. UFF, a Full Periodic Table Force Field for Molecular Mechanics and Molecular Dynamics Simulations. *J. Am. Chem. Soc.* **114**, 10024–10035 (1992).
20. Martin, M. G. & Siepmann, J. I. Transferable Potentials for Phase Equilibria. 1. United-Atom Description of n -Alkanes. *J. Phys. Chem. B* **102**, 2569–2577 (1998).
21. Dellis, D. & Samios, J. Molecular force field investigation for Sulfur Hexafluoride: A computer simulation study. *Fluid Phase Equilib.* **291**, 81–89 (2010).

22. Baker, J. An algorithm for the location of transition states. *J. Comput. Chem.* **7**, 385–395 (1986).
23. Pranata, J., Wierschke, S. G. & Jorgensen, W. L. OPLS Potential Functions for Nucleotide Bases. Relative Association Constants of Hydrogen-Bonded Base Pairs in Chloroform. *J. Am. Chem. Soc.* **113**, 2810–2819 (1991).
24. Jorgensen, W. L. & Tirado-Rives, J. The OPLS [optimized potentials for liquid simulations] potential functions for proteins, energy minimizations for crystals of cyclic peptides and crambin. *J. Am. Chem. Soc.* **110**, 1657–1666 (1988).
25. WL, J., DS, M. & J, T. Development and Testing of the Opls All-Atom Force-Field on Conformational Energetics and Properties of Organic Liquids. *J. Am. Chem. Soc.* **118**, 11225–11236 (1996).
26. Sun, H. Ab Initio Calculations and Force Field Development for Computer Simulation of Polysilanes. *Macromolecules* **28**, 701–712 (1995).
27. Gelb, L. D. & Gubbins, K. E. Pore Size Distributions in Porous Glasses: A Computer Simulation Study. *Langmuir* **15**, 305–308 (1999).
28. García-Sánchez, A., Dubbeldam, D. & Calero, S. Modeling adsorption and self-diffusion of methane in LTA zeolites: The influence of framework flexibility. *J. Phys. Chem. C* **114**, 15068–15074 (2010).

Chapter 4

A molecular-level understanding of linear and branched alkanes adsorption and separation in porous organic cages

4.1 Introduction

POCs are composed of discrete organic cages assembled by nonbonded interactions (Van der Waals and electrostatic interactions), unlike the extended network materials connected with covalent or coordinated bonds. These new type of materials have attracted attention from practitioners due to their rare properties including decent solubility in common organic solvents and solution processability.¹⁻⁸ These properties benefit the use of stationary phase in narrow-bore columns in GC, while it can be technically challenging to add insoluble MOFs or COFs. Currently, the use of POCs for alkanes' separation is still scarce. Cooper et al. pioneered the initial experimental investigation of POCs for alkanes' separation. The alkanes' adsorption and separation properties have been investigated with the most famous POCs CC3. CC3 is an imine-linked cage material that synthesis by one-step [4+6] condensation reaction of 1,3,5-triformylbenzene with 1,2-diaminocyclohexane. 1,2-diaminocyclohexane can be homochiral (R, R or S, S) to form CC3R or CC3S, or racemate (R, S) to form CC3RS.⁹ Cooper et al. showed that the homochiral CC3R shows selectivity capabilities towards several racemate mixtures including rac-2-butanol, rac-2-pentanol, rac-2-heptanol, rac-2-octanol, rac-2-nonanol, and rac-2-decanol. The racemate CC3RS was reported to be capable of separating linear C6 separation from its branched isomers.¹⁰ Later on, Yuan and coworkers investigated the use of CC3R in GC to separate a series of isomers, which demonstrated that CC3R exhibited better selectivity than commercial β -DEX 120 and Chirasil-L-Val columns.¹¹ Apart from alkane adsorption and separation applications, CC3 was also reported with shape sorting capability of aromatic molecules,¹² membranes,^{13,14} separation of rare gases and chiral alcohols,¹⁵ and most recently, the separation of SF₆ from N₂.¹⁶

Computational simulations at a molecular level provide accurate insight to understand as well as experimental works guiding. For alkanes' adsorption and separation in POCs, molecular simulations can provide the molecular-level understanding of alkanes' adsorption in POCs, which is crucial for the design and utilisation of novel POCs for separation applications. Grand

canonical Monte Carlo (GCMC) methods are generally used to study and understand gas adsorption behaviour in porous materials. In this method, the adsorption happens at constant temperature T , volume V and chemical potential μ is varied to equilibrium by a fluctuation of number N of molecules in the adsorbate phase.¹⁷

During a GCMC simulation, the crystal structures information of POCs were either taken from the Cambridge Crystallographic Data Center (CCDC) database, literature or crystal structure prediction (CSP) methods. Adsorbent framework atoms are usually kept fixed during conventional GCMC simulations, which is defined as “rigid host approach”. There are only intermolecular interactions of paired non-bonded host-guest atoms are required to be addressed. Rigid host approach is computationally inexpensive; this approach has been used for large-scale screening of gas/liquid adsorption and separation for both experimental existing and hypothetical porous materials.^{18,19,20} For POCs, it is possible to reproduce reasonable adsorption isotherm of small gas molecules with rigid host approach. The noble gases adsorption in CC3-R has been well fitted with experimental results by 69% DREIDING force field.¹⁵ In many cases, intermolecular interaction force fields need to be re-parameterised for different porous molecular materials to represent the weak intermolecular forces well. Moreover, rigid host approach cannot address host structure change due to guest loading and pores without porosity, which was recently found in POCs. Hence, a new technique which allows structural change of framework responds to guest loading is required for the computational study of adsorption simulations. Several existing methods were reported to address the structural change of host POCs one approach is to conduct GCMC adsorption simulations with rigid host crystal structures at different structural change stages. for instance, MIL-53, a “breathing” MOF which structure shows profoundly changed during guest loading. The crystal structures at different stages of the guest loading were used to obtain the adsorption isotherm curves.²¹ This method requires the structure change information before the simulation, which is not very practical to explore and understand the local structure change, such as structural response to the guest in POCs, which is hard to be captured and recorded using X-Ray diffraction. Another way is to

perform the hybrid grand canonical Monte Carlo/molecular dynamic Monte Carlo (GCMC/MD) simulation. Herein it is defined as the flexible host approach. For POCs, the adsorption study based on GCMC/MD has never been attempted before. The hybrid MDMC method allows framework atoms to be flexible by employing molecular dynamic (MD) move. It is a promising technique to address the local structural change of POCs during guest molecules adsorption simulation. This chapter focus on the adsorption application studies of POCs, investigating the performance of general force fields transferability with the implement of GCMC/MD algorithm. The effect of flexibility on guest molecules adsorption simulation in POCs will be investigated by comparing the difference between rigid and flexible host approach.

Rigid host approach has been used in simulation studies of extended networks which Structures are unlikely to be alerted. For instance, the influence of framework flexibility on hydrocarbons adsorption in zeolite has been reported, framework flexibility effect on the heat of adsorption (HOA) is negligible at low loading.²² However, the flexibility of zeolite shows significant influences on the adsorption capability towards big molecules.²² The flexibility of frameworks largely influences the C8 aromatic molecules adsorption capabilities of MOF.²³ The degrees of flexibility of porous organic cages are greater than extended networks. Cooper's group has reported simulation studies based on POCs flexibility.¹⁵ To investigate the potential of bigger molecules' diffusions and adsorptions in CC3, the pore limiting size histogram was generated by monitoring the MD process of CC3, while pore restricts sizes are enveloped between 3 Å to 4.5 Å. This MD simulations investigate the flexibility caused by a molecular crystal itself. Porosity changes caused by the influence of guest molecules are still missing. More recently, research aimed at understanding static, dynamic and cooperative porosity was published.²⁴

4.2 Methodology

MD and GCMC algorithms are combined in a hybrid scheme to address the host structure flexibility during adsorption simulations of alkanes. This algorithm is termed as GCMC/MD simulation in this work. Hybrid GCMC/MD method is implemented in RASPA 2.0.²⁵ GCMC simulation is the most used approach to study thermodynamic adsorption equilibrium in microporous materials. In the Monte Carlo algorithm, trial configurations are generated randomly and accepted according to the Metropolis sampling criteria. During hybrid Monte Carlo moves, there are possibilities that short MD simulations will be conducted based in-between Monte Carlo moves then produce new trial configurations.²⁶ The configurations will either be accepted or rejected according to the Metropolis sampling criteria.²⁷ Comparing with the fast-computed MC steps, MD part is time-consuming. In this work, chemical potential (μ), temperature (T) and pressure (P), as well as all the atoms of adsorbent, were held fixed in GCMC simulations. MD simulations with an isoenthalpic-isobaric NPH ensemble was inserted into the GCMC adsorption simulations to relax host CC3-R structure loaded with gas molecules. In each cycle of the hybrid GCMC/MD simulations, translational, rotational and addition/deletion Monte Carlo (MC) moves were tried for gas molecules with equal probability. MD simulation was attempted with a possibility of 2.44% in the cycle. This process is repeated until the adsorption capacity was converged. A total of 1,000,000 simulation cycles were used for these simulations, in which 500,000 cycles were used for equilibration run, 500,000 cycles were used for the production run.

To conducting simulations with flexible host, proper use of force fields for the host structure is vital. The algorithm-based parameterised force field for flexible COFs by Schmid,²⁸ ab initio calculation parameterised consistent valence force field (CVFF) force field for IRMOF1,²⁹ and AMBER force field has been used to study porous molecular crystal-like calixarenes.³⁰ Daniel et al. report the universal force field (UFF) and the COMPASS force field cannot accurately reproduce structures of porous organic cages.³¹ Recently, Daniel et al. developed a density

functional theory (DFT) fitted bespoke force field for porous organic cages, which is also named as cage specific force field (CSFF), which allowed us to reproduce the CC3-R structure matches well with the experimental crystal structure.³¹

Chapter three shows that the DREIDING assigned host-guest and guest-guest non-bonding force field gives the best agreement with experimental results. Here, those three generic force fields (DREIDING, OPLS, UFF) have also been tested for their performance on alkanes adsorption simulations. In total 1,000,000 cycles (500,000 equilibrium cycles and 500,000 production cycles) of GCMC simulation were run. Those alkanes adsorption isotherms (figure S12) that computed by generic force fields show the same order to the small gases adsorption in figure 3.3. Adsorption quantities that suggest by generic force fields of an alkane at a certain pressure are ranked as DREIDING < OPLS < UFF. Linear or branched alkanes is not more than the methane group stacking with each other. As the DREIDING force field gives the best agreement to the methane adsorption isotherm (figure 3.3a), So the DREIDING force field were chosen as non-bonding force field for the host-guest and guest-guest potential representation.

Hence, the flexible host force field used for this GCMC/MD simulations is same as chapter three and the force field details are listed in table S1 to S3. Alkanes are generally inert to chemical reagents, especially in this case, the adsorption happened in a molecular crystal formed with organic elements (C, N, H). First, the carbon to carbon and carbon to hydrogen bonds are durable, and rarely break unless heated to high temperatures. Second, the alkane molecules are non-polar and composed by a small number of groups. Hence, it is logical to lump the CH₃, CH₂ and CH into single interaction centres, which is so-called the united atom (UA) approach. The non-bonded parameters of these alkane molecules were taken directly from TraPPE force field developed by Martin and Siepmann,³² The UA approach allows longer simulation cycles and shorter computational time due to the CH_x groups are charge neutral and charge-charge interaction can be neglected. Herein, The CH_x groups are treated as individual, chargeless interaction centres with their effective potentials. The composed alkane molecules

are considered as flexible chains and branched chains. A harmonic model is used to describe the bond stretching of alkane molecules (equation 4.1), so does the bonding potential model (equation 4.2). The torsional angle distortions were defined by a three-cosine potential model (equation 4.3).

$$U_{guest}^{bond} = \frac{1}{2} k_b (r - r_0)^2 \quad (4.1)$$

$$U_{guest}^{bend} = \frac{1}{2} k_\theta (\theta - \theta_0)^2 \quad (4.2)$$

$$U_{guest}^{torsion} = c_0 + c_1[1 + \cos(\phi)] + c_2[1 - \cos(2\phi)] + c_3[1 + \cos(3\phi)] \quad (4.3)$$

The k_b is the bond stretching constant, r_0 is the reference bond length, k_θ is the bend energy constant, θ_0 is the reference bend angle, ϕ is the torsional angle, c_n/k_B is in K denote the four torsion parameters, and these potential parameters are shown in Table 4.1.

Table 4.1. Stretch, bend, torsion and LJ parameters for alkanes from TraPPE force field.³²

Stretch	$r_0(\text{\AA})$	k_b (K)	LJ	\mathcal{E} (K)	σ (Å)
CH_x-CH_x	1.54	96500	CH_4	158.5	3.72
Bend	θ_0	k_θ (K)	CH_3	108	3.76
$CH_x-(CH_2)-CH_y$	114	62500	CH_2	56	3.96
$CH_x-(CH)-CH_y$	112	62500	CH	17	4.67
$CH_x-(C)-CH_y$	109.47	62500	C	0.8	6.38
Torsion	c_0 (K)	c_1 (K)	c_2 (K)	c_3 (K)	
$CH_x-(CH_2)-(CH_2)-CH_y$	0	335.03	-68.19	791.32	
$CH_x-(CH_2)-(CH)-CH_y$	-251.06	428.73	-111.85	441.27	
$CH_x-(CH_2)-(C)-CH_y$	0	0	0	461.29	
$CH_x-(CH)-(CH)-CH_y$	-251.06	428.73	-111.85	441.27	
$CH_x-(CH)-(C)-CH_y$	0	0	0	1635.7	

To test the reliance of the combination of force fields and simulation length, the average volumes and standard deviations were taken from a production run of nC4 to nC8 adsorption simulations at 433 K, 1 bar are listed in table S7 to check whether the simulation length is sufficient for the equilibrium of flexible host simulation. Simulation are start from the experimental crystal structure with a cell volume of 15253 Å³. According to table S7, the average sizes of each simulation models are expanded by 1000 Å³ to 16300 Å³. The standard deviations of each simulation are around 140

\AA^3 among the production section, and the volume variation ratios are less than 1 % for all the listed simulations. Therefore, the simulation results from flexible host simulations with 500,000 + 500,000 cycles are trustworthy.

The simulation box contains one unit cell ($1 \times 1 \times 1$ unit cell, $\alpha = \beta = \gamma = 90^\circ$), with 1344 atoms. For the rigid model simulation, each atom of the crystal structure is fixed at their reference positions during simulation, while host atoms can vibrate to relax their energy with flexible host assumptions. For the insertion of long alkane chains, the acceptance rate of adsorbate insertion is quite low, especially in this case, the CC3-R cage cavity and window cavities are in a similar dimension to alkane chains. Configurational-Bias Monte Carlo (CBMC) is now the widely used technique for the insertion of a big molecule.³³⁻³⁶ In the CBMC technique, a molecule grows segment by segment. For each successfully inserted segment, a set of trial orientations are computed according to the former segment's internal energy, which improves the sampling efficiency of long alkane chains.

To compare to the adsorption behaviour of each adsorbate computed with both rigid and flexible host assumptions, radial distribution function (RDF) histograms were calculated for each adsorption simulations which implemented in RASPA 2.0.²⁵ The RDF is a statistical mechanics to describe how adsorbates density varies as a function of distance from a reference particle. For the chain-like alkanes, the reference atoms are the CH_3 hydrocarbon atom. The RDF histograms show to adsorption density as the function of CH_3 to CH_3 hydrocarbon distance, and for the branched alkane chains, the reference atoms are the branched centre, CH for the mono-branched alkane chain chains and C for the di-branched and tri-branched alkane chains.

To present the adsorption behaviour of each alkane via both flexible and rigid approaches, the coordinations of adsorbates from 50 snapshots were be extracted and overlapped in the same cage structure after equilibrium. For the flexible host assumption, the CC3-R cage will vibrate to relax the steric effect. Hence, the positions of each atom are different from each extracted

snapshot. For the clarity of adsorption snapshots, only the final host structure will be presented in diagrams of adsorption snapshots.

For the competitive adsorption of linear and branched alkanes mixture, C4 to C6 alkanes have been included. All these simulations were conducted under the flexible host assumption with equimolar of each linear and branched isomer at 433 K, 0 to 1.1 bars. Besides the insertion/deletion, translational and rotational trials of guest molecules in GCMC moves and vibration of host molecules, the identity change trials³⁷ have been introduced. In total 1,000,000 cycles (500,000 equilibrium cycles + 500,000 production cycles) have been performed for these simulations.

4.3 Results and discussion

4.3.1 Flexibility effects on linear hydrocarbon adsorption

Figure 4.1 shows the adsorption isotherms of pure linear alkanes butane (nC4), pentane (nC5), hexane (nC6), heptane (nC7), and octane (nC8) in CC3-R calculated by both flexible and rigid host approaches at 433 K from 0.001 bar to 1.1 bar. Overall, cage flexibility shows a negligible effect on adsorption capability. The nC4 adsorption isotherms computed by both approaches are rather similar among the pressure range. With one hydrocarbon atom increment, considerable nC5 amount rising with cage flexibility. For nC6, nC7 and nC8, cage flexibility allowed more adsorbates captured at low-pressure range and saturations were reached at the lower pressure. Superficially, the saturation of nC8 was reached almost instantly. The adsorption acceleration may cause by the better geometric fitting with the flexible host.

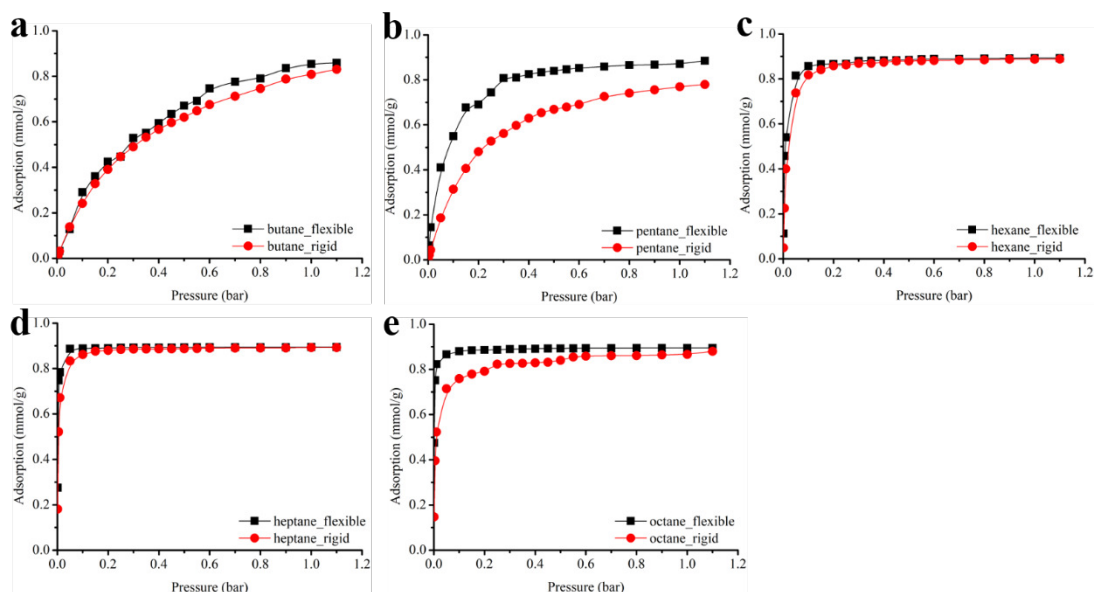


Figure 4.1 Adsorption isotherm of pure linear alkanes nC4 (a), nC5 (b), nC6 (c), nC7 (d), and nC8 (e) in CC3-R cage at 433 K with rigid (red line, sphere) and flexible (black line, square) host assumption.

The HOD energy against guest uptakes by both models is presented in figure 4.2, while host-guest and guest-guest HOD energy are plotted against adsorption quantities. Generally, the host-guest HOD energy computed by the flexible model is stronger with the same amount of loading, which proves the former assumption that linear alkanes are stronger interacted with flexible cages than the rigid, due to that cages allow to adjust themselves to fit the loading of guests. The decreasing interaction energies indicate there are more than one types of adsorption sites.³⁸ Both flexible and rigid cages computed nC4 HOD shows similar decreasing trends, which suggests adsorption sites are filled gradually by both models. Therefore, these adsorption isotherms are rather identical (figure 4.1, solid). This hypothesis also supported by the guest-guest HOD interactions (figure 4.1, open), the incline gradients are jumped for both assumptions while the loading quantities surpass 0.6 mmol/g, due to the closer adsorption sites filling. The rigid cage model suggests a flat nC5 host-guest HOD (figure 4.2b) as only one type of adsorption site, while the flexible cage model presents a decreasing trend over 0.8 mmol/g, which is nC5 saturation rigid cage adsorption quantities limitation. Host-guest HOD energy decreasing or guest-guest HOD energy increasing against the adsorption quantity increasing are

the trace of filling multiple adsorption sites. For nC6 to nC8, no clear sign of host-guest HOD energy reduction was observed. However, stronger host-guest interactions explain rapid adsorption saturation.

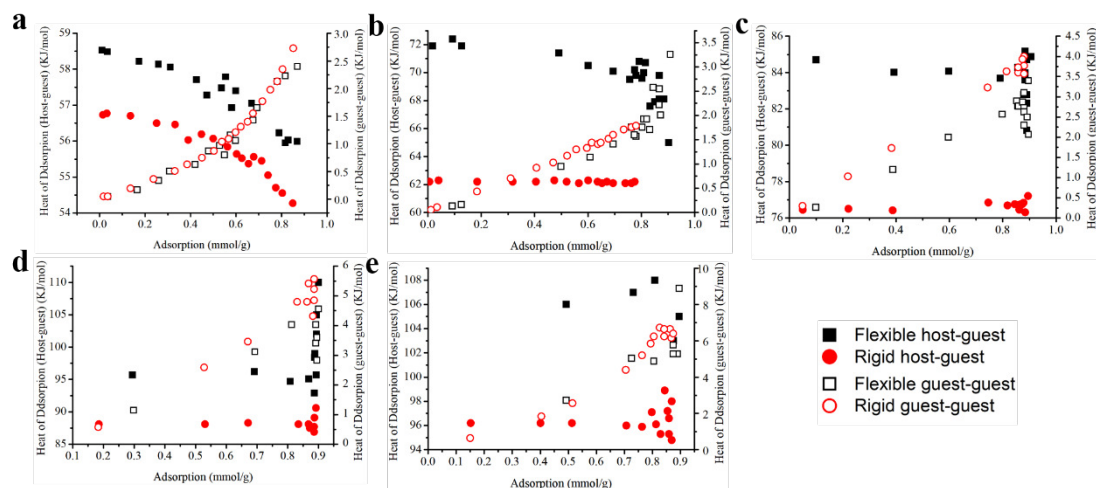


Figure 4.2. Comparison of linear alkanes HOD between the rigid (red sphere) and flexible (black squire) assumptions against guest loading quantities. The host-guest (solid) and guest-guest (open) interactions are presented separately, including nC4 (a), nC5 (b), nC6 (c), nC7 (d), and nC8 (e).

Pure linear alkanes (nC2 to nC8) adsorption simulation with flexible host assumption is summarised in figure 4.3a. Adsorption of long-chain alkanes (nC6, nC7 and nC8) in CC3-R at 433K can quickly reach saturation under 0.01 bar. The slopes of adsorption isotherms of linear alkanes are generally proportional to the chain length because the long alkane chains own more interaction sites with CC3-R cage than these short alkanes, as it is supported by the calculated Henry coefficients and HOD values in figure 4.3c and 4.3d. The host-guest HOD values against adsorption quantities are compared in figure 4.3b. The longer the alkanes, the higher the values of host-guest HOD at the certain loading quantities, which indicate the stronger host-guest interaction. The numerical values of the limiting adsorption properties were listed in this set of figures, including the host-guest HOD values (E_{HG} , figure 4.3c) at low coverage and Henry coefficients (K_h , figure 4.3d) against the number of hydrocarbon atoms (n) of linear alkanes. For these linear alkanes with different chain length n , the longer the length, the higher the

magnitudes of the limiting properties. This phenomenon is expected as the longer alkanes contain more interaction sites with the flexible host. The linear regression was treated on both host-guest HOD and Henry coefficients to quantify these limiting properties, which are presented in the insets of each figure (figure 4.3c, 4.3d). According to these equations, the host-guest HOD and Henry coefficients for the longer linear alkanes can be estimated.

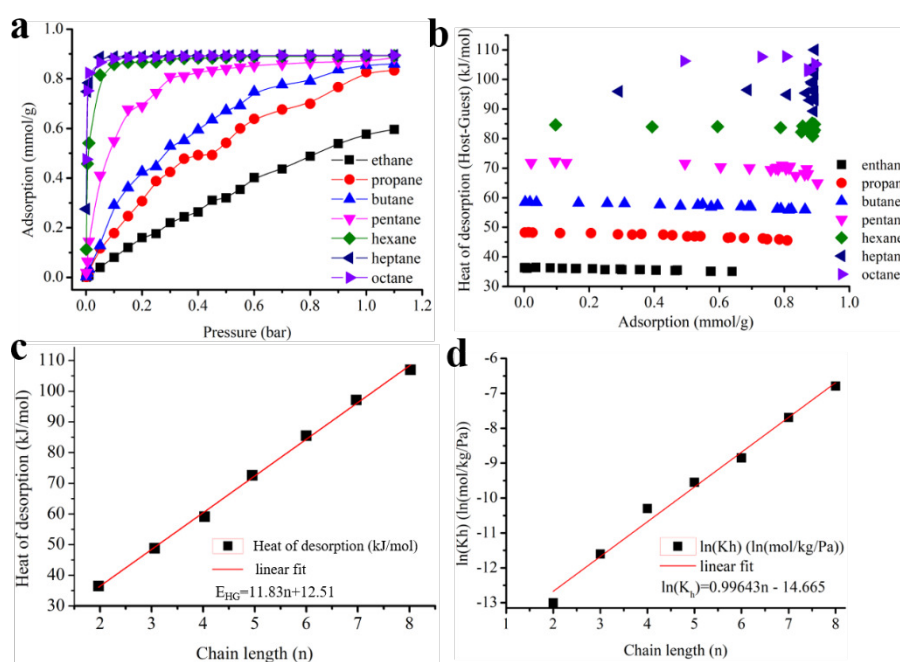


Figure 4.3. The comparison of adsorption behaviours of linear alkanes from C2 to nC8 within the flexible host. (a) The flexible host linear alkanes adsorption isotherms including C2 (black line, square), C3 (red line, sphere), nC4 (blue line, up triangle), nC5 (magenta line, down triangle), nC6 (green line, diamond), nC7 (navy line, left triangle), and nC8 (violet line, right triangle) at 433 K, 0.001 to 1.1 bar. (b) Host-guest part HOD of linear alkanes including C2 (black, square), C3 (red, sphere), nC4 (blue, up triangle), nC5 (magenta, down triangle), nC6 (green, diamond), nC7 (navy, left triangle), and nC8 (violet right triangle) against the adsorption quantities. These HOD values were computed at 433k. Limiting adsorption properties of alkanes (c) HOD (E_{HG}) and (d) Henry constant (K_H) at the low coverage of linear alkanes as the function n, the carbon number of chains.

4.3.2 Flexibility effects on branched hydrocarbon adsorption

4.3.2.1 branched C4 adsorption

The adsorption isotherms of isobutane (iso-C4) comparison between rigid and flexible host approaches are presented in figure 4.4a. Both approaches suggested similar adsorption capacities and saturated at 0.8 bar. However, flexible host approach gives the slightly slower adsorption quantities increasing rate, due to the weaker host-guest interaction (figure 4.4b). The host-guest interactions decreasing and guest-guest interactions increasing as the adsorption quantities surpass 0.6 mmol/g. multi-types of adsorption sites were filled in the flexible model. To insight investigate the adsorption patterns, adsorption snapshots extracted from both flexible (Figure 4.4c) and rigid (Figure 4.4d) models. Two adsorption sites (cage cavity and window cavity) are capable of loading iso-C4 in the flexible CC3-R, which explains the HOD energy reduction in figure 4.4b. For the rigid model, only the cage cavity is capable of capturing iso-C4, which lead the unchanged host-guest HOD interaction.

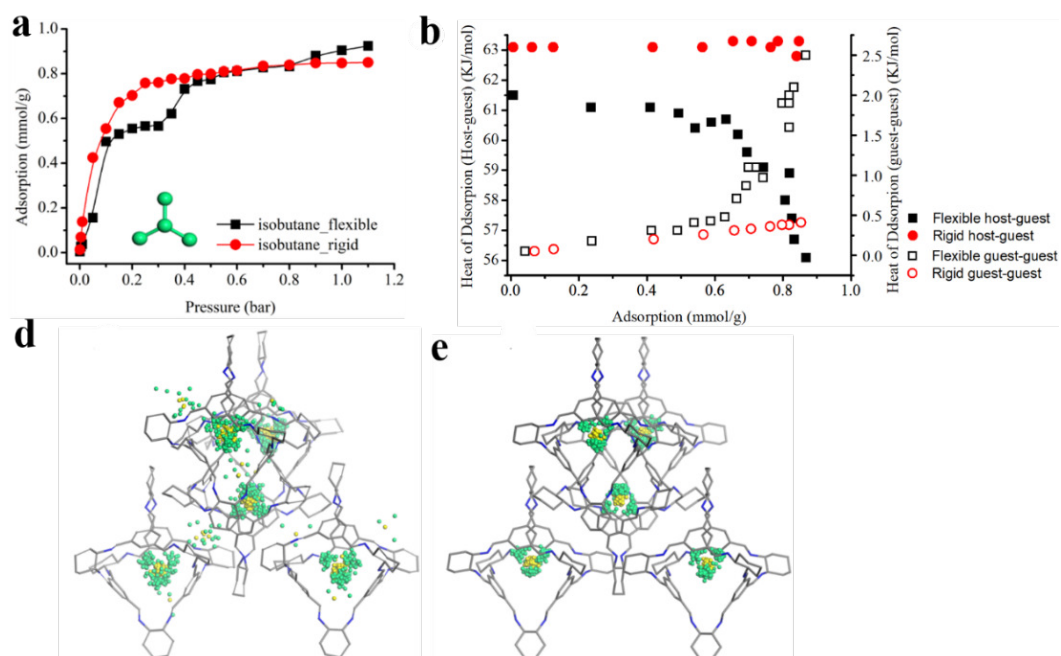


Figure 4.4. (a) The adsorption of branched C4 alkane, isobutane. The adsorption quantities were computed by both rigid host (red line, squire) and flexible host (black line, sphere) assumptions at 433 K, from 0.001 to 1.1 bar. The figure of adsorbate is shown above, and the united

hydrocarbon atom is coloured by green. (b) The HOD of branched C4 alkanes, iso-butane. Both host-guest (solid) and guest-guest (open) interaction parts are presented above. The HOD values are varied with the adsorption quantities. Both HOD values are computed with the rigid host (red sphere), and flexible host (black squire) assumptions. The adsorption snapshots extract from the flexible host (d) and rigid host (e) simulations. For each adsorption snapshots, both are overlapped by 50 simulation models. For the clarity of both figures, the hydrogen atoms are omitted. For the guest molecule, the CH₃ hydrocarbon molecules are coloured with green, and the CH hydrocarbon molecules are presented as yellow dots.

4.3.2.2 Branched C5 adsorption

The adsorption isotherms of branched C5, 2-methylbutane (2mb-C5) and dimethylpropane (dmp-C5) are shown in figure 4.5a. The flexible model suggests a better loading capability of 2mb-C5 compare to the rigid host approaches (figure 4.5a, black). The adsorption trends of both models are similar but slightly faster increasing rate shown with the flexible model at the low-pressure range. For the adsorption isotherm of dmp-C5 (figure 4.5a, red), the adsorption isotherms from both assumptions are quite similar, and the adsorption quantity reaches the same value at 1 bar. For the 2mb-C5 host-guest HOD (figure 4.5b, solid), flexible host approach shows stronger interactions than the rigid model, and the decreasing trend indicates the filling of multi-type adsorption sites. For the guest-guest HOD of 2mb-C5 (figure 4.5b, open), the values are similar within the rigid model adsorption capacity, and guest-guest interactions increased rapidly when the adsorption quantities surpass the rigid host limitation, which supports the idea of uptaking in multi-type adsorption sites. For the di-branched dmp-C5, the host-guest HOD values are similar between both assumptions (figure 4.5c, solid), and no substantial magnitudes fluctuation among the adsorption quantities range. Therefore, only one type of adsorption site is suitable for the loading of dmp-C5. The guest-guest HOD diagrams (figure 4.5c, open) computed by both approaches suggest the distance between each adsorbate are similar, which support there is only one type of adsorption site is suitable for the loading of

dmp-C5.

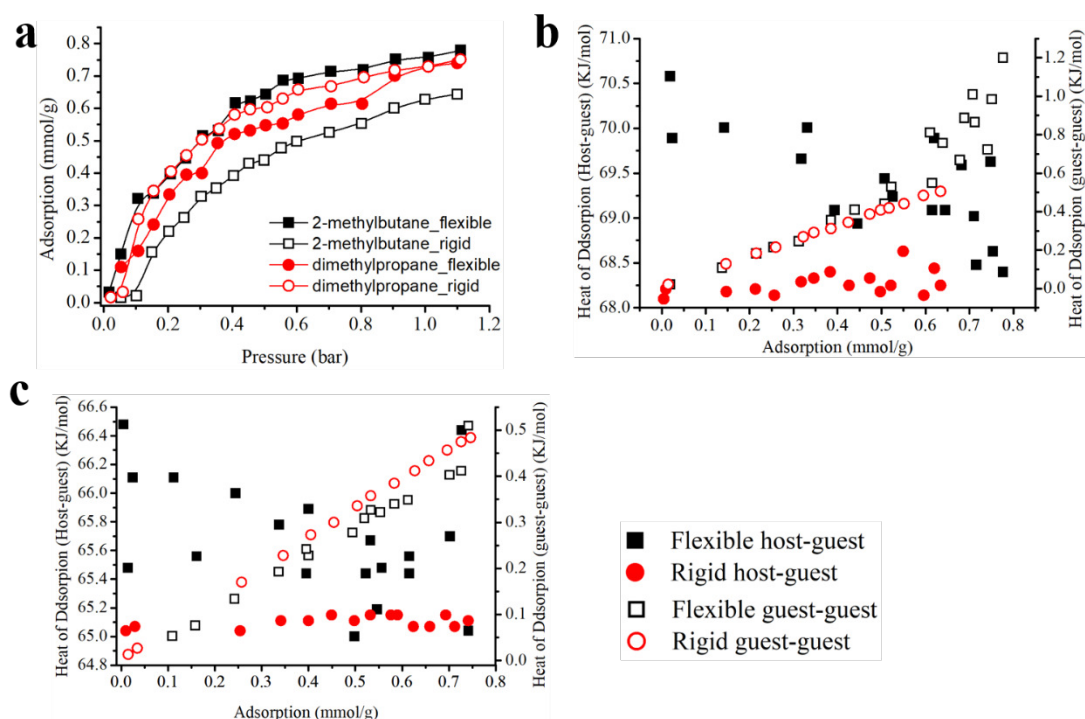


Figure 4.5. (a) The adsorption of branched C5 alkanes of 2mb-C5 and dmp-C5. The adsorption quantities were computed by both rigid host (open) and flexible host (solid) assumptions at 433 K, from 0.001 to 1.1 bar. The figures of both adsorbates are shown above, and united hydrocarbon atoms are coloured by green. The comparison between HOD values computed from the flexible host (black squire) with rigid host (red sphere) assumptions. These HOD values are varied as the function of adsorption quantities. Both C5 isomers, 2mb-C5 (b) and dmp-C5 (c), are presented above. For these HOD diagrams of C5 isomers, the host-guest (solid) and guest-guest (open) parts are demonstrated separately.

The branched C5 overlapped adsorption snapshots generated by both approaches are shown in figure 4.6. Two types of adsorption sites are capable of loading 2mb-C5 with the flexible model adsorption (figure 4.6a). The probability of the 2mb-C5 adsorbed in the window cavities is quite low, which supports the unclear corresponding host-guest HOD diagrams (figure 4.5b, solid) and explain the adsorption capability improvement. The adsorption of dmp-C5 happens in the cage cavity of both models (figure 4.6c, 4.6d). Hence, Flexible and rigid host assumptions output similar host-guest and guest-guest HOD values (figure 4.5c). Overall, only cage cavities

are capable of adsorbing dmp-C5, even with flexibility.

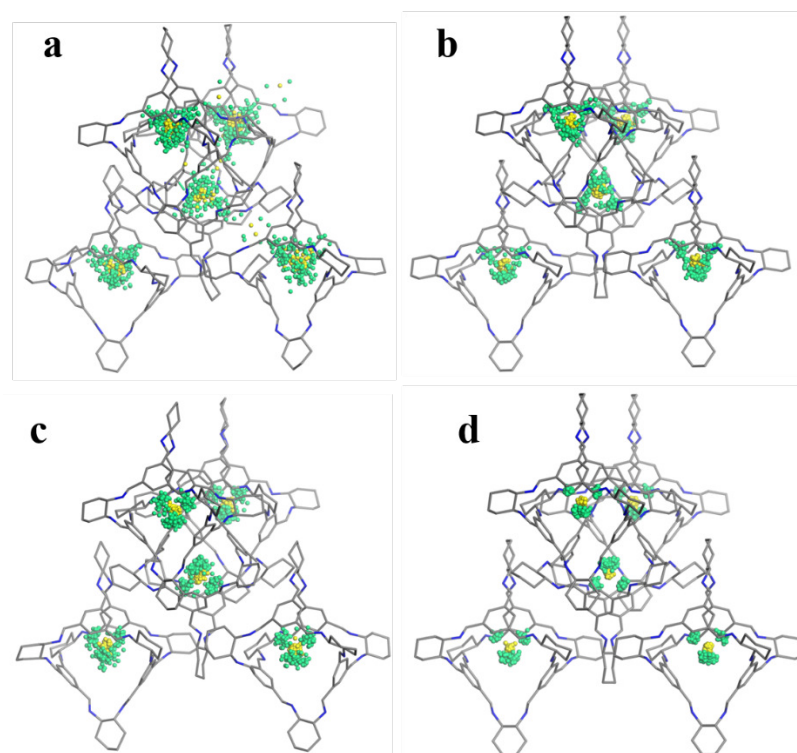


Figure 4.6. The adsorption snapshots from the flexible host (a, c) and rigid host (b, d) assumptions. Fifty simulation snapshots were overlapped. For the clarity of these figures, the hydrogen atoms are omitted. The CH₃ hydrocarbons are coloured with green, CH hydrocarbons (2mb-C5) molecules, and C atoms (dmp-C5) are presented as yellow dots.

4.3.2.3 Branched C₆ adsorption

Figure 4.7a shows the adsorption isotherms of branched C₆ alkanes with both flexible and rigid host assumptions. Adsorption capacities of the flexible host are significantly higher than rigid host. The adsorption of 2-methylpentane (2mp-C₆) in CC3-R is rapidly saturated at 0.2 bar with the flexible model (figure 4.7a, solid black symbol), while with the rigid model (figure 4.7a, black open symbol) yields the slowly increasing trend against pressure. For the mono-branched 3-methylpentane (3mp-C₆), the flexible host can adsorb enormously higher quantities of guests (figure 4.7a, red). Flexible host approach suggests a solid 0.8 mmol/g of 3mp-C₆, while less than 0.15 mmol/g of guests were loaded in rigid host within studied pressure range. For the

adsorption of di-branched isomers, negligible guests were captured in the rigid host (figure 4.7a, blue and magenta open symbol), and more than 30 times 22dmb-C6 molecules are loaded in flexible host model (figure 4.7a, solid blue symbol), so does the 23dmb-C6 adsorption (figure 4.7a, solid magenta symbol). The cage flexibility shows a significant influence on the adsorption of branched C6 isomers. Without consideration of flexibility, this simulation accuracy could be largely compromised.

Figure 4.7b to 4.7e present the C6 branched alkanes host-guest and guest-guest HOD energies with both rigid and flexible cages. For the host-guest HOD of 2mp-C6 (figure 4.7b, solid symbol), the interactions suggested by flexible host approach are stronger, which explains the faster adsorption increment at low pressure. The host-guest HOD values of both assumptions are flat within the rigid host adsorption quantity, and a declining tendency arises as the adsorption quantities exceed this limitation. This decline tendency suggests the other adsorption sites start to be loaded with 2mp-C6. The corresponding guest-guest HOD (figure 4.7b, open symbol) increased by a steeper trend as the adsorption quantities exceed 0.8 mmol/g, as closer adsorption sites are loaded with the guest molecules. For the host-guest HOD of 3mp-C6 (figure 4.7c, solid symbol), the flexible host presents stronger interactions compared to the rigid host. It means 3mp-C6 is energetically more feasible in a flexible cage model, which leads to faster adsorption increasing (figure 4.7a, solid red symbol). Both models show no clear decline trend of HOD values, and corresponding guest-guest HOD diagrams (figure 4.7c, open symbol) show rather linear increase trends against adsorption quantities with both approaches, the major adsorption of 3mp-C6 happens in one type of adsorption site. For the di-branched isomers (22dmb-C6 and 23dmb-C6), both host-guest (figure 4.7d, 4.7e solid symbol) HOD interactions computed by both approaches are unchanged against the increase of adsorption, which means only one type of cavity is capable of loading these isomers, which is also supported by the guest-guest HOD energies. (figure 4.7d, 4.7e open symbol)

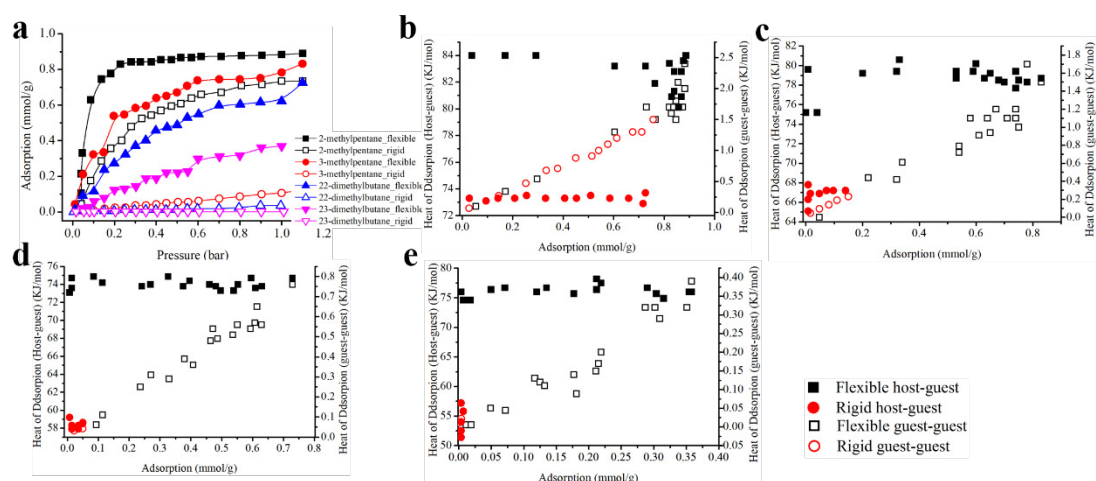


Figure 4.7. (a) The adsorption of branched C6 alkanes, 2mp-C6 (black), 3mp-C6 (red), 22dmb-C6 (blue) and 23dmb-C6 (magenta). The adsorption quantities were computed by both rigid (open) and flexible host (solid) assumptions at 433 K, from 0.001 to 1.1 bar. The figures for all adsorbates are shown above, and green colours hydrocarbon atoms. The comparison between HOD calculated by the flexible host (black square) and rigid host (red sphere) approaches. These HOD values are varied as the function of adsorption quantities. All C6 isomers, 2mp-C6 (b), 3mp-C6 (c), 22dmb-C6 (d) and 23dmb-C6 (e) are presented above. For these HOD diagrams, the host-guest (solid) and guest-guest (open) are demonstrated separately.

The RDF histograms of C6 branched isomers are presented in figure 4.8, and the corresponding overlapped snapshots are exhibited in figure 4.9. For 2mp-C6, RDF histograms of distances between CH hydrocarbons are presented (figure 4.8a). Both approaches show sharp peaks around 11 Å, which is the distances between CH hydrocarbons in adjacent cage cavities (figure 4.9a, 9a'). Hence, 2mp-C6 molecules are majorly loaded in cage cavities by both simulation models. Flexible host RDF histograms show lower peaks around 6.49 Å (figure 4.8a, black), which indicate the distance between widow cavities and its cage cavities (figure 4.9a), a small portion of 2mp-C6 loads in window cavities of flexible model. RDF histograms of 3mp-C6 are presented in figure 4.8b, window cavities of flexible cage show capability to load 3mp-C6 (figure 4.9b). For these di-branched isomers, the negligible amount of 22dmb-C6 and 23dmb-C6 molecules which loaded in the rigid model (figure 4.7a, blue and magenta open symbol), so

the numeric data is not enough to generate RDF histograms. Consequently, only flexible host RDF histograms are presented (figure 4.8c, 4.8d). For both RDF histograms, sharp peaks are located around 11 Å, which suggest dominant adsorption occurred in the cage cavities. It can be directly observed in the corresponding adsorption snapshots (figure 4.9c, 4.9d). A peak around 6.64 Å is shown in the 22dmb-C6 RDF histograms (figure 4.8c), which suggest there is a small chance that the 22dmb-C6 can be loaded into flexible interstitial cavities. However, this adsorption configuration was not captured by these random snapshots. The flexible host cage cavities can load these di-branched alkanes by expanding their sizes. For the guest molecule 22dmb-C6, only one hydrocarbon is prolonged comparing with dmp-C5. However, the adsorption quantities differences between rigid and host approaches are largely increased. The rigid host model massively lost its adsorption capability with one hydrocarbon growth, while the flexible host shows better geometry tolerances, and maintains its adsorption capability.

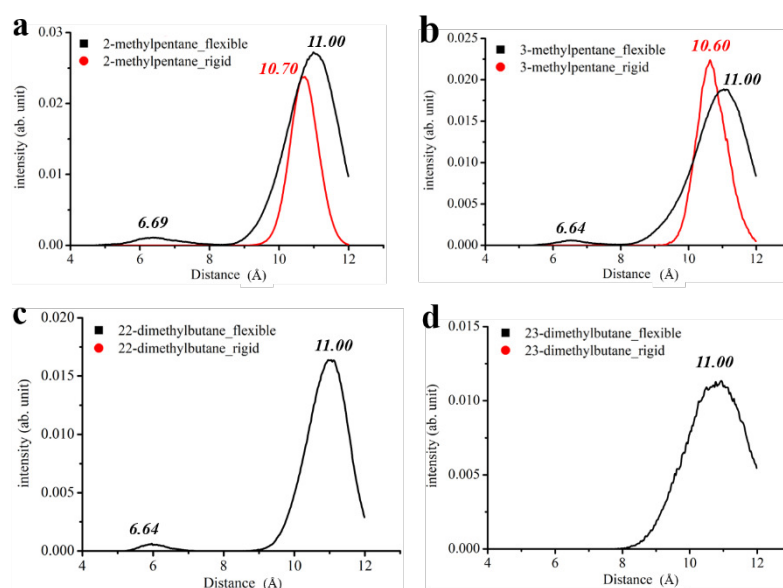


Figure 4.8. The RDF histograms of adsorbates CH hydrocarbon to CH hydrocarbon atoms (a, b) or C to C atoms (c, d) from both flexible host (black) and rigid host (red) assumptions at 1 bar are shown above. The histograms under pressures within 1.1 bar are presented in all figures. C6 branched isomer are presented including 2mp-C6 (a), 3mp-C6 (b), 22dmb-C6 (c) and 23dmb-C6 (d).

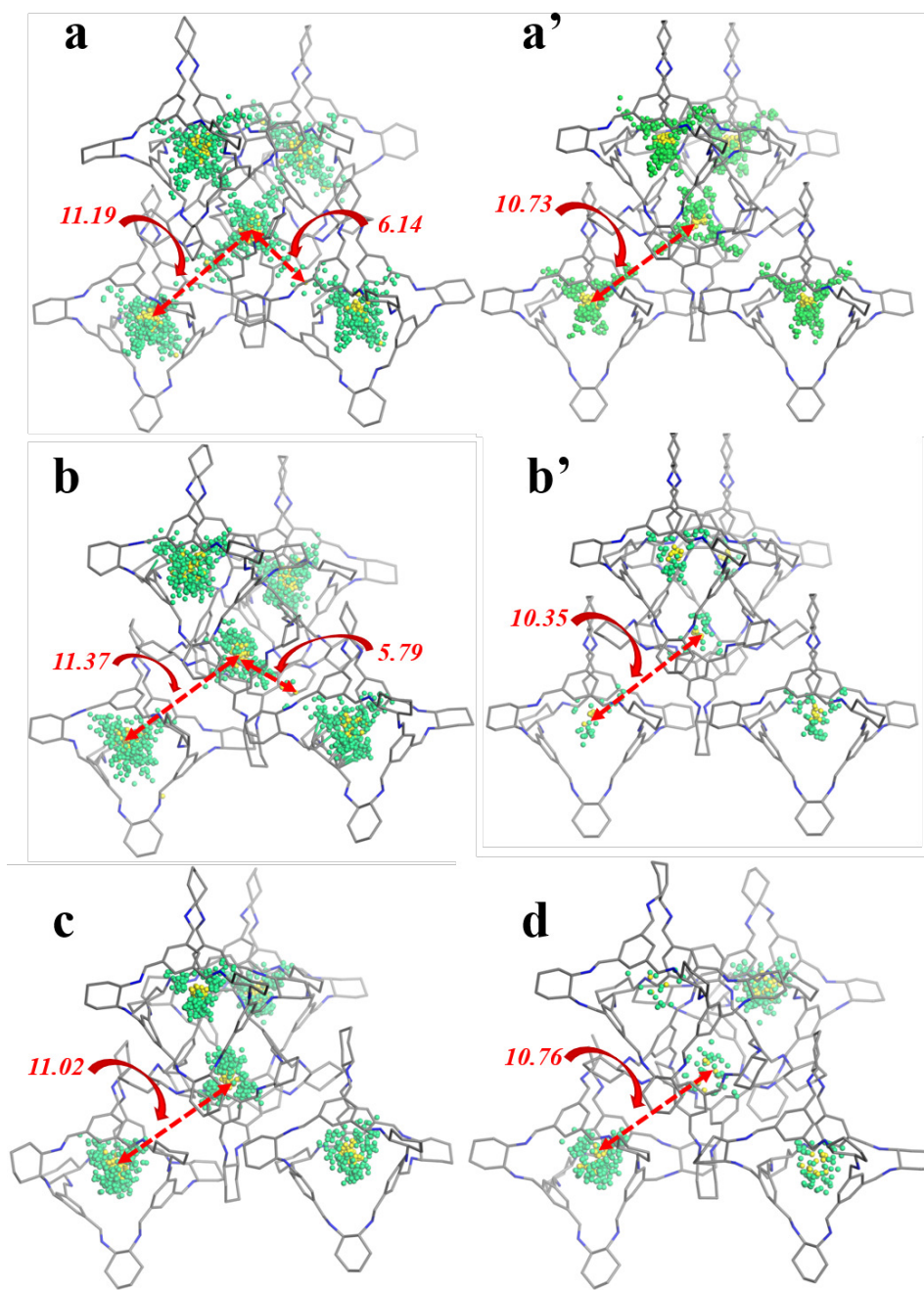


Figure 4.9. The overlapped adsorption snapshots from both flexible host (a, b, c, d) and rigid host (a', b') approximations except 23dmb-C6, due to there is no adsorption from rigid host approximation. For each adsorption snapshots, all of them are overlapped by 50 simulation models include 2mp-C6 (a, a'), 3mp-C6 (b, b'), 22dmb-C6 (c) and 23dmb-C6 (d). For the clarity of both figures, the hydrogen atoms are omitted. For the guest molecule, the CH₃ hydrocarbon molecules are coloured with green, the CH hydrocarbon molecules and C are presented as yellow dots.

4.3.2.4 Branched C7 adsorptions

The adsorption isotherms of branched C7 alkanes computed by both rigid and flexible host approaches are presented in figure 4.10a. For the 2-methylhexane (2mh-C7), flexible host approach suggested a similar capacity but faster adsorption than rigid approach, while the saturation reached at 0.015 bar. For both 3-methylhexane (3mh-C7) and 2,2-dimethylpentane (2,2dmp-C6), the rigid model suggests slow linear increasing trends, while the flexible models yield much faster saturation and higher adsorption capacity. For the other two di-branched C7 isomers, 2,3-dimethylpentane (2,3dmp-C7) and 3,3-dimethylpentane (3,3dmp-C7), negligible adsorption are predicted by the rigid model. However, decent amounts of 2,2dmp-C7 and 2,3dmp-C7 can be adsorbed in the flexible cage model. For the other branched C7 isomers, 2,4-dimethylpentane (2,4dmp-C7) and 2,2,3-trimethylbutane (2,2,3tmb-C7) are not capable of being loaded in CC3-R with both approaches among the pressure range. Hence, they are not shown in this section.

Figure 4.10b – 4.10f presents the host-guest and guest-guest HOD values against the adsorption quantities calculated by both approaches. For the host-guest HOD of 2mh-C6 (figure 4.10b, solid symbol), the flexible host shows stronger interactions with guest molecules, which leads to the faster adsorption quantities increment. For the guest-guest HOD of 2mh-C6 (figure 4.10b, open symbol), both approaches output similar values and increasing trends, we speculate the adsorption locations should be similar. According to figure 4.10c, the host-guest HOD values of 3mh-C7 yielded with rigid host simulation are 20 kJ/mol less than flexible host approaches. The rigid host host-guest HOD energies are unchanged with the adsorbate number increment, which means only one type of adsorption site is feasible to capture 3mh-C7 in rigid cage model. For the flexible model host-guest HOD values, a declining trend against adsorption quantities are presented, which means there is a certain possibility for 3mh-C6 to be loaded in a less favourable adsorption site. For the guest-guest HOD of 3mh-C6, the majority of HOD values of both assumptions laid on the same line, which means principal adsorptions occur at the same type of adsorption site. The HOD diagrams of di-branched C7 isomer 2,2dmb-C7 (figure 4.10d)

are alike with the HOD of 3mh-C6. No apparent change in host-guest HOD values via both approaches. Hence, the majority number of adsorbates should be captured by the same type of adsorption site. The guest-guest HOD values also support this speculation. For the other two di-branched C7 isomers, both HOD figures of 23dmp-C7 (figure 4.10e) and 33dmp-C7 (figure 4.10f) are alike. The host-guest HOD values are unchanged with the increment adsorption quantities, which means only one type of adsorption site can be loaded with these two di-branched isomers, and the guest-guest HOD figures also approve this speculation.

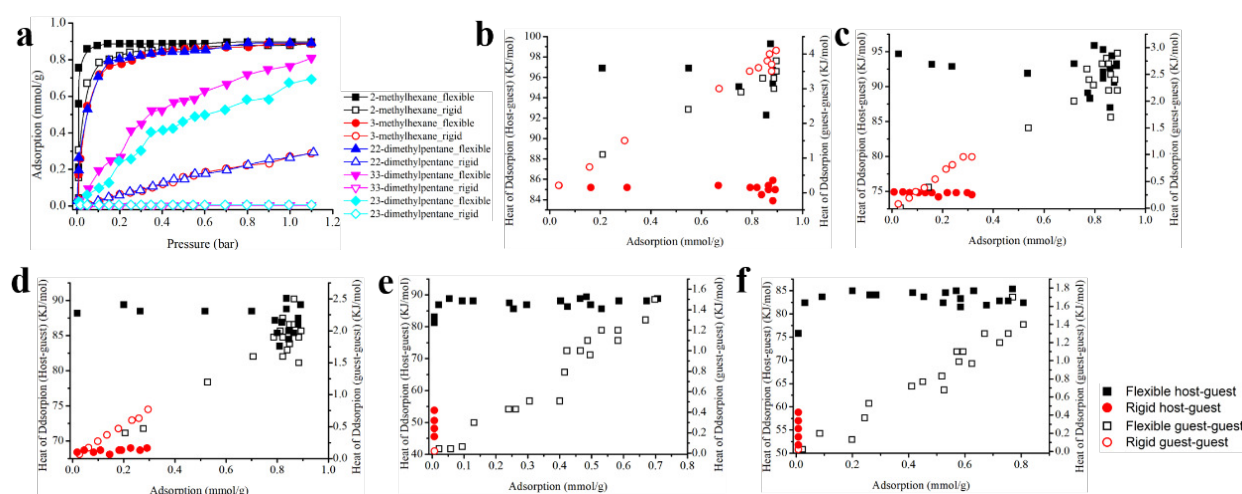


Figure 4.10. (a) The adsorption of branched C7 alkanes, 2mh-C7 (black), 3mh-C7 (red), 22dmp-C7 (blue), 23dmp-C7 (d) and 33dmp-C7 (magenta). The adsorption quantities were computed by both rigid (open) and flexible host (solid) approaches at 433 K, from 0.001 to 1.1 bar. All adsorbates are shown above, and green colours united hydrocarbon atoms. The comparison between HOD from the flexible host (black squire) with rigid host (red sphere) assumptions. These HOD values are varied as the function of adsorption quantities, and the host-guest HOD parts (solid) and guest-guest HOD parts (open) are presented separately. The HOD histograms of C7 branched isomers except for 24dmp-C7 (Due to there are no adsorption quantities from both assumption) are included. 2mh-C7 (b), 3mh-C7 (c), 22dmp-C7 (d), 23dmp-C7 (e) and 33dmp-C7 (f).

The RDF histograms of the CH to CH hydrocarbon (2mh-C7, 3mh-C7) and C to C atoms (22dmp-C7, 23dmp-C7 and 33dmp-C7) distances of branched C7 isomers computed from both approaches are presented in figure 4.11, and the corresponding overlapped adsorption snapshots are presented in figure 4.12. For the 2mh-C7 (figure 4.12a), 3mh-C7 (figure 4.12b), 22dmp-C7 (figure 4.12c), primary RDF peaks are placed around 11 Å in both approaches, which refer to adsorption snapshots adsorbates between adjacent cage cavities are about 11 Å (figure 4.12 a, a', b, b', c, c'). Hence, these RDF histograms and adsorption snapshots confirm the adsorption majorly occurred in cage cavities via both approaches. There are minor peaks around 6.35 Å, which refer to distances between the adsorbates in cage cavities and the adjacent window cavities are around 6.38 Å. There is a certain possibility that these isomers can be adsorbed in the flexible window cavities. For the other two di-branched C7 isomers, the flexible model RDF histograms of 23dmp-C7 (figure 4.11d) and 33dmp-C7 (figure 4.11e) indicate that only cage cavities can be loaded with 23dmp-C7 and 33dmp-C7 as all peaks are around 11 Å.

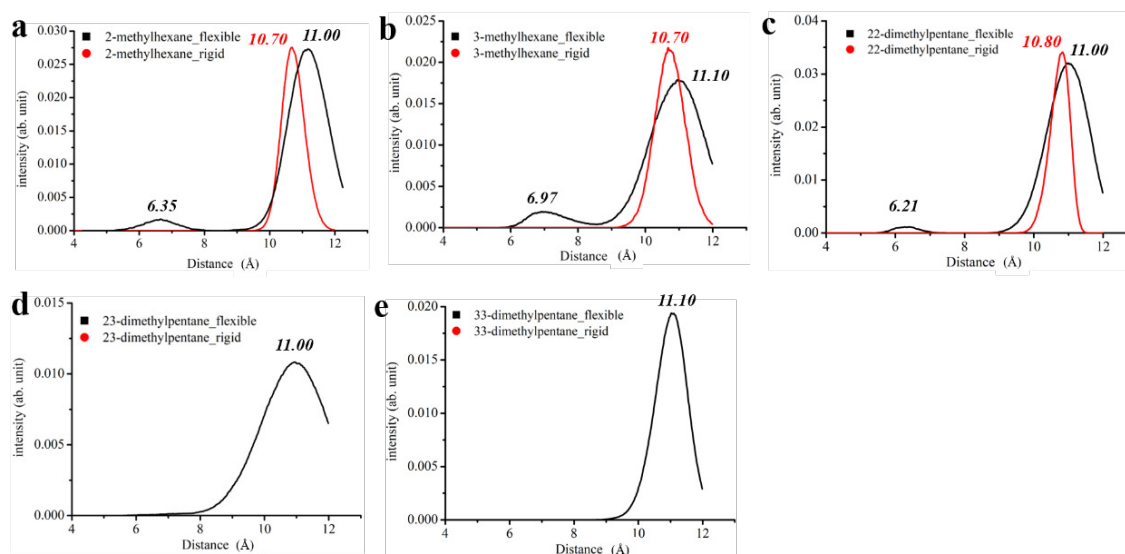


Figure 4.11. The RDF histograms of adsorbates mono-branched CH hydrocarbon to CH hydrocarbon atoms (a, b) and di-branched C to C atoms (c, d, e) from both flexible host (black) and rigid host (red) assumptions are shown above. The histograms under pressures within 1.1 bar are presented in all figures. All the C7 branched isomer are included. 2mh-C7 (a), 3mh-C7 (b), 22dmp-C7 (c), 23dmp-C7 (d) and 33dmp-C7 (e).

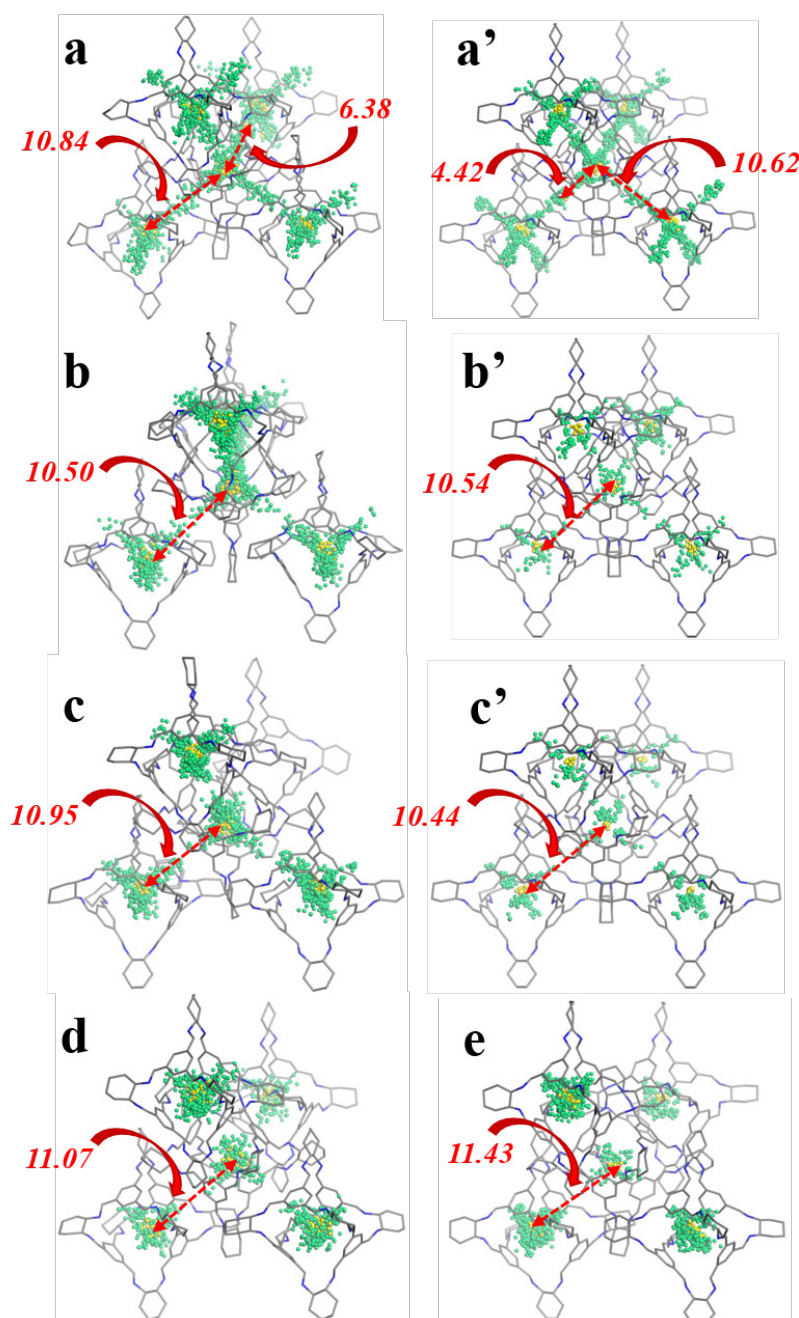


Figure 4.12. The overlapped adsorption snapshots from both flexible host (a, b, c, d, e) and rigid host (a', b', c') approximations except 23dmp-C7 and 33dmp-C7, due to there is no adsorption from rigid host approximation. For each adsorption snapshots, all of them are overlapped by 50 simulation models include 2mh-C7 (a, a'), 3mh-C7 (b, b'), 22dmp-C7 (c, c'), 23dmp-C7 (d) and 33dmp-C7 (e). For the clarity of both figures, the hydrogen atoms are omitted. For the guest molecule, the CH₃ hydrocarbon molecules are coloured with green and the mono-branched central atom CH hydrocarbon molecules and di-branched central atoms C are presented as yellow dots.

Table 4.2 presents the cage flexibility effects for those alkanes discussed above, by comparing the adsorption quantities ratio difference between flexible host and rigid host. For those smaller alkanes (C4, C5), the host flexibility shows a modest influence on the adsorption quantities. Even for some C6 (nC6, 2mp-C6) and C7 (nC7, 2mh-C7), the differences are acceptable. For those alkanes in the red dash square, the differences become vital. CC3 contains 3D diamondoid pore network (figure 3.1b), linear alkanes just lie in the channel without the requirement of sizeable local structure adjustment, which lead to the ignorable flexibility influence on the adsorption quantities. Significant structure adjustments are required for the adsorption of long branched alkanes (inside the red dash box) which causes the intensive flexibility influence. We suggest structure flexibility should be considered for adsorption simulations that the smallest size of the guest molecule is close or larger than the pore size of the host.

Table 4.2. The adsorptions ratio difference (flexible divided by rigid) at 1 bar for C4 to C7 alkanes in CC3R. The colours changes from yellow to red with the increasing of difference.

C4 alkanes	nC4	ibu				
R	1.04	1.09				
C5 alkanes	nC5	2mb	dmp			
R	1.12	1.21	1.03			
C6 alkanes	nC6	2mp	3mp	23dmb	22dmb	
R	1.01	1.21	5.25	8.48	11.18	
C7 alkanes	nC7	2mh	3mh	22dmp	23dmp	33dmp
R	1.02	1.01	2.73	2.81	16.51	19.07

$$R = \frac{\text{Loading}_{flexible\ host, 1bar}}{\text{Loading}_{rigid\ host, 1bar}}$$

4.3.3 Competitive adsorption

Adsorption-based separation technique is promising to separate alkanes' isomers. In this work, competitive adsorptions of alkanes' isomers are evaluated by simulating the mixtures alkanes' isomers adsorptions. Isotherms of linear and branched alkanes mixture of C4, C5, and C6 isomers are presented in figure 4.13, while all these adsorption quantities were computed with flexible host approaches. For each competitive adsorption simulation, the numbers of each adsorbate are identical at the start point. The flexible CC3-R shows no prominent adsorptive separation capability for the nC4 and isobutane (figure 4.13a). The adsorption quantities are

quite alike within the studied pressure range. The pure component adsorption isotherms of C4 isomers are quite similar, and the adsorption quantities are almost identical among 0.7 to 1.1 bar pressure range according to figure 4.1a. For both nC4 and isobutane pure component simulations, the loading amounts are around 0.85 mmol/g at 1.1 bar. For the competitive C4 isomers adsorptions, the loading quantities of nC4 are 0.88 mmol/g at 1 bar, while 0.69 mmol/g of isobutane are loaded within CC3-R. Slightly more nC4 is loaded compared to pure component adsorption. Furthermore, 1.57 mmol/g C4 adsorbates in total (0.89 mmol/g nC4 and 0.69 mmol/g isobutane) can be loaded at the same time. Hence, there is a codependent adsorption property of C4 isomers in CC3-R. Figure 4.13b shows C5 competitive adsorption isotherms, the loading quantities of nC5 is considerably greater than the 2mb-C5 and dmp-C5. The adsorptive selectivity of nC5 to 2mb-C5 is more than 3 among the whole simulated pressure range, nC5 to dmp-C5 is around 12 from 0.9 to 1.1 bar, and 2mb-C5 to dmp-C5 is more than 3 among 0.6 to 1.1 bar. Hence, CC3-R cage is capable of separating the nC5 from its branched isomers, and mono-branched 2mb-C5 to di-branched dmp-C5. As it is shown in C6 competitive adsorption isotherms (figure 4.13c), CC3-R shows significant better adsorptive selectivity of nC6 towards its branched isomers. According to figure 4.11, the rank of host-guest HOD values is $nC6 > 2mp-C6 > 3mp-C6 > 23dmb-C6 > 22dmb-C6$, which is in the same order of adsorption quantities of each C6 isomer from this competitive adsorption simulation. Hence, the host-guest HOD relates to loading capability of competitive adsorptions. The host-guest HOD values of linear C6 and 2mp-C6 are similar, but the adsorptive selectivities are around 3.5 among the pressure range. Therefore, nC6 is geometrically more feasible in the CC3-R cage compared to its branched isomers. The CC3-R shows decent adsorptive selective potential for nC6 towards the other mono-branched C6 isomer 3mp-C6 (adsorptive selectivity: 17.11 at 0.1 bar), and di-branched isomers 22dmb-C6 (adsorptive selectivity: 52.44 at 0.1 bar) and 23dmb-C6 (adsorptive selectivity: 84.70 at 0.1 bar). Overall, the competitive adsorption capability is linearly related to the values of host-guest HOD. The big HOD value difference can lead to the great adsorptive selectivity. The CC3-R shows the potential of separating linear alkanes from its branched isomers and mono-branched isomers from its di-branched isomers.

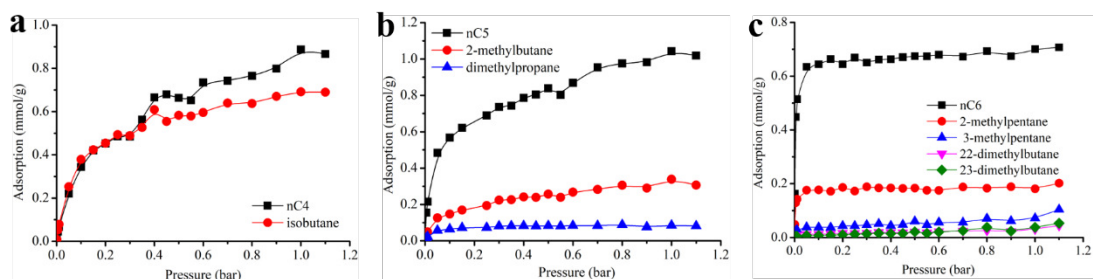


Figure 4.13. The competitive adsorptions of linear alkanes with branched alkanes, all these guest molecules are in the same equivalence at the beginning of each simulation. (a) C4 linear alkane nC4 (black line, square) and branched isomer isobutane (red line, sphere) competitive adsorption at 433 K, within 1.1 bar. (b) C5 linear alkane nC5 (black line, square), mono-branched isomers 2mb-C5 (red line, sphere) and di-branched dmp-C5 (blue line, up triangle) competitive adsorption at 433 K, within 1.1 bar. (c) C6 linear alkane nC6 (black line, square), mono-branched isomers 2mp-C6 (red line, sphere), 3mp-C6 (blue line, up triangle) and di-branched 22dmb-C6 (magenta line, down triangle) and 23-dmbfC (olive line, diamond) competitive adsorption at 433 K, within 1.1 bar.

4.4 Conclusion

We have investigated the adsorption of pure linear and branched alkanes in the CC3-R cage via both flexible and rigid host approaches to examine the influence of cage flexibility. For the adsorption of linear alkanes, there are no significant adsorption quantities difference between rigid and host approaches (nC4 to nC7). The cage flexibility allows the interplay between host and guests that leads to energetically more favourable adsorption configurations and faster saturations. Cage flexibility shows a significant influence on the adsorption capability towards these branched alkanes. Adsorption quantities differences increased with the increasing of chain length and branch level. For the adsorptions of C6 branched isomers (22dmb-C6 and 23dmb-C6), and C7 isomers (22dmp-C7, 23dmp-C7, 33dmp-C7), decent adsorption quantities were

yielded by the flexible host approach, while negligible numbers of adsorbates located in rigid CC3-R. Branched alkanes are stronger interacted flexible cages, and the window cavity is capable of loading with several branched alkanes such as ibu-C₄, 2mh-C₇ and 3mh-C₇. Even for these adsorbates show similar adsorption quantities between flexible and rigid host assumptions, the adsorption behaviours could be entirely different. However, the accuracy of both assumptions needs to be further validated with experimental techniques. CC3-R cage shows adequate separation capability for linear alkanes towards its branched isomers, and mono-branched isomers to its di-branched alkanes. The adsorptive selectivity of linear C₆ to 23dmb-C₆ is 84.70 at 0.1 bar.

4.6 References

1. Mitra, T. *et al.* A soft porous organic cage crystal with complex gas sorption behavior. *Chem. - A Eur. J.* **17**, 10235–10240 (2011).
2. Little, M. a, Chong, S. Y., Schmidtman, M., Hasell, T. & Cooper, A. I. Guest control of structure in porous organic cages. *Chem. Commun. (Camb)*. **50**, 9465–8 (2014).
3. Hasell, T., Chong, S. Y., Jelfs, K. E., Adams, D. J. & Cooper, A. I. Porous organic cage nanocrystals by solution mixing. *J. Am. Chem. Soc.* **134**, 588–598 (2012).
4. Hasell, T., Chong, S. Y., Schmidtman, M., Adams, D. J. & Cooper, A. I. Porous organic alloys. *Angew. Chemie - Int. Ed.* **51**, 7154–7157 (2012).
5. Jones, J. T. a *et al.* Modular and predictable assembly of porous organic molecular crystals. *Nature* **474**, 367–371 (2011).
6. Holst, J. R., Trewin, A. & Cooper, A. I. Porous organic molecules. *Nat. Chem.* **2**, 915–920 (2010).
7. Zhang, G. & Mastalerz, M. Organic cage compounds--from shape-persistency to function. *Chem. Soc. Rev.* **43**, 1934 (2014).
8. Jones, J. T. a. *et al.* On-Off Porosity Switching in a Molecular Organic Solid. *Angew.*

- Chemie Int. Ed.* **50**, 749–753 (2011).
9. Tozawa, T. *et al.* Porous Organic Cages. *Nat. Mater.* **8**, 973–978 (2009).
 10. Kewley, A. *et al.* Porous organic cages for gas chromatography separations. *Chem. Mater.* **27**, 3207–3210 (2015).
 11. Zhang, J. H. *et al.* Homochiral Porous Organic Cage with High Selectivity for the Separation of Racemates in Gas Chromatography. *Anal. Chem.* **87**, 7817–7824 (2015).
 12. Mitra, T. *et al.* Molecular shape sorting using molecular organic cages. *Nat. Chem.* **5**, 276–281 (2013).
 13. Evans, J. D. *et al.* Feasibility of mixed matrix membrane gas separations employing porous organic cages. *J. Phys. Chem. C* **118**, 1523–1529 (2014).
 14. Bushell, A. F. *et al.* Nanoporous organic polymer/cage composite membranes. *Angew. Chemie - Int. Ed.* **52**, 1253–1256 (2013).
 15. Chen, L. *et al.* Separation of rare gases and chiral molecules by selective binding in porous organic cages. *Nat. Mater.* **13**, 954–60 (2014).
 16. Hasell, T. *et al.* Porous organic cages for sulfur hexafluoride separation. *J. Am. Chem. Soc.* (2016). doi:10.1021/jacs.5b11797
 17. D. A., Mcq. & Reid, C. E. *Statistical Mechanics.* **1**, (1997).
 18. Wilmer, C. E. *et al.* Large-scale screening of hypothetical metal–organic frameworks. *Nat. Chem.* **4**, 83–89 (2011).
 19. Dubbeldam, D., Krishna, R., Calero, S. & Yazaydin, A. Ö. Computer-assisted screening of ordered crystalline nanoporous adsorbents for separation of alkane isomers. *Angew. Chemie - Int. Ed.* **51**, 11867–11871 (2012).
 20. Yazaydin, a O. *et al.* Screening of Metal-Organic Frameworks for Carbon Dioxide Capture from Flue Gas Using a Combined Experimental and Modeling Approach. *J. Am. Chem. Soc.* **131**, 18198–18199 (2009).
 21. Salles, F. *et al.* Molecular insight into the adsorption and diffusion of water in the versatile hydrophilic/hydrophobic flexible MIL-53(Cr) MOF. *J. Phys. Chem. C* **115**, 10764–10776 (2011).

22. Vlugt, T. J. H. Influence of Framework Flexibility on the Adsorption Properties of Hydrocarbons in the Zeolite Silicalite. 12757–12763 (2002).
23. Gee, J. A. & Sholl, D. S. Effect of Framework Flexibility on C8 Aromatic Adsorption at High Loadings in Metal-Organic Frameworks. *J. Phys. Chem. C* **120**, 370–376 (2016).
24. Holden, D. *et al.* Understanding Static, Dynamic and Cooperative Porosity in Molecular Materials. *Chem. Sci.* **00**, 1–5 (2016).
25. Dubbeldam, D., Calero, S., Ellis, D. E. & Snurr, R. Q. RASPA: molecular simulation software for adsorption and diffusion in flexible nanoporous materials. *Mol. Simul.* **7022**, 1–21 (2015).
26. Mehlig, B., Heermann, D. & Forrest, B. Hybrid Monte Carlo method for condensed-matter systems. *Phys. Rev. B* **45**, 679–685 (1992).
27. Gilks, W. R., Best, N. G. & Tan, K. K. C. Adaptive Rejection Metropolis Sampling within Gibbs Sampling. *Appl. Stat.* **44**, 455 (1995).
28. Schmid, R. & Tafipolsky, M. An Accurate Force Field Model for the Strain Energy Analysis of the Covalent Organic Framework COF-102. *J. Am. Chem. Soc.* **130**, 12600–12601 (2008).
29. Huang, B. L., McGaughey, A. J. H. & Kaviany, M. Thermal conductivity of metal-organic framework 5 (MOF-5): Part I. Molecular dynamics simulations. *Int. J. Heat Mass Transf.* **50**, 393–404 (2007).
30. Alavi, S. *et al.* Hydrogen adsorption and diffusion in p-tert-butylcalix[4]arene: An experimental and molecular simulation study. *Chem. - A Eur. J.* **16**, 11689–11696 (2010).
31. Holden, D., Jelfs, K. E., Cooper, A. I., Trewin, A. & Willock, D. J. Bespoke force field for simulating the molecular dynamics of porous organic cages. *J. Phys. Chem. C* **116**, 16639–16651 (2012).
32. Martin, M. G. & Siepmann, J. I. Transferable Potentials for Phase Equilibria. 1. United-Atom Description of n -Alkanes. *J. Phys. Chem. B* **102**, 2569–2577 (1998).
33. Smit, B. & Krishna, R. Monte Carlo simulations in zeolites. *Curr. Opin. Solid State Mater. Sci.* **5**, 455–461 (2001).

34. van Erp, T. S., Dubbeldam, D., Caremans, T. P., Calero, S. & Martens, J. a. Effective Monte Carlo Scheme for Multicomponent Gas Adsorption and Enantioselectivity in Nanoporous Materials. *J. Phys. Chem. Lett.* **1**, 2154–2158 (2010).
35. Jiang, J., Sandler, S. I., Schenk, M. & Smit, B. Adsorption and separation of linear and branched alkanes on carbon nanotube bundles from configurational-bias Monte Carlo simulation. *Phys. Rev. B - Condens. Matter Mater. Phys.* **72**, 1–11 (2005).
36. Gutierrez-Sevillano, J. J. *et al.* Analysis of the ITQ-12 Zeolite Performance in Propane-Propylene Separations Using a Combination of Experiments and Molecular Simulations. *J. Phys. Chem. C* **114**, 14907–14914 (2010).
37. Martin, M. G. & Siepmann, J. I. Predicting multicomponent phase equilibria and free energies of transfer for alkanes by molecular simulation. *J. Am. Chem. Soc.* **119**, 8921–8924 (1997).
38. Thu, K., Mitra, S. & Saha, B. B. Theoretical development on the isosteric heat of adsorption and experimental confirmation. 1–6 (2017).

Chapter 5

Molecular simulations on volatile nuclides and hydrogen isotope separation

5.1 Introduction

Unlike MOFs, which feature the extended network framework, porous molecular crystals (PMCs) are formed by packing discrete molecular units into a solid-state with permanent porosity.¹ The pores can be characterised as either intrinsic pore, which is the internal void of the molecular unit, or extrinsic pore, which is caused by inefficient packing of the molecular units. Due to the non-covalent packing of the molecular units, most PMCs are soluble in certain solvents, which grants PMCs unique solution-processable that is not possible for MOFs with extended framework structure.² We previously reported CC3-R have unprecedented selectivity for the rare gas separation (Xe to Kr) due to the size-selective effect.³ Additionally, CC3-R and its enantiomer CC3-S can form a stable racemic microporous CC3-RS.⁴ Both cages pack window-to-window, forming 3D interconnected pore structures. Both cages are chemically robust and solution-processable, which make them appealing for the use of the stationary phase of capillary columns.⁵ Most recently, we presented CC3-R that could act as a host to be doped by I₂ vapour sublimation.⁶ To the best of our knowledge, the potential use of PMCs to capture the volatile iodic species is still scarce. Molecular simulation acts as a safe and effective method to study the separation of iodic compounds that pose harmful threats to humans and equipment. Up to now, Grand Canonical Monte Carlo (GCMC), which treat the host porous material structure to be rigid, allows fast screening of the adsorption and separation of gas molecules in porous materials. Studies also showed that PMCs, like CC3, could possess significant adsorbate-assisted structure changes, which could facilitate the diffusion and adsorption of adsorbate inside PMCs.^{3,7,8} In these cases, a static, fixed treatment of the crystal structures is inadequate to predict the potential adsorption and separation capabilities. Therefore, a hybrid molecular dynamic Monte Carlo (GCMC/MD) simulation method⁹, which allows the structure of host porous materials to be flexible, is implemented in our study to study the adsorption and separation of these iodic species and explore the effects of the flexibility towards the adsorption and separation in PMCs.

The downside of implementing the hybrid GCMC/MD simulation is its sizeable computational

cost. A strategic screening approach is needed to allow the costly hybrid GCMC/MD simulations aim at the PMCs with the good potent to capture iodine species. In this study, we developed a screening approach which combined the fast geometric characterisation method that could evaluate the accessibility of iodine species in PMCs. The fast GCMC simulations with rigid PMCs structures that could give a quick estimation of the adsorption performance of iodine species and the computationally expensive hybrid GCMC/MD simulations that could give the accurate adsorption performance and behaviour of iodine species in PMCs. With the screening approach, we aim to investigate the performance of PMCs in capturing low concentrated volatile iodine species mimicking the realistic industrial condition. In this work, we present a top-down computational screening study of 51 existing PMCs to investigate their I_2 and CH_3I capture performance.

Various porous materials have been applied on the D_2 separation, including carbon^{10,11}, carbon nanotubes¹², MOFs^{13,14}, COFs¹⁵ and 2D materials¹⁶. In this chapter, The D_2 separation capability of CC3S, 6ET-RCC3 and the 1:1 cocrystal of these two cages were computationally investigated.

5.2 Computational methodology

These crystallographic information files (CIFs) of the PMCs in this work were extracted from experimental literature¹⁷⁻⁴⁶ and the robotic synthesised cages we recently reported.⁴⁷ 51 PMCs, which are inherently shape-persistent after the removal of solvents, were chosen to form a screening pool. The naming rule for these PMCs in this work follows the work of Miklitz and co-workers.⁴⁸ For our recently reported PMCs, the names are kept consistent with the original paper.⁴⁷ The geometric characteristics detail of the PMCs is listed in table S8.

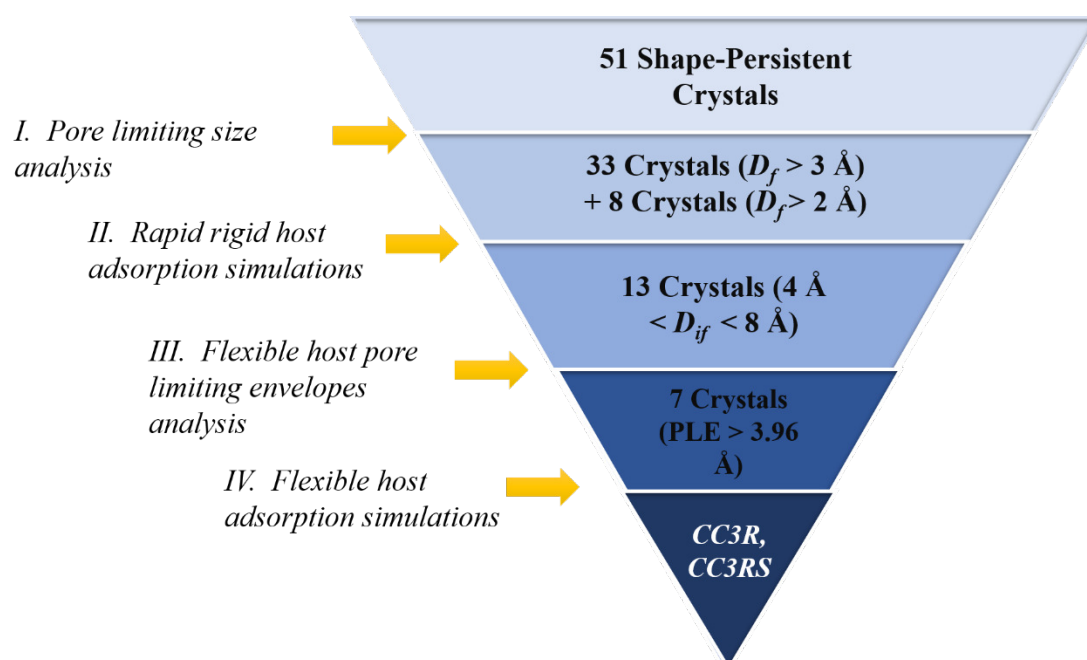


Figure 5.1. Schematic demonstration of the top-down approach applied in this screening study. Four key steps are used for narrowing down the promising PMCs pool for capturing I_2 and CH_3I . D_f indicates the PLD of the PMCs, and D_{if} represents the pore size of each PMCs and PLE is the pore limiting envelope of the PMCs.

Figure 5.1 presents a schematic top-down screening scheme for identifying the promising PMCs for capturing the volatile I_2 and CH_3I . For the step (I) in figure 1, PMCs was firstly characterized by the Zeo++ with the high-accuracy setting.⁴⁹ The geometric characterisation with Zeo++ is computationally cost-efficient. Voronoi decomposition was used to find the probe accessible pore channel, accessible volume, largest cavity diameter (LCD), pore limiting diameter (PLD), and the largest diameter along the accessible channel (LDAC).⁴⁹ The initial analysis of LCD, PLD and LDAC exclude PMCs with small pores that are impossible to admit I_2 and CH_3I molecules.

In step II, fast GCMC simulations with the rigid PCMs structures were conducted to predict the separation performance of I_2 and CH_3I of 300 ppm, 500 ppm, and 700 ppm from N_2 of 1 bar bulk pressure in these PMCs at 423K using RASPA software package.⁹ Four types of MC moves were attempted with equal probability during the GCMC simulations:

- (1) Translational or rotational displacement MC move,
- (2) Insertion with continuous fractional component Monte Carlo (CFCMC) method,⁵⁰
- (3) Addition or deletion of an adsorbate molecule,
- (4) Adsorbate (CH₃I, I₂ with N₂) exchange MC move.

Considering that the size of CH₃I and I₂ molecules are comparable to the pore size of these PMCs, CFCMC method allows a better insertion efficiency compare to the usual addition/deletion MC moves.⁵¹ All the host atoms of these PMCs were treated rigid during the GCMC simulations. 2×10^7 MC cycles were performed, in which the first half of the total cycles were used to equilibrate the simulation system, and the other cycles were for the production run. The Leonard Jones (LJ) parameters and point charges of these PMCs were taken from the optimised potential for liquid simulation atomic atom (OPLS-AA),^{52,53} The detail can be found in table S9. The LJ parameters of CH₃I⁵⁴, I₂⁵⁵ and N₂ are listed in table 1. CH₃I model was taken from the work of Munzebrock and Doge⁵⁴. I₂ was modelled as a united atom, whose parameters were taken from the pure I₂ viscosity calculation⁵⁵. This united atom model has been proved to be accurate in predicting I₂ adsorption capacity in MOFs.^{56,57,58} Jorgensen mixing rule, $\sigma_{ij} = \sqrt{\sigma_i \sigma_j}$, and $\epsilon_{ij} = \sqrt{\epsilon_i \epsilon_j}$, was applied to treat pairs of different atoms. The cut-off distance was set to 12 Å for both LJ interaction and electrostatic interaction, which was computed by Ewald summation with 10⁻⁶ precision.⁵⁹ The pores of PMCs that are inaccessible to CH₃I and I₂ were blocked during GCMC or hybrid GCMC/MD simulations.⁴⁹ The isosteric heat of adsorption Q_{st} was obtained from RASPA implemented Widom particle insertion method.^{60,61}

Table 5.1. LJ parameters and charge of CH₃I⁵⁴, I₂⁵⁵ and N₂⁶² used in this work

Atomic type	σ_i (Å)	ϵ_i (K)	$q(e)$
(I ₂) Iodine			
I_I ₂	4.98	550.0	0
(CH ₃ I) Methyl Iodide			
H_CH ₃ I	2.2	10.01	0.052
C_CH ₃ I	3.5	51.22	-0.02
I_CH ₃ I	4.12	324.06	-0.137
(N ₂) Nitrogen			
N_N ₂	36.0	3.31	-0.482
N_com	0.0	0.0	0.964

CSFF have been used as flexible host force field in Chapter three and Chapter four. This force field is a bespoke force field that developed to describe the dynamic nature of CC1, CC2 and CC3,⁶³ which is insufficient for the screening study based on various types of PMCs. To find out the performance difference between CSFF and OPLS force field, the CH₃I and I₂ adsorption simulations based on the flexible approach with both flexible force fields and three generic force fields described nonbonding interactions are presented in figure S13. The OPLS host field gives almost identical CH₃I adsorption isotherms and I₂ capacity to the CSFF with DREIDING.

After the rapid rigid host GCMC simulation, 13 of the PMCs with good I₂ and CH₃I separation performance were chosen to further investigate the accessibility of I₂ and CH₃I to PMCs by considering the flexibility of the PMCs (step III in figure 1). We have previously reported that assessing PLD only is not sufficient to know if the guest molecules are accessible to the pores of PMCs. The pore limiting envelopes (PLEs), which provides the dynamic distribution information of PLD, were obtained by computing the time-averaged PLDs during the MD simulations. Moreover, the flexibility of PMCs can possess significant adsorbate-assisted structure changes.^{3,7} In this works, we use both the MD and the hybrid GCMC/MD simulations to address the dynamic pore envelope change and the adsorbate induced pore size change of the PMCs.

MD simulations were also carried out using RASAP.⁹ The MD simulations of the empty PMCs were conducted to generate the PLE of the empty PMCs. The MD simulations were run by isothermal-isobaric (NPT) ensemble at 423K and 1 bar with Hoover barostat and thermostat.⁶⁴ The time step was 0.5 fs, and the system was allowed to equilibrate for 1.5 ns, and the data were collected from another 1.5 ns production run.

In step IV of figure 5.1, the hybrid GCMC/MD simulations were used to address the adsorption and separation performance of I₂ and CH₃I in the flexible PMCs. The isoenthalpic-isobaric (NPH) ensemble MD simulation was inserted into the GCMC simulations to relax to guest loaded PMCs. The MD simulations were attempted with 2.44% over the whole simulation process. For the GCMC part, it was kept consistent with the rigid host simulation. OPLS forcefield was used to describe the bonding and non-bonding terms of the PMCs for both MD and the hybrid GCMC/MD simulation.^{52,53,65-67} OPLS forcefield has been reported with good capacity to reproduce the structures and predicts the dynamic features of PMCs.^{26,47,48,68-70} The detail OPLS force field parameters, including bonding, bending, torsional and non-bonding interactions, for the PMCs can be found in table S10-S12 in the supporting document.

FH tail potential modification is used in this section to address the quantum effects in molecular-level simulations of H₂/D₂ adsorption in PMCs at very low temperature (70K). The hydrogen model is taken from the work of Levesque et al.⁷¹ that two hydrogen atoms were fixed with a distance of 0.74 Å. The positive partial charges (0.468 *e*) were placed at two hydrogen atoms, and negative charge (-0.936 *e*) placed at the mass centre so does the LJ potential (2.96 Å, 36.7 k_B).

5.3 Results and discussion

PMCs that are suitable for gas separation applications should contain interconnected pore

network which is accessible to gas molecules. Analysis of PLD and LCD of the PMCs allows the quick exclusion of PMCs with pores and pore apertures that are too small to admit I_2 and CH_3I . Hence, LCD should be the factor to analyze the pore size effect in the guest molecule capture application. Therefore, it is necessary to block these pockets in a GCMC simulation, or the uptake quantities will be considerably overestimated. Table 5.2 gives the pore network properties of these 51 porous organic molecules. In this work, the minimal molecular van der Waals (vdW) diameter (3.96 Å) of I_2 is used to compare with the PLDs and LCDs of the PMCs.⁷² PMCs whose PLDs/LCDs are larger than 3.96 Å are included for further study. PMCs with PLDs/LCDs that are slightly less than 3.96 Å should also have the potential to capture I_2 and CH_3I due to the dynamic or the adsorbate induced pore size change. In the first screening step, we excluded PMCs whose PLDs/LCDs is smaller than half of the van der Waals (vdW) diameter of I_2 . This exclusion reduces the size of the PMC pool from 51 to 41.

Table 5.2. Pore network analysis for the 51 PMCs.

<i>Probe Diameter (Å)</i>	<i>dimensionality</i>	<i>LCD (Å)</i>	<i>PLD (Å)</i>	<i>LDAC (Å)</i>
1AT-RCC3	3	5.57978	3.13225	5.57978
B1	0	5.41357	1.64008	5.2577
B2	2	4.60836	3.42948	4.60836
B9	1	4.67598	3.71626	4.67598
B11	3	7.6692	4.99471	7.6692
B11_P-3	2	6.63248	2.68061	6.63248
B13	1	5.51439	2.29442	5.51439
B13	2	7.934	2.68433	7.934
B15_CH2C12	2	9.15276	3.5661	9.15276
B15_CH2C12	1	6.77195	4.31355	6.77195
B15_CHC13	2	7.67588	5.34477	7.67576
B23	3	7.17844	4.29076	7.1778
B24	3	10.1998	5.21406	10.1897
B26	3	14.9498	9.11575	14.9498
C1	1	8.3451	5.01901	8.3451
C2	1	4.45055	2.87844	4.45055
C7	1	6.45217	4.47974	6.45217
C9	2	5.42195	3.61739	5.42195
C13	1	4.73428	2.10131	4.73428
C14	0	5.00187	1.96855	5.00114
C21_Tri2Di3	0	4.65577	1.55599	4.63699
C21_Tri4Di6	3	7.98602	3.99541	7.98602
C23	3	8.21522	4.97173	8.21485
C26	3	14.9498	9.11575	14.9498
CB6	1	5.02701	2.05061	5.02701
CB7	1	7.52103	4.08516	7.52103
CC1	0	5.27983	1.67478	5.2796
CC3R	3	5.39462	3.65193	5.39156
CC3RS	3	5.49926	3.73638	5.49902
CC4	2	5.47761	3.57355	5.47761
CC5	3	8.88845	5.90788	8.88726
CC9	3	4.98339	2.19229	4.98296
CC10	1	3.70453	2.78762	3.70453
CD1	0	4.62358	1.97393	4.621
CD3	1	9.08276	7.07326	9.08276
CD3	1	8.10996	5.26106	8.10996
CP1	0	4.81749	1.3304	2.00608
CP3	0	4.42091	1.27589	2.9475
CP5	0	3.98418	1.09505	3.95372
FTRCC3	3	5.81817	3.45099	5.81817
HC1	3	5.74946	4.03978	5.74946
IC2	1	7.88764	4.20055	7.88764
MC3	3	7.01686	4.66601	7.01677
MC4	3	8.20835	3.65185	8.20793
MC5	3	10.11659	4.88446	10.11659
MC7	1	6.61021	4.26589	6.61021
NC1	1	5.5042	4.12378	5.5042
NC2	3	9.53482	4.14522	9.53479
RCC1a	0	5.77676	1.53114	5.76367
RCC1b	3	5.41831	3.13479	5.41744
RCC1c	3	6.82509	4.11798	6.82314
RCC1d	3	6.07562	4.52484	6.07058
WC2	0	5.68907	1.81412	5.68744
WC4	3	7.55414	2.01511	7.55412

GCMC simulations with the rigid host assumption (treating all the host atoms to be rigid) have been widely used to calculate the adsorption of gases in porous crystals. The rigid host assumption allows the fast and cost-efficient calculations but also sacrifice certain accuracy because the dynamic flexibility of the host structure is lost due to the rigid host assumption. Appropriate treatment of flexibility of the host structure may not be necessary for materials with rigid extended frameworks, such as MOFs, but it has an adsorption capability improve the

effect to PMCs, as shown in our previous work.⁷³ In our work, fast GCMC simulations with the rigid host assumption were carried out to screen the 41 PMCs in our second screening step for the separation performance of CH₃I and I₂ at low concentrations. The CH₃I and I₂ capture performance at 300 ppm level (The partial pressure of CH₃I or I₂ is 300 ppm, the total pressure of the system mixed with N₂ is 1 bar) are presented as coloured dots in Figure 5.2a, 5.2b, and the capture performance of 500 ppm and 700 ppm levels are presented in table S13. It has been suggested that pore size and the isosteric heat of adsorption (Q_{st}) should be mainly correlated with the gases adsorption capacity at a low pressure^{74,75}. In Figure 5.2, the adsorption capacities of CH₃I and I₂ in the PMCs are also plotted against both LDAC and Q_{st} . LDAC represents the largest size among the interconnected channel of a PMC. The PMCs with the best I₂ (over 0.32 mmol/g) and CH₃I (over 0.62 mmol/g) adsorption capacity feature a LDAC between 5 Å to 8 Å. The same group of PMCs also have strong affinities with I₂ and CH₃I, whose Q_{st} exceed -50 kJ/mol. Among the PMCs, CB6 possessing a LDAC of 5.43 Å and the highest Q_{st} with CH₃I showing the best CH₃I capture capacity (1.28 mmol/g) at 300 ppm presents the strongest Q_{st} with I₂ and CH₃I (CH₃I, -105.22 kJ/mol; I₂, -110.38 kJ/mol). , On the other hand, CC3RS with a LDAC of 5.49 Å shows the best I₂ uptake (2.49 mmol/g) at 300 ppm. Overall, the screening of GCMC simulations with the rigid host assumption have quickly identified some PMCs with good potent to capture I₂ and CH₃I. In this step, 13 PMCs with LDAC size between 4 Å to 8 Å are selected from the pool for further analysis. The candidates for CH₃I capture are 1AT-RCC3, CB6, FTRCC3, CB7, C9 and B13, while 1AT-RCC3, RCC1c, RCC1b, CB6, CB7, C7, RCC1d, FTRCC3, CC3R, CC3RS, HC1 are identified as potential I₂ capture candidates for further study.

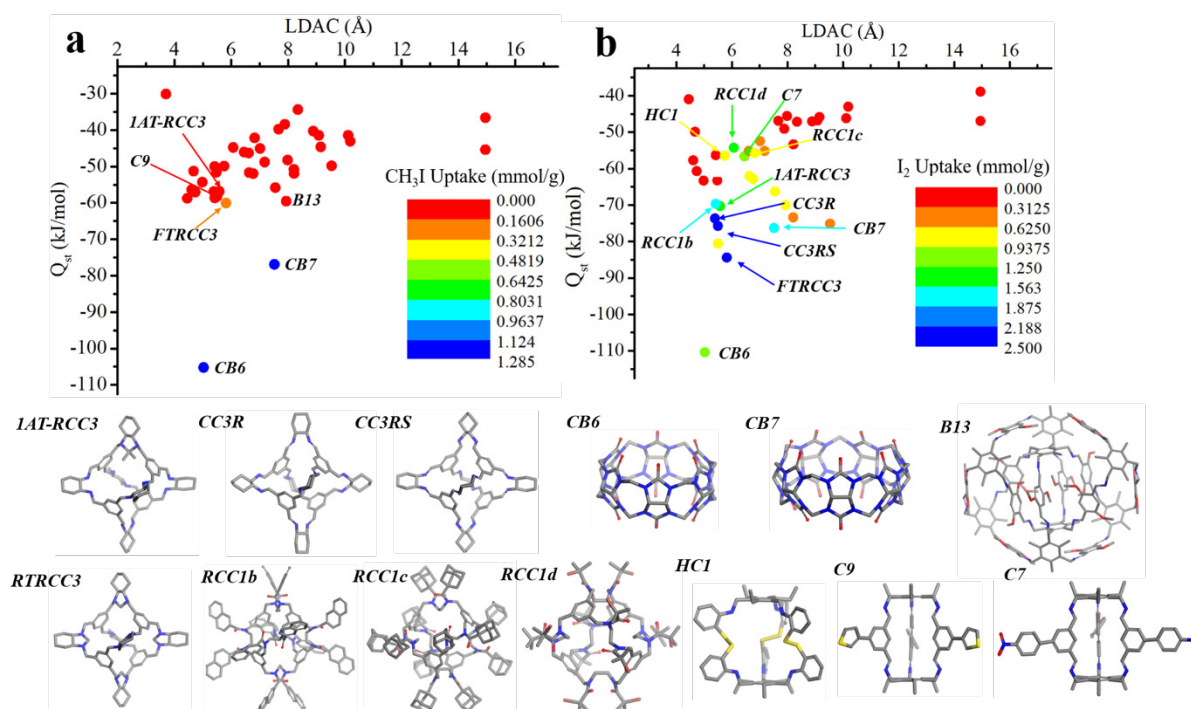


Figure 5.2. GCMC simulations of CH_3I (a) and I_2 (b) capture at 300 ppm, 423 K against LDAC and adsorption energy. The adsorption capacity was coloured with the ascendancy of the colour bar (from red to blue). The molecular units of 13 selected PMCs are listed below (a) and (b). Atom colour code: C, grey; N, blue; O, red; S, yellow. For the clarity of these figures, hydrogen atoms were ignored.

The porosity of a porous material can be described in three different terms: static porosity, dynamic porosity, and cooperative porosity.⁷ Static porosity is measured assuming the structure of the porous material is static. PLD is evaluated directly from the static porosity. Dynamic porosity is measured when the host structure is treated to be flexible. Cooperative porosity is measured when the adsorbate induced structure change is considered. Guest adsorbate with its size being bigger than the PLD of an adsorbent may still be accessible to the adsorbent due to the dynamic or the adsorbate assisted porosity.^{76,77} In our third step of the top-down screening approach, we measured PLEs of the PMCs with and without I_2 and CH_3I adsorbed, which reflect the dynamic pore window change with and without adsorbates. The PLEs for the 13 PMCs that are illustrated in Figure 5.3 were calculated using the time-averaged PMCs structures data from the MD simulations. PLEs from the empty PMCs are used to describe the dynamic pore

apertures (Figure 5.3a). PLEs calculated from MD simulations of the PMCs loaded with CH₃I or I₂ are used to describe the cooperative pore apertures (Figure 5.3b and 5.3c). The criteria to define the accessibility of CH₃I and I₂ to the PMCs is that at least one snapshot of the PLE distribution should be wider than 4.23 Å (CH₃I) and 3.96 Å (I₂), which are the minimal molecular diameters. As can be seen from Figure 3a, there are only CC3R and CC3RS possessing the dynamic PLEs larger than 3.96 Å, when their cages have zero loadings of CH₃I and I₂. If the accessibility of PMCs is only considered using PLEs with zero loadings of adsorbate, all other PMCs seem to be inaccessible to CH₃I and I₂. Nevertheless, PLEs calculated by considering the guest induced pore aperture change give very different results. As shown in Figure 5.3b, parts of the PLEs of CB7 and C9 are larger than 3.96 Å after loaded with CH₃I. However, none of them reach 4.23 Å. Figure 5.3c illustrates that 5 extra PMCs appear to be accessible to I₂ molecule, including CB7, HC1, C7, RCC1c, and RCC1d, after loaded with I₂ through GCMC simulations. Herein, we emphasize the importance of considering the adsorbate-induced pore aperture change in the PMCs, as most of the PMCs show the pore apertures expansion due to the loaded CH₃I or I₂. The dynamic PLEs screening analysis proposed in this work is crucial to determine the accessibility of guest molecules to the porous materials. In this stage, the PCMs pool has been narrowed down from 13 to 7, with none for CH₃I capture, and CB7, HC1, C7, CC3R, CC3RS, RCC1c and RCC1d for I₂ capture.

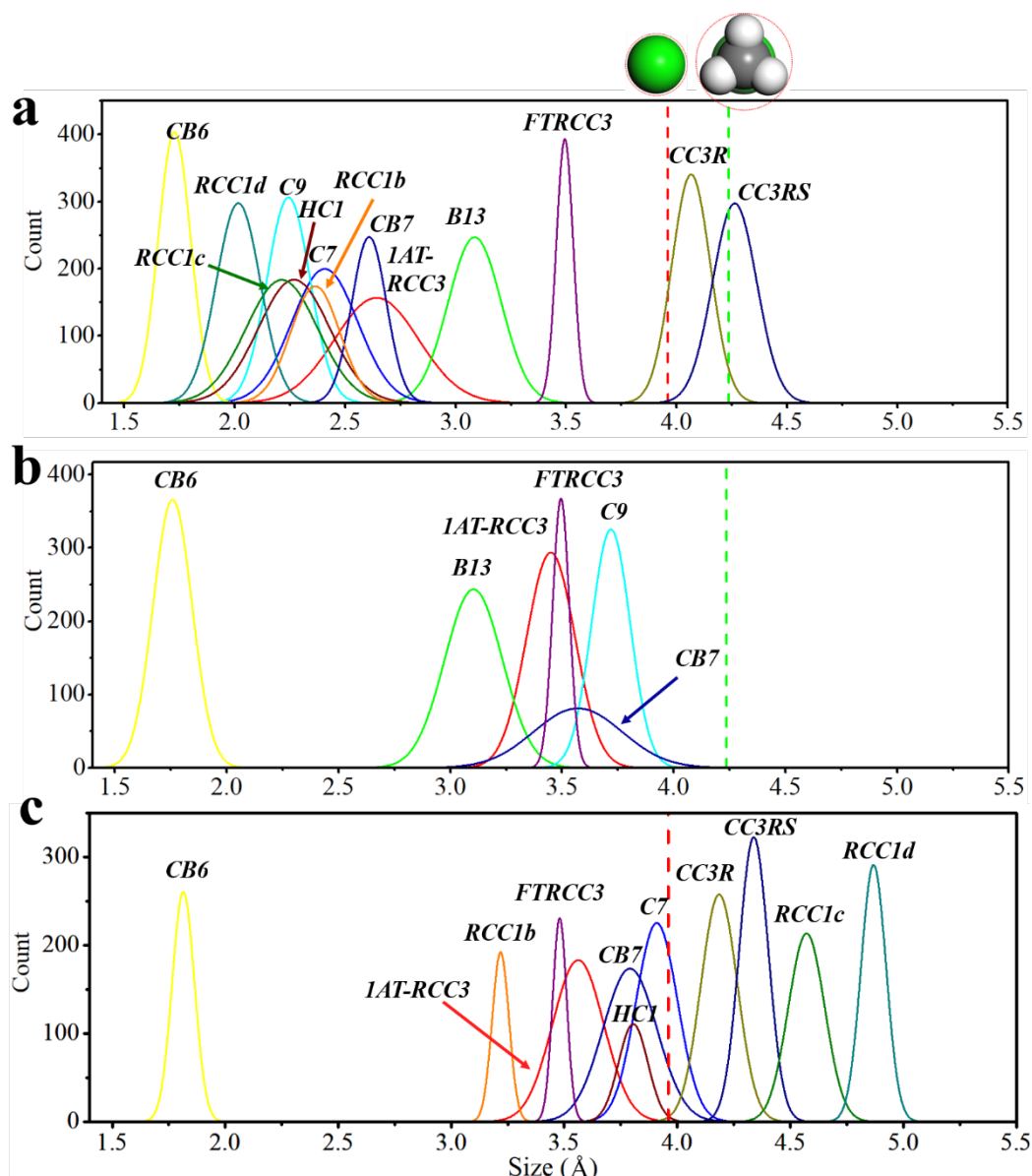


Figure 5.3. PLEs computed from MD simulations with no presence of gas of all these 13 materials (a), CH_3I interacted structures of its 7 candidates (b) and I_2 interacted structures of its 12 candidates. PLEs Colouring: IAT-RCC3, red; B13, green; C7, blue; C9, cyan; CB6, yellow; CC3R, dark yellow; CC3RS, navy; FTRCC3, purple; HCl, wine; RCC1c, olive; RCC1d, dark cyan; CB7, royal; RCC1b, orange, and the red dash line in these figures indicate the smallest sizes (I_2 : 3.96 Å, CH_3I : 4.23 Å).

Up to now, the PMC pool we have narrowed down should be accessible 7 candidates that have good potential to capture I_2 . In this step, we performed the hybrid GCMC/MD simulations of I_2 (figure 5.4a) adsorption at 300ppm, 500 ppm and 700 ppm in the PMCs to further obtain the

accurate adsorption capacity and behaviour. The results from the hybrid GCMC/MD simulation, which allows the PMCs' host structure to be flexible, suggested lower I_2 adsorption quantities in the PMCs, except CC3R, and CC3RS, compared to the results from the GCMC simulation with the rigid host assumption. Our previous experience suggested that the hybrid GCMC/MD would usually generate higher uptakes of CH_4 , CO_2 and SF_6 in CC3R than the results from the GCMC simulations due to the expansion of the size of the pores from 0.01 to 1 bar.⁷³ This may not be applicable on the low concentration capture of gases. Both the hybrid GCMC/MD and GCMC simulation suggest that CC3R and CC3RS are the most promising materials for I_2 capture at such low pressure, and the adsorption snapshots are shown in figure 5.4b and 5.4c.

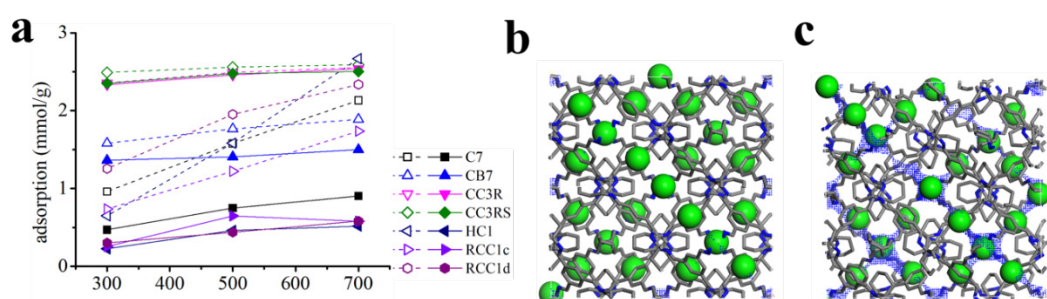


Figure 5.4. Low concentration adsorption simulations based on both rigid host (GCMC, Dash line with open interior) and flexible host (MD/GCMC, line with solid interior) at 423 K of I_2 (a), and the adsorption snapshots for CC3RS (b) and CC3R (c) carbon atoms were coloured in grey, nitrogen in blue, iodine in green, hydrogen is white, the host atoms were ignored for the clarity of figures and the blue dots indicate the accessible channels.

Till the last step, CC3R and CC3RS show outstanding I_2 capture capabilities and adequate dynamic aperture size for the diffusion. However, none of those PMCs passes that top-down approach for the capture of CH_3I . PMCs from step II have been tested to find out promising pore sizes for iodine species capture (figure 5.5) without the consideration of aperture size. CB6 shows excellent CH_3I capture capability (figure 5.5a, yellow), which indicates there is a promising pore with the size around 5.1 Å. The other promising size is around 7.4 Å, which is happened in CB7 (figure 5.5a, blue). The adsorption snapshots of CB6 and CB7 shows the adsorption pattern difference between these two ranges of pore sizes. The CH_3I molecule is

loaded in the intrinsic pore of CB6, and the extrinsic pore of CB7. For I_2 capture (figure 5.5b), the most promising pore sizes are around 5.5 to 6.5 Å, while more than 2.5 mmol/g of I_2 can be captured in CC3R, CC3RS and FTRCC3. However, the current database may not sufficient enough, but those pore size ranges are promising for iodine species capture.

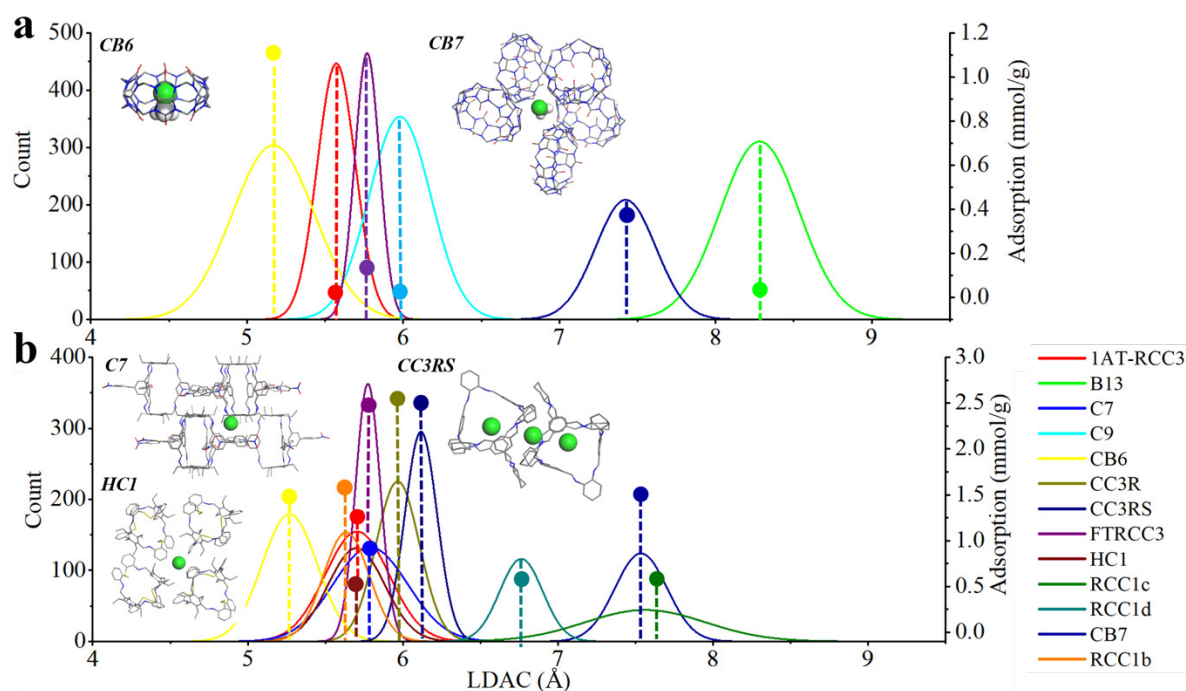


Figure 5.5. The LDAC distributions of each PMCs with the interactions of CH_3I (a) and I_2 (b). The spheres indicates the adsorption quantity. 1AT-RC,C3 (red), B13 (green), C7 (blue), C9 (cyan), CB6 (yellow), CC3R (dark yellow), CC3RS (navy), FTRCC3 (purple), HC1 (wine), RCC1c (olive), RCC1d (dark cyan), CB7 (royal), RCC1b (orange). The adsorption snapshots are also presented, and each elements are coloured as grey (carbon), blue (nitrogen), red (oxygen), iodine (green) and hydrogen of CH_3I model is white. The hydrogen atoms of PMCs is omitted for the clarity of figures.

The binary H_2/D_2 competitive adsorption isotherms computed by FH tail modified GCMC simulation with hybrid MD algorithm.⁷¹ All those three cages were predicted with the capability of selecting D_2 to H_2 . The cocrystal, the mixture of CC3 and 6ET-RCC3 shows even higher than 6ET-RCC3. Free energy barriers compare the diffusion of hydrogen isotopes of three cages. From figure 5.6 D to F, the diffusions from one mass centre of a cage to the mass centre of its

adjacent cage were monitored by free energy. For CC3, both H₂ and D₂ moved freely from one cage to the other as the unchanged low free energy line (figure 5.6c). By contrast the narrow window of 6ET-RCC3 cause the sharp free-energy barriers which largely reduce the diffusivity of both guests. When two methyl groups restrict a window, 6ET-RCC3's pore space became disconnected, and the diffusion barrier became too large to cross (figure 5.6d, cage on the left). However, windows with one methyl group (figure 5.6d, cage on the right) proposed continuously pore structure and the free-energy barriers for H₂ and D₂ were lowered substantially. Crucially, 6ET-RCC3 cage windows containing one methyl group provided diffusion barriers that were different for D₂ and H₂ and acted as a kinetic sieve. This feature was also carried over into Cocryst1 (figure 5.6e). In Cocryst1, the large CC3 cavities also provided good dynamical relaxation, resulting in improved D₂ kinetics and higher D₂ uptakes.

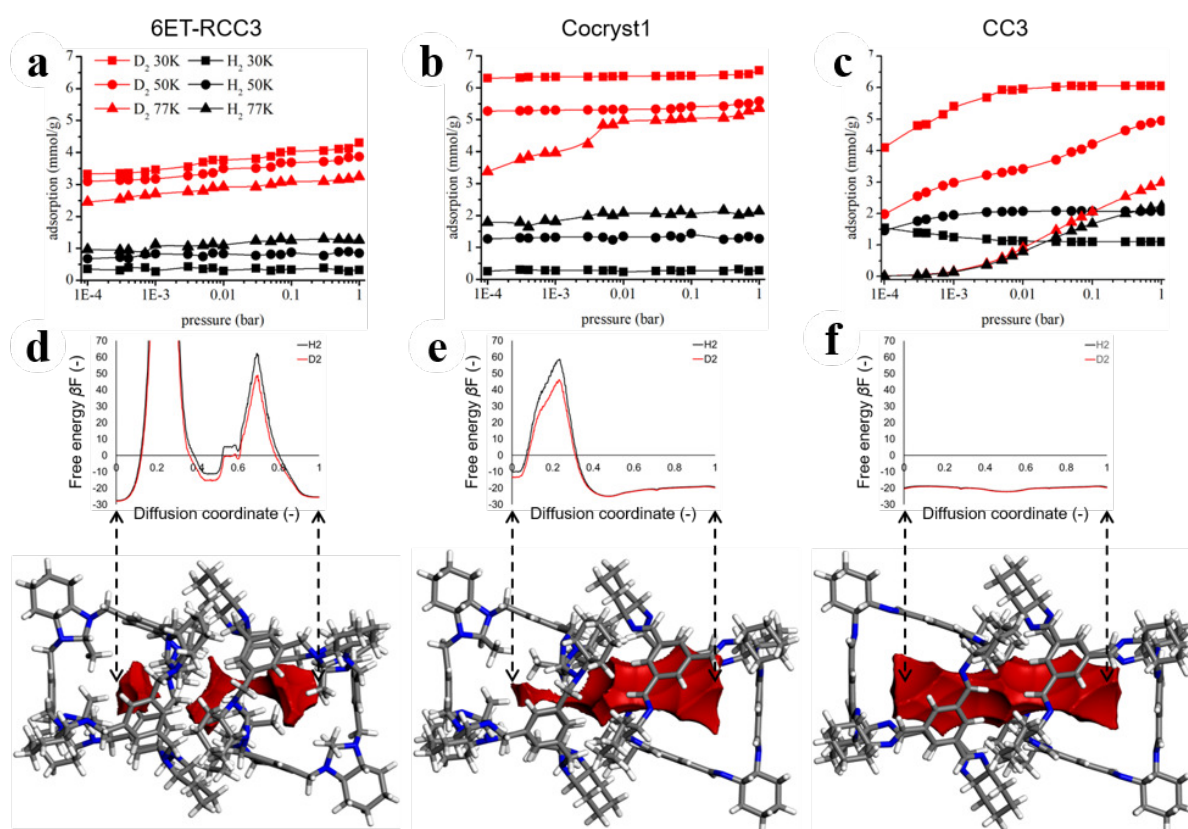


Figure 5.6 Simulations provide insights into the mechanism for hydrogen isotope separation by the porous organic cages. Predicted competitive adsorption (A–C) of an equimolar H₂/D₂ mixture and simulated free energy profiles (D–F) of a single H₂ or D₂ molecule diffusing between the centers of mass of two neighboring cage molecules for 6ET-RCC3 (A, D), Cocryst1

(B, E), and CC3 (C, F), respectively. Free energy profiles were calculated for the diffusion pathways using the respective crystal structures; only the relevant two cage molecules involved are shown here. The diffusion pathway in D runs through a 6ET-RCC3 cage window with two methyl groups (left cage) and a second 6ET-RCC3 cage window with one methyl group (right cage); the diffusion pathway in E runs through a 6ET-RCC3 cage window with one methyl group (left cage) and a neighbouring CC3 cage window (right cage). Gray, white and blue atoms represent carbon, hydrogen and nitrogen, respectively; pore spaces inside the cage molecules, defined by a spherical probe with diameter 2.2 Å, are coloured in red.

5.4 Conclusion

In this chapter, we proposed a computational top-down screening method to find PMCs with excellent iodine species capture capability. CC3R and CC3RS show the excellent potential of I₂ capture out of 51 PMCs. None of those PMCs shows both excellent CH₃I capture capability and sufficient apertures for CH₃I to pass through. This screening method proposed in this chapter considers both accuracy and computational expense. Rapid aperture analysis and GCMC simulations give the focus the range of PMCs; Flexible host approach (GCMC/MD) and PLEs accurately judged the capture and diffuse capabilities. However, The major drawback of this method is the size of the PMCs database that a precise pore size range cannot be decided for the best iodine species capture. We need to combine crystal structure prediction (CSP) in the future work to compensate for this drawback.

Flexible host computational studies helped to explain the H₂/D₂ separation performance of the cocrystal. While these calculations post-rationalised the experimental observations, the excellent agreement between theory and experiment suggests that the a priori design of new systems might be possible, perhaps using methods such as crystal structure prediction to identify suitable hypothetical systems.

5.5 References

1. Mastalerz, M. Permanent porous materials from discrete organic molecules-towards ultra-high surface areas. *Chem. - A Eur. J.* **18**, 10082–10091 (2012).
2. Giri, N. *et al.* Liquids with permanent porosity. *Nature* **527**, 216–220 (2015).
3. Chen, L. *et al.* Separation of rare gases and chiral molecules by selective binding in porous organic cages. *Nat. Mater.* **13**, 954–60 (2014).
4. Hasell, T., Chong, S. Y., Jelfs, K. E., Adams, D. J. & Cooper, A. I. Porous organic cage nanocrystals by solution mixing. *J. Am. Chem. Soc.* **134**, 588–598 (2012).
5. Kewley, A. *et al.* Porous organic cages for gas chromatography separations. *Chem. Mater.* **27**, 3207–3210 (2015).
6. Hasell, T., Schmidtman, M. & Cooper, A. I. Molecular doping of porous organic cages. *J. Am. Chem. Soc.* **133**, 14920–14923 (2011).
7. Holden, D. *et al.* Understanding Static, Dynamic and Cooperative Porosity in Molecular Materials. *Chem. Sci.* **00**, 1–5 (2016).
8. Atwood, J. L., Barbour, L. J., Jerga, A. & Schottel, B. L. Guest transport in a nonporous organic solid via dynamic van der Waals cooperativity. *Science (80-.)*. **298**, 1000–1002 (2002).
9. Dubbeldam, D., Calero, S., Ellis, D. E. & Snurr, R. Q. RASPA: molecular simulation software for adsorption and diffusion in flexible nanoporous materials. *Mol. Simul.* **7022**, 1–21 (2015).
10. Garberoglio, G., DeKlavon, M. M. & Johnson, J. K. Quantum sieving in single-walled carbon nanotubes: Effect of interaction potential and rotational- translational coupling. *J. Phys. Chem. B* **110**, 1733–1741 (2006).
11. Kowalczyk, P. *et al.* Nuclear quantum effects in the layering and diffusion of hydrogen isotopes in carbon nanotubes. *J. Phys. Chem. Lett.* **6**, 3367–3372 (2015).
12. Wang, Q., Challa, S. R., Sholl, D. S. & Johnson, J. K. Quantum sieving in carbon nanotubes and zeolites. *Phys. Rev. Lett.* **82**, 956 (1999).

13. Oh, H., Savchenko, I., Mavrandonakis, A., Heine, T. & Hirscher, M. Highly effective hydrogen isotope separation in nanoporous metal-organic frameworks with open metal sites: direct measurement and theoretical analysis. *ACS Nano* **8**, 761–770 (2014).
14. Chen, B. *et al.* Surface interactions and quantum kinetic molecular sieving for H₂ and D₂ adsorption on a mixed metal-organic framework material. *J. Am. Chem. Soc.* **130**, 6411–6423 (2008).
15. Oh, H., Park, K. S., Kalidindi, S. B., Fischer, R. A. & Hirscher, M. Quantum cryo-sieving for hydrogen isotope separation in microporous frameworks: an experimental study on the correlation between effective quantum sieving and pore size. *J. Mater. Chem. A* **1**, 3244–3248 (2013).
16. Lozada-Hidalgo, M. *et al.* Sieving hydrogen isotopes through two-dimensional crystals. *Science (80-.)*. **351**, 68–70 (2016).
17. Acharyya, K. & Mukherjee, P. S. A fluorescent organic cage for picric acid detection. *Chem. Commun.* **50**, 15788–15791 (2014).
18. Avellaneda, A. *et al.* Kinetically controlled porosity in a robust organic cage material. *Angew. Chemie - Int. Ed.* **52**, 3746–3749 (2013).
19. Horng, Y. C. *et al.* Preparation of a reversible redox-controlled cage-type molecule linked by disulfide bonds. *European J. Org. Chem.* 1511–1514 (2009). doi:10.1002/ejoc.200900044
20. Jones, J. T. a *et al.* Modular and predictable assembly of porous organic molecular crystals. *Nature* **474**, 367–371 (2011).
21. Joseph, A. I. *et al.* Rim-functionalized cryptophane-111 derivatives via heterocapping, and their xenon complexes. *Chem. Commun.* **50**, 15905–15908 (2014).
22. Joseph, A. I., Lapidus, S. H., Kane, C. M. & Holman, K. T. Extreme confinement of xenon by cryptophane-111 in the solid state. *Angew. Chemie - Int. Ed.* **54**, 1471–1475 (2015).
23. Kazuaki, H. The structure of the cyclodotrin complex. V. crystal structures of α -cyclodextrin complexes with p-nitrophenol and p-hydroxybenzoic acid. *Bull. Chem. Soc.*

- Jpn.* **50**, 1416–1424 (1977).
24. Kim, J. *et al.* New cucurbituril homologues: Syntheses, isolation, characterization, and X-ray crystal structures of cucurbit[n]uril (n = 5, 7, and 8). *J. Am. Chem. Soc.* **122**, 540–541 (2000).
 25. Kudo, H. *et al.* Molecular waterwheel (noria) from a simple condensation of resorcinol and an alkanedial. *Angew. Chemie - Int. Ed.* **45**, 7948–7952 (2006).
 26. Liu, M. *et al.* Acid- and base-stable porous organic cages: Shape persistence and pH stability via post-synthetic ‘tying’ of a flexible amine cage. *J. Am. Chem. Soc.* **136**, 7583–7586 (2014).
 27. Matsui, K., Segawa, Y. & Itami, K. All-benzene carbon nanocages: Size-selective synthesis, photophysical properties, and crystal structure. *J. Am. Chem. Soc.* **136**, 16452–16458 (2014).
 28. Mitra, T. *et al.* A soft porous organic cage crystal with complex gas sorption behavior. *Chem. - A Eur. J.* **17**, 10235–10240 (2011).
 29. Bardelang, D. *et al.* Cucurbit[n]urils (n = 5–8): A comprehensive solid state study. *Cryst. Growth Des.* **11**, 5598–5614 (2011).
 30. Park, B. S., Knobler, C. B., Eid, C. N., Warmuth, R. & Cram, D. J. Chiral and somewhat hydrophilic hemicarceplexes. *Chem. Commun.* **1**, 55–56 (1998).
 31. Schneider, M. W., Oppel, I. M., Griffin, A. & Mastalerz, M. Post-modification of the interior of porous shape-persistent organic cage compounds. *Angew. Chemie - Int. Ed.* **52**, 3611–3615 (2013).
 32. Schneider, M. W., Oppel, I. M. & Mastalerz, M. Exo-functionalized shape-persistent [2+3] cage compounds: Influence of molecular rigidity on formation and permanent porosity. *Chem. - A Eur. J.* **18**, 4156–4160 (2012).
 33. Skowronek, P. & Gawronski, J. Chiral iminospherand of a tetrahedral symmetry spontaneously assembled in a [6 + 4] cyclocondensation. *Org. Lett.* **10**, 4755–4758 (2008).
 34. Steiner, T. & Saenger, W. Channel-Type Crystal Packing in the Very Rare Space Group

- P4212 with $Z' = 3/4$: Crystal Structure of the Complex γ -Cyclodextrin-Methanol-n-Hydrate †. *Acta Crystallogr. Sect. B Struct. Sci.* **54**, 450–455 (1998).
35. Taratula, O., Hill, P. A., Khan, N. S., Carroll, P. J. & Dmochowski, I. J. Crystallographic observation of ‘induced fit’ in a cryptophane host-guest model system. *Nat. Commun.* **1**, 147–148 (2010).
 36. Tian, J., Thallapally, P. K., Dalgarno, S. J., McGrail, P. B. & Atwood, J. L. Amorphous molecular organic solids for gas adsorption. *Angew. Chemie - Int. Ed.* **48**, 5492–5495 (2009).
 37. Tozawa, T. *et al.* Porous organic cages. *Nat. Mater.* **8**, 973–978 (2009).
 38. Warmuth, R., Maverick, E. F., Knobler, C. B. & Cram, D. J. Through-shell alkyllithium additions and borane reductions. *J. Org. Chem.* **68**, 2077–2088 (2003).
 39. Zhang, J., Ren, H. & Liu, L. Trifluoromethanesulfonate Anion-linked Supramolecular Frameworks of Cucurbit[5]uril and Cucurbit[7]uril. *Chem. Lett.* **39**, 1016–1017 (2010).
 40. Bojdys, M. J. *et al.* Supramolecular engineering of intrinsic and extrinsic porosity in covalent organic cages. *J. Am. Chem. Soc.* **133**, 16566–16571 (2011).
 41. Brotin, T. & Dutasta, J.-P. Cryptophanes and Their Complexes—Present and Future. *Chem. Rev.* **109**, 88–130 (2009).
 42. Christoforides, E., Mentzafos, D. & Bethanis, K. Structural studies of the inclusion complexes of the (+)- and (-)-borneol enantiomers in α - And β -cyclodextrin. *J. Incl. Phenom. Macrocycl. Chem.* **81**, 193–203 (2015).
 43. Crini, G. Review: A history of cyclodextrins. *Chem. Rev.* **114**, 10940–10975 (2014).
 44. Culshaw, J. L. *et al.* Dodecaamide cages: Organic 12-arm building blocks for supramolecular chemistry. *J. Am. Chem. Soc.* **135**, 10007–10010 (2013).
 45. Freeman, W. A., Mock, W. L. & Shih, N. Y. Cucurbituril. *J. Am. Chem. Soc.* **103**, 7367–7368 (1981).
 46. Givélet, C. *et al.* Templated dynamic cryptophane formation in water. *Chem. Commun.* **47**, 4511–4513 (2011).
 47. Greenaway, R. L. *et al.* High-throughput discovery of organic cages and catenanes using

- computational screening fused with robotic synthesis. *Nat. Commun.* 1–27 (2018).
doi:10.1038/s41467-018-05271-9
48. Miklitz, M. *et al.* Computational Screening of Porous Organic Molecules for Xenon/Krypton Separation. *J. Phys. Chem. C* **121**, 15211–15222 (2017).
 49. Willems, T. F., Rycroft, C. H., Kazi, M., Meza, J. C. & Haranczyk, M. Algorithms and tools for high-throughput geometry-based analysis of crystalline porous materials. *Microporous Mesoporous Mater.* **149**, 134–141 (2012).
 50. W, S. & EJ, M. Continuous Fractional Component Monte Carlo: An Adaptive Biasing Method for Open System Atomistic Simulations. 1451–63 (2015).
 51. Torres-Knoop, A., Balaji, S. P., Vlugt, T. J. H. & Dubbeldam, D. A comparison of advanced monte carlo methods for open systems: CFCMC vs CBMC. *J. Chem. Theory Comput.* **10**, 942–952 (2014).
 52. Kaminski, G. a, Friesner, R. a, Tirado-rives, J. & Jorgensen, W. L. Comparison with Accurate Quantum Chemical Calculations on Peptides †. *J. Phys. Chem. B* **105**, 6474–6487 (2001).
 53. Jorgensen, W. L., Maxwell, D. S. & Tirado-Rives, J. Development and Testing of the OLPS All-Atom Force Field on Conformational Energetics and Properties of Organic Liquids. *J. Am. Chem. Soc.* **118**, 11225–11236 (1996).
 54. Crone-Munzebrock, H. & Doge, G. Computer Simulation of Liquid Methyl Iodide. **3300**, 297–300 (1990).
 55. Rappé, A. K., Casewit, C. J., Colwell, K. S., Goddard III, W. A., Skiff, W. M. UFF, a full periodic table force field for molecular mechanics and molecular dynamics simulations. *J. Am. Chem. Soc.* **114**, 10024–10035 (1992).
 56. Sava, D. F. *et al.* Competitive I₂ Sorption by Cu-BTC from Humid Gas Streams. *Chem. Mater.* **25**, 2591–2596 (2013).
 57. Assfour, B., Assaad, T. & Odeh, A. In silico screening of metal organic framework for iodine capture and storage. *Chem. Phys. Lett.* **610–611**, 45–49 (2014).
 58. Yuan, Y., Dong, X., Chen, Y. & Zhang, M. Computational screening of iodine uptake in

- zeolitic imidazolate frameworks in a water-containing system. *Phys. Chem. Chem. Phys.* **18**, 23246–23256 (2016).
59. Ewald, P. P. Die Berechnung optischer und elektrostatischer Gitterpotentiale. *Ann. Phys.* **369**, 253–287 (1921).
60. Frenkel, D., Smit, B. & Ratner, M. A. *Understanding Molecular Simulation: From Algorithms to Applications*. *Phys. Today* **50**, 66–66 (1997).
61. Vlugt, T. J. H., García-Pérez, E., Dubbeldam, D., Ban, S. & Calero, S. Computing the Heat of Adsorption using Molecular Simulations: The Effect of Strong Coulombic Interactions. *J. Chem. Theory Comput.* **4**, 1107–1118 (2008).
62. Potoff, J. J. & Siepmann, J. I. Vapor–liquid equilibria of mixtures containing alkanes, carbon dioxide, and nitrogen. *AIChE J.* **47**, 1676–1682 (2001).
63. Holden, D., Jelfs, K. E., Cooper, A. I., Trewin, A. & Willock, D. J. Bespoke force field for simulating the molecular dynamics of porous organic cages. *J. Phys. Chem. C* **116**, 16639–16651 (2012).
64. Melchionna, S., Ciccotti, G. & Lee, B. Hoover NPT dynamics for systems varying in shape and size. *Mol. Phys.* **78**, 533–544 (1993).
65. Pranata, J., Wierschke, S. G. & Jorgensen, W. L. OPLS Potential Functions for Nucleotide Bases. Relative Association Constants of Hydrogen-Bonded Base Pairs in Chloroform. *J. Am. Chem. Soc.* **113**, 2810–2819 (1991).
66. Jorgensen, W. L. & Tirado-Rives, J. The OPLS [optimized potentials for liquid simulations] potential functions for proteins, energy minimizations for crystals of cyclic peptides and crambin. *J. Am. Chem. Soc.* **110**, 1657–1666 (1988).
67. Martin, M. G. & Siepmann, J. I. Transferable Potentials for Phase Equilibria. 1. United-Atom Description of n -Alkanes. *J. Phys. Chem. B* **102**, 2569–2577 (1998).
68. Pyzer-Knapp, E. O. *et al.* Predicted crystal energy landscapes of porous organic cages. *Chem. Sci.* **5**, 2235 (2014).
69. Hasell, T. *et al.* Porous organic cages for sulfur hexafluoride separation. *J. Am. Chem. Soc.* (2016). doi:10.1021/jacs.5b11797

70. Jelfs, K. E. *et al.* In silico design of supramolecules from their precursors: Odd-even effects in cage-forming reactions. *J. Am. Chem. Soc.* **135**, 9307–9310 (2013).
71. Sesé, L. M. Feynman-Hibbs potentials and path integrals for quantum Lennard-Jones systems: Theory and Monte Carlo simulations. *Mol. Phys.* **85**, 931–947 (1995).
72. Bondi, A. Van der waals volumes and radii. *J. Phys. Chem.* **68**, 441–451 (1964).
73. Yang, S. *et al.* Understanding the effect of host flexibility on the adsorption of CH₄, CO₂ and SF₆ in porous organic cages. (2019).
74. Getman, R. B., Bae, Y.-S., Wilmer, C. E. & Snurr, R. Q. Review and analysis of molecular simulations of methane, hydrogen, and acetylene storage in metal-organic frameworks. *Chem. Rev.* **112**, 703–23 (2012).
75. Düren, T., Bae, Y.-S. & Snurr, R. Q. Using molecular simulation to characterise metal-organic frameworks for adsorption applications. *Chem. Soc. Rev.* **38**, 1237 (2009).
76. Belosludov, R. V. *et al.* Self-Accelerating CO Sorption in a Soft Nanoporous Crystal. *Science (80-.).* **343**, 167–170 (2013).
77. Warren, J. E. *et al.* Shape selectivity by guest-driven restructuring of a porous material. *Angew. Chemie - Int. Ed.* **53**, 4592–4596 (2014).

Chapter 6

Conclusion

GCMC/MD is an indispensable tool to study and understand gas adsorption and separation in porous molecular crystal. This technique gives the molecular-level insight on the investigation of flexibility effects, which may not easily accessible by experimental method. This thesis proves this hybrid simulation technique is valuable guides and complement to experiments. Throughout this thesis, GCMC/MD simulations have been extensively used to predict gas uptake and structure changes with gas uptakes.

For pure gases CH_4 , CO_2 and SF_6 , chapter 3 shows that the structural flexibility of the porous molecular crystal CC3-R must be taken into account to adequately describe the adsorption of SF_6 and, by analogy, other large guest molecules. Chapter 4 investigated the adsorption of pure linear and branched alkanes with the influence of cage flexibility. For the adsorption of linear alkanes, there is no significant difference between the adsorption quantities computed from rigid and host approaches (nC4 to nC8). or the branched alkanes adsorption, the flexibility shows significant influence on the adsorption capability towards these branched alkanes. For the adsorptions of C6 branched isomers (22dmb-C6 and 23dmb-C6), and C7 isomers (22dmp-C7, 23dmp-C7, 33dmp-C7), decent adsorption quantities were yielded by the flexible host approach, while negligible numbers of adsorbates located in rigid CC3-R. Hence, the flexibility of CC3-R cage is the necessary cause for the adsorption of these long, and high-level branched isomers. Secondly, adsorbates are stronger interacted with flexible host than the rigid host. The interplay between host and guest molecules leads energetically favorable adsorption configuration. Thirdly, the flexibility of cages allows these branched isomers to be adsorbed in interstitial sites for both short or long branched alkanes.

Hence, for both linear and branched alkanes, the flexibility of CC3-R plays a vital role in the adsorption of alkanes, especially for the longer, higher-level branched alkanes. Even for these adsorbates show similar adsorption quantities between flexible and rigid host assumptions, the adsorption behaviours could be entirely different.

Fifth chapter used GCMC/MD simulations to screen PMCs for iodine species capture with four steps methods for the PMCs selection. 1, pore limiting size analysis on the experimental structures to eliminates the PMCs with extremely narrow apertures; 2, Rapid rigid host GCMC simulation to select the promising PMCs; 3, Analyse the PLEs of these selected PMCs to eliminates PMCs with no accessible channel even with interaction of guest molecules; 4, Flexible host GCMC simulation on these promising PMCs to select the PMCs with best capture performance. The rigid host simulation could largely overestimate the capture performance under low concentration of gas, which could compromise the accuracy of the screen result. The pore size and the accessible volume of PMCs are the main factors for the capture performance at low concentration. CC3R, CC3RS are the best I₂ low concentration capture material among our studied range. Flexible host computational studies helped to explain the H₂/D₂ separation performance of the cocrystal of CC3-S and 6ET-RCC3. This model could combine with crystal structure prediction to identify suitable hypothetical systems.

Appendix

A.1. Porous Organic Cages in The Cooper's Group

Mastalerz said “these initial papers were the seeds of a new research topic - porous organic cage compounds - which has flourished ever since”.¹ Till now, Cooper's group has published 56 papers regards the issue of porous organic cages (POCs).²⁻⁵⁷ I will briefly go through these papers in this section.

In 2009, Cooper et al. published the three tetrahedral POCs, CC1, CC2 and CC3, which were synthesised by one-step [4 + 6] imine condensation.⁵⁸ The structures for those three cages are listed in figure S1. All these POCs contains a prefabricated intrinsic cavity and different by the vertices.

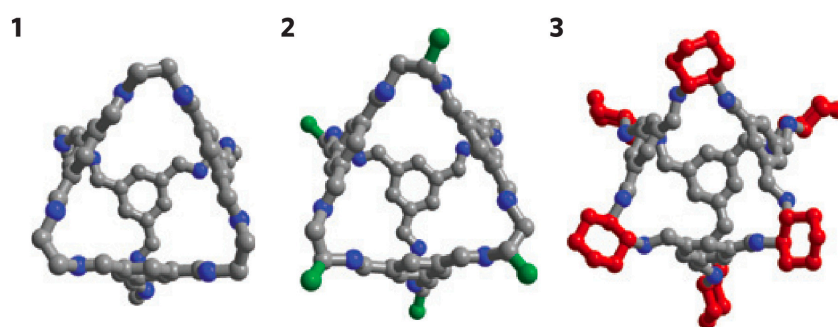


Figure S1. The structures for (1) CC1, (2) CC2, and (3) CC3 that taken from the work of Cooper et al.² Hydrogen atom are omitted for clarity. The methyl and cyclohexyl groups are coloured by green and red.

The different of vertices cause significant symmetry change. CC1 was reported with crystal to crystal transformation and exhibit “on-off porosity” with the induce of guests.³⁶ This cage can be recrystallised to three polymorphic structures $CC1\alpha'$, $CC1\beta'$, and $CC1\gamma'$ (figure S2a). $CC1\alpha'$ is a nonporous phase. The vertices of a cage aim to the window of the adjacent cage, which blocks the channel of diffusion lead to the “off” porosity. $CC1\beta'$ is the porous phase with the selectivity of H_2 towards N_2 , (figure S2b) which may cause by the interconnected 3D channel of $CC1\beta'$. $CC1\alpha'$ and $CC1\beta'$ can be interconverted reversibly. With the trigger of dichloromethane (DCM) or ethyl acetate (EtOAc), $CC1\alpha'$ and $CC1\beta'$ can transform to the other (figure S2a). $CC1\gamma'$ possess a extrinsic 1D channel that branched to each cage cavities, where shows porous to both N_2 and H_2 (figure S2b).

The $CC1\gamma'$ can be produced by the transformation of $CC1\alpha'$ triggered by *ortho*-xylene, and $CC1\gamma'$ can transfer to $CC1\beta'$ by the trigger of DCM.

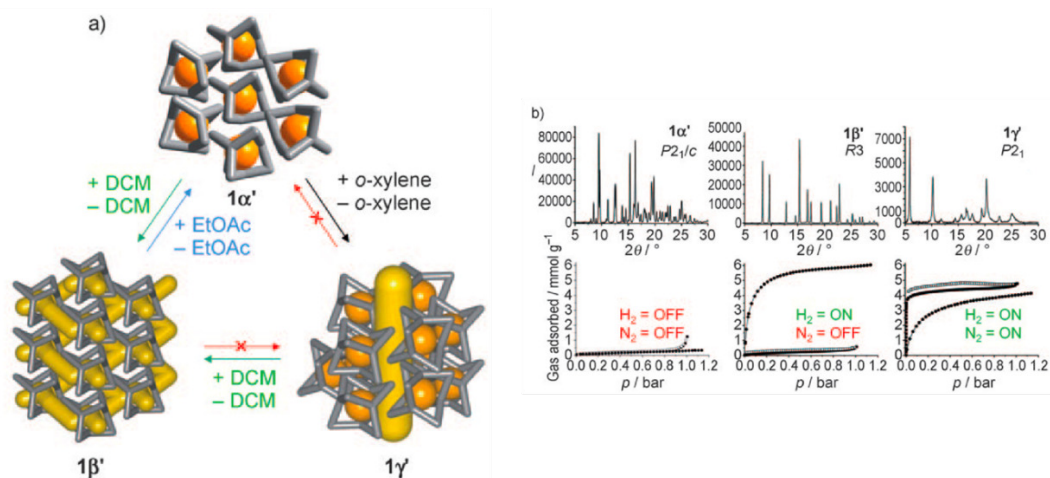


Figure S2. The “on-off” porosity switching scheme (a) and the corresponding powder XRD and H₂, N₂ adsorption isotherm (b) that taken from the work of Cooper et al.³⁶

CC3 is the most well-known cage. It is a chiral molecule that synthesis from the [4 + 6] imine condensation of 1,3,5-triformylbenzene (TFB) with either R, R- or S, S-cyclohexanediamine (CHDA), and result in CC3R or CC3S (figure S3). The CC3 cages contain four windows that packing towards the adjacent cages that leads to the 3D diamondoid pore structure. This 3D pore structure can also be found in the racemate CC3RS, which crystallised from the mixture solution of CC3R and CC3S.⁷ These CC3 materials were easy to prepare and synthesis. Cooper et al. optimised the synthesis procedure and yield in almost 100%.⁴⁷ Cooper et al. reported CC3 with excellent hydrolytic stability, and decent water adsorption capability despite the hydrophobic nature of imine cages.⁸

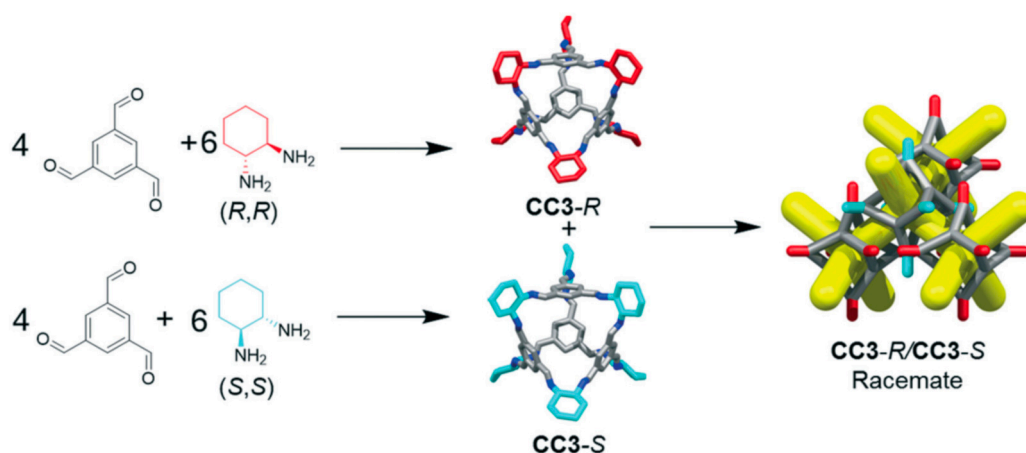


Figure S3. Reaction scheme for the CC3R and CC3S synthesis and the cocrystallized by the mixing of two cages to form CC3RS that taken from the work of Cooper et al.⁴⁶ Hydrogen atom are omitted for the clarity of this figure. The 3D diamondoid porous network is shown in yellow, and cyclohexyl groups were labelled by red (-R) and turquoise (-S).

Later, they presented CC3 and CC4 possess a similar phase transformation property to CC1 with the interaction of the guest molecules.²⁶ CC3 prefer packing in the diamondoid arrangement (figure S4, CC3 α), but with the interaction of Et₂O in the solution of DCM, the CC3 crystalize into its R3 space group (figure S4, CC3 β).

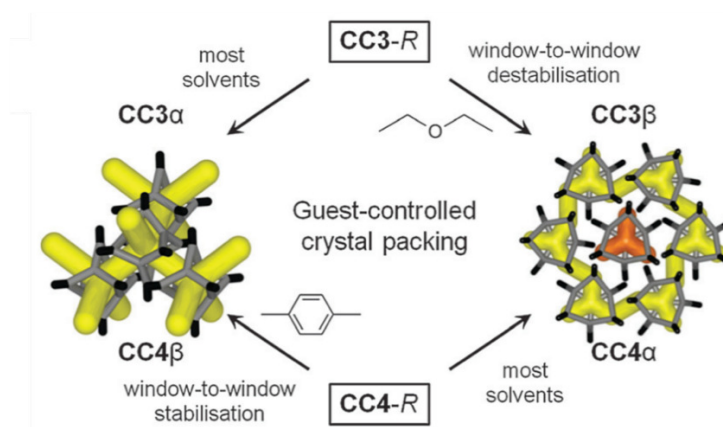


Figure S4. The structure transformation scheme for the CC3 and CC4 with the interaction of guest molecules from the work of Cooper et al.²⁶ The interconnected channel is coloured with the yellow and disconnected channel was coloured by orange.

In 2014, Cooper et al. reported CC3 with unprecedented selectivity of Xe to Kr.²⁷ Other than that, they show the guest molecule can diffuse through the window with even small size in the static view.

Then, they found the CC3 is also suitable for the adsorption of some bigger molecule, such as I₂⁵⁷ and SF₆³⁴, and presented the application in gas chromatography (GC) to coat capillary columns⁵⁹ and molecular sieving membranes³⁵.

Cooper et al. presented CC4 in 2011, where the six members ring in the vertices of CC3 was changed to five members ring.⁵⁶ CC4 is also a [4 + 6] imine condensation produced cage by 1,2-diaminocyclopentane and 1,3,5-triformylbenzene.⁵⁶ CC4 is generally crystallised to trigonal R3 space group but “window to window” packing form by the interaction of *para*-xylene (figure S4).

CC5 is a [4 + 6] imine condensation between tri(4-formylphenyl)amine and the chiral diamine (R,R) or (S,S)-1,2-cyclopentanediamine.⁵⁴ CC5 is significantly larger than the CC1 to CC4, with 3.8 times larger volume of the cage cavity than CC1, with BET surface area of 1333 m²/g.⁵⁴ Later in the same year, Cooper et al. presented two big cages CC7 and CC8.⁶ Both cages were synthesis by [8 + 12] imine condensation with tris(4-formylphenyl)amine (figure S5, **A**) and chiral diamines (R, R)-1,2-cyclohexanediamine (figure S5, **B1**) and (R, R)-1,2-cyclohex-4-enedia-mine (figure S5, **B2**) with the yield of 85 to 90 %.⁶ CC7 and CC8 possess the intrinsic cavity with a diameter of 1.2 nm, but activation leads to the amorphous crystal structure.⁶

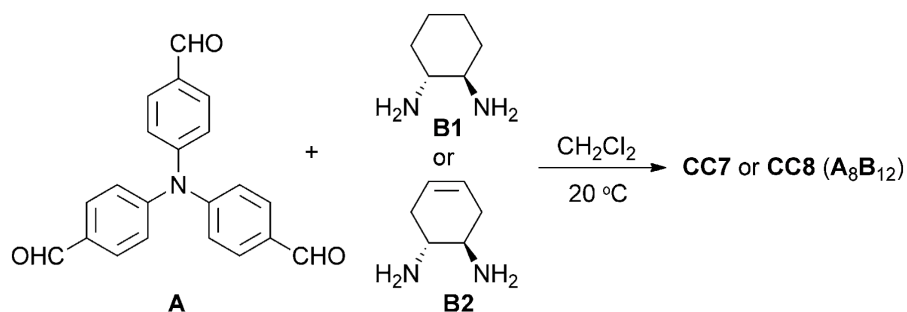


Figure S5. The scheme for the synthesis of CC7 (**A** + **B1**) and CC8 (**A** + **B2**) from the work of Cooper et al.⁶

CC6 is a [2 + 3] cage synthesis by imine condensation with tri(4-formylphenyl)benzene and 1,5-pentane-diamine. CC6 possess an extrinsic 1D channel that allows the diffusion of gases, and this cage shows the capability to select H₂ and CO₂ over N₂.⁵⁵

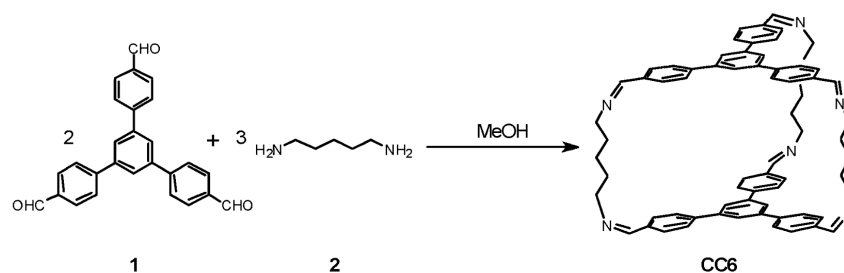


Figure S6. The synthesis scheme of the [2 + 3] CC6 from the work of Cooper et al.⁵⁵

Modification of vertices is a way to control the crystal packing and the porous network as presented above. Cooper et al. reported the CC9 and CC10 with bulky aryl groups decorated vertices.⁴ CC9 and CC10 were synthesized by the [4 + 6] imine condensation with 1,3,5-triformylbenzene and (R, R)-1,2-diphenylethylenediamine (CC9) and (R, R)-1,2-bis(4-fluorophenyl)ethane-1,2-diamine (CC10). (figure S7)⁴ CC9 shows the crystal structure transformation while crystallised from the mixture of DCM with acetone leads to the P3 space group, and chloroform leads to R3 space group, which results in different BET surface area (P3, 501 m²/g; R3, 460 m²/g). CC9 (R3) and CC10 were reported with adsorption capacity to the N₂ of 7.5 mmol/g at 77 K, while CC9 (P3) double that to 14.3 mmol/g.⁴

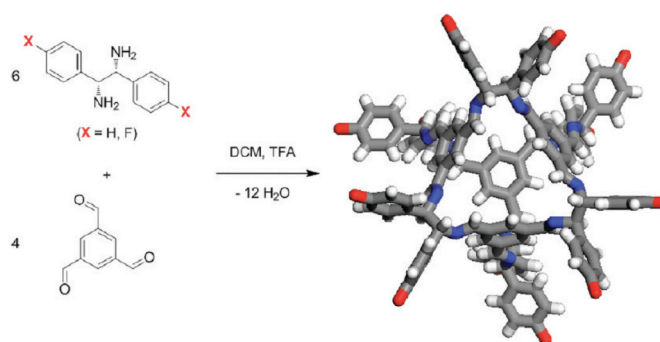


Figure S7. The synthesis scheme for CC9 and CC10 that taken from the work of Cooper et al.⁴ The red X (left) and sticks (right) are referred to the element of H and F, CC9 and CC10 respectively.

In 2013, Cooper et al. modified the structure of CC1 to synthesis a several dodecaamide cages.¹⁸ First, CC1 was reduced from imine cage to corresponding amine cage RCC1. (figure S8 left to medium) Then, decorate the vertices of RCC1 with 4-bromobenzoyl chloride, 2-naphthoyl chloride, 1-adamantanecarbonyl chloride, and 2-bromoisobutyryl bromide to give RCC1a, RCC1b, RCC1c

and RCC1d respectively (figure S9). However, no porosity was found after desolvation.

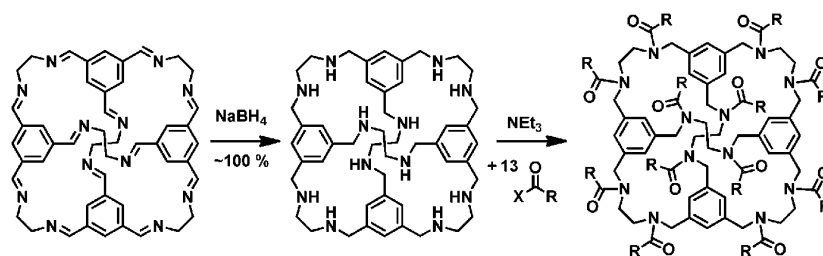


Figure S8. the synthesis scheme of dodecaamide cages from CC1 to RCC1 from the work of Cooper et al.¹⁸

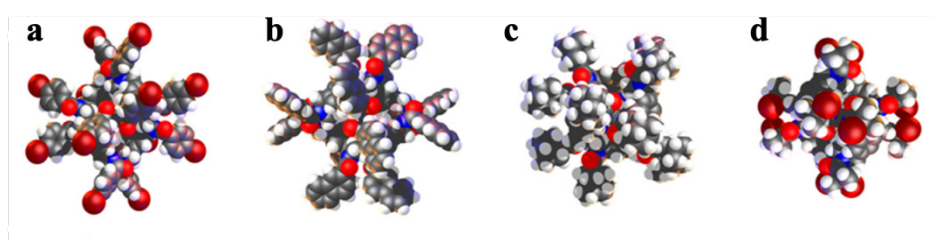


Figure S9. Structure of RCC1a (a), RCC1b (b), RCC1c (c), RCC1d (d) that taken from the work of Cooper et al.¹⁸

Later in 2014, Cooper et al. further explored the reduction of imine cages and presented another two amine cages.²² Similar to RCC1, CC3 was first reduced to amine cage RCC3, but this amine cannot maintain its tetrahedral shape after desolvation.²² As one of the diamine was replaced by acetone, the acetone tied RCC3, AT-RCC3. AT-RCC3 crystallises into the same space group, $F4_132$, to the CC3, and packs window-to-window.²² AT-RCC3 is capable of adsorbing 1.11 mmol/g N_2 or 1.29 mmol/g H_2 at 77 K with BET surface area of 67 m^2/g . Other than AT-RCC3, They presented FT-RCC3.²² As the smallest carbonyl molecule, formaldehyde is the excellent candidate for the “tie”. The six diamine vertices in the RCC3 were tied by formaldehyde. FT-RCC3 remains the tetrahedral symmetry and crystallises in $F4_132$ space group, and shows excellent chemical stability toward water and acids and bases.²² FT-RCC3 presented high N_2 adsorption capacity of 11.2 mmol/g with BET surface area of 377 m^2/g .²²

Recent, Cooper et al. presented a POCs discovery workflow by combining both computation and robotic synthesis method and formed 33 cages.⁵³ The broad range of aldehydes (1-26) and amines

(A-C) that used robotic synthesis to form three topology Tri^2Di^3 , Tri^4Di^6 and Tri^4Tri^4 . The Tri refers to tri-topic and Di is di-topic precursors incorporated to cages. 78 cages were investigated where 33 cages were synthesised cleanly. These cages were be studied in fifth chapter of this thesis.

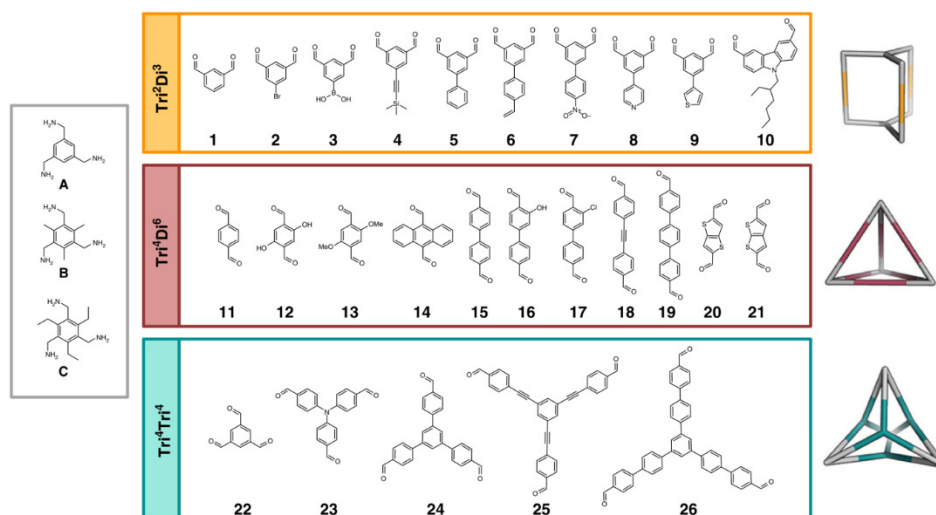


Figure S10. The cage precursors, target topologies that are taken from the work of Cooper's work.⁵³ three triamines (A-C) and aldehydes to target Tri^2Di^3 , Tri^4Di^6 and Tri^4Tri^4 cages were collected above.

Table S2. Angle bending potentials of CSFF in this work.¹²

Angles			θ_0 (°)	k_2 (K)	k_3 (K)	k_4 (K)
$E_{bend} = k_2(\theta - \theta_0)^2 + k_3(\theta - \theta_0)^3 + k_4(\theta - \theta_0)^4$						
H5	C5	H5	107.66	19948.46	-6502.21	-1223.75
H6	C6	H6	107.66	19948.46	-6502.21	-1223.75
C2	C1	H1	117.94	17691.38	-6274.35	0.00
H4	C4	C5	109.77	18847.40	-5336.23	2581.06
H4	C4	C4	109.77	18847.40	-5336.23	2581.06
C4	C5	H5	109.77	18847.40	-5336.23	2581.06
H5	C5	C6	109.77	18847.40	-5336.23	2581.06
C5	C6	H6	109.77	18847.40	-5336.23	2581.06
C6	C6	H6	109.77	18847.40	-5336.23	2581.06
C2	C3	H3	117.41	15853.64	-5594.59	-5242.13
N1	C3	H3	122.00	17109.75	-4529.05	-7548.42
N1	C4	H4	109.70	18128.64	504.84	0.00
C4	C5	C6	112.67	19885.56	-3745.53	-4810.00
C4	C4	C5	112.67	19885.56	-3745.53	-4810.00
C6	C6	C5	112.67	19885.56	-3745.53	-4810.00
C1	C2	C1	119.90	31211.51	-499.76	0.00
C3	C2	C1	115.42	18685.41	327.60	664.26
N1	C3	C2	123.67	28684.00	-10440.37	19267.24
C3	N1	C4	110.50	29136.90	-33716.33	26016.94
C2	C1	C2	119.90	31211.51	-499.76	0.00
N1	C4	C5	110.00	26894.06	-29690.45	0.00
C4	C4	N1	110.00	26894.06	-29690.45	0.00

Table S3. Torsion potentials of CSFF in this work.¹²

torsional angle				V ₁	V ₂	V ₃
$V(\phi) = \sum_3^{n=1} \frac{v_n}{2} [1 - \cos(n\phi - \delta_n)]$						
C3	N1	C4	C5	201.29	10.06	50.32
C3	N1	C4	C4	201.29	10.06	50.32
N1	C4	C5	C6	24.46	18.17	-64.94
C4	C4	C5	C6	0.00	12.93	-35.98
N1	C4	C4	N1	127.59	59.10	-59.10
C5	C4	C4	N1	24.46	18.17	-64.94
C5	C4	C4	C5	0.00	12.93	-35.98
C4	C5	C6	C6	0.00	12.93	-35.98
C5	C6	C6	C5	0.00	12.93	-35.98
C3	N1	C4	H4	359.81	-281.81	217.12
N1	C4	C5	H5	-5.74	7.05	-46.88
H4	C4	C5	H5	-111.52	-65.85	-32.28
H4	C4	C5	C6	0.00	7.95	-42.30
C4	C4	C5	H5	0.00	7.95	-42.30
H4	C4	C4	N1	-5.74	7.05	-46.88
H4	C4	C4	H4	-111.52	-65.85	-32.28
C5	C4	C4	H4	0.00	7.95	-42.30
C4	C5	C6	H6	0.00	7.95	-42.30
H5	C5	C6	H6	-111.52	-65.85	-32.28
H5	C5	C6	C6	0.00	7.95	-42.30
H6	C6	C6	C5	0.00	7.95	-42.30
H6	C6	C6	H6	-111.52	-65.85	-32.28
C1	C2	C3	H3	251.61	279.22	0.00
C1	C2	C3	N1	0.00	251.61	0.00
C1	C2	C1	H1	-1761.30	519.86	0.00
C1	C2	C1	C2	2105.18	1055.07	0.00
C3	C2	C1	H1	1761.30	630.85	0.00
C3	C2	C1	C2	-754.84	832.14	244.07
C4	N1	C3	H3	754.84	1383.88	100.65
C4	N1	C3	C2	-251.61	1987.75	-201.29

Table S4. Non-bonded potential parameters for CC3-R from CSFF,¹² DREIDING,⁶⁰ OPLS,⁶¹ and UFF⁶².

atoms	CSFF		OPLS		DREIDING		UFF		charge (e)
	ϵ (K)	σ (Å)							
C1	32.21	4.01	35.25	3.55	47.88	3.47	52.87	3.43	-0.1268
C2	32.21	4.01	35.25	3.55	47.88	3.47	52.87	3.43	0.0000
C3	32.21	4.01	52.84	3.75	47.88	3.47	52.87	3.43	0.1732
C4	27.17	4.01	33.23	3.50	47.88	3.47	52.87	3.43	0.2470
C5	27.17	4.01	33.23	3.50	47.88	3.47	52.87	3.43	-0.1060
C6	27.17	4.01	33.23	3.50	47.88	3.47	52.87	3.43	-0.1060
H1	10.06	3.00	15.11	2.42	7.65	2.85	22.16	2.57	0.1268
H3	10.06	3.00	15.11	2.42	7.65	2.85	22.16	2.57	0.1268
H4	10.06	3.00	7.55	2.50	7.65	2.85	22.16	2.57	0.0530
H5	10.06	3.00	15.11	2.50	7.65	2.85	22.16	2.57	0.0530
H6	10.06	3.00	15.11	2.50	7.65	2.85	22.16	2.57	0.0530
N1	40.26	3.80	85.60	3.25	38.97	3.26	34.74	3.26	-0.6000

A.3. Cage special force field validation

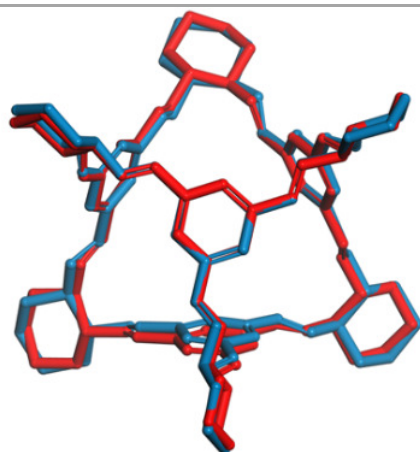
Table S5. Cell lengths comparison between generic force fields minimized structures and experimental structure.

Cages	Cell length (Å)					
	experiment ²	OPLS ^[b]	CSFF ^[b]	PCFF ^[c]	UFF ^[c]	DREIDING ^[c]
CC1($a = b \neq c$) ^[a]	21.22/21.16	21.68/21.62	21.48/21.43	21.20/21.56	21.35/20.87	21.50/21.03
CC3($a = b = c$)	24.80	25.14	24.76	25.41	25.42	25.64

[a] the cell lengths of CC1 obey the rule of $a = b \neq c$, the lengths of a and c are listed due to the isotropic change of optimization. [b] baker minimization by the RASPA software package.⁶³ [c] Geometry optimization by the Forcite module build in Materials Studio 7.0.⁶⁴

Table S6. Comparison of Bond lengths and bend angles between the CSFF-optimized CC3-R cage with experimental cage structure.

bond ^[a]	bond length [Å]		deviation	angle	bend angle [°]		deviation
	exp.	sim.			exp.	sim.	
C1C2	1.38	1.395	1.09%	C1 C2 C1	118.62	120.01	1.17%
C2C3	1.461	1.468	0.48%	C2 C1 C2	121.38	120.05	1.09%
C4C4	1.505	1.573	4.52%	C2 C1 H1	119.35	120.05	0.58%
C4C5	1.516	1.549	2.18%	C2 C3 H3	117.98	114.32	3.11%
C4N1	1.447	1.457	0.69%	C3 C2 C1	119.70	120.19	0.41%
C5C6	1.525	1.545	1.31%	C3 N1 C4	119.07	118.47	0.51%
C6C6	1.491	1.54	3.29%	C4 C4 C5	110.37	111.81	1.30%
N1C3	1.232	1.278	3.73%	C4 C4 N1	109.20	111.79	2.37%
C1H1	0.928	1.08	16.38%	C4 C5 C6	110.24	111.05	0.74%
C3H3	0.931	1.103	18.47%	C4 C5 H5	109.63	109.30	0.30%
C4H4	0.98	1.104	12.65%	C5 C6 H6	109.91	109.73	0.16%
C5H5	0.97	1.102	13.61%	C6 C6 C5	108.74	112.15	3.14%
C6H6	0.969	1.101	13.62%	C6 C6 H6	109.99	110.24	0.23%
				H4 C4 C4	109.64	107.62	1.84%
				H4 C4 C5	109.60	107.61	1.82%
				H5 C5 C6	109.53	109.93	0.36%
				H5 C5 H5	108.09	106.55	1.43%
				H6 C6 H6	108.30	107.27	0.95%
				N1 C3 C2	123.71	123.63	0.07%
				N1 C3 H3	118.31	112.43	4.97%
				N1 C4 C5	108.50	106.79	1.58%
				N1 C4 H4	109.51	111.10	1.45%



[a] Atom-type definitions used in the table are given in the figure inset (only a fraction of the cage molecule is shown): carbon, grey; nitrogen, blue; hydrogen, white. Overlay of CSFF-optimized (blue) and experimental (red) structures of the CC3-R molecule; hydrogen atoms were omitted for clarity.

A.4. Force fields validation for alkane adsorptions

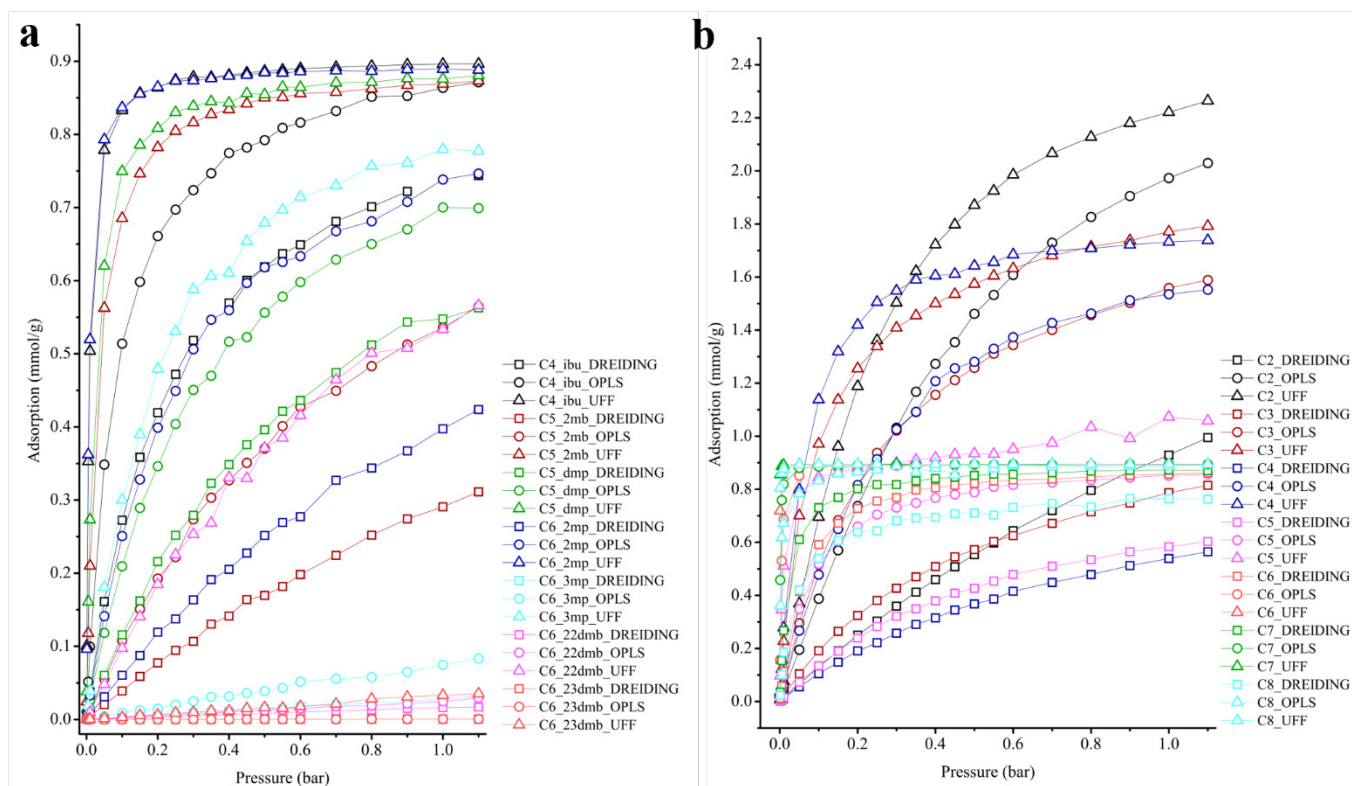


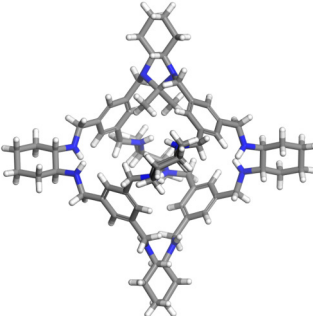
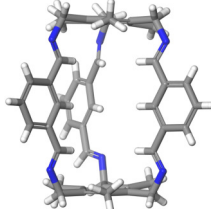
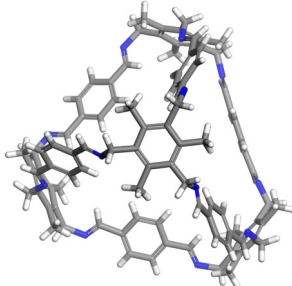
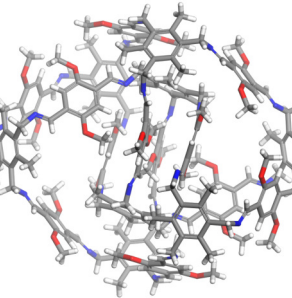
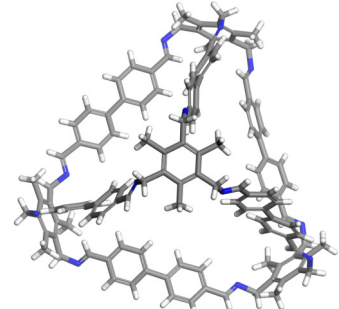
Figure S12. The adsorption isotherms for both linear (a) and branched (b) alkanes with rigid host assumption with DREIDING,⁶⁰ (black) OPLS,⁶¹ (sphere) and UFF⁶² (triangle).

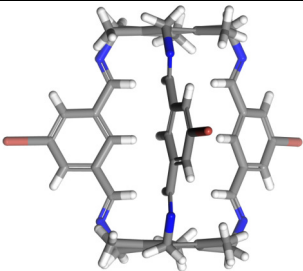
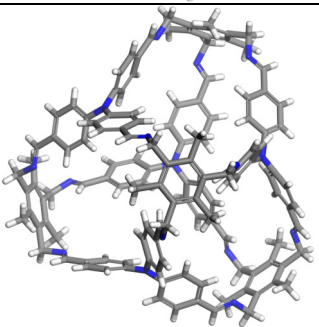
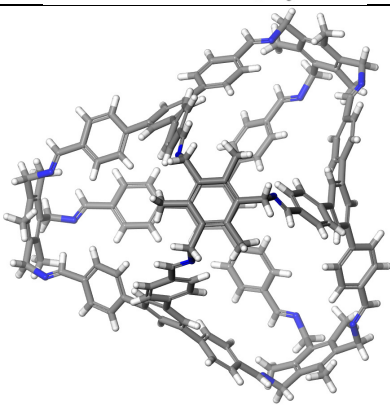
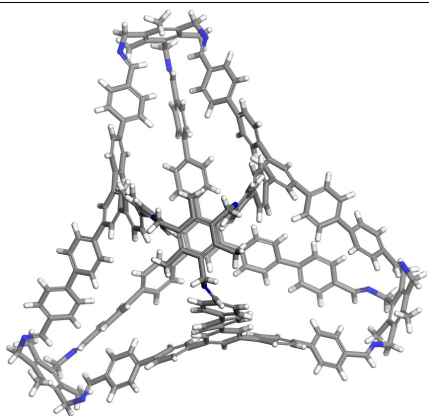
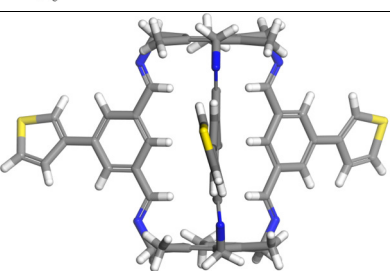
Table S7. The cell volume change from the production cycles at 433 K, 1 bar. These cell volumes were averaged from 500,000 cycles of production simulation.

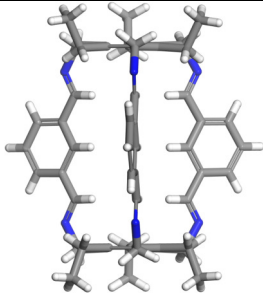
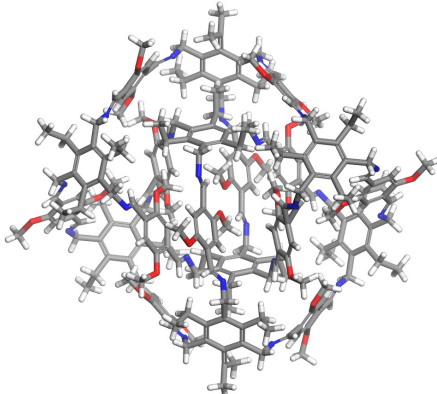
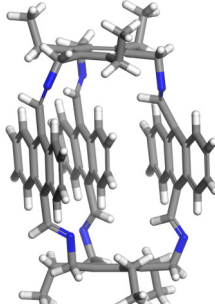
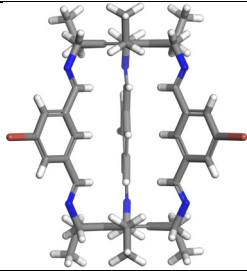
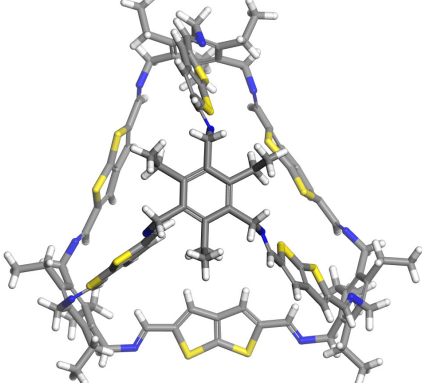
Production run	C4	C5	C6	C7	C8
Average volume (\AA^3)	16239	16237	16299	16350	16367
Standard deviation (\AA^3)	137.05	134.90	148.42	149.47	137.42
ratio	0.84 %	0.83 %	0.91 %	0.91 %	0.84 %

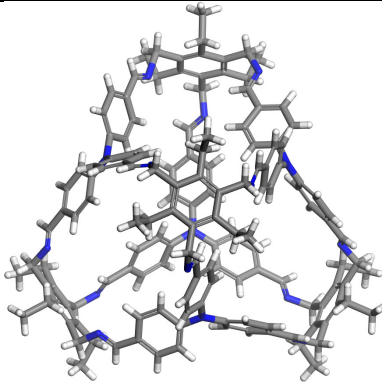
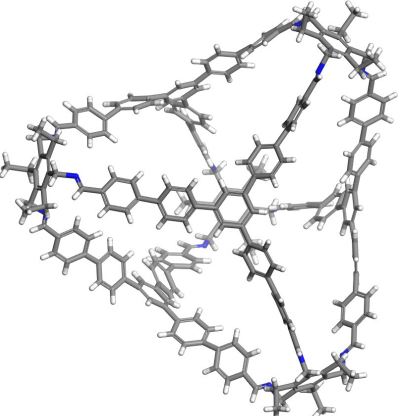
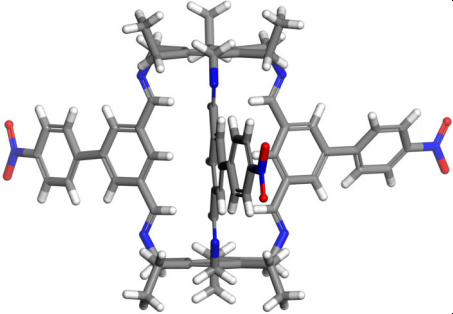
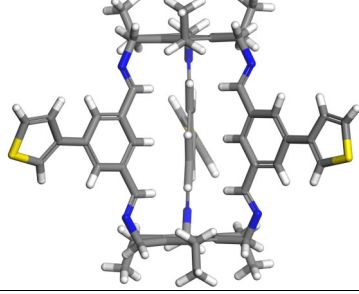
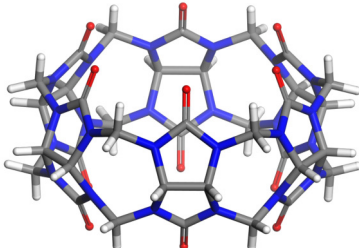
A.5. PMCs molecular units Database

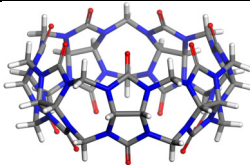
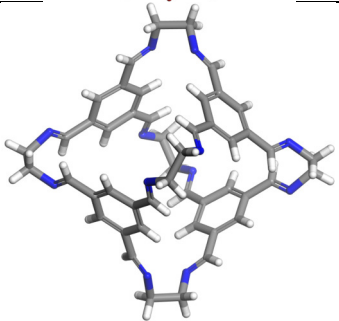
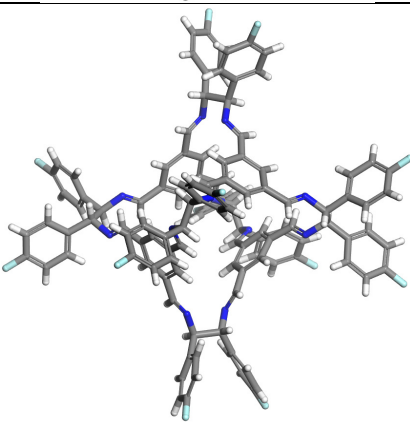
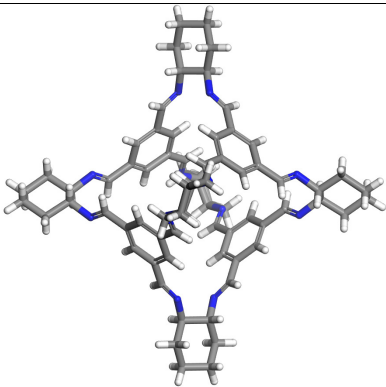
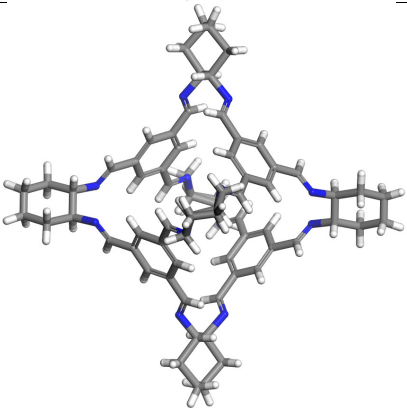
Table S8: A List of porous organic molecules in this study.

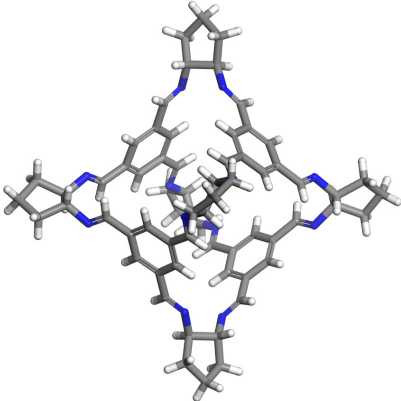
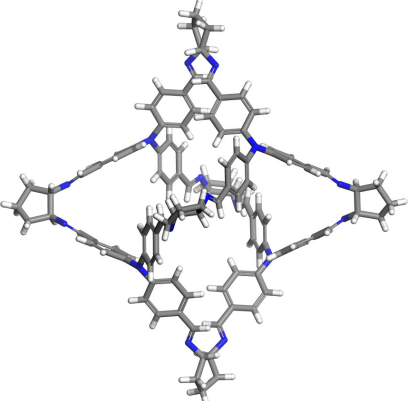
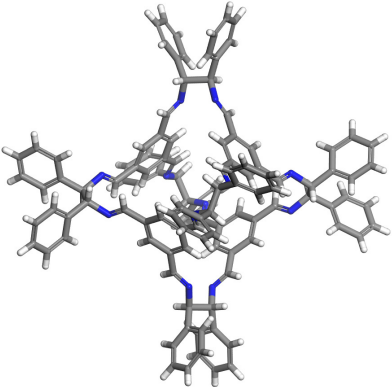
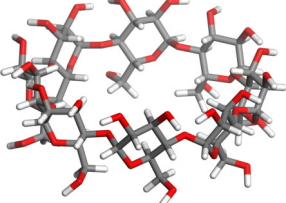
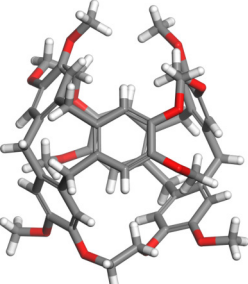
<i>Materials Name</i>	<i>super cells</i>	<i>cell angles (α, β, γ, [°])</i>	<i>super cell size (a, b, c, [Å])</i>	<i>images</i>	<i>reference no.</i>
IAT-RCC3	1, 1, 1	90, 90, 90	25.456, 25.456, 25.456		22
B1	3, 2, 2	73.955, 70.599, 88.033	35.7747, 28.3304, 29.1052		
B11	2, 2, 1	90, 90, 90	36.9996, 36.9996, 37.5158		
B11_P-3	2, 2, 4	90, 90, 120	39.0208, 39.0208, 56.4624		53
B13	2, 2, 2	112.027, 112.92, 95.17	35.048, 39.362, 43.896		
B15_CH2Cl 2	2, 2, 2	103.931, 93.49, 114.824	37.6468, 41.6838, 44.8108		
B15_CHCl3	2, 2, 4	90, 90, 120	45.9078, 45.9078, 65.8028		

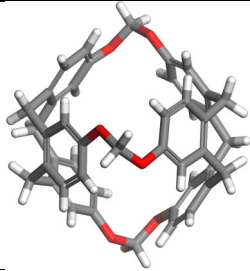
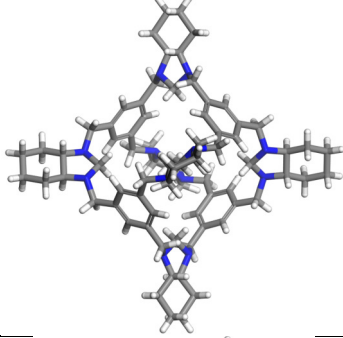
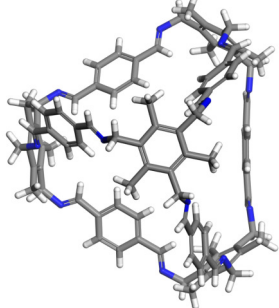
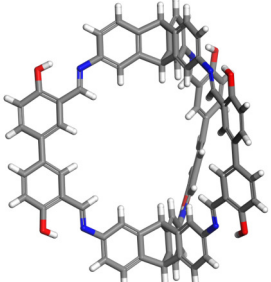
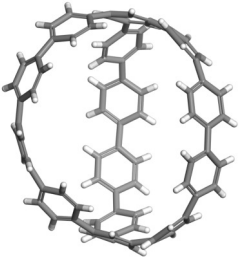
<i>Materials Name</i>	<i>super cells</i>	<i>cell angles</i> (α, β, γ , [$^\circ$])	<i>supercel l size</i> (a, b, c , [\AA])	<i>image</i>	<i>referenc e no.</i>
B2	2, 2, 2	90, 90, 120	32.3714, 32.3714, 33.2208		
B23	2, 2, 1	94.735, 102.18, 109.008	31.978, 34.944, 31.697		
B24	1, 1, 1	90, 102.385, 90	33.688, 33.545, 33.801		53
B26	1, 2, 1	90, 115.819, 90	42.199, 48.536, 40.276		
B9	2, 2, 2	94.0179, 92.5322, 91.79	24.7886, 24.9704, 36.5132		

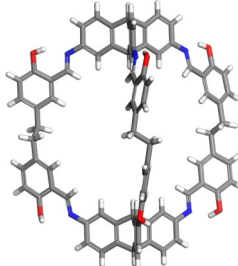
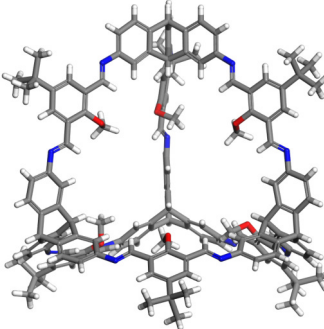
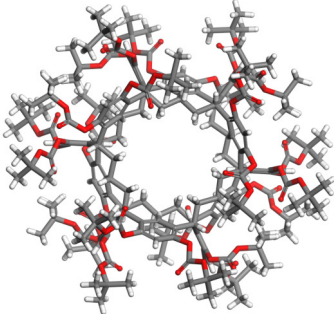
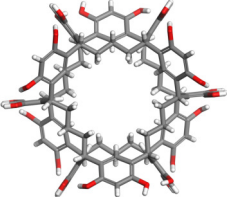
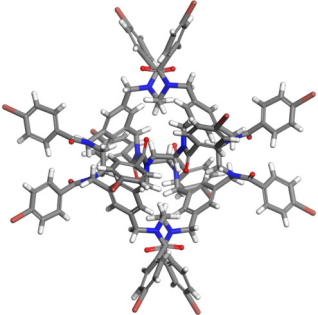
<i>Materials Name</i>	<i>super cells</i>	<i>cell angles</i> (α, β, γ , [$^\circ$])	<i>supercel l size</i> (a, b, c , [\AA])	<i>image</i>	<i>referenc e no.</i>
C1	4, 2, 4	60.8167, 81.767, 76.8256	60.0096, 30.546, 61.1116		
C13	2, 2, 2	109.669, 95.102, 104.266	36.156, 37.264, 40.564		
C14	3, 3, 3	75.682, 81.032, 72.388	39.6699, 40.1814, 59.4873		53
C2	3, 3, 2	117.2705, 104.1249, 93.9722	41.9679, 45.1386, 32.3588		
C21_Tri2Di3	2, 4, 2	87.075, 68.588, 82.365	25.8002, 51.9952, 34.3932		
C21_Tri4Di6	2, 1, 1	90, 95.934, 90	37.552, 31.091, 26.235		

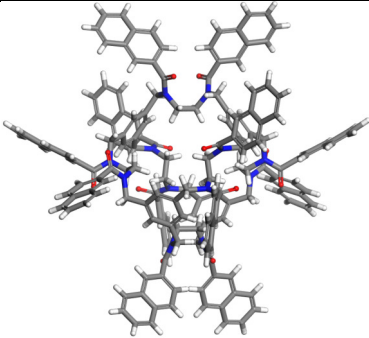
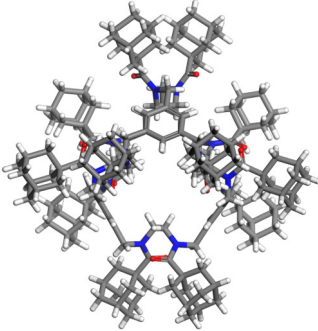
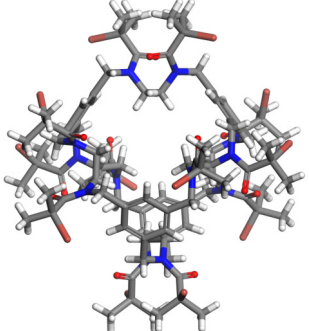
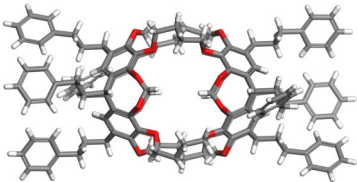
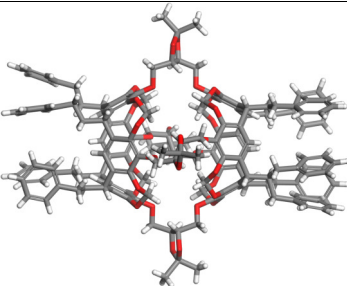
<i>Materials Name</i>	<i>super cells</i>	<i>cell angles</i> (α, β, γ , [$^\circ$])	<i>supercel l size</i> (a, b, c , [\AA])	<i>image</i>	<i>referenc e no.</i>
C23	1, 2, 1	90, 98.7932, 90	26.591, 32.7348, 39.525		
C26	1, 1, 2	90, 90, 90	41.493, 41.493, 40.826		53
C7	2, 2, 1	90, 109.508, 90	43.072, 30.294, 27.037		
C9	2, 2, 2	100.2965 98.7148, 113.347	27.2232, 31.7366, 40.7598		
CB6	2, 2, 2	90, 90, 90	39.1484, 31.6096, 31.6804		65

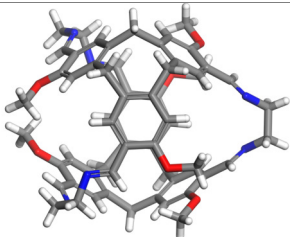
<i>Materials Name</i>	<i>super cells</i>	<i>cell angles</i> (α, β, γ , [$^\circ$])	<i>supercel l size</i> (a, b, c , [\AA])	<i>image</i>	<i>referenc e no.</i>
CB7	1, 1, 2	90, 90, 120	32.3851, 32.3851, 72.27		66, 67
CC1	2, 3, 1	90, 97.49, 90	25.62, 32.73, 36.81		58
CC10	1, 1, 2	90, 90, 120	30.128, 30.128, 41.492		4
CC3R	1, 1, 1	90, 90, 90	24.8, 24.8, 24.8		58, 68
CC3RS	2, 2, 2	90, 90, 90	49.1754, 49.1754, 49.1754		7

<i>Materials Name</i>	<i>super cells</i>	<i>cell angles</i> (α, β, γ , [$^\circ$])	<i>supercel l size</i> (a, b, c , [\AA])	<i>image</i>	<i>referenc e no.</i>
CC4	1, 1, 3	90, 90, 120	24.073, 24.073, 65.826		56
CC5	1, 1, 1	90, 90, 90	30.115, 30.115, 30.115		69
CC9	3, 2, 2	90, 90, 120	40.8348, 31.7366, 40.7598		4
CD3	2, 2, 2	90, 90, 90	47.616, 47.616, 46.28		70, 71
CP1	2, 6, 2	90, 117.599, 90	44.098, 68.4654, 41.5604		72, 73

<i>Materials Name</i>	<i>super cells</i>	<i>cell angles</i> (α, β, γ , [$^{\circ}$])	<i>supercel l size</i> (a, b, c , [\AA])	<i>image</i>	<i>referenc e no.</i>
CP3	2, 2, 2	90, 93.076, 90	24.154, 38.3206, 30.6116		72, 74
CP5	3, 1, 3	90, 94.216, 90	32.5773, 30.5071, 33.2421		72, 75
FTRCC3	1, 1, 1	90, 90, 90	25.316, 25.316, 25.316		22
HC1	2, 2, 1	90, 90, 120	35.166, 35.166, 48.345		76
MC3	2, 2, 2	94.648, 116.848, 110.901	43.9802, 44.6398, 47.6008		78
IC2	2, 2, 1	90, 90, 90	31.314, 40.068, 26.302		77

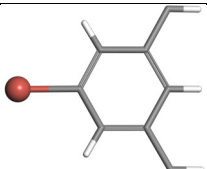
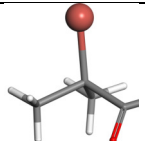
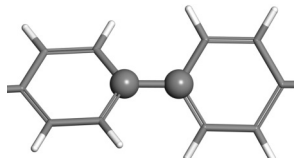
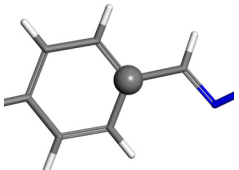
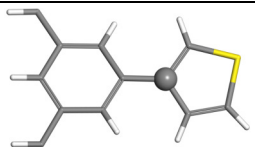
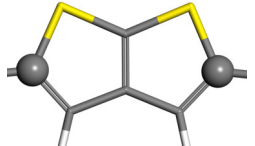
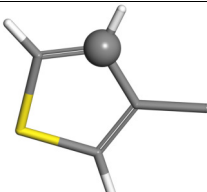
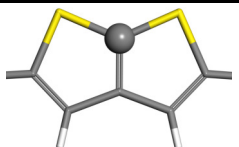
<i>Materials Name</i>	<i>super cells</i>	<i>cell angles</i> (α, β, γ , [$^{\circ}$])	<i>super cell size</i> (a, b, c , [\AA])	<i>image</i>	<i>reference no.</i>
MC4	2, 2, 1	90, 90, 120	38.258, 38.258, 50.923		78
MC5	1, 1, 2	90, 90, 120	30.374, 30.374, 51.702		79
MC7	1, 2, 2	90, 90.698, 90	26.9032, 32.7398, 38.3054		80
NC1	2, 2, 2	107.992, 106.857, 94.7	34.8326, 39.1786, 40.0126		81
NC2	2, 3, 3	99.509, 111.21, 100.259	30.338, 46.911, 56.514		81, 82
RCC1a	2, 2, 2	90, 90, 90	39.4538, 39.4538, 39.4538		18

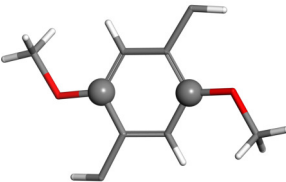
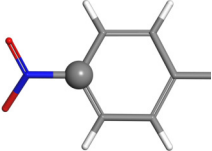
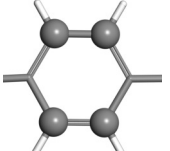
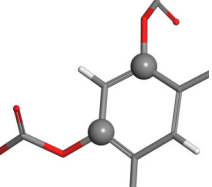
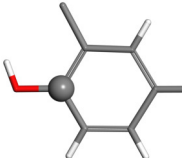
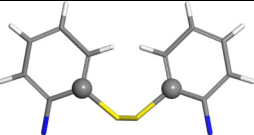
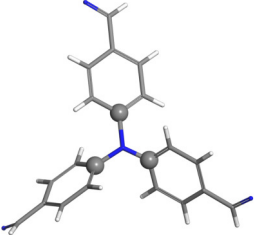
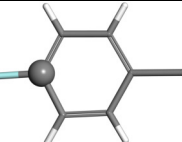
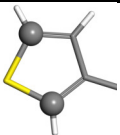
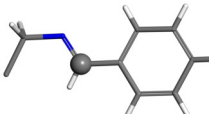
<i>Materials Name</i>	<i>super cells</i>	<i>cell angles</i> (α, β, γ , [$^{\circ}$])	<i>supercel l size</i> (a, b, c , [\AA])	<i>image</i>	<i>referenc e no.</i>
RCC1b	2, 2, 2	90, 90, 90	40.6578, 40.6578, 40.6578		18
RCC1c	1, 1, 1	90, 90, 90	33.479, 33.479, 42.914		18
RCC1d	2, 2, 2	90, 90, 90	40.6602, 40.6602, 40.6602		18
WC2	2, 2, 2	90, 99.53, 90	33.472, 40.958, 40.276		83
WC3	2, 2, 1	90, 107.2, 90	35.4966, 39.085, 26.231		84

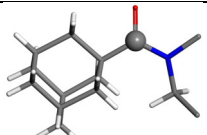
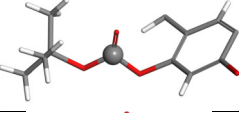
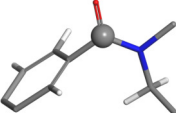
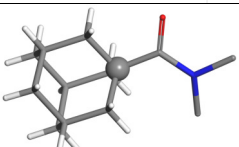
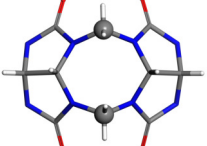
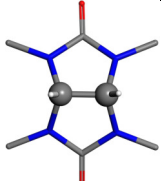
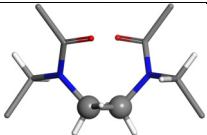
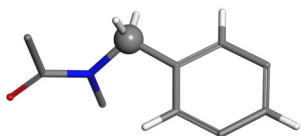
WC4	2, 2, 2	90, 90, 90	32.4146, 32.4146, 46.9514		S ⁸⁵
-----	---------	------------------	---------------------------------	--	-----------------

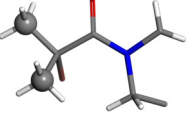
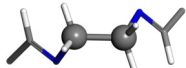
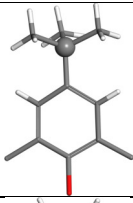
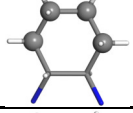
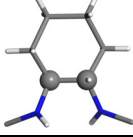
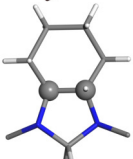
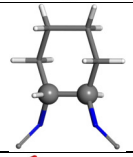
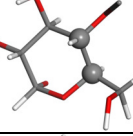
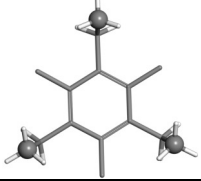
A.6 OPLS nonbonding parameters

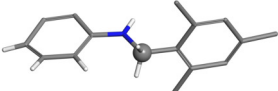
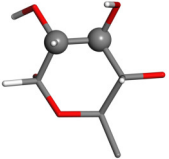
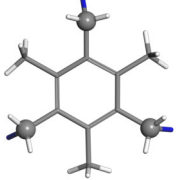
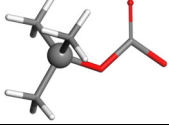
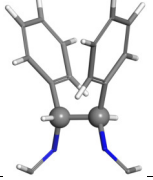
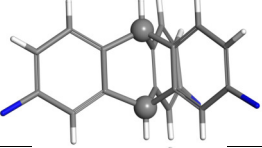
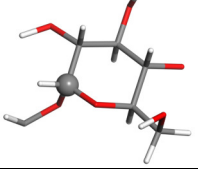
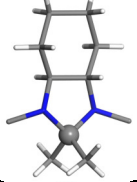
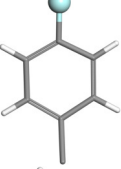
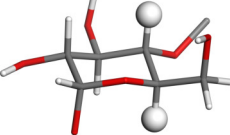
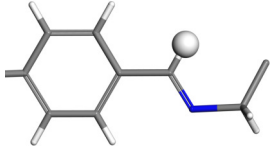
Table S9: OPLS nonbonding forcefield for porous organic molecules in this study.⁸⁶⁻⁹¹

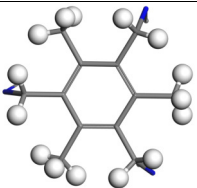
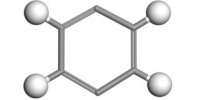
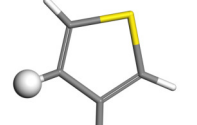
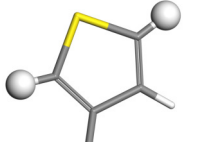
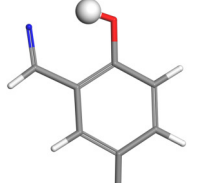
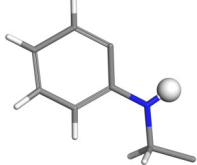
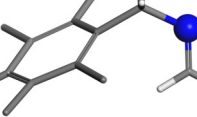
<i>Atom types</i>	<i>images</i>	ϵ/k_b [K]	σ [Å]	<i>Charge (e)</i>
Br		236.514677	3.47	-0.2
Br		236.514677	3.47	-0.204
C2		35.2255902	3.55	0
C2		35.2255902	3.55	0.004
C2		35.2255902	3.55	0.047
C2		35.2255902	3.55	-0.064
C2		35.2255902	3.55	-0.074
C2		35.2255902	3.55	0.079
C2		35.2255902	3.55	-0.08

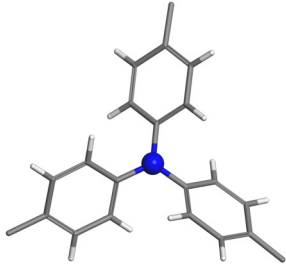
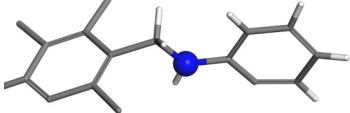
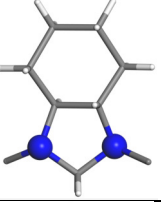
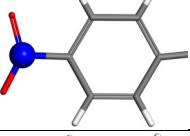
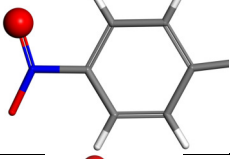
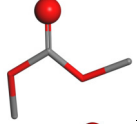
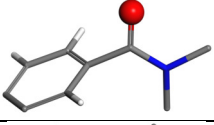
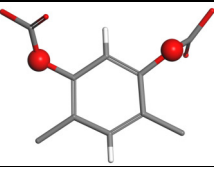
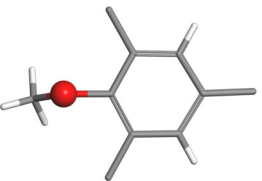
<i>Atom types</i>	<i>images</i>	ϵ/k_b [K]	σ [Å]	<i>Charge (e)</i>
C2		35.2255902	3.55	0.085
C2		35.2255902	3.55	0.09
C2		35.2255902	3.55	-0.115
C2		35.2255902	3.55	0.135
C2		35.2255902	3.55	0.15
C2		35.2255902	3.55	0.153
C2		35.2255902	3.55	0.21
C2		35.2255902	3.55	0.22
C2		35.2255902	3.55	-0.326
C2		35.2255902	3.55	0.345
C2		35.2255902	3.55	0.35

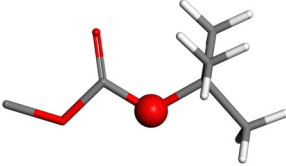
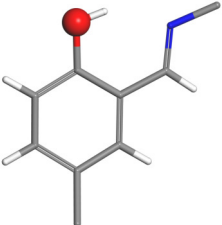
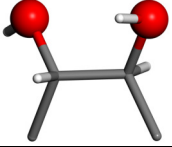
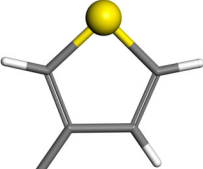
<i>Atom types</i>	<i>images</i>	ϵ/k_b [K]	σ [Å]	<i>Charge (e)</i>
C2		52.8383853	3.75	0.5
C2		52.8383853	3.75	0.59
C2		52.8383853	3.75	0.615
C2		52.8383853	3.75	0.861
C3		40.2578174	3.85	0
C3		33.2126993	3.5	-0.005
C3		33.2126993	3.5	-0.017
C3		33.2126993	3.5	-0.021
C3		33.2126993	3.5	0.039
C3		33.2126993	3.5	-0.05
C3		33.2126993	3.5	-0.06
C3		33.2126993	3.5	0.065

<i>Atom types</i>	<i>images</i>	ϵ/k_b [K]	σ [Å]	<i>Charge (e)</i>
C3		33.2126993	3.5	-0.065
C3		33.2126993	3.5	-0.069
C3		33.2126993	3.3	0.1
C3		33.2126993	3.5	0.11
C3		33.2126993	3.5	0.115
C3		33.2126993	3.5	-0.12
C3		33.2126993	3.5	0.14
C3		33.2126993	3.5	0.145
C3		33.2126993	3.5	0.15
C3		33.2126993	3.5	0.16
C3		33.2126993	3.5	0.17
C3		33.2126993	3.5	-0.18

<i>Atom types</i>	<i>images</i>	ϵ/k_b [K]	σ [Å]	<i>Charge (e)</i>
C3		33.2126993	3.5	0.195
C3		33.2126993	3.5	0.205
C3		33.2126993	3.5	0.215
C3		33.2126993	3.5	0.25
C3		33.2126993	3.5	0.275
C3		85.5478619	3.8	0.285
C3		33.2126993	3.5	0.3
C3		40.2578174	3.8	0.42
F0		30.6965857	2.94	-0.22
H1		15.0966815	2.5	0.03
H1		15.0966815	2.5	0.04

<i>Atom types</i>	<i>images</i>	ϵ/k_b [K]	σ [Å]	<i>Charge (e)</i>
H1		15.0966815	2.5	0.06
H1		15.0966815	2.5	0.1
H1		15.0966815	2.42	0.115
H1		15.0966815	2.42	0.121
H1		15.0966815	2.42	0.262
H2		0	0	0.418
H2		0	0	0.435
H3		0	0	0.38
N2		85.5478619	3.25	-0.14
N2		85.5478619	3.25	-0.222
N2		85.5478619	3.25	-0.468
N2		85.5478619	3.25	-0.61

<i>Atom types</i>	<i>images</i>	ϵ/k_b [K]	σ [Å]	<i>Charge (e)</i>
N2		85.5478619	3.3	-0.63
N2		85.5478619	3.3	-0.78
N3		85.5478619	3.3	-0.63
N3		85.5478619	3.3	-0.78
N4		60.3867261	3.25	0.65
O2		85.5478619	2.96	-0.37
O2		105.676771	2.96	-0.43
O2		105.676771	2.96	-0.5
O2		105.676771	2.96	-0.616
O3		85.5478619	3	-0.215
O3		70.4511804	2.9	-0.285

<i>Atom types</i>	<i>images</i>	ϵ/k_b [K]	σ [Å]	<i>Charge (e)</i>
O3		85.5478619	3	-0.33
O3		70.4511804	2.9	-0.4
O3		85.5478619	3.07	-0.585
O3		85.5478619	3.12	-0.683
S1		125.805679	3.55	0.033
S1		125.805679	3.55	-0.153

Nonbonding forcefield parameters for the Lennard-Jones (LJ) 12-6 potential equation, while ϵ indicates the LJ energy well depth and σ stands for the LJ diameter. Atom colouring: hydrogen, white; carbon, grey; nitrogen, blue; oxygen, red; fluorine, cyan; bromine, wine; sulfur, yellow. The aimed atoms of each set of parameters were set as ball model.

Table S10. The OPLS forcefield of bond stretching potential parameters for porous organic molecules in this study.⁸⁶⁻⁹¹

bond identifier		K _r [K]	R _{eq} [Å]	bond identifier		K _r [K]	R _{eq} [Å]
$E_{\text{bond}} = K_r (r - r_{\text{eq}})^2$							
S1	S1	167069.9421	2.038	Br	C3	246579.1	1.99
C2	O3	215379.3229	1.327	N2	C3	339172.1	1.449
C3	H1	342191.4477	1.09	O3	H2	556564.3	0.945
C3	C3	251611.3586	1.527	N3	C3	384462.2	1.448
C2	H1	369365.4744	1.08	C3	N2	384462.2	1.448
C3	C3	269727.3764	1.529	C2	N2	402578.2	1.385
N2	H3	436797.3185	1.01	F0	C2	422707.1	1.354
N3	H3	436797.3185	1.01	C2	C2	402578.2	1.425
C2	S1	251611.3586	1.76	Br	C2	301933.6	1.903
O3	C3	322062.539	1.38	C2	N2	417674.9	1.402
N3	C3	306965.8575	1.454	N4	C2	402578.2	1.46
C2	C2	306965.8575	1.466	C2	O3	452900.4	1.364
C3	O3	322062.539	1.41	C2	N2	503222.7	1.261
N2	C3	317030.3118	1.435	N2	C2	503222.7	1.261
C2	S1	266708.0401	1.745	N4	O2	553545	1.225
C2	C3	319043.2027	1.51	C2	O2	573673.9	1.229
C2	C2	332126.9933	1.454	C3	O2	573673.9	1.307

K_r is the harmonic stretching factors and r_{eq} is the equilibrium bond length, while the atom identifiers can be found in table S9.

Table S11: The OPLS forcefield of angle bending potential parameters for porous organic molecules in this study.⁸⁶⁻⁹¹

Angle identifier		K_θ	θ_{eq}	Angle identifier		K_θ	θ_{eq}		
$E_{\text{angle}} = K_\theta (\theta - \theta_{eq})^2$									
H1	C3	H1	33212.7	107.8	C2	C2	O3	70451.18	120
C2	C2	H1	35225.59	120	C2	C2	C3	70451.18	120
C2	C3	H1	35225.59	109.5	C2	C3	C2	70451.18	112.047
H1	C3	O3	35225.59	109.5	C3	C3	N2	70451.18	110.723
H1	C3	N2	35225.59	109.5	Br	C3	C2	70451.18	111.12
H1	C3	N3	35225.59	109.5	Br	C3	C3	70451.18	109.177
C2	O3	H2	35225.59	113	C2	N2	C2	70451.18	113.965
C2	N2	H3	35225.59	113.5	N2	C2	C3	70451.18	116.6
C3	N2	H3	35225.59	112.5	C2	O3	C3	75483.41	111
C3	N3	H3	35225.59	109.5	C2	C3	N3	75483.41	112.33
C3	C3	H1	37741.7	110.7	N2	C3	C2	75483.41	111.964
H1	C2	S1	40257.82	122.382	Br	C2	C2	75483.41	120
N2	C2	H1	45290.04	120.553	F0	C2	C2	80515.63	120
C3	N2	C2	50322.27	121.9	N2	C2	O2	80515.63	122.9
C3	N2	C3	50322.27	118	O2	N4	C2	80515.63	117.5
C3	C3	O3	50322.27	109.5	O2	C2	C3	80515.63	120.4
C2	C2	C2	50322.27	136.087	N2	C3	N2	80515.63	111.23
C3	N3	C3	52133.87	107.2	O2	C2	C2	80515.63	120.4
C3	O3	H2	55354.5	108.5	O2	C2	O3	83534.97	123.4
C3	C3	N3	56562.23	109.47	C2	C2	N4	85547.86	120
C3	C3	C3	58726.09	112.7	C2	O3	C2	85547.86	115.98
C3	O3	C3	60386.73	109.5	C2	S1	S1	85547.86	104.86
S1	C2	S1	60386.73	120	N3	C3	N3	85547.86	109
C2	C3	C3	63406.06	111.1	N2	C2	N2	90580.09	111.917
N2	C2	C2	65418.95	124.338	O3	C3	O3	93196.85	111.55
S1	C2	C2	65418.95	121.04	C2	S1	C2	110709	90.411
O3	C2	O3	125805.7	106					

K_θ is the harmonic angle bending factors and θ_{eq} is the equilibrium angle, while the atom identifiers can be found in table S9.

Table S12: The OPLS forcefield of the proper and improper torsion potential parameters for porous organic molecules in this study.⁸⁶⁻⁹¹

Proper torsion identifier				V ₀ (K)	V ₁ (K)	V ₂ (K)	V ₃ (K)
$V(\phi) = \frac{1}{2} V_0 + \frac{1}{2} V_1 [1 + \cos(\phi)] + \frac{1}{2} V_2 [1 - \cos(2\phi)] + \frac{1}{2} V_3 [1 + \cos(3\phi)]$							
C2	S1	S1	C2	0	0	-3519.54	752.8212
O3	C3	C3	O3	0	3717.809	-1840.79	0
O3	C3	O3	C3	0	-537.442	-789.053	340.1786
N3	C3	C3	N3	0	4503.843	-606.887	0
C2	N2	C3	N2	0	0	-503.223	0
C3	C3	O3	C2	0	-260.669	-473.029	117.7541
C2	O3	C3	O3	0	-257.65	-402.578	349.2366
C2	C3	N3	C3	0	831.3239	-323.069	1026.574
O3	C3	C3	C3	0	631.0413	-311.998	274.7596
C2	N2	C3	C2	0	-702.499	-214.373	0
C2	C3	C3	C3	0	-963.168	-183.173	295.895
C2	N2	C3	C3	0	-125.806	-125.806	251.6114
C3	C3	C3	N3	0	1543.887	-100.645	57.36739
C3	C3	O3	H2	0	-116.748	-94.6059	214.3729
N2	C2	C3	C3	0	1407.011	-79.5092	-189.212
N2	C3	C3	C2	0	570.6546	-75.4834	201.2891
C3	C3	C3	C3	0	570.6546	-75.4834	201.2891
N2	C3	C3	C3	0	570.6546	-75.4834	201.2891
N2	C3	C3	C3	0	570.6546	-75.4834	201.2891
C3	C3	O3	C3	0	62.39962	-11.0709	281.8047
N2	C2	C3	Br	0	0	0	0
H1	C3	C2	C2	0	0	0	0
H1	C3	C3	C2	0	0	0	434.7844
H1	C3	N2	C2	0	0	0	0
H1	C3	C3	C3	0	0	0	150.9668
H1	C3	O3	C3	0	0	0	372.3848
H1	C3	N3	C3	0	0	0	281.8047
C2	O3	C3	H1	0	0	0	80.51563
H1	C3	C3	H1	0	0	0	150.9668
O3	C3	C3	H1	0	0	0	235.5082
C3	N2	C3	H1	0	0	0	0
N2	C3	C3	H1	0	0	0	150.9668
Br	C3	C3	H1	0	0	0	400.5653
H3	N3	C3	H1	0	0	0	201.2891
H1	C3	O3	H2	0	0	0	195.2504
C2	C3	N2	H3	0	0	0	0
H1	C3	N2	H3	0	0	0	0
H1	C3	C3	N3	0	0	0	150.9668
HC	CT	CT	NI	0	0	0	150.9668
C2	C2	S1	S1	0	0	0	0
C3	N3	C3	C3	0	236.5147	21.13535	253.6242

Proper torsion identifier				V ₀ (K)	V ₁ (K)	V ₂ (K)	V ₃ (K)
C3	N3	C3	N3	0	233.4953	21.13535	251.6114
C3	C3	C2	C2	0	0	41.26426	0
C2	C3	C2	C2	0	0	43.27715	0
N2	C3	C2	C2	0	0	43.27715	0
C2	C3	N3	H3	0	769.9308	57.36739	-914.859
C3	N2	C3	C3	0	1962.569	159.0184	56.36094
C3	N2	C3	N2	0	0	179.1473	0
C3	N2	C3	C2	0	0	179.1473	0
N3	C3	C2	C2	0	0	186.1924	140.9024
O2	C2	C3	Br	0	0	302.9401	0
O2	C2	C3	C3	0	0	302.9401	0
S1	C2	C2	H1	0	0	302.9401	167.0699
C3	N2	C2	N2	0	4597.443	319.0432	0
H3	N3	C3	C3	0	32.20625	340.1786	0
N2	C2	C2	C2	0	761.8792	349.2366	332.127
C2	C2	C2	C2	0	-195.25	637.08	75.48341
H1	C2	C2	C2	0	147.9475	655.196	0
O2	N4	C2	C2	0	0	704.5118	0
H2	O3	C2	C2	0	0	846.4206	0
C2	C2	O3	C2	0	13.08379	985.3101	-560.59
C2	N2	C2	C2	0	0	1006.445	0
C2	C2	N2	H3	0	0	1006.445	0
N2	C2	C2	S1	0	0	1029.594	0
O2	C2	C2	C2	0	0	1056.768	0
C2	C2	N2	C3	0	-1006.45	1258.057	0
C2	C3	C3	C2	0	-949.078	1334.547	-71.4576
C3	N2	C2	C3	0	1507.655	1548.92	0
C2	C2	O3	C3	0	0	1970.62	0
O3	C2	O3	C2	0	0	2012.891	0
O3	C2	O3	C3	0	0	2012.891	0
O2	C2	O3	C2	0	0	3019.336	0
O2	C2	O3	C3	0	0	3019.336	0
C3	N2	C2	O2	0	0	3064.626	0
C2	S1	C2	C2	0	0	3648.365	0
Br	C2	C2	C2	0	0	3648.365	0
C2	C2	C2	C3	0	0	3648.365	0
C3	C2	C2	C3	0	0	3648.365	0
C3	C2	C2	H1	0	0	3648.365	0
H1	C2	C2	H1	0	0	3648.365	0
C2	C2	C2	O3	0	0	3648.365	0
O3	C2	C2	O3	0	0	3648.365	0
C3	C2	C2	O3	0	0	3648.365	0
H1	C2	C2	O3	0	0	3648.365	0
C2	S1	C2	S1	0	0	3648.365	0
H1	C2	C2	Br	0	0	3648.365	0
S1	C2	C2	C2	0	0	3648.365	0
N4	C2	C2	C2	0	0	3648.365	0

Proper torsion identifier				V ₀ (K)	V ₁ (K)	V ₂ (K)	V ₃ (K)
F0	C2	C2	C2	0	0	3648.365	0
H1	C2	S1	C2	0	0	3648.365	0
H1	C2	C2	F0	0	0	3648.365	0
N2	C2	C2	H1	0	0	3648.365	0
N4	C2	C2	H1	0	0	3648.365	0
C2	N2	C2	H1	0	0	4025.782	0
H1	C2	N2	C3	0	-27.174	5310.006	0
Improper torsion identifier				V ₀	V ₁	V ₂	V ₃
C2	C2	C2	C3	0	0	4025.782	0
H1	C2	N2	C2	0	0	10567.68	0
C2	C2	C2	C2	0	0	4025.782	0
H1	C2	C2	C2	0	0	1107.09	0
C2	C2	C2	H1	0	0	1107.09	0
C2	C2	N2	H1	0	0	10567.68	0
C2	C2	C3	C2	0	0	4025.782	0
C3	C2	C2	C2	0	0	4025.782	0
C2	C2	O3	C2	0	0	4025.782	0
C2	C2	C2	Br	0	0	4025.782	0
C2	N2	C2	C2	0	0	1006.445	0
C2	C2	N2	C2	0	0	4025.782	0
H1	C2	C2	S1	0	0	1107.09	0
C2	C2	H1	S1	0	0	1107.09	0
C2	C2	Br	C2	0	0	4025.782	0
C2	C2	C2	S1	0	0	4025.782	0
S1	C2	C2	S1	0	0	4025.782	0
C2	C2	H1	C2	0	0	1107.09	0
C2	C2	C2	N2	0	0	4025.782	0
C2	C2	N4	C2	0	0	4025.782	0
C2	C2	C2	N4	0	0	4025.782	0
C2	C2	S1	H1	0	0	1107.09	0
S1	C2	C2	H1	0	0	1107.09	0
C2	C2	F0	C2	0	0	4025.782	0
H3	N2	C3	C2	0	0	1006.445	0
O3	C2	C2	C2	0	0	4025.782	0
C2	C2	C2	O3	0	0	4025.782	0
O3	C2	O2	O3	0	0	10567.68	0
C3	N2	C3	C2	0	0	1006.445	0
N2	C2	O2	C3	0	0	10567.68	0
H1	C2	C2	N2	0	0	10567.68	0
C2	C2	H1	N2	0	0	10567.68	0
N2	C2	N2	O2	0	0	10567.68	0
C3	N2	C2	C3	0	0	1006.445	0
N2	C2	C2	O2	0	0	10567.68	0
Br	C2	C2	C2	0	0	4025.782	0

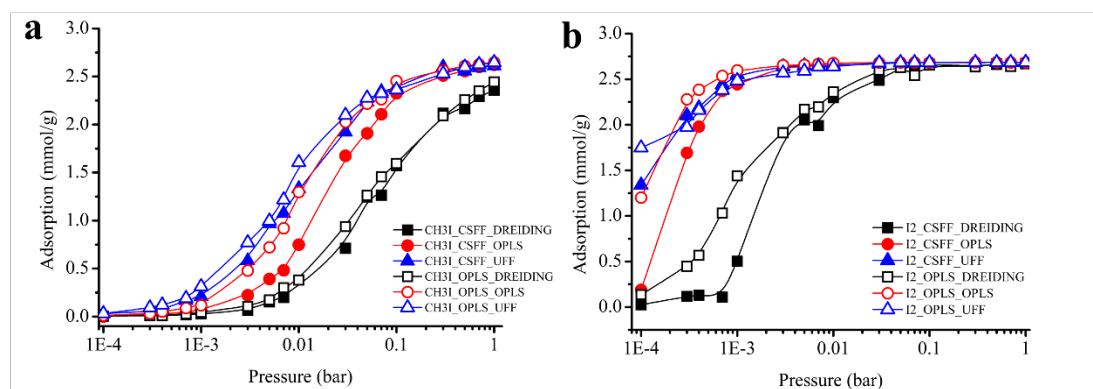


Figure S13. The CH₃I (a) and I₂ (b) adsorption isotherms in CC3R that computed from flexible host approach with both CSFF (solid symbol) and OPLS (open symbol) fully flexible force fields. The DREIDING (black), OPLS (red), and UFF (blue) nonbonding force fields have been used.

Table S13: The rigid host adsorption values of diluted CH₃I and I₂ with N₂ mixture at 423K.

PMCs	CH ₃ I (mmol/g)			I ₂ (mmol/g)		
	300ppm	500ppm	700ppm	300ppm	500ppm	700ppm
<i>IAT-RCC3</i>	0.12861	0.1900	0.2884	1.44965	1.57138	1.673
<i>B11</i>	0.01059	0.0194	0.0256	0.10235	0.17514	0.24682
<i>B11_P-3</i>	0.03937	0.0613	0.0850	0.64132	0.75227	0.80818
<i>B13</i>	0.07228	0.1154	0.1426	0.89444	1.09159	1.20941
<i>B15_CH2Cl2</i>	0.00534	0.0108	0.0152	0.03804	0.06023	0.08443
<i>B15_CHCl3</i>	0.03487	0.0557	0.0785	0.68953	0.92001	1.07205
<i>B2</i>	0.01675	0.0269	0.0401	0.04122	0.07076	0.0992
<i>B23</i>	0.02495	0.0379	0.0651	0.31299	0.49314	0.67556
<i>B24</i>	0.00863	0.0152	0.0227	0.04429	0.07651	0.0998
<i>B26</i>	0.00547	0.0065	0.0107	0.06502	0.11101	0.14524
<i>B9</i>	0.00851	0.0105	0.0173	0.00458	0.00655	0.01048
<i>C1</i>	0.00424	0.0069	0.0100	0.16325	0.25908	0.34307
<i>C13</i>	0.02109	0.0296	0.0401	0.05057	0.08323	0.09687
<i>C2</i>	0.00607	0.0108	0.0185	1.34955E-4	2.69909E-4	2.69909E-4
<i>C21_Tri4Di6</i>	0.01437	0.0294	0.0386	0.05395	0.09067	0.14398
<i>C23</i>	0.02384	0.0495	0.0712	0.25123	0.42796	0.57727
<i>C26</i>	0.00442	0.0063	0.0121	0.00768	0.01268	0.01671
<i>C7</i>	0.03462	0.0465	0.0649	0.96167	1.57772	2.13265
<i>C9</i>	0.05937	0.0862	0.1225	0.17148	0.28781	0.41637
<i>CB6</i>	1.28447	1.4129	1.4851	1.00891	1.01267	1.01628
<i>CB7</i>	1.13412	1.3788	1.5418	1.58138	1.76593	1.88906
<i>CC10</i>	0	0.0000	0.0000	0	0.0000	0.0000
<i>CC3R</i>	0.03414	0.0369	0.0576	2.35578	2.49011	2.5556
<i>CC3RS</i>	0.04296	0.0705	0.0956	2.49011	2.55951	2.58974
<i>CC4</i>	0.0113	0.0139	0.0217	0.11191	0.17325	0.2249
<i>CC5</i>	0.00257	0.0096	0.0077	0.05475	0.08746	0.12016

PMCs	CH ₃ I (mmol/g)			I ₂ (mmol/g)		
	300ppm	500ppm	700ppm	300ppm	500ppm	700ppm
<i>CC9</i>	0.00603	0.0078	0.0166	0.2027	0.33762	0.46618
<i>CD3</i>	0.01165	0.0222	0.0299	0.25033	0.4229	0.59554
<i>FTRCC3</i>	0.17727	0.3200	0.4983	2.47298	2.47247	2.47247
<i>HCI</i>	0.03688	0.0593	0.0736	0.65002	1.58324	2.66727
<i>IC2</i>	0.00853	0.0144	0.0212	0.23384	0.38003	0.55033
<i>MC3</i>	0.02826	0.0475	0.0642	0.44239	0.7219	0.98805
<i>MC4</i>	0.01618	0.0269	0.0392	0.40049	0.47209	0.5256
<i>MC5</i>	0.01304	0.0109	0.0228	0.05722	0.09054	0.12458
<i>MC7</i>	0.02788	0.0422	0.0570	0.57681	0.84309	1.0398
<i>NC1</i>	0.03683	0.0627	0.0828	0.67276	0.72892	0.74384
<i>NC2</i>	0.02118	0.0313	0.0419	0.57144	0.63401	0.68893
<i>RCC1b</i>	0.02838	0.0451	0.0670	1.81288	1.84278	1.85169
<i>RCC1c</i>	0.01878	0.0285	0.0398	0.73704	1.22176	1.73726
<i>RCC1d</i>	0.0378	0.0620	0.0855	1.2562	1.953	2.33617
<i>WC4</i>	0.03622	0.0510	0.0768	0.92034	1.2444	1.46694

A.7 Simulation inputs and computational expense

RASPA simulation input example for CH₄ GCMC/MD simulation

SimulationType: MonteCarlo NumberOfCycles: 200000 NumberOfInitializationCycles: 800000 NumberOfEquilibrationCycles : 0 PrintEvery: 1000 RestartFile: no ComputeRDF: yes WriteRDFEvery: 2000	Forcefield: CC3R_alpha_CSFF_DREIDING ChargeMethod: Ewald CutOffVDW: 12.0 CutOffChargeCharge: 12.0 EwaldPrecision: 1e-6	Framework 0 FrameworkName: CC3R_alpha Asymmetric: yes InputFileType: cif UnitCells: 1 1 1 ExternalTemperature: 275 ExternalPressure: 110000.0
Movies: yes WriteMoviesEvery: 10000 RestrictFrameworkAtomsToBox no HybridNPHMoveProbability: 0.1 NumberOfHybridNPHSteps: 5 TimeStep: 0.0005 ComputePolarization: no	FlexibleFramework: yes FrameworkDefinitions: CC3R_alpha_flexible_CSFF InternalFrameworkLennardJonesInteractions: yes RemoveBondNeighboursFromLongRangeInteraction: yes RemoveBendNeighboursFromLongRangeInteraction: yes RemoveTorsionNeighboursFromLongRangeInteraction: no	Component:0 MoleculeName: methane MoleculeDefinition: TrapPE MolFraction: 1.0 TranslationProbability: 1.0 SwapProbability: 1.0 RotationProbability: 1.0 CreateNumberOfMolecules: 0 IdealGasRosenbluthWeight: 1 ReinsertionProbability: 1.0

Here is a general RASPA simulation input example of GCMC/MD simulation. The type of simulation is defined as “MonteCarlo”. 80,000 of equilibrium cycles and 20,000 of production cycles consist of this simulation. The RDF is sampled every 2000 cycles, and the adsorption snapshots are extracted every 10000. “HybridNPHMoveProbability” is the key component of flexible host simulation with the probability of this move is 2.44%, and 5 steps of NPH MD moves are performed that allows the flexibility of system. This simulation costs 157 hours to finish, which is a typical time consuming for a system of 1358 particles system (framework: 1344, average

number of guests: 14)

A.8. Reference

1. Mastalerz, M. Porous Shape-Persistent Organic Cage Compounds of Different Size, Geometry, and Function. *Acc. Chem. Res.* **51**, 2411–2422 (2018).
2. Tozawa, T. *et al.* Porous Organic Cages. *Nat. Mater.* **8**, 973–978 (2009).
3. Holst, J. R., Trewin, A. & Cooper, A. I. Porous organic molecules. *Nat. Chem.* **2**, 915–920 (2010).
4. Bojdys, M. J. *et al.* Supramolecular engineering of intrinsic and extrinsic porosity in covalent organic cages. *J. Am. Chem. Soc.* **133**, 16566–16571 (2011).
5. Jelfs, K. E. *et al.* Conformer interconversion in a switchable porous organic cage. *Phys. Chem. Chem. Phys.* **13**, 20081–20085 (2011).
6. Jelfs, K. E. *et al.* Large self-assembled chiral organic cages: Synthesis, structure, and shape persistence. *Angew. Chemie - Int. Ed.* **50**, 10653–10656 (2011).
7. Hasell, T., Chong, S. Y., Jelfs, K. E., Adams, D. J. & Cooper, A. I. Porous organic cage nanocrystals by solution mixing. *J. Am. Chem. Soc.* **134**, 588–598 (2012).
8. Hasell, T., Schmidtman, M., Stone, C. A., Smith, M. W. & Cooper, A. I. Reversible water uptake by a stable imine-based porous organic cage. *Chem. Commun.* **48**, 4689–4691 (2012).
9. Giri, N. *et al.* Alkylated organic cages: From porous crystals to neat liquids. *Chem. Sci.* **3**, 2153–2157 (2012).
10. Hasell, T., Chong, S. Y., Schmidtman, M., Adams, D. J. & Cooper, A. I. Porous organic alloys. *Angew. Chemie - Int. Ed.* **51**, 7154–7157 (2012).
11. Cooper, A. I. Molecular organic crystals: From barely porous to really porous. *Angew. Chemie - Int. Ed.* **51**, 7892–7894 (2012).
12. Holden, D., Jelfs, K. E., Cooper, A. I., Trewin, A. & Willock, D. J. Bespoke force field for simulating the molecular dynamics of porous organic cages. *J. Phys. Chem. C* **116**, 16639–

- 16651 (2012).
13. Hasell, T., Zhang, H. & Cooper, A. I. Solution-processable molecular cage micropores for hierarchically porous materials. *Adv. Mater.* **24**, 5732–5737 (2012).
 14. McKeown, N. B. Nanoporous molecular crystals. *J. Mater. Chem.* **20**, 10588 (2010).
 15. Bojdys, M. J. *et al.* Porous organic cage crystals: Characterising the porous crystal surface. *Chem. Commun.* **48**, 11948–11950 (2012).
 16. Mitra, T. *et al.* Molecular shape sorting using molecular organic cages. *Nat. Chem.* **5**, 276–281 (2013).
 17. Jelfs, K. E. *et al.* In silico design of supramolecules from their precursors: Odd-even effects in cage-forming reactions. *J. Am. Chem. Soc.* **135**, 9307–9310 (2013).
 18. Culshaw, J. L. *et al.* Dodecaamide cages: Organic 12-arm building blocks for supramolecular chemistry. *J. Am. Chem. Soc.* **135**, 10007–10010 (2013).
 19. Hasell, T. *et al.* High-pressure carbon dioxide uptake for porous organic cages: Comparison of spectroscopic and manometric measurement techniques. *Chem. Commun.* **49**, 9410–9412 (2013).
 20. Jelfs, K. E. & Cooper, A. I. Molecular simulations to understand and to design porous organic molecules. *Curr. Opin. Solid State Mater. Sci.* **17**, 19–30 (2013).
 21. Hasell, T. *et al.* Controlling the crystallization of porous organic cages: Molecular analogs of isorecticular frameworks using shape-specific directing solvents. *J. Am. Chem. Soc.* **136**, 1438–1448 (2014).
 22. Liu, M. *et al.* Acid- and base-stable porous organic cages: Shape persistence and pH stability via post-synthetic ‘tying’ of a flexible amine cage. *J. Am. Chem. Soc.* **136**, 7583–7586 (2014).
 23. Pyzer-Knapp, E. O. *et al.* Predicted crystal energy landscapes of porous organic cages. *Chem. Sci.* **5**, 2235–2245 (2014).
 24. Holden, D. *et al.* Gas diffusion in a porous organic cage: Analysis of dynamic pore connectivity using molecular dynamics simulations. *J. Phys. Chem. C* **118**, 12734–12743 (2014).

25. Hasell, T. *et al.* Triply interlocked covalent organic cages. *Nat. Chem.* **2**, 750–755 (2010).
26. Little, M. A., Chong, S. Y., Schmidtman, M., Hasell, T. & Cooper, A. I. Guest control of structure in porous organic cages. *Chem. Commun.* **50**, 9465–9468 (2014).
27. Chen, L. *et al.* Separation of rare gases and chiral molecules by selective binding in porous organic cages. *Nat. Mater.* **13**, 954–960 (2014).
28. Manurung, R. *et al.* Tunable Porosity through Cooperative Diffusion in a Multicomponent Porous Molecular Crystal. *J. Phys. Chem. C* **119**, 22577–22586 (2015).
29. Briggs, M. E. *et al.* Dynamic flow synthesis of porous organic cages. *Chem. Commun.* **51**, 17390–17393 (2015).
30. Giri, N. *et al.* Liquids with permanent porosity. *Nature* **527**, 216–220 (2015).
31. Reiss, P. S. *et al.* Periphery-Functionalized Porous Organic Cages. *Chem. - A Eur. J.* **22**, 16547–16553 (2016).
32. Liu, M. *et al.* Three-dimensional protonic conductivity in porous organic cage solids. *Nat. Commun.* **7**, 1–9 (2016).
33. Holden, D. *et al.* Understanding Static, Dynamic and Cooperative Porosity in Molecular Materials. *Chem. Sci.* **00**, 1–5 (2016).
34. Hasell, T. *et al.* Porous Organic Cages for Sulfur Hexafluoride Separation. *J. Am. Chem. Soc.* **138**, 1653–1659 (2016).
35. Song, Q. *et al.* Porous Organic Cage Thin Films and Molecular-Sieving Membranes. *Adv. Mater.* **28**, 2629–2637 (2016).
36. Jones, J. T. a. *et al.* On-Off Porosity Switching in a Molecular Organic Solid. *Angew. Chemie Int. Ed.* **50**, 749–753 (2011).
37. Slater, A. G. *et al.* Reticular synthesis of porous molecular 1D nanotubes and 3D networks. *Nat. Chem.* **9**, 17–25 (2017).
38. Greenaway, R. L. *et al.* Understanding gas capacity, guest selectivity, and diffusion in porous liquids. *Chem. Sci.* **8**, 2640–2651 (2017).
39. Briggs, M. E. & Cooper, A. I. A perspective on the synthesis, purification, and

- characterization of porous organic cages. *Chem. Mater.* **29**, 149–157 (2017).
40. Cooper, A. I. Porous Molecular Solids and Liquids. *ACS Cent. Sci.* **3**, 544–553 (2017).
 41. Hasell, T. *et al.* Chirality as a tool for function in porous organic cages. *Nanoscale* **9**, 6783–6790 (2017).
 42. Tothadi, S. *et al.* Modular assembly of porous organic cage crystals: Isoreticular quasiracemates and ternary co-crystal. *CrystEngComm* **19**, 4933–4941 (2017).
 43. Slater, A. G. *et al.* Computationally-Guided Synthetic Control over Pore Size in Isostructural Porous Organic Cages. *ACS Cent. Sci.* **3**, 734–742 (2017).
 44. Jiang, S. *et al.* Oriented Two-Dimensional Porous Organic Cage Crystals. *Angew. Chemie - Int. Ed.* **56**, 9391–9395 (2017).
 45. Hughes, A. R. *et al.* Ultra-Fast Molecular Rotors within Porous Organic Cages. *Chem. - A Eur. J.* **23**, 17217–17221 (2017).
 46. Slater, A. G., Little, M. A., Briggs, M. E., Jelfs, K. E. & Cooper, A. I. A solution-processable dissymmetric porous organic cage. *Mol. Syst. Des. Eng.* **3**, 223–227 (2018).
 47. Lydon, D. P., Campbell, N. L., Adams, D. J. & Cooper, A. I. Scalable synthesis for porous organic cages. *Synth. Commun.* **41**, 2146–2151 (2011).
 48. Pugh, C. J. *et al.* Cage Doubling: Solvent-Mediated Re-equilibration of a [3 + 6] Prismatic Organic Cage to a Large [6 + 12] Truncated Tetrahedron. *Cryst. Growth Des.* **18**, 2759–2764 (2018).
 49. McMahon, D. P. *et al.* Computational modelling of solvent effects in a prolific solvatomorphic porous organic cage. *Faraday Discuss.* **211**, 383–399 (2018).
 50. Hernández-Ibáñez, N. *et al.* pH effects on molecular hydrogen storage in porous organic cages deposited onto platinum electrodes. *J. Electroanal. Chem.* **819**, 46–50 (2018).
 51. Jiang, S. *et al.* Core–Shell Crystals of Porous Organic Cages. *Angew. Chemie - Int. Ed.* **57**, 11228–11232 (2018).
 52. Berardo, E. *et al.* Computationally-inspired discovery of an unsymmetrical porous organic cage. *Nanoscale* **10**, 22381–22388 (2018).

53. Greenaway, R. L. *et al.* High-throughput discovery of organic cages and catenanes using computational screening fused with robotic synthesis. *Nat. Commun.* 1–27 (2018). doi:10.1038/s41467-018-05271-9
54. Jones, J. T. a *et al.* Modular and predictable assembly of porous organic molecular crystals. *Nature* **474**, 367–371 (2011).
55. Jiang, S. *et al.* Selective gas sorption in a [2+3] ‘propeller’ cage crystal. *Chem. Commun.* **47**, 8919–8921 (2011).
56. Mitra, T. *et al.* A soft porous organic cage crystal with complex gas sorption behavior. *Chem. - A Eur. J.* **17**, 10235–10240 (2011).
57. Hasell, T., Schmidtman, M. & Cooper, A. I. Molecular doping of porous organic cages. *J. Am. Chem. Soc.* **133**, 14920–14923 (2011).
58. Tozawa, T. *et al.* Porous organic cages. *Nat. Mater.* **8**, 973–978 (2009).
59. Kewley, A. *et al.* Porous organic cages for gas chromatography separations. *Chem. Mater.* **27**, 3207–3210 (2015).
60. Mayo, S. L., Olafson, B. D., Iii, W. a G., Eb, E. & El, E. a E. T. DREIDING: A Generic Force Field for Molecular Simulations. *J. Phys. Chem.* **101**, 8897–8909 (1990).
61. Jorgensen, W. L. *et al.* Development and Testing of the OLPS All-Atom Force Field on Conformational Energetics and Properties of Organic Liquids. *J. Am. Chem. Soc.* **118**, 11225–11236 (1996).
62. Rappé, A. K., Casewit, C. J., Colwell, K. S., Goddard, W. A. & Skiff, W. M. UFF, a Full Periodic Table Force Field for Molecular Mechanics and Molecular Dynamics Simulations. *J. Am. Chem. Soc.* **114**, 10024–10035 (1992).
63. Dubbeldam, D., Calero, S., Ellis, D. E. & Snurr, R. Q. RASPA: molecular simulation software for adsorption and diffusion in flexible nanoporous materials. *Mol. Simul.* **7022**, 1–21 (2015).
64. Accelry. Materials Studio 7.0. (2013).
65. Bardelang, D. *et al.* Cucurbit[n]urils (n = 5-8): A comprehensive solid state study. *Cryst.*

- Growth Des.* **11**, 5598–5614 (2011).
66. Kim, J. *et al.* New cucurbituril homologues: Syntheses, isolation, characterization, and X-ray crystal structures of cucurbit[n]uril (n = 5, 7, and 8). *J. Am. Chem. Soc.* **122**, 540–541 (2000).
67. Zhang, J., Ren, H. & Liu, L. Trifluoromethanesulfonate Anion-linked Supramolecular Frameworks of Cucurbit[5]uril and Cucurbit[7]uril. *Chem. Lett.* **39**, 1016–1017 (2010).
68. Skowronek, P. & Gawronski, J. Chiral iminospherand of a tetrahedral symmetry spontaneously assembled in a [6 + 4] cyclocondensation. *Org. Lett.* **10**, 4755–4758 (2008).
69. Jones, J. T. A. *et al.* Modular and predictable assembly of porous organic molecular crystals. *Nature* **474**, 367–371 (2011).
70. Crini, G. Review: A history of cyclodextrins. *Chem. Rev.* **114**, 10940–10975 (2014).
71. Steiner, T. & Saenger, W. Channel-Type Crystal Packing in the Very Rare Space Group P4212 with $Z' = 3/4$: Crystal Structure of the Complex γ -Cyclodextrin-Methanol-n-Hydrate †. *Acta Crystallogr. Sect. B Struct. Sci.* **54**, 450–455 (1998).
72. Brotin, T. & Dutasta, J.-P. Cryptophanes and Their Complexes—Present and Future. *Chem. Rev.* **109**, 88–130 (2009).
73. Taratula, O., Hill, P. A., Khan, N. S., Carroll, P. J. & Dmochowski, I. J. Crystallographic observation of ‘induced fit’ in a cryptophane host-guest model system. *Nat. Commun.* **1**, 147–148 (2010).
74. Joseph, A. I., Lapidus, S. H., Kane, C. M. & Holman, K. T. Extreme confinement of xenon by cryptophane-111 in the solid state. *Angew. Chemie - Int. Ed.* **54**, 1471–1475 (2015).
75. Joseph, A. I. *et al.* Rim-functionalized cryptophane-111 derivatives via heterocapping, and their xenon complexes. *Chem. Commun.* **50**, 15905–15908 (2014).
76. Horng, Y. C. *et al.* Preparation of a reversible redox-controlled cage-type molecule linked by disulfide bonds. *European J. Org. Chem.* 1511–1514 (2009).
doi:10.1002/ejoc.200900044
77. Matsui, K., Segawa, Y. & Itami, K. All-benzene carbon nanocages: Size-selective synthesis,

- photophysical properties, and crystal structure. *J. Am. Chem. Soc.* **136**, 16452–16458 (2014).
78. Schneider, M. W., Oppel, I. M. & Mastalerz, M. Exo-functionalized shape-persistent [2+3] cage compounds: Influence of molecular rigidity on formation and permanent porosity. *Chem. - A Eur. J.* **18**, 4156–4160 (2012).
79. Schneider, M. W., Oppel, I. M., Griffin, A. & Mastalerz, M. Post-modification of the interior of porous shape-persistent organic cage compounds. *Angew. Chemie - Int. Ed.* **52**, 3611–3615 (2013).
80. Acharyya, K. & Mukherjee, P. S. A fluorescent organic cage for picric acid detection. *Chem. Commun.* **50**, 15788–15791 (2014).
81. Kudo, H. *et al.* Molecular waterwheel (noria) from a simple condensation of resorcinol and an alkanedial. *Angew. Chemie - Int. Ed.* **45**, 7948–7952 (2006).
82. Tian, J., Thallapally, P. K., Dalgarno, S. J., McGrail, P. B. & Atwood, J. L. Amorphous molecular organic solids for gas adsorption. *Angew. Chemie - Int. Ed.* **48**, 5492–5495 (2009).
83. Warmuth, R., Maverick, E. F., Knobler, C. B. & Cram, D. J. Through-shell alkyllithium additions and borane reductions. *J. Org. Chem.* **68**, 2077–2088 (2003).
84. Park, B. S., Knobler, C. B., Eid, C. N., Warmuth, R. & Cram, D. J. Chiral and somewhat hydrophilic hemicarceplexes. *Chem. Commun.* **1**, 55–56 (1998).
85. Givélet, C. *et al.* Templated dynamic cryptophane formation in water. *Chem. Commun.* **47**, 4511–4513 (2011).
86. Pranata, J., Wierschke, S. G. & Jorgensen, W. L. OPLS Potential Functions for Nucleotide Bases. Relative Association Constants of Hydrogen-Bonded Base Pairs in Chloroform. *J. Am. Chem. Soc.* **113**, 2810–2819 (1991).
87. Jorgensen, W. L. & Tirado-Rives, J. The OPLS [optimized potentials for liquid simulations] potential functions for proteins, energy minimizations for crystals of cyclic peptides and crambin. *J. Am. Chem. Soc.* **110**, 1657–1666 (1988).
88. WL, J., DS, M. & J, T. Development and Testing of the Opls All-Atom Force-Field on Conformational Energetics and Properties of Organic Liquids. *J. Am. Chem. Soc.* **118**,

- 11225–11236 (1996).
89. Damm, W., Frontera, A., Tirado-Rives, J. & Jorgensen, W. L. OPLS all-atom force field for carbohydrates. *J. Comput. Chem.* **18**, 1955–1970 (1997).
90. Kaminski, G. a, Friesner, R. a, Tirado-rives, J. & Jorgensen, W. L. Comparison with Accurate Quantum Chemical Calculations on Peptides †. *J. Phys. Chem. B* **105**, 6474–6487 (2001).
91. Jorgensen, W. L., Maxwell, D. S. & Tirado-Rives, J. Development and Testing of the OLPS All-Atom Force Field on Conformational Energetics and Properties of Organic Liquids. *J. Am. Chem. Soc.* **118**, 11225–11236 (1996).